

# NOTE TO USERS

This reproduction is the best copy available.

**UMI<sup>®</sup>**



# **COMPUTER SIMULATION OF THE FILM BLOWING PROCESS INCORPORATING CRYSTALLIZATION AND VISCOELASTICITY**

**Iyad A. Muslet**

**Department of Chemical Engineering  
McGill University, Montreal, Quebec, Canada**

**June 2004**

A thesis submitted to the faculty of graduate studies and research in partial fulfillment of  
the requirements for the degree of Doctor of Philosophy

©Iyad A. Muslet (2004). All rights reserved



Library and  
Archives Canada

Bibliothèque et  
Archives Canada

Published Heritage  
Branch

Direction du  
Patrimoine de l'édition

395 Wellington Street  
Ottawa ON K1A 0N4  
Canada

395, rue Wellington  
Ottawa ON K1A 0N4  
Canada

*Your file    Votre référence*

*ISBN: 0-494-06329-7*

*Our file    Notre référence*

*ISBN: 0-494-06329-7*

#### NOTICE:

The author has granted a non-exclusive license allowing Library and Archives Canada to reproduce, publish, archive, preserve, conserve, communicate to the public by telecommunication or on the Internet, loan, distribute and sell theses worldwide, for commercial or non-commercial purposes, in microform, paper, electronic and/or any other formats.

The author retains copyright ownership and moral rights in this thesis. Neither the thesis nor substantial extracts from it may be printed or otherwise reproduced without the author's permission.

#### AVIS:

L'auteur a accordé une licence non exclusive permettant à la Bibliothèque et Archives Canada de reproduire, publier, archiver, sauvegarder, conserver, transmettre au public par télécommunication ou par l'Internet, prêter, distribuer et vendre des thèses partout dans le monde, à des fins commerciales ou autres, sur support microforme, papier, électronique et/ou autres formats.

L'auteur conserve la propriété du droit d'auteur et des droits moraux qui protègent cette thèse. Ni la thèse ni des extraits substantiels de celle-ci ne doivent être imprimés ou autrement reproduits sans son autorisation.

---

In compliance with the Canadian Privacy Act some supporting forms may have been removed from this thesis.

Conformément à la loi canadienne sur la protection de la vie privée, quelques formulaires secondaires ont été enlevés de cette thèse.

While these forms may be included in the document page count, their removal does not represent any loss of content from the thesis.

Bien que ces formulaires aient inclus dans la pagination, il n'y aura aucun contenu manquant.

  
**Canada**



# Abstract

A comprehensive two-dimensional simulation of the film blowing process is developed based on a mathematical model that incorporates the Phan-Thien and Tanner (PTT) and the Neo-Hookean constitutive equations with crystallization effects. The PTT constitutive equation is employed in the liquid-like region, while the Neo-Hookean constitutive equation is employed in the solid-like region, to describe the rheological behavior of the film. The effects of the process variables and parameters on the stress balance and overall behavior of the film were evaluated. The orientation-induced crystallization is accounted for by incorporating the Nakamura non-isothermal equation along with the Ziabicki equation. The proposed model provides predictions of the bubble shape and dimensions, the position of the freeze-line, and the evolution of temperature, crystallinity, birefringence, stresses and deformation in the blown film. The predictions of the model show good agreement with experimental results reported by various workers.

# Résumé

Une simulation à deux dimensions du procédé de soufflage de gaine est développée à partir d'un modèle mathématique qui incorpore les équations constitutives de Phan-Thien and Tanner (PTT) et Neo-Hookeiennes, et les effets de la cristallisation. L'équation constitutive PPT est utilisée dans la région liquide, tandis que l'équation constitutive Neo-Hookeienne est utilisée dans la région solide, pour décrire le comportement rhéologique du film. Les effets des paramètres et des variables du procédé de gonflage sur les contraintes et le comportement global du film ont été évalués. La cristallisation induite par l'orientation est incorporée dans la simulation en utilisant les équations non-isotherme de Nakamura et celle de Ziabicki. Le modèle proposé fournit des prédictions sur la forme et les dimensions de la gaine, la position de la ligne de solidification, et sur l'évolution de la température, la cristallinité, la biréfringence, les contraintes, et la déformation du film gonflé. Les prédictions du modèle sont en bon accord avec les résultats expérimentaux de plusieurs chercheurs.

# Acknowledgment

I would like to express my profound gratitude for my supervisor, professor Musa R. Kamal for his encouragement and guidance. This work could not be accomplished without his unbounded help and deep knowledge.

I am grateful to professor John Dealy and professor Martin Weber for their fruitful discussion. I would like to thank Dr. M. Hussien, Dr. P. LeBot, Dr. L. Capt, and all members of polymer research group for the lively discussion. I would like to thank Linda Lockwood for helping in preparing this thesis.

I would like to gratefully acknowledge Nova Chemicals for providing the film samples and Natural Science and Engineering Council (NSERC) for their financial support.

Last but not least, I am utterly grateful to my parents, my wife, my daughters Leena and Jenna, and all my friends for their love and support.

# TABLE OF CONTENTS

1	INTRODUCTION .....	1
2	TECHNICAL BACKGROUND .....	4
2.1	GENERAL DESCRIPTION OF THE PROCESS.....	4
2.2	MODELING AND SIMULATION OF FILM BLOWING .....	5
2.2.1	ONE DIMENSIONAL SIMULATION .....	5
2.2.1.1	Stability of One-Dimensional Solutions .....	9
2.2.1.2	Effects of the Initial Blowing Angle on Stability.....	10
2.2.1.3	Effects of Viscosity and Relaxation Time on Stability .....	11
2.2.1.4	Effect of the Inflation Pressure on the Process Stability .....	12
2.2.2	TWO-DIMENSIONAL SIMULATION .....	13
2.2.2.1	Rheological Zones.....	13
2.2.2.2	Effects of the Crystallinity .....	16
2.2.2.3	Effects of Cooling and Aerodynamics .....	18
2.3	EXPERIMENTAL STUDIES.....	24
2.3.1	STRAIN RATE AND ORIENTATION MEASUREMENTS .....	24
2.3.2	PROCESS STABILITY .....	26
2.3.3	EFFECT OF CRYSTALLIZATION.....	30
2.4	RHEOLOGICAL CONSIDERATIONS.....	35
3	SCOPE AND OBJECTIVES.....	38
4	MATHEMATICAL MODEL.....	40
4.1	DESCRIPTION OF THE FILM BLOWING PROCESS .....	40
4.2	MASS BALANCE .....	43
4.3	FORCE BALANCE .....	43
4.3.1	FORCE BALANCE IN THE NORMAL DIRECTION .....	44
4.3.2	FORCE BALANCE IN THE MACHINE DIRECTION .....	45
4.3.3	FINAL EQUATIONS OF MOTION.....	46
4.4	ENERGY BALANCE.....	48
4.4.1	MAIN ENERGY EQUATION.....	48
4.4.2	BOUNDARY CONDITIONS.....	49
4.4.3	HEAT TRANSFER COEFFICIENT.....	50
4.4.3.1	Previous Work.....	50
4.4.3.2	Proposed Method to Estimate the Heat Transfer Coefficient (HTC).....	53
4.5	RHEOLOGICAL DESCRIPTION OF THE PROCESS .....	60
4.5.1	CONSTITUTIVE EQUATIONS IN MOLTEN PHASE .....	60
4.5.2	CRYSTALLINITY AND ORIENTATION.....	64
4.5.3	CONSTITUTIVE EQUATION FOR THE SOLID-LIKE PHASE.....	66

<b>4.6</b>	<b>CRYSTALLIZATION KINETICS .....</b>	<b>69</b>
<b>4.7</b>	<b>BOUNDARY CONDITIONS .....</b>	<b>70</b>
<b>4.8</b>	<b>NUMERICAL METHODS.....</b>	<b>71</b>
4.8.1	ALGORITHM .....	71
4.8.2	INPUT PARAMETERS .....	74
4.8.3	EVALUATION OF THE NUMERICAL SCHEME.....	77
4.8.3.1	Convergence Evaluation .....	77
4.8.3.1.1	Richardson Extrapolation.....	78
4.8.3.1.2	Effects of Step Size.....	79
4.8.3.2	Stability of the Numerical Solution.....	80
4.8.3.3	Robustness of the Model .....	82
4.8.3.3.1	Effect of Rheological Parameters .....	82
4.8.3.3.2	The Parameters $\psi$ , $\phi$ , and $A$ .....	88
<b>5</b>	<b>VALIDATION OF THE MODEL .....</b>	<b>91</b>
<b>5.1</b>	<b>COMPARISON WITH ANALYTICAL AND NUMERICAL SOLUTIONS .....</b>	<b>91</b>
5.1.1	ANALYTICAL SOLUTION FOR ISOTHERMAL NEWTONIAN MELT .....	91
5.1.2	NON-ISOTHERMAL NEWTONIAN SOLUTION.....	92
5.1.3	ISOTHERMAL VISCOELASTIC MELT .....	94
<b>5.2</b>	<b>COMPARISON WITH EXPERIMENTAL RESULTS.....</b>	<b>95</b>
5.2.1	SOURCES OF EXPERIMENTAL DATA.....	95
5.2.2	EXPERIMENTAL DATA .....	96
5.2.3	COMPARISON OF EXPERIMENTAL RESULTS WITH MODEL PREDICTIONS.....	100
5.2.3.1	General Comparison.....	100
5.2.3.2	Comparison With Results of Butler (1993).....	101
5.2.3.3	Comparison With Results of Ghaneh-Fard (1997) .....	103
5.2.3.4	Comparison With Results of Tas (1994).....	104
<b>5.3</b>	<b>PREDICTION OF MICROSTRUCTURAL PROPERTIES.....</b>	<b>111</b>
5.3.1	BACKGROUND .....	111
5.3.1.1	Interaction Between Crystallization and Orientation.....	111
5.3.1.2	Orientation in Polyethylene Films.....	112
5.3.2	EXPERIMENTAL .....	116
5.3.2.1	Materials.....	116
5.3.2.2	Differential Scanning Calorimetry (DSC).....	118
5.3.2.2.1	Apparatus .....	118
5.3.2.2.2	Procedure .....	118
5.3.2.3	Birefringence.....	119
5.3.2.3.1	Apparatus .....	121
	The Polarized Light Microscope.....	121
	Rotatable Analyzer.....	121
	Compensators .....	121
5.3.2.3.2	Procedure .....	122
5.3.2.4	FTIR Experiments.....	123
5.3.2.4.1	Apparatus .....	128
5.3.2.4.2	Procedure .....	129

5.3.3	RESULTS AND DISCUSSION .....	130
5.3.3.1	Effects of Blow-up Ratio and Draw Ratio .....	130
5.3.3.2	Comparison Between the Measured and Predicted Crystallinity.....	140
5.3.3.3	Orientation in the Blown Films.....	141
5.3.3.4	FTIR Analysis .....	146
5.3.3.4.1	Orientation of the Crystallographic Axes and the Amorphous Chains in the Films.....	148
5.3.3.4.2	The Effects of Blow-up and Draw Ratios.....	150
5.3.3.5	Comparative Film Blowing Behavior of HDPE, LDPE, and LLDPE .....	152
6	CONCLUSIONS, ORIGINAL CONTRIBUTIONS, AND FUTURE WORK .....	157
6.1	SUMMARY .....	157
6.2	CONCLUSIONS .....	158
6.3	ORIGINAL CONTRIBUTIONS .....	159
6.4	SUGGESTED FUTURE STUDY.....	160
	REFERENCES.....	162
	APPENDIX A .....	172
	APPENDIX B .....	175

# LIST OF FIGURES

Figure 1: A comparison of the deformation rate in the machine direction. Gupta's measurements are shown as the diamonds, and the line represents Luo and Tanner calculations. <i>Source: Luo and Tanner (1985).</i> .....	8
Figure 2: A comparison of the deformation rate in the hoop direction. Gupta's measurements are shown as the diamonds, and the line represents Luo and Tanner calculations. <i>Sources: Luo and Tanner (1985).</i> .....	8
Figure 3: The dimensionless bubble shape as a function of the dimensionless distance from the die exit for various initial blowing angles: (- - -) $\theta_0 = 9$ degrees, .....	11
Figure 4: The two-phase model proposed by Cao and Campbell (1990). <i>Source: Kanai (1999).</i> .....	14
Figure 5: The bubble radius and film velocity as predicted by the simulation proposed by Doufas and McHugh (2001). .....	18
Figure 6: The velocity profile of the cooling air with two different air ring gap widths ( $s=5$ mm and $s = 7.5$ mm) at two freeze line heights ( $z= 1.5$ cm and $z= 3$ cm). <i>Source: Hauck and Michaeli (1998).</i> .....	22
Figure 7: The bubble shape and temperature profile as a result of changing the gap width of the air ring from 5 mm to 7.5 mm. <i>Source: Hauck and Michaeli (1998).</i> .....	23
Figure 8: Bubble shape for various PE types. <i>Source: Kanai and White (1984).</i> .....	27
Figure 9: Thickness reduction-BUR map showing regions of stable and unstable behavior of three types of PE at a dimensionless freeze line height of 16. <i>Source: Kanai and White (1984).</i> .....	28
Figure 10: The effect of the freeze line height on the HDPE bubble. <i>Source: Kanai and White (1984).</i> .....	28
Figure 11: Apparent viscosity as a function of percent crystallinity. <i>Source: Kanai and White (1985).</i> .....	31
Figure 12: The effect of the freeze line height (FLH), the take-up ratio (TUR), the blow-up ratio (BUR), and the extrusion temperature on the in- plane birefringence. <i>Source: Ghaneh-Fard et al. (1997).</i> .....	34
Figure 13: Schematic of the film blowing process. ....	41
Figure 14: The film is assumed to be a thin membrane that has two radii of curvature. ...	42
Figure 15: Dimensional representation of the differential element of the film. ....	44
Figure 16: The HTC profiles on LLDPE film surface as shown by Sidiropoulos (2000) for different flow rates of the cooling air .....	54
Figure 17: The heat transfer coefficient as a function of temperature .....	56
Figure 18: The heat transfer coefficient as a function of the bubble radius. ....	56
Figure 19: A comparison between the predicted heat transfer coefficient (lines) and the heat transfer coefficient reported (symbols) by Sidiropoulos, (2000) for three different volumetric flow rates. ....	57
Figure 20: The behavior of the heat transfer coefficient when it is defined as a function of temperature and radius only. ....	59
Figure 21: The effect of eliminating the initial turbulence near the die exit on the heat transfer coefficient. ....	59
Figure 22: A mesh map of a portion of the film. ....	71

Figure 23: The algorithm of the numerical computation .....	73
Figure 24: The estimated $R_g$ for the approximated solution of the blow-up ratio, draw ratio, and thickness reduction as a function of the step size. <i>The properties of resin G583 were employed.</i> .....	79
Figure 25: The estimated relative error, $R$ , for the approximated solution of the blow-up ratio as a function of the step size. The employed polymer is film G583. All information regarding the properties and processing conditions are specified in Tables 3-5. ....	80
Figure 26: The location of the induced error did not affect the solution for the blow-up ratio. The employed polymer is film G583. All information regarding the properties and processing conditions are specified in Tables 3-5. ....	81
Figure 27: The induced error in the solution for the blow-up ratio did not propagate, which was an indication of the stability of the numerical scheme. The employed polymer is film G583. All information regarding the properties and processing conditions are specified in Tables 3-5. ....	81
Figure 28: The induced error in the solution for the thickness ratio did not propagate, which was an indication of the stability of the numerical scheme. The employed polymer is film G583. All information regarding the properties and processing conditions are specified in Tables 3-5. ....	82
Figure 29: The effect of $\xi$ on the bubble shape. The employed polymer is film G583. All information regarding the properties and processing conditions are specified in Tables 3-5. ....	83
Figure 30: The effect of $\xi$ on the evolution of the stresses. The employed polymer is film G583. All information regarding the properties and processing conditions are specified in Tables 3-5. ....	83
Figure 31: The effect of $\varepsilon$ on the shape of the bubble. The employed polymer is film G583. All information regarding the properties and processing conditions are specified in Tables 3-5. ....	84
Figure 32: The effect of $\varepsilon$ on the evolution of the stresses. The employed polymer is film G583. All information regarding the properties and processing conditions are specified in Tables 3-5. ....	84
Figure 33: The effect of $c_1$ on the film velocity. The employed polymer is film G583. All information regarding the properties and processing conditions are specified in Tables 3-5. Simulation value: -10. ....	86
Figure 34: The effect of $c_2$ on the film velocity. The employed polymer is film G583. All information regarding the properties and processing conditions are specified in Tables 3-5. The simulation value: 470. ....	87
Figure 35: The effect of $c_3$ on the film velocity. The employed polymer is film G583. All information regarding the properties and processing conditions are specified in Tables 3-5. The simulation value: 0.0165. ....	87
Figure 36: The effect of $\psi$ on the bubble shape. The employed polymer is film G583. All information regarding the properties and processing conditions are specified in Tables 3-5. ....	88
Figure 37: The effect of $\varphi$ on the evolution of the draw ratio. The employed polymer is film G583. All information regarding the properties and processing conditions are specified in Tables 3-5. ....	89



Figure 38: The effect of $A$ on the evolution of the blow-up ratio. The employed polymer is film G583. All information regarding the properties and processing conditions are specified in Tables 3-5. ....	90
Figure 39: The effect of $A$ on the evolution of the draw ratio. The employed polymer is film G583. All information regarding the properties and processing conditions are specified in Tables 3-5. ....	90
Figure 40: The numerical solutions (lines) for the Newtonian cases when $F=3B$ are consistent with the analytical solutions (symbols) reported by Cain and Denn (1988). ....	92
Figure 41: Comparison of predicted bubble shapes, using 1-D nonisothermal Newtonian model [lines] with the predictions of Kanai and White [symbols] (1985) at different dimensionless take-up force ( $F$ ) and constant dimensionless inflation pressure ( $B = 0.309$ ). ....	93
Figure 42: Comparison of predicted draw ratio, using 1-D nonisothermal Newtonian model [lines] with the predictions of Kanai and White [symbols] (1985) at different dimensionless take-up force ( $F$ ) and constant dimensionless inflation pressure ( $B = 0.309$ ). ....	93
Figure 43: Comparison of bubble shapes predicted by the proposed model, using 1-D isothermal Maxwell model [lines] with the predictions of Luo and Tanner [symbols] (1985) at different Deborah numbers ( $De$ ) and constant dimensionless Take up force ( $F=0.1.34$ ) and inflation pressure ( $B = 0.2$ ). ....	94
Figure 44: The melt viscosity profiles of the LLDPE used in this study. ....	99
Figure 45: Comparison of predicted bubble radius and film thickness with Butler's measured results at the conditions specified in Tables 6-9. ....	102
Figure 46: The effect of the ultimate crystallinity on the predicted temperature and crystallinity development, for conditions specified in the tables for experimental conditions employed by Butler (1993). ....	102
Figure 47: Comparison of predicted bubble radius and film velocity with measured results of Ghaneh-Fard (1997), at the conditions specified in Tables 6-9. ....	103
Figure 48: Comparison of predicted bubble radius and film velocity (lines) with measured results (symbols) of Tas (1994), at the conditions specified in Tables 6-10. Exp 3 (inflation pressure = 135 Pa, Take-up Force = 6.6 N), Exp 6 (120 Pa, 6.7 N), Exp 9 (105 Pa, 5.7 N). ....	105
Figure 49: Comparison of predicted bubble radius and film velocity (lines) with measured results (symbols) of Tas (1994), at the conditions specified in Tables 6-10. Exp.12 (inflation pressure=118 Pa, Take-up Force=7.6 N), Exp.15 (108 Pa, 7.7 N), Exp.18 (95 Pa, 6.9 N). ....	106
Figure 50: Comparison between the predicted film thickness (lines) and the measured results (symbols) of Tas (1994). The processing conditions are specified in Tables 6-10. ....	107
Figure 51: Comparison of predicted temperature profiles (lines) with measured results (symbols) of Tas (1994), at the conditions specified in Tables 6-10. Exp 3 (inflation pressure = 135 Pa, Take-up Force = 6.6 N), Exp 6 (120 Pa, 6.7 N), Exp 9 (105 Pa, 5.7 N). ....	108
Figure 52: Comparison of predicted temperature profiles (lines) with measured results (symbols) of Tas (1994), at the conditions specified in Tables 6-10. Exp.12	

(inflation pressure=118 Pa, Take-up Force=7.6 N), Exp.15 (108 Pa, 7.7 N), Exp.18 (95 Pa, 6.9 N). .....	109
Figure 53: The predicted temperature difference between the external and internal surfaces of the films. The processing conditions are specified in Tables 6-10.....	110
Figure 54: (A) is the <i>c-model</i> postulation of the orientation structure. (B) is the <i>a-model</i> postulation of the orientation structure. <i>Source: Aggarwal et al. (1959)</i> .....	114
Figure 55: Crystallite structure of polyethylene [Samuels (1973)].....	116
Figure 56: A schematic of the orientation of the chain axis and its transition moment with respect to the sample directions. ....	125
Figure 57: The polarized IR in parallel position to the MD (a), parallel to TD (b), and 45° position (c).....	130
Figure 58: Larger blow-up ratios and smaller draw ratios decrease the cooling rate. ....	132
Figure 59: The predicted bubble shapes for the various blown films. ....	133
Figure 60: The predicted evolution of absolute crystallinity for the various blown films. ....	134
Figure 61: The temperature profile along the machine direction for the various blown films. The processing conditions are shown in Table 12. ....	135
Figure 62: The draw ratio for various films. The processing conditions are shown in Table 12.....	136
Figure 63: The stress profiles for various films. The processing conditions are shown in Table 12.....	137
Figure 64: The predicted thickness profiles for various films. The processing conditions are shown in Table 12. ....	138
Figure 65: The predicted amorphous orientation for various films. The processing conditions are shown in Table 12.....	139
Figure 66: Comparison between the measured (squares with error bars) and predicted (triangles) crystallinity. ....	140
Figure 67: A comparison between the overall birefringence estimated by the FTIR and the birefringence measured by the polarized light microscope (PLM). ....	144
Figure 68: A comparison between the crystalline contribution to birefringence obtained by FTIR and the crystalline contribution to birefringence estimated using the model and the PLM results.....	145
Figure 69: The FTIR parallel (top), perpendicular (middle), and 45° tilted angle (bottom) spectra of film C583 and the fitted peaks of interest.....	147
Figure 70: The average orientation of the all axes: a-axis (black), b-axis (dark gray), c-axis (light gray), and amorphous chain (white) in the machine (M), transverse (T), and thickness directions of the samples: C587 (circle), C863 (down-triangle), D582 (square), F571 (diamond), G583 (up-triangle), and H866 (hexagon). ....	149
Figure 71: The average orientation of the all axes: a-axis (black), b-axis (dark gray), c-axis (light gray), and amorphous chain (white) in the machine (M), transverse (T), and thickness directions of the samples: C24 (circle), C26 (down-triangle), C28 (square), C30 (diamond), C32 (up-triangle), and C34 (hexagon). ....	151
Figure 72: A comparison between the bubble shapes, draw ratios, and reduction in the thickness in HDPE, LDPE, and LLDPE. ....	153
Figure 73: The stress profiles in HDPE, LDPE, and LLDPE. ....	154

Figure 74: HDPE, LDPE, and LLDPE films have significant differences in the temperature and crystallinity profiles.....	155
Figure 75: HDPE, LDPE, and LLDPE have significant levels of amorphous orientations due to the differences in stress and crystallinity profiles. ....	156

# LIST OF TABLES

Table 1: Nusselt number formulation for some cases at Laminar flow. ....	52
Table 2: Values of A, B, and C used. ....	58
Table 3: Processing conditions for the film blowing process. ....	74
Table 4: Material properties used in the computations. ....	75
Table 5: Rheological properties for polymers used in this work ....	76
Table 6: Processing conditions for the film blowing process. ....	96
Table 7: Material properties used in the computations ....	97
Table 8: Rheological properties for polymers used in the study. ....	98
Table 9: General differences among Butler (1993), Ghaneh-Fard (1997), and Tas (1994). .....	99
Table 10: Predicted solution for key parameters. ....	100
Table 11: The resin properties for the blown films used in this study, <i>Kamal (2001)</i> . ....	117
Table 12: The tested films and related film blowing parameters and processing conditions. ....	117
Table 13: The rheological properties for resins of the blown films tested in this study. ....	117
Table 14: The measuring range of the compensators, $\lambda = 546.1 \text{ nm}$ ( <i>e-line</i> ). ....	121
Table 15: Constants of the compensators. ....	123
Table 16: Peaks of interest in polyethylene films. ....	129
Table 17: The measured crystallinity from DSC spectra. The processing conditions at which the films were manufactured are listed in Table12. ....	132

# Nomenclature

$A$  : Ziabicki's empirical constant of stress-induced orientation (*dimensionless*).

$B$  : dimensionless inflation pressure;  $B = (\pi r_0^3 \Delta P) / (\eta_0 Q)$

BUR : blow-up ratio;  $r^* = r / r_0$

$c$  : stress- optical constant ( $Pa^{-1}$ )

$C_p$  : mass heat capacity ( $J.g^{-1}.^0K^{-1}$ )

$C_v$  : volumetric heat capacity ( $J.m^{-3}.^0K^{-1}$ )

$D$  : deformation (*dimensionless*)

$\dot{D}$  : deformation rate (*dimensionless*)

$De$  : Deborah number;  $De = \lambda v_0 / r_0$

$DR$  : draw ratio;  $DR = v^* = v / v_0$ ,

$E$  : activation energy ( $J.mol^{-1}$ )

$F$  : take-up force (N);  $F^* = (r_0 F_z) / (\eta_0 Q) - B(BUR)^2$

$f$  : orientation function (*dimensionless*)

$G$  : relaxation modulus (Pa);  $G^* = G / G_0$

$h$  : film thickness (m);  $h^* = h / h_0$

$H_f$  : heat of fusion ( $J.g^{-1}$ )

HDPE: high density polyethylene.

$HTC_{combined}$  : effective heat transfer coefficient ( $J.m^{-2}.s^{-1}.^0K^{-1}$ )

$II_2$  : second invariant of the deformation rate tensor (*dimensionless*)

$K$  : crystallization rate constant ( $s^{-1}$ )

$K_{max}$  : Avrami crystallization rate constant ( $s^{-1}$ )  
 $k$  : thermal conductivity ( $J.m^{-1}.s^{-1}.K^{-1}$ )  
 $L$  : axial distance from the die exit to the nip rolls ( $m$ )  
 LDPE: low density polyethylene  
 LLDPE: linear low density polyethylene  
 $\dot{m}$  : mass flow rate ( $g.s^{-1}$ )  
 $N$  : Avrami constant (*dimensionless*)  
 $n$  : birefringence (*dimensionless*)  
 $n_0$  : intrinsic birefringence (*dimensionless*)  
 $P$  : pressure ( $Pa$ )  
 $Q$  : volumetric flow rate of the polymer ( $m^3.s^{-1}$ )  
 $r$  : the bubble radius ( $m$ );  $r^* = r/r_0$   
 $R_1$  : radius of curvature in the machine direction ( $m$ )  
 $R_3$  : radius of curvature in the hoop direction ( $m$ )  
 $T$  : temperature ( $^{\circ}C$ );  $T^* = T/T_0$   
 $t$  : time ( $s$ )  
 $v$  : film velocity ( $m.s^{-1}$ )  
 $z$  : axial distance from the die exit;  $z^* = z/z_0$   
 $X$  : crystallinity (*dimensionless*)  
 $X_{\infty}$  : ultimate crystallinity of the polymer (*dimensionless*)  
 $\alpha$  : thermal diffusivity ( $m^2.s^{-1}$ )

$\beta$  : half-width of the empirically observed curve for the temperature dependence of the crystallization rate constant

$\varepsilon$  : PTT extensional parameter (*dimensionless*)

$\eta$  : viscosity (*Pa.s*);  $\eta^* = \eta/\eta_0$

$\eta_0$  : zero-shear viscosity (*Pa.s*)

$\lambda$  : relaxation time (*s*)

$\theta$  : blowing angle (*degrees*)

$\rho$  : density (*kg.m<sup>-3</sup>*)

$\sigma_i$  : extensional stresses in 'i' direction (*Pa*);  $\sigma_i^* = (r_0 \sigma_i)/(\eta_0 v_0)$

$\tau_i$  : extensional deviatoric stresses in 'i' direction (*Pa*)

$\xi$  : PTT slippage parameter (*dimensionless*)

***Subscripts and Superscripts:***

$0$  : initial conditions at the die exit

$a$  : cooling air

$FL$  : freeze line

$i$  : 1,2, and 3 or machine, normal, and hoop directions, respectively

$r$  : reference

# Chapter 1

## 1 INTRODUCTION

Film blowing is the most widely used process to produce thin plastic films at high processing speeds. Blown films have a wide range of applications from grocery bags to surgically implanted materials. The film blowing industry continues rapid growth around the world. The annual average growth rate of films in the U.S. is 7% reaching 1.6 million tons. Polyethylenes are the most commonly used polymers by the film blowing industry. Linear-low density polyethylene accounts for more than 75% of the material for heavy-duty sacks [Anderton (2000)]. Packaging is the most important film market. Inexpensive film products with high performance and great consistency have gained significant demand in North America and Europe.

Polyolefins, such as low (LDPE), linear low (LLDPE), and high (HDPE) density polyethylene are extensively used in film manufacturing [Baird (1998), Anderton (2000)]. Polyolefin films have distinct processing advantages, such as clarity, puncture resistance, and low cost. The final properties of blown films, made of semi-crystalline polymers (such as LLDPE), are determined by the processing history of the blown film and the structural development during processing.

The film blowing industry is still in need of a comprehensive predictive model of the film blowing process to reduce production costs and enhance film properties via process and resin optimization. Useful predictive models should include the following characteristics.

1. The ability to describe the entire process from the die lip to the nip-rolls.
2. A realistic description of the physical and rheological properties of the polymer throughout the entire process.
3. A description of the interactions between the dynamics of the process and the film properties.



The pioneering work of Pearson and Petrie (1970) established the framework for a one-dimensional simulation of the film blowing process. They employed the Newtonian constitutive model. Their work was widely used and extended by incorporating more complex constitutive equations to deal with the effect of elasticity. Various constitutive models were employed, including the Maxwell and Leonov [Luo and Tanner (1985)], Marrucci [Cain and Denn (1988)], Phan-Thien and Tanner equations [Sidiropoulos (2000)], etc. Others incorporated important aspects, such as the crystallinity effect on the viscosity [Kanai and White (1984, 1985), Doufas and McHugh (2001), Pirkle and Braatz (2003)], the cooling effect [Cao and Campbell (1990), Sidiropoulos (2000)], the effects of the initial blowing angle [André (1998)], and the effect of the transition in the film state from melt to solid [Cao and Campbell (1990)].

Because of the low thermal conductivity of molten polymers, a temperature difference occurs between the internal and external surfaces of the molten polymer [Cao (1990), André (1998)]. Therefore, a two-dimensional energy equation with the proper thermal boundary conditions should be used to predict the temperature variations in the machine and thickness directions [Cao (1990), Sidiropoulos (2000)]. The most important thermal boundary condition is the heat transfer coefficient at the external surface of the bubble. The heat transfer coefficient changes significantly, because it depends on the complex interaction between the bubble shape, the cooling air velocity, and the cooling ring design. Employing an accurate prediction of the heat transfer coefficient in the machine direction is necessary to predict the bubble shape and film properties [Sidiropoulos (2000)].

As a result of the strong cooling, the molten polymer is transformed to a solid film quickly and the rheological properties, such as viscosity and shear modulus, change rapidly near the freeze line, where the bubble radius reaches a plateau. Thus, more than one type of constitutive equation should be employed to model the film blowing process. Moreover, in the case of partially crystalline polymers, such as polyethylene, the crystallization can cause significant change in the rheological properties, such as viscosity and the viscoelastic behavior of the film [Kanai and White (1985), Doufas and McHugh (2001)]. The development of the crystallinity depends on the combined effects

of under-cooling and induced orientation [Ziabicki (1976)]. Induced-orientation is due to the development of the stresses. The changes in the viscoelastic behavior and crystallization produce significant changes in the bubble shape, film velocity, and thickness.

Most of the models found in the literature cover the process from the die exit to the freeze line region, which is the region where the bubble radius stops expanding. Even the few models that extended beyond the freeze line, incorporated empirical rheological functions and employed restricted definitions of the cooling system. Generally, these studies lacked the ability of predicting the absolute crystallinity and the stress-induced orientation in the final films. Such properties are of great importance to the end user because they determine the optical and mechanical properties of the blown films. Therefore, the ability to predict the aforementioned properties and relate them to the resin properties and processing conditions represent a necessary feature in any useful simulation of the film blowing process.

In the view of the above, the present work aims at developing a microstructure and product oriented model of the film blowing process, which incorporates the rheological and morphological changes in the film and covers the entire process from the die exit to the nip rolls. The model should predict important characteristics of the process and product, such as bubble radius, film velocity and thickness, temperature, stresses, crystallinity, and orientation. This work builds on earlier achievements reported by various researchers. These include Cao and Campbell (1990), who proposed a two-phase rheological model in order to provide a more realistic rheological description, André et al. (1998, 1999), who demonstrated the importance of the initial blowing angle, and Sidiropoulos (2000), who conducted a detailed analysis of the variation of the heat transfer coefficient. There is a large gap regarding the incorporation of the effects of crystallization on film blowing dynamics for partially crystalline polymers, such as polyethylene. Semicrystalline polymers represent an important class of polymers. The present work attempts to deal with the limitations of existing models. Furthermore, an effort is made to validate the predictions of the model by comparison with experimental data.

# Chapter 2

## 2 TECHNICAL BACKGROUND

In this chapter, a general description of the film blowing process and its main characteristics is followed by an extensive review of the relevant literature. The review is divided into two main sections. The first section describes the work done in the past regarding the mathematical modeling of the process. The second section reviews the relevant experimental studies, which were carried out to investigate the process, characterize the blown films produced under various processing conditions, and identify the dominant rheological parameters of the resins used to produce blown films.

### 2.1 General Description of the Process

In the film blowing process, a molten polymer tube is extruded from an annular film die. The tube is drawn upward by a take-up roll device. Simultaneously, the tube is blown by air that is supplied through a hole at the center of the die. This air creates a small difference in pressure,  $\Delta P$ , between the inside the bubble and the ambient pressure. Cooling air is blown around the bubble from an air ring surrounding the tube near the die exit. In some cases, a mechanism is employed to cool the inside surface of the film [Sidiropoulos (2000)]. The processing conditions define the evolution of the bubble radius ( $r$ ), the blowing angle ( $\theta$ ), and the film velocity ( $v$ ). The inflated bubble is then guided to pass through nip rolls by a series of guide rolls. The speed of the nip rolls is controlled according to the desired draw ratios. Schematics of the film blowing process and detailed pictures of the plastic film at various stages of the process are shown in Appendix A.

The most significant forces affecting the film are the boundary traction and the force resulting from the pressure difference in the bubble. The produced films are biaxially oriented, which improves the strength of the film in the machine and hoop directions and allows good control over the mechanical and optical properties of the final

product. The most important parameters in the film blowing process are the blow-up ratio (BUR), film thickness ( $h$ ), and the draw ratio (DR). The blow-up ratio is the ratio of the bubble radius to the die radius ( $r_0$ ). The BUR is normally kept between 1.5 and 5 [Baird (1998)]. The thickness reduction is the ratio of the die annular gap ( $h_0$ ) to the final thickness of the film and is usually kept between 20 and 200 [Liu *et al.* (1995)]. The draw ratio is the ratio of the maximum film velocity to the velocity at the die exit. DR is normally kept between 5 and 25 [Baird (1998)]. The radius of the die exit is typically between 1 and 25 cm, while the gap thickness of the die exit is typically between 1 and 2 mm. The pressure difference inside the bubble is reportedly 50 Pa higher than the ambient pressure, and the initial velocity is between 1 and 5 cm/s [Micic *et al.* (1998)]. In the last fifty years or so, extensive studies were conducted on blown films. The studies can be classified into two major areas; 1) Modeling and simulation, and 2) Experimental investigation.

## 2.2 Modeling and Simulation of Film Blowing

### 2.2.1 One Dimensional Simulation

Pearson and Petrie (1970a,b) formulated the theoretical analysis of the film blowing process. They developed a mathematical model for the process by considering the film as a thin membrane in tension. They made the following assumptions:

- i) The flow is axisymmetric
- ii) The bubble radius grows until it freezes at a particular line called “the freeze line”.
- iii) The fluid is Newtonian.
- iv) The film was supported by longitudinal traction ( $F$ ) and internal air pressure ( $B$ ).
- v) The effects of the inertia, surface tension, air drag, and gravity forces are negligible.

They derived and solved a system of equations based on the force balance and the Newtonian constitutive equations in conjunction with the continuity equation (*all derivations are shown in Chapter 4, and all symbols are defined in the nomenclature*):

$$2r^2(F^* + Br^2)r'' = 6\eta r' + (1 + r'^2)(F^* - 3Br^2)r \quad (1)$$

$$\frac{h'}{h} = -\frac{1}{2} \frac{r'}{r} - \frac{1}{4\eta} (1 + r'^2)(F^* + Br^2) \quad (2)$$

where  $r$  is the bubble radius,  $F$  is the traction force,  $B$  is the inflation pressure,  $\eta$  is viscosity, and  $h$  is the film thickness. Superscript “\*” indicates dimensionless quantities as defined in the nomenclature. Pearson and Petrie (1970a, b) predetermined the freeze line height and the blow-up ratio to solve the above equations backwards from the freeze line to the die exit. If the solution yielded  $BUR = 1$  at the die exit, then the solution was obtained. Otherwise, a new iteration with a new value for the blow-up ratio was employed. The boundary conditions were the initial values of the bubble radius and film thickness, along with the derivative of the bubble radius at the freeze line ( $r' = 0$ ). No additional boundary conditions can be imposed because the problem becomes over-determined. It is clear that the above approach is an oversimplification, since it does not take into consideration the nonisothermal and viscoelastic nature of the process. In order to deal with viscoelasticity, Petrie (1975) employed the Maxwell model. Petrie (1988) employed a heat transfer coefficient for convection and radiation, which depended on the volumetric flow rate of the cooling air. Petrie and Petrie (1999) conducted experimental work to study the relations between processing conditions and the LDPE film properties. They concluded that the work of Tas (1994) was the most dependable for evaluating the effects of the process input parameters, such as the take up force. Other researchers reported only output variables such as the BUR and DR without reference to input parameters, such as the actual force, pressure, or other factors that determine the BUR and DR. For instance, the BUR can be controlled in many ways, such as lowering the take-up speed or increasing the amount of inflating air. Petrie also argued that providing predictions of the stresses and comparing them to real observations is an important test of any simulation of the film blowing process. The need to predict the stresses was also emphasized by Kurtz (1992, 1995), who suggested that the pre-process variables, such as the die swell and stresses in the die, were important elements. Petrie and Petrie (1999), based on the behavior of soap bubbles [Adamson (1967)] indicated that it would be

inaccurate to assume that an increase in the bubble radius is obtained by increasing the inflation pressure.

Most subsequent studies utilized the approach followed by Petrie and Pearson (1970,a, b) to model the film kinematics and dynamics (there are few exceptions that will be mentioned later in this chapter). Luo and Tanner (1985) extended the work to non-isothermal viscoelastic flow and employed the Convective Maxwell and Leonov models. They reported that the numerical method employed by Petrie and Pearson, to solve the system of equations backwards (from the freeze line to the die exit), was a major reason for the difficulties in obtaining convergence for some processing conditions. So, they employed a 4<sup>th</sup>-order Runge-Kutta method and solved the equations forward from the die exit to the freeze line. They assumed a constant heat transfer coefficient. The freeze line was identified as the region where the derivative of the bubble radius becomes null. The Maxwell constitutive equations employed by Luo and Tanner and most other researchers are shown below (*detailed definition of all terms is included in the nomenclature at the end of the thesis, and derivations of similar equations are shown in chapter 4*):

$$\tau_1 + \lambda v \cos \theta \frac{d\tau_1}{dz} - 2\lambda \tau_1 \cos \theta \frac{dv}{dz} = 2\eta \cos \theta \frac{dv}{dz} \quad (3)$$

$$P + \lambda v \cos \theta \frac{dP}{dz} - 2\lambda P \frac{v}{h} \cos \theta \frac{dh}{dz} = 2\eta \frac{v}{h} \cos \theta \frac{dh}{dz} \quad (4)$$

$$\tau_3 + \lambda v \cos \theta \frac{d\tau_3}{dz} - 2\lambda \tau_3 \frac{v}{a} \cos \theta \frac{dr}{dz} = 2\eta \frac{v}{r} \cos \theta \frac{dr}{dz} \quad (5)$$

where  $\tau_i$  is the stress in the machine (1), thickness (2), or hoop (3) direction.  $\theta$  is the blowing angle,  $\lambda$  is the relaxation time,  $v$  is the film velocity, and  $z$  is the axial distance. They compared the results of their work with the experimental results of Gupta (1981) to validate their simulation. They obtained qualitative agreement between model predictions and experimental results regarding the deformation rates in the machine direction (Figure 1) and in the hoop direction (Figure 2)

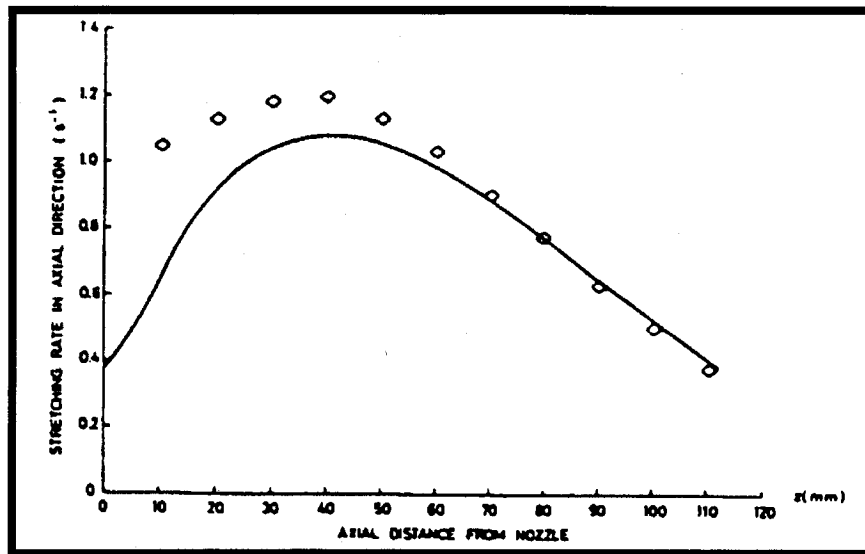


Figure 1: A comparison of the deformation rate in the machine direction. Gupta's measurements are shown as the diamonds, and the line represents Luo and Tanner calculations. *Source: Luo and Tanner (1985).*

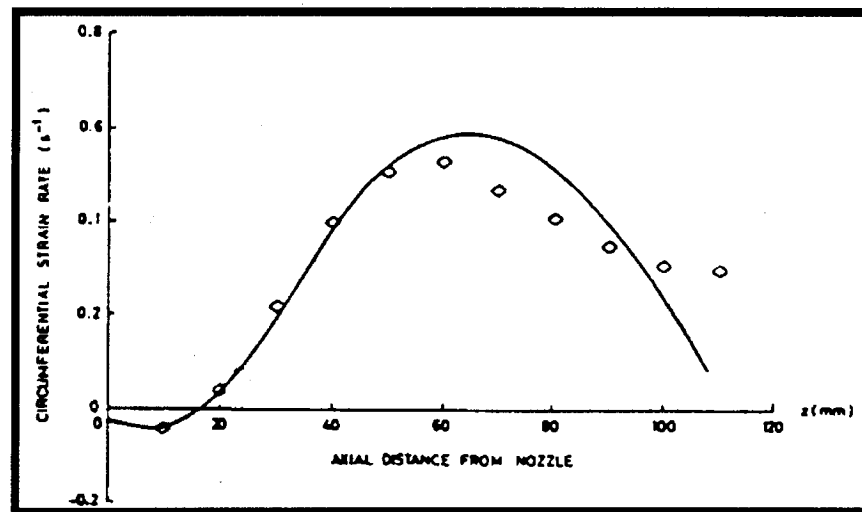


Figure 2: A comparison of the deformation rate in the hoop direction. Gupta's measurements are shown as the diamonds, and the line represents Luo and Tanner calculations. *Sources: Luo and Tanner (1985).*

Unlike Petrie and Pearson (1970a,b, 1975), Luo and Tanner (1985) guessed the initial blowing angle by repeating the integration and changing the blow-up ratio until the derivative of the radius became null, with respect to the machine direction. They did that for various inflation pressures and take-up ratios and reported agreement with the results of Petrie and Pearson (1970a, b). They also studied the effect of the relaxation time and showed that the BUR increased by lowering the dimensionless relaxation time. They found that the Leonov model was not the best choice to describe the process, since extensional flow is dominant and the Leonov model was not sufficiently stiff at high deformation rates. Moreover, they reported agreement with Gupta's (1980) experimental data on polystyrene (Styron 666).

### 2.2.1.1 Stability of One-Dimensional Solutions

The different approaches of Pearson and Petrie (1970a, b) and Luo and Tanner (1985) for solving the resulting system of equations suggested the need to investigate the origin of the solution instability and to determine whether it is numerical or physical. Cain and Denn (1988) compared the Newtonian, Maxwell and Marrucci models and reported that several types of numerical and physical instabilities existed. These instabilities were dependent on the set of operating temperatures and input parameters. In the Newtonian formulation, they were able to obtain an analytical solution similar to that obtained by Pearson and Petrie (1970), when the blow-up ratio was set to unity (BUR=1) as follow:

$$DR = \exp\left(-\frac{F^* z^*}{3}\right) \quad (6)$$

They conducted a linear stability analysis, in which they employed Newman's banded matrix method to solve the boundary value problem. This method is an extension of the Thomas method [Matlosz and Newman (1987)] to a system of coupled equations. They indicated that it was possible to avoid the need for iteration in solving for the take-up force and inflation pressure by treating the inflation pressure and the take-up force as variables and adding the following two equations to the system.



$$\overset{*}{F}' = 0 \quad (7)$$

$$\overset{*}{B}' = 0 \quad (8)$$

Cain and Denn (1988) were able to overcome some instability problems due to the shooting method by employing Newman's band method [Matlosz and Newman (1987)] for boundary value problems. They reported various types of instabilities, such as non-uniqueness in the bubble shape, and showed that the blow-up ratio increased when the inflation pressure decreased, for blow-up ratios higher than 1.0. They also observed that increasing the viscosity contributed to the stability of the process.

Yoon and Park (1999) followed the approach of Cain and Denn (1988), but with an isothermal Newtonian model and a different material. They employed data for LLDPE, while Cain and Denn employed polymer properties reported by Gupta (1980) for Polystyrene (Styron 666). They reached the same conclusion as Cain and Denn, indicating that the film blowing process is mostly unstable, except for a small range of blow-up and draw ratios. Yewo (1976), who employed the Newton-Raphson shooting method, contradicted the results of Cain and Denn. He concluded that the film blowing process was mostly stable, except at very high draw ratios.

### 2.2.1.2 Effects of the Initial Blowing Angle on Stability

André et al. (1998) simulated the film blowing behavior for the Newtonian (Equations 1 and 2) and the upper convected Maxwell constitutive models (Equations 3-5). The integration was carried out forward from the die exit to the point where the blowing angle was zero. At that point, the velocity, bubble radius, and film thickness, determined the final blow-up ratio, draw ratio, and thickness reduction. They employed the 4<sup>th</sup> order Runge-Kutta method to solve the resulting system of equations. They also employed Newton's shooting method to find the initial blowing angle that yielded a stable solution under given processing conditions. A precise guess of the initial angle was required to obtain a stable solution, which was not unique for some trials, as shown in Figure 3. They validated their predictions of the bubble shape and stresses, and obtained

good agreement with cases found in the literature, such as the results of Pearson and Petrie (1970) and those of Luo and Tanner (1985). Their analysis of the stable region was similar to that of Cain and Denn (1988), but the numerical method and the boundary condition treatment were different. The nonisothermal effects were treated by solving the one-dimensional energy equation, which incorporated the effect of heat convection due to the cooling air.

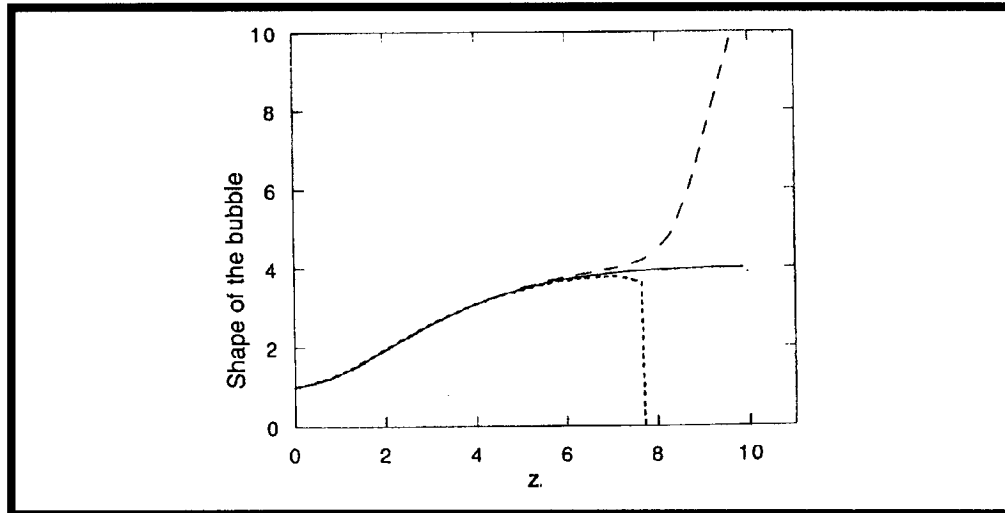


Figure 3: The dimensionless bubble shape as a function of the dimensionless distance from the die exit for various initial blowing angles: (- - -)  $\theta_0 = 9$  degrees, (—)  $\theta_0 = 9.59$  degrees, (. . . .)  $\theta_0 = 10$  degrees. . Source: André (1999).

### 2.2.1.3 Effects of Viscosity and Relaxation Time on Stability

André et al. [(1998), (1999)] investigated the effects of the dimensionless viscosity and relaxation time on process stability and reported similar findings to those of Cain and Denn (1988). They found that the region of attainable solution for draw ratio decayed exponentially as the dimensionless relaxation time (the period of time that melts maintain stresses after the cessation of deformation) increased. Most of the time, they were able to obtain a solution only when the relaxation time was relatively small ( $<0.007$ ), which can be seen more clearly in André's thesis (1999). They found that a constant heat transfer coefficient was better than one assuming a linear temperature gradient with axial distance at the outer surface of the film. When a constant heat transfer

coefficient was employed, the temperature profiles and bubble shapes were better predicted. However, most of the cases and the comparisons were based on a linear temperature gradient, as the thermal boundary condition at the outer surface of the film.

### 2.2.1.4 Effect of the Inflation Pressure on the Process Stability

Liu et al. (1995a,b) reported, based on both simulations and experiments, that increasing the inflation pressure was accompanied by a larger bubble volume. They reported that this “intuitive” behavior was observed in most cases only for  $BUR < 2$ . However, their data showed that the inflation pressure showed no effect, and in some cases the reverse effect, on the bubble radius for  $BUR > 2$ . They measured the inflation pressure with an inclined manometer. They did not supply information regarding the magnitude or variability of the take-up force. They employed the following assumptions:

- i) The effect of the axial curvature in the machine direction is negligible.
- ii) The inflation pressure does not contribute to the stress in the machine direction.
- iii) The fluid is non-Newtonian.
- iv) The viscosity follows an empirical function defined below:

$$\eta = \frac{\alpha_1 \exp\left(\frac{\beta_1}{T}\right) \exp\left(\alpha_2 \left(\frac{X}{X_f}\right)^{\beta_2}\right)}{1 + (\gamma_1 \lambda \sqrt{II_2})^{\gamma_2}}$$

where  $T$  is the temperature,  $II_2$  is the second invariant of the deformation rate,  $X$  is the local crystallinity,  $X_f$  is the final crystallinity, and  $\lambda$  is the relaxation time.  $\alpha_i$ ,  $\beta_i$ ,  $\gamma_i$  are empirical constants.

- v) The flow is axisymmetric.
- vi) The effects of inertia, surface tension, air drag, and gravity forces are negligible

It appears that their model only worked for  $BUR < 2$  and  $DR < 8$ . Common ranges employed industrially are  $3 < BUR < 4$ , and  $DR > 10$ . Their model incorporated the effect

of crystallinity on the viscosity. The crystallinity was also incorporated in the energy equation.

## 2.2.2 Two-Dimensional Simulation

### 2.2.2.1 Rheological Zones

Campbell and Cao (1987) proposed a two-phase model incorporating viscoplasticity and crystallization to predict bubble shape, film velocity, temperature, and deformation rate. They suggested that when the yield stress was greater than the hoop stress, the film rheological behavior was best described by the Kelvin-Voigt model. They divided the process into several regions (Figure 4): a melt with no crystallization, followed by the crystallizing melt (which was treated as two phases), and finally, the solid stage. Cao et al. (1989) proposed a two-dimensional energy analysis and showed significant temperature differences across the film thickness, especially near the die exit. The difference was larger when strong cooling was applied. Cao and Campbell (1990a, b) investigated different constitutive models and introduced a two-phase model: liquid-like phase and solid-like phase. The Maxwell model was employed in the liquid-like phase, while a perfect plastic-elastic model was used in the solid-like phase. They employed an empirical definition of the yield stress ( $YS_{eff}$ ) and used it as the criterion to switch from one stage to another. The initial conditions of the blowing angle and the extensional stresses were selected according to their experiments. The heat transfer coefficient was treated as a fitted constant that was not always consistent. They defined the yield stress as an inverse function of temperature. They also employed “the structure memory function”,  $\vartheta$ , to quantify the alignment strength, which is an empirical rheological definition by Larson (1988).

$$\vartheta = C_h \int_{-\infty}^t \sqrt{II_2} \left( |I_1 - I_2| \frac{I_1}{I_2} \right) \exp \left( -\frac{(t-t')}{\lambda_{eff}} \right) dt'$$

where  $C_h$  is an empirical constant and  $t$  is time.  $II_2$  is the second invariant of the deformation rate tensor.  $I_1$  and  $I_2$  are the first and the second variants of the Finger tensor.

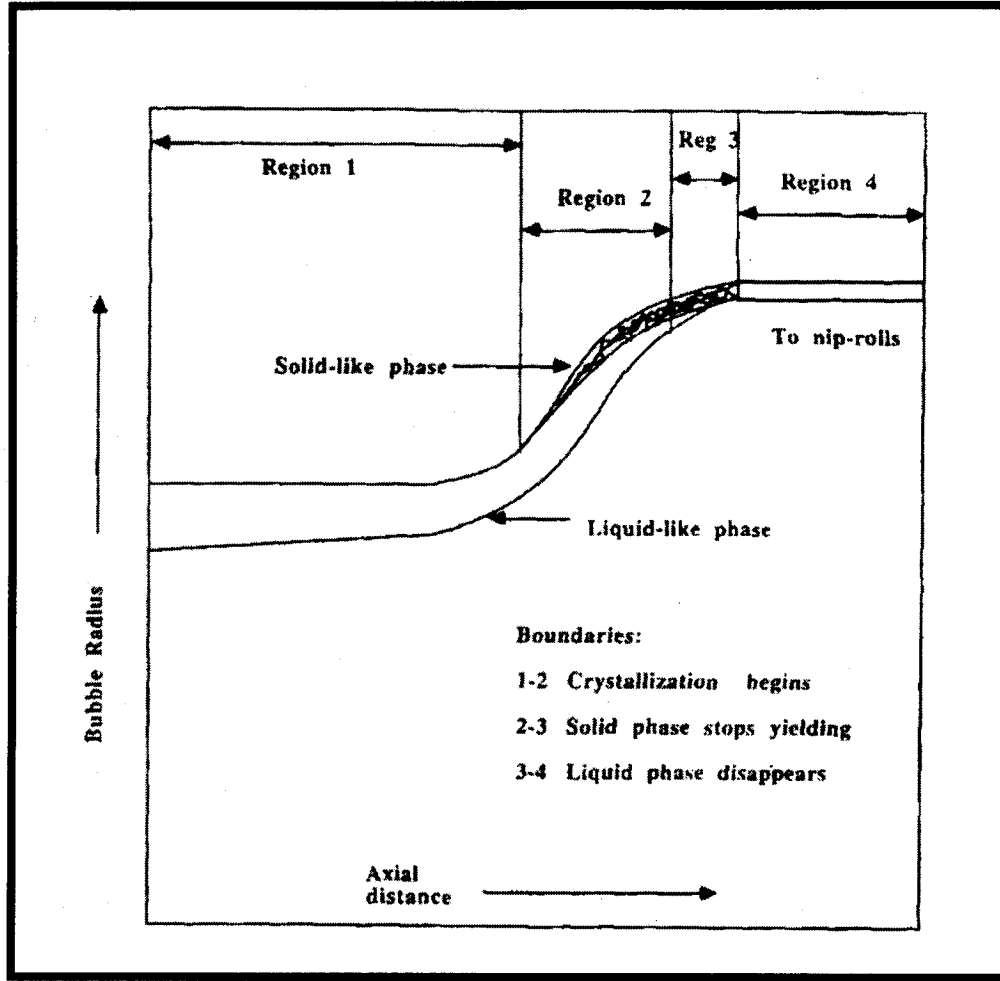


Figure 4: The two-phase model proposed by Cao and Campbell (1990). Source: Kanai (1999).

The structure memory function was multiplied by all the rheological functions, such as the viscosity, the relaxation modulus, and the yield stress, in order to replace these functions with the effective functions, so they can be employed in the simulation.

$$\eta_{eff} = \vartheta \eta = \vartheta \left( 88000 + \exp \left( 18904 \left( \frac{1}{T} - \frac{1}{443} \right) \right) \right) \quad (Pa.s)$$

$$\lambda_{eff} = \frac{\eta_{eff}}{G_{eff}} \quad (s)$$

$$G_{eff} = \vartheta G = \vartheta(1000 \times (80 + (393 - T))) \quad (Pa)$$

The final form of their model is summarized by the following equations [Cao (1990)]:

$$\tau_i + \lambda_{eff} \left[ \frac{d\tau}{dt} - [\nabla v][\tau_i] - [\tau_i][\nabla v]^T + 2(\tau_i \dot{D}_i) \right] = 2\eta_{eff} \dot{D}_i \quad \text{if} \quad YS_{eff} < \sqrt{3II_\tau}$$

$$\tau_i = 2G_{eff} D_i \quad \text{if} \quad YS_{eff} \geq \sqrt{3II_\tau}$$

$$YS_{eff} = \vartheta.YS = \vartheta \left( 1 \times 10^{-15} \exp \left( \frac{20000}{RT} \right) \right)$$

where  $II_\tau$  is the second invariant of the stress tensor.  $T$  is the film temperature and  $R$  is the universal gas constant.

Babel et al. (1993) employed the model proposed by Cao (1990) to predict uniaxial extension. They compared the predictions to experimental data for LDPE, two types of Polystyrene, and several blends of LDPE and LLDPE. They obtained good agreement between the predicted and measured uniaxial extensional viscosity. Babel and Campbell (1993) conducted experiments on LDPE blown films to verify the predicted relation between the plastic strain history and the physical properties of the blown films. They measured the surface and bulk temperatures of the film using an infrared technique to detect the starting point of crystallization. They also employed a video digitization technique to record the bubble shape and the film velocity. They found a correlation between the amount of plastic strain and the film properties. Later, Babel et al. (1995), and Campbell and Babel (1996) extended the experiments to LLDPE blown films to verify the predicted relations between the final film properties and the amount of strain and strain derivatives. They proposed changes in the processing conditions and equipment in order to optimize film mechanical properties.

### 2.2.2.2 Effects of the Crystallinity

Doufas and McHugh (2001) employed a two-phase microstructural model. They followed the approach of Liu *et al.* (1995) in formulating a momentum balance. They employed the following assumptions:

- i) The effect of the axial curvature in the machine direction is negligible.
- ii) The inflation pressure does not contribute to the stress in the machine direction.
- iii) The flow is axisymmetric.
- iv) The effects of the inertia, surface tension, air drag, and gravity forces are negligible.
- v) The freeze line occurs when crystallization starts.
- vi) No further reduction occurs in the thickness after the freeze line.
- vii) The shear modulus is constant.

The melt was treated as a modified Giesekus fluid characterized by the conformational tensor. The semi-crystallized phase was assumed to consist of oriented rigid rods described by an orientation tensor. They treated crystallinity as the degree of transformation of statistical segments in the semicrystalline medium. The equations of evolution for the microstructural variables were summarized in three types:

- i) Conformation tensor ( $c$ ), which represents the second moment of the end-to-end vector of the polymer chains, as follows:

$$c_i = -\frac{I - X}{\lambda_m} \left[ (I - \alpha)I + \frac{\alpha Ec}{I - X} \right] \quad (9)$$

where  $X$  is the crystallization ratio,  $\lambda_m$  is the amorphous relaxation time,  $\alpha$  is Giesekus molecular parameter,  $I$  is the identity tensor, and  $E$  is the nonlinear spring force factor.

- ii) Orientational tensor ( $S$ ), which represents the conformational state of the semicrystalline phase, as follows:

$$S_i = -\frac{\ell}{\lambda_c} S + \frac{I}{3} [\nabla v + (\nabla v)^T] - 2(\nabla v)^T : \langle uuuu \rangle \quad (10)$$

where  $\ell$  is an anisotropic drag parameter of the semi-crystalline phase,  $\lambda_c$  is the semi-crystalline relaxation time,  $v$  is the velocity vector, and  $u$  is the unit vector along the rod axis.

iii) Crystallization rate, which is represented by the differential form of the non-isothermal Nakamura equation.

$$\frac{DX}{Dt} = NK(T)(1-X)[- \ln(1-X)]^{\frac{N-1}{N}} \exp(\vartheta \text{tr} \sigma) \quad (11)$$

where  $D/Dt$  indicates the substantial derivative.  $N$  is the Avrami exponent,  $K(T)$  is the rate constant of crystallization,  $\vartheta$  is a model parameter, and  $\sigma$  is the total stress.

The bubble radius and film thickness were not affected by the stresses after the freeze line, but rather they were kept constant after the start of crystallization. Accordingly, the velocity was forced to plateau, and thus the deformation rate tensor was forced to vanish causing the growth of the stresses to stop. The resulting model proposed by Doufas and McHugh (2001) is thus similar to the model of Liu and Spruiell (1995). Therefore, they obtained qualitative agreement with the experimental results of Liu and Spruiell, as shown in Figure 5. The results obtained were for  $BUR < 2$ . In this region, increasing the inflation pressure produced larger bubble. They did not provide information regarding the take-up force. The die dimensions were very small in comparison with the common dies employed industrially.



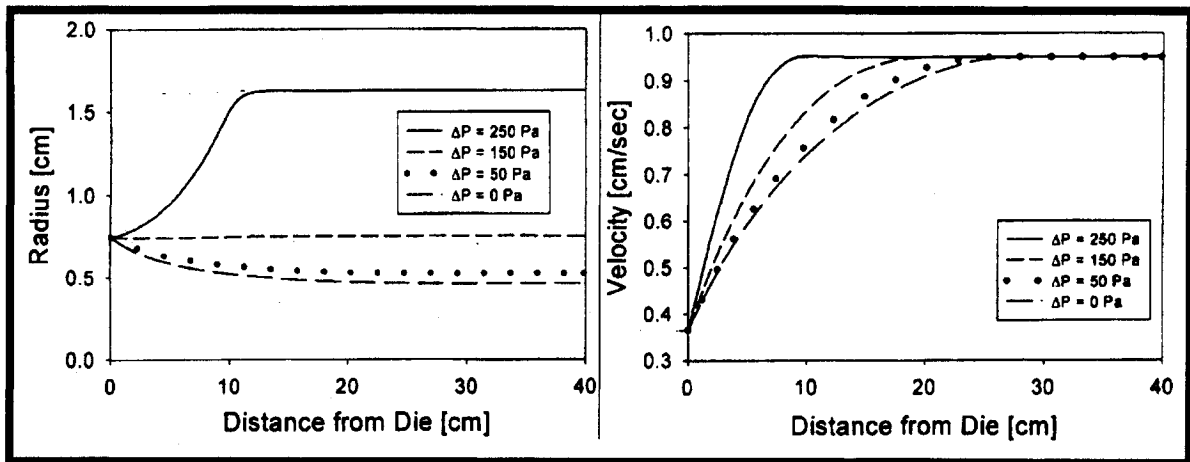


Figure 5: The bubble radius and film velocity as predicted by the simulation proposed by Doufas and McHugh (2001).

Pirkle and Braatz (2003) followed the assumptions of Doufas and McHugh (2001). However, they treated the melt as a non-Newtonian fluid. They obtained quantitative agreement with the works of Doufas and McHugh (2001) and Liu and Spruiell (1995), although, they employed a simpler constitutive equation similar that used by of Liu and Spruiell (1995). They employed five measured or adjusted parameters in the dimensionless viscosity function. They set the derivative of the radius with respect to the machine direction to zero at the freeze line, and they employed a constant heat transfer coefficient, which was the same for the entire process. The crystallinity effects appeared in the viscosity function (same function as that of Liu and Spruiell (1995)) and in the energy equation.

### 2.2.2.3 Effects of Cooling and Aerodynamics

All the above researchers employed empirical constants for the heat transfer coefficient. The values used by different researchers were not always the same. Since the film blowing process is highly nonisothermal, the cooling process has a significant influence on the bubble shape and film behavior. Such influence may be predicted by using the proper description of the heat transfer coefficient. Extensive work was done to model and simulate the heat transfer coefficient. Menges and Predohl (1972) developed correlations to describe the heat transfer coefficient as a function of the volumetric flow rate of the cooling air. Their correlations were employed between the die exit and the

freeze line. Kanai and White (1984, 1985) expanded the approach of Menges and Predohl (1972) to calculate the heat transfer coefficient in (Kcal/m<sup>2</sup>hr.°C) by dividing the machine direction into three zones:

1. above the freeze line ( $z_f$ ) :

$$h = 2.5V_{max}^{1.6}, \quad \text{where } V_{max} \text{ is local maximum air velocity}$$

2. below the freeze line:

- a. between the die exit and the location of the highest value of heat transfer coefficient:

$$h = c_1 \quad \text{where } c_1 \text{ is 50 for LDPE, 40 for LLDPE, and 35 for HDPE}$$

- b. between the freeze line and the location of the highest value of heat transfer coefficient:

$$h = c_2 / z^{1.6} \quad \text{where } z \text{ is the distance from the die exit and } c_2 \text{ is 1140 for } z_f=7 \text{ cm, 1020 for } z_f=9 \text{ cm, and 836 for } z_f=12 \text{ cm}$$

The above correlations appear to be limited to situations where the freeze line and the location of the maximum value of the heat transfer coefficient are known. It also seems that the correlations are limited to polyethylene films. Discontinuity is expected as the simulation changes the correlation that calculates the heat transfer coefficient in each zone, due to the possible jump in the HTC value.

Feron et al. (1997) and Wolf et al. (1997) considered the turbulence in the flow of the cooling air and developed a numerical simulation to optimize the cooling process by incorporating air flow rate, air temperature, the jet angle, and the location of the air ring. The simulation employed the finite element method (FIDAP Software ©) to solve the near-wall  $\kappa$ - $\epsilon$ -turbulence model. They reported that air flow vortices occurred as a result of the complex interaction between the bubble shape and the air flow, which could be the principal influence in shaping the bubble and causing the instabilities.

In an extensive study, Sidiropoulos et al. (1996, 1997, 1999, 2000) modeled the cooling system to account for variable cooling dynamics, along the machine direction, and calculated a variable heat transfer coefficient. They followed an approach similar to that developed by Feron et al. (1997) and Wolf et al. (1997), but with stronger interaction with the viscoelastic behavior of the melt. Sidiropoulos et al. (1996, 1997, 1999, 2000) employed Fluent Software ©, which is based on the finite difference method to predict the heat transfer coefficient profiles. Then, they used these profiles along with the proper constitutive equations to predict the stress in the blown film. Both FIDAP and Fluent require knowing the bubble shape prior to performing the calculations. Sidiropoulos et al. (1996, 1997) employed a non-Newtonian polymer model by defining the viscosity as a function of the melt temperature. They obtained good agreement with Butler's (1993) experiments. Later, Sidiropoulos et al. (1998,1999) improved the simulation and predicted the Venturi effect by employing various air jets impinging at various angles on the bubble, by incorporating various types of air rings. They modeled the heat transfer using the two-dimensional renormalized group (RNG)  $k-\varepsilon$  model. The stresses in the film were calculated by employing the Phan-Thien and Tanner constitutive equation. They employed the following approach to analyze the film blowing process:

1. LLDPE was employed in a film blowing experiment similar to that of Butler et al. (1993) to obtain a bubble with BUR=3. The die exit diameter was 10 cm, and the freeze line height was 68 cm.
2. The air rings were assumed to encapsulate the bubble for the first 12.5 cm.
3. The air velocity and temperature were assumed to be design parameters. These parameters were entered in the computational domain with predetermined values.
4. The air density was assumed to be a function of both temperature and pressure.
5. The temperature profile of the experimentally produced bubble was employed in the computation of the aerodynamics of cooling.

Sidiropoulos et al. showed significant differences between the cooling effects of single-lip and dual-lip air rings and showed that the heat transfer coefficient was not constant, but, in fact, it exhibited maxima right above the air ring location and minima

below the freeze line. They also showed that when the air emerged near an inclined curved surface, it formed eddies attached to the surface, as a result of the Coanda effect [Sidiropoulos et al. (1999b, 2000)]. Sidiropoulos (2000) provided profiles for the heat transfer coefficient at three different air flow rates, which were used in the current work to obtain correlations of the heat transfer coefficient in the film blowing process. Sidiropoulos (2000), Sidiropoulos et al. (2001), and Sidiropoulos and Vlachopoulos (2002) incorporated the PTT constitutive equation for the melt and studied the effect of internal cooling. However, they obtained the bubble shape and temperature profile experimentally. Then, they used the PTT model to calculate the stresses. They also divided the thickness into 20 equal layers, which deformed at equal rates. Also, they considered the stress variation across these layers to occur only as a result of the temperature drop across the thickness. Sidiropoulos (2000) defined the initial deformation rate at the die exit as follows:

$$\dot{D} = -\frac{2n+1}{n} v_{av} \left( \frac{2y-h_0}{h_0} \right)^{\frac{1}{n}} \quad (12)$$

where  $v_{av}$  is the average melt velocity,  $h_0$  is the initial film thickness,  $n$  is power law constant, and  $y$  varied from 0 at the inner surface of the film to  $h_0$  at the outer surface of the film.

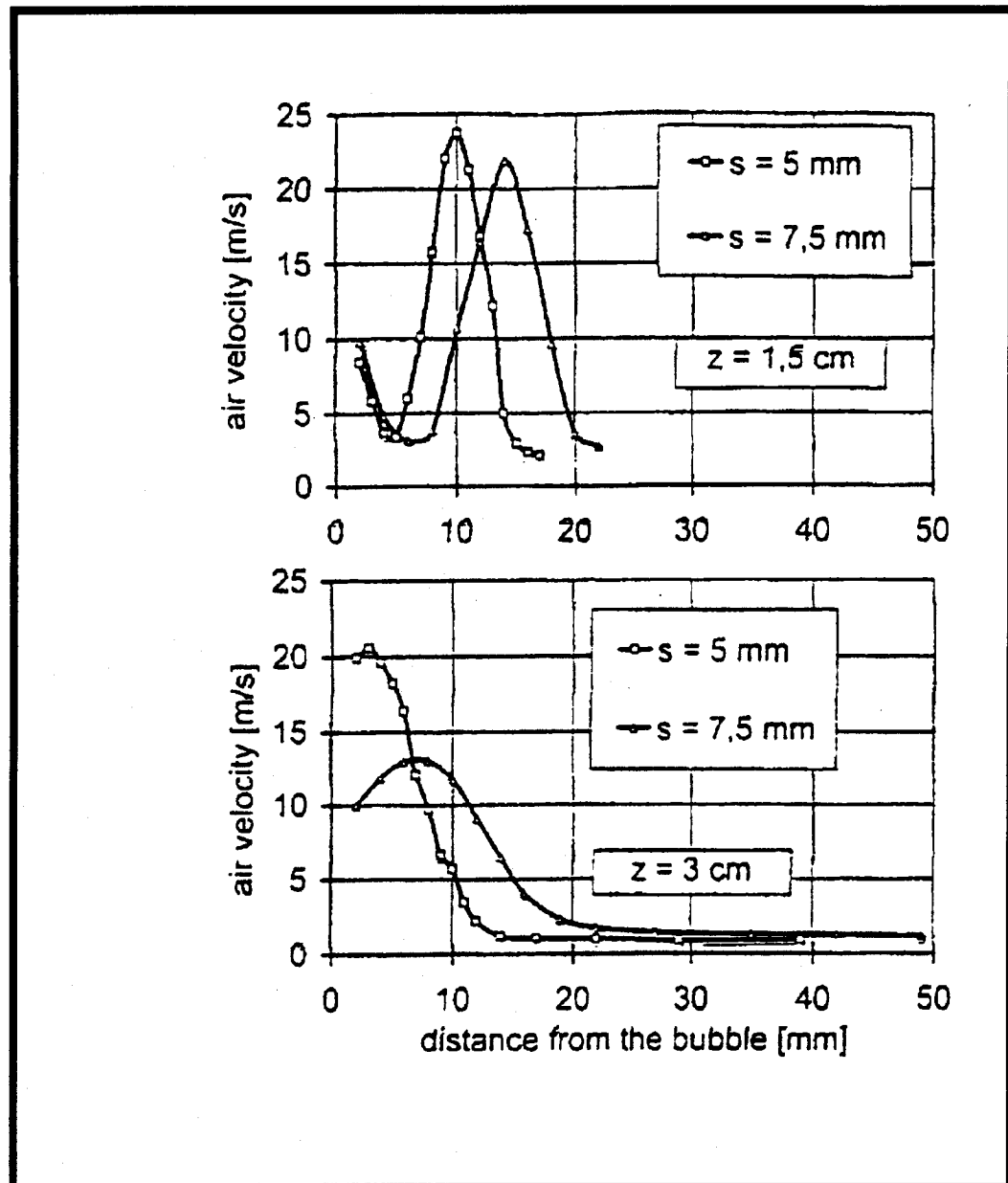


Figure 6: The velocity profile of the cooling air with two different air ring gap widths ( $s=5 \text{ mm}$  and  $s = 7.5 \text{ mm}$ ) at two freeze line heights ( $z= 1.5 \text{ cm}$  and  $z= 3 \text{ cm}$ ). Source: Hauck and Michaeli (1998).

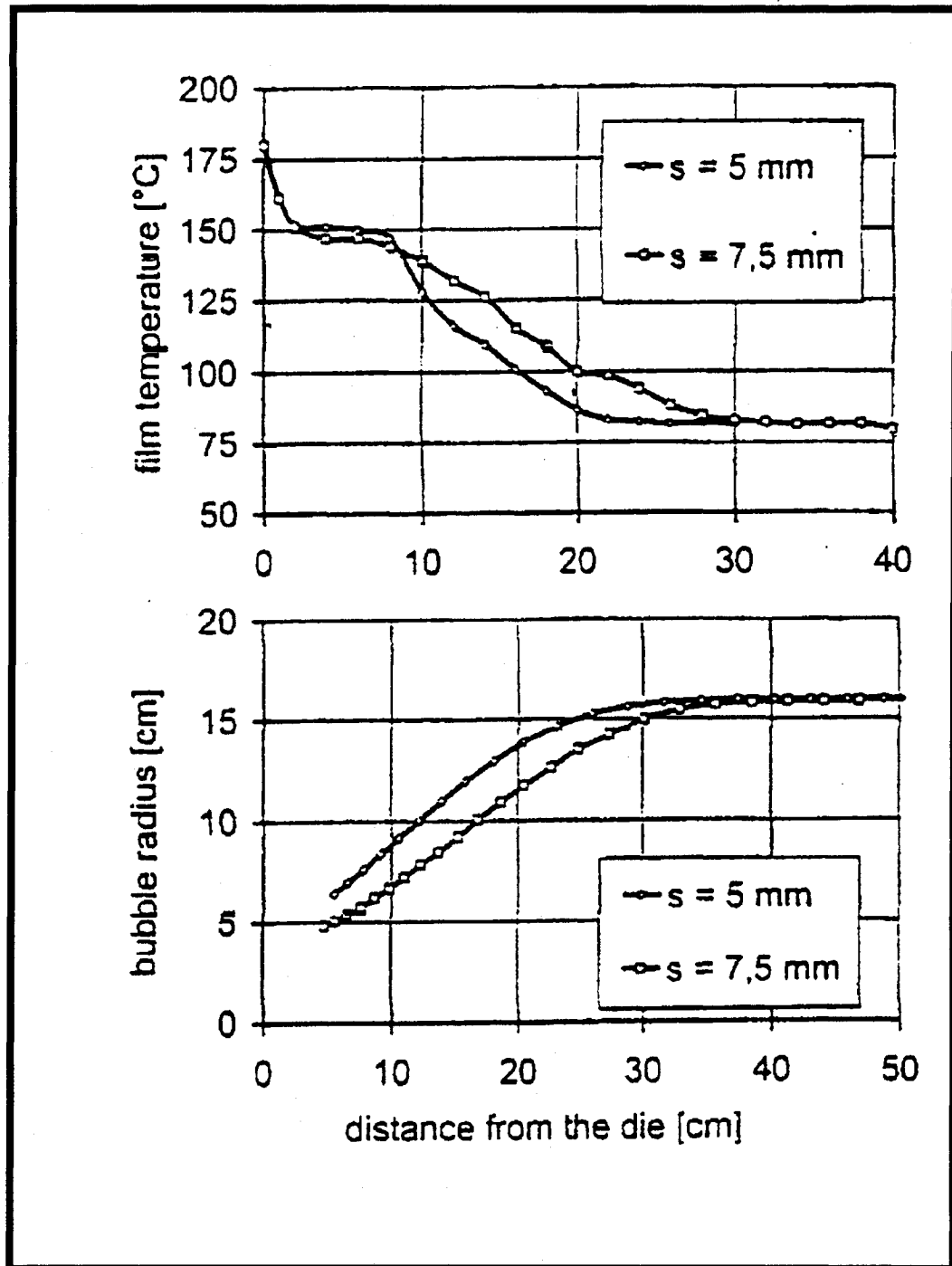


Figure 7: The bubble shape and temperature profile as a result of changing the gap width of the air ring from 5 mm to 7.5 mm. Source: Hauck and Michaeli (1998).

Hauck and Michaeli (1998) analyzed the cooling air conditions using a power law velocity profile in the boundary layer, as shown in Equation (13). They calculated the thickness of the boundary layer by using Equation (14). Then, they calculated the average velocity profile of the cooling air by using Equation (15). The calculated air velocity profile was similar to the profile of the heat transfer coefficient obtained by Sidiropoulos (2000). In both cases, there was always a plateau in the temperature profile in the same regions where there was a decrease in the air velocity (heat transfer coefficient) profile, as shown in Figures 6 and 7.

a. *Between the film and the maximum air velocity (boundary layer):*

$$V(x, y) = V_{max} \left( \frac{y}{\delta} \right)^{\frac{1}{7}} \quad (13)$$

$$\delta(x) = 0.37x \left( \frac{V_{max}x}{V} \right)^{-0.2} \quad (14)$$

b. *Between the maximum air velocity and infinity (free jet region):*

$$V(x, y) = V_{max} \left( \frac{x}{4b} \right)^{0.5} \exp \left( - \ln 2 \left( 1 - \frac{y}{\delta} \right)^2 \right) \quad (15)$$

where  $\delta$  is boundary layer width,  $x$  is the distance covered by the cooling air,  $y$  is the distance normal to the bubble,  $b$  is the air ring gap width, and  $V_{max}$  is the maximum air velocity.

## 2.3 Experimental Studies

### 2.3.1 Strain Rate and Orientation Measurements

Farber and Dealy (1974) determined the deformation rates in the machine and hoop directions in the melt zone during film blowing experiments by analyzing motion pictures. They employed a highly branched polyethylene film resin and used a 6.4 cm diameter die. The film thickness range was 50-200 microns, while the BUR range was 1.8-3.4. The temperature profile of the film was measured using a radiation pyrometer. They estimated the orientation by employing a shrinkage test, and found that the

deformation rate and orientation in the machine direction were both higher than those in the hoop direction. They also found that, in some experiments, although the deformation rate might be higher in the hoop direction near the freeze line, the orientation in the machine direction was always higher than that in the hoop direction.

Ghaneh-Fard (1999) showed that there was no general correlation between birefringence and the tensile modulus. They also confirmed the observation of Farber and Dealy (1974) that there was no correlation between the deformation rate and the final film properties. For LLDPE, they showed that increasing the take-up ratio lowered Young's modulus in both the machine and hoop directions.

Kamal et al. (1988) and Haber and Kamal (1992) used Wide angle X-ray diffraction, infrared spectroscopy, sonic modulus, birefringence, differential scanning calorimetry, density column, and tensile tests to characterize LDPE films blown at two different blow-up ratios: 4 and 2. The thickness was kept constant for these samples. The orientation of the crystalline phase was found to be characteristic of a row type structure. The amorphous phase was mainly oriented in the transverse direction. The a-axis was oriented in the machine direction at an angle in the range of 30-80° from the plane of the film, and a linear relationship was found between the tensile modulus and the angle of inclination of the a-axis. Tensile modulus decreased as the inclination angle decreased. The results indicate that the orientation of the a-axis shifted towards the transverse direction as the blow-up ratio increased. The degree of surface roughness, which has a linear relationship with the angle of inclination, decreased as the blow-up ratio increased. Using the rheoptical law to establish the relationship between birefringence and stress they, the angle of inclination of the a-axis from the film plane increases as the stress level increases. The effect of stress on a- axis orientation is consistent with the structure proposed by Keller and Machin (1967) under intermediate level of stress.

Gupta (1981) employed polystyrene (Styron 666) in film blowing experiments. He carried out fourteen nonisothermal runs. Only four of the nonisothermal experiments had a BUR > 1. Natural cooling (without employing cooling air) was employed since the size of the bubble was relatively small (the radius of the die exit was 13 mm). The



temperature at the freeze line was approximately 130 degrees higher than room temperature. One expects substantial rheological and structural changes will occur while the polymer cools to room temperature [Cao (1990)]. He observed that the deformation rate in the machine and hoop directions continued to change after the freeze line (see Figures 1 and 2).

### 2.3.2 Process Stability

Kanai and White (1984, 1999) investigated the kinematics and stability of the process over a wide range of draw ratios, blow-up ratios, and freeze-line heights for three different types of polyethylene: LDPE, LLDPE, and HDPE. They employed a nonisothermal Newtonian model, along with extensive experimental work, to identify the process stability windows by mapping the draw ratio versus the blow-up ratio at various freeze line heights. The above polymers exhibited different behavior in terms of the bubble shape (Figure 8) and the regions of stability (Figure 9). LDPE has a larger relaxation time than LLDPE and HDPE. The difference in the relaxation time causes different extension hardening, and thus different bubble shapes [Yoon and Park (1992)]. Also, LDPE had the widest region of stability and LLDPE had the narrowest. They also observed the “draw resonance” phenomena and reported that various operating conditions could produce stable, unstable, or metastable conditions. The metastable condition implies the existence of two stable states with ready passage between them. The freeze line height, which was controlled by the cooling air flow, was shown to have significant effect on the bubble shape (Figure 10). They found that increasing the air flow produced HDPE bubbles with shorter freeze line height and with wider BUR.

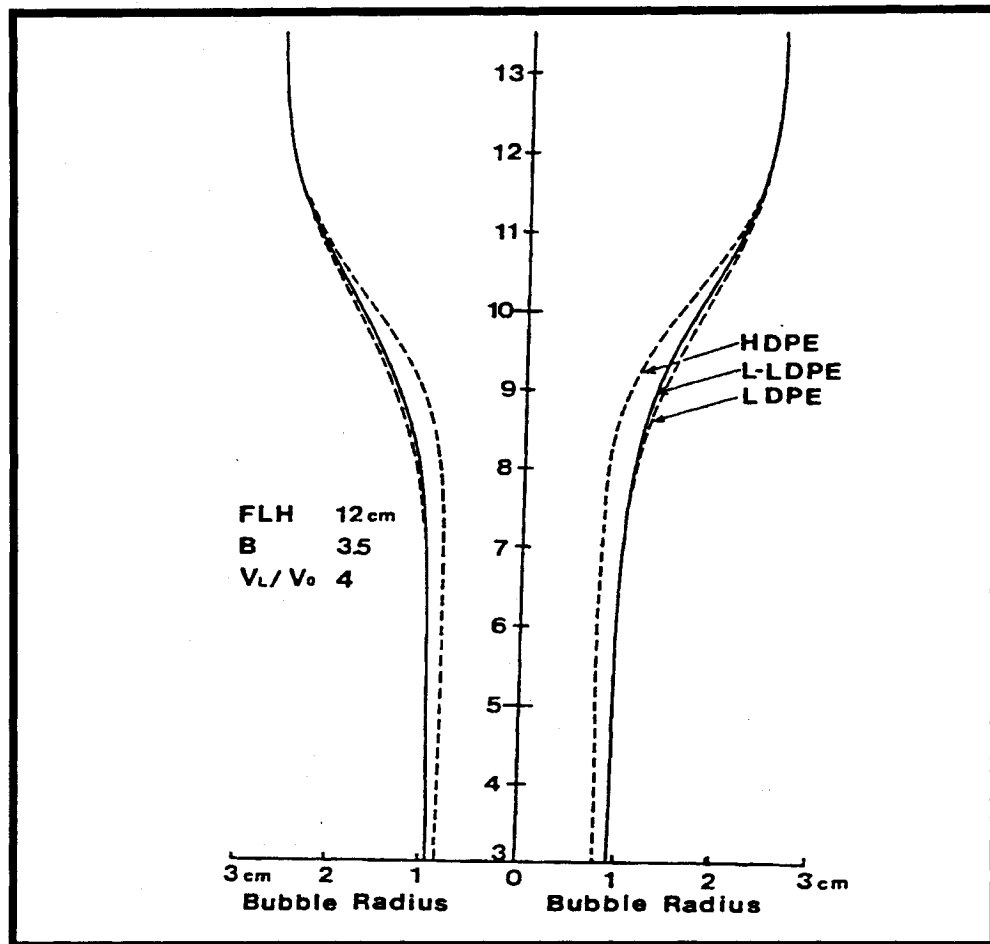


Figure 8: Bubble shape for various PE types. Source: Kanai and White (1984).

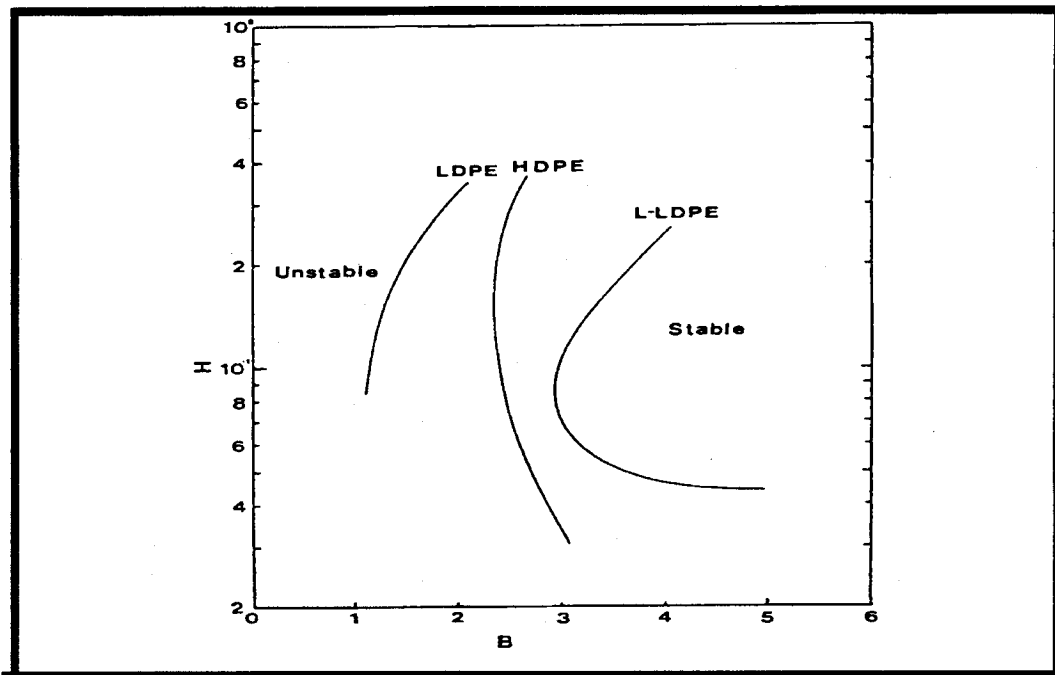


Figure 9: Thickness reduction-BUR map showing regions of stable and unstable behavior of three types of PE at a dimensionless freeze line height of 16. Source: Kanai and White (1984).

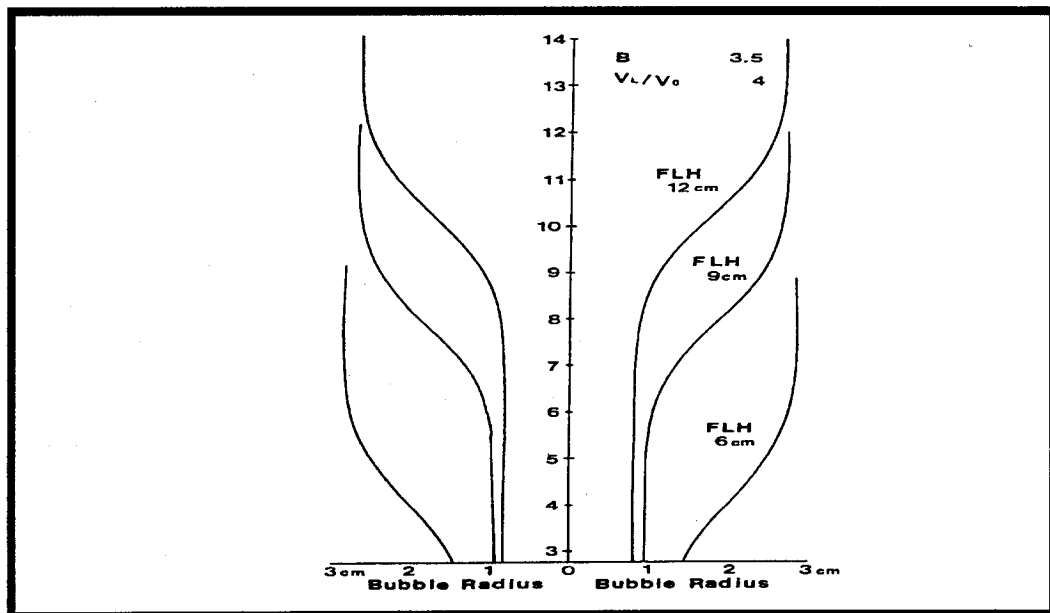


Figure 10: The effect of the freeze line height on the HDPE bubble. Source: Kanai and White (1984).

Ghaneh-Fard et al. (1996a, b) carried out extensive experimental studies to investigate the influence of the rheological properties and the processing parameters (DR, BUR, FL) on the stability of the film blowing process for four polymers (LDPE, LLDPE, HDPE, and PP). LLDPE showed the lowest birefringence, and it exhibited the least stability, while LDPE showed the highest birefringence and it exhibited the highest stability. They classified three forms of instabilities: axisymmetric periodic variations of the bubble diameter, helical motion of the bubble, and variations in the position of the solidification line. In the LDPE cases, they found an interesting response of the freeze line to the cooling air flow rate. As they increased the cooling air flow rate, the freeze line height decreased until it reached a point where a small increase in the air flow rate decreased the freeze line height significantly. The freeze line height instability was less severe in the case of HDPE. They found that the order of stability is as follows:

$$LDPE > HDPE > LLDPE > PP$$

These findings were confirmed by several subsequent studies [Ghaneh-Fard et al. (1997), (1999), Fang et al. (2001)].

Fang et al. (2001) employed the birefringence method of Ghaneh Fard et al. (1996, 1997), along with rheological correlations, to study the effect of rheological properties on the processability and the stability of various polyethylenes in the film blowing process. The shear viscosity of the resins was determined by a piston-driven capillary and in-line capillary rheometers. The uniaxial extensional viscosity was determined by using two different hyperbolic converging dies. The tensile stress was calculated from the birefringence data, and the biaxial extensional viscosity was calculated as follows:

$$\eta_{bi} = \frac{2\sigma_1 + \sigma_3}{\sqrt{0.5II_2}} \quad (16)$$

They found that the stability of the bubble was proportional to the elasticity ( $G'$ ) of the polymer. They showed that the order of stability for the polymers was as follows:

$$LDPE_a / LDPE_b > HDPE > LLDPE_m$$

The properties of the above polymers can be found elsewhere [Fang et al. (2001)].

Laffargue et al. (2002) quantified the stability by using an online video device developed for that purpose. The online system was used to measure the bubble instabilities by capturing the three-dimensional behavior of the bubble. They classified three types of instabilities:

- Draw Resonance (DR): periodic oscillation of the bubble diameter.
- Helicoidal Instability (HI): helicoidal motion of the bubble around the axial direction.
- Frost line height instability (FLH): variation in the location of the frost line.

They found that increasing the draw ratio, freeze line height, and the blow-up ratio made the bubble less stable. Kim et al. (2003) used the system in the stability comparison between metallocene catalyzed PE and PE with broad molecular weight distribution. They showed that bubbles produced from metallocene catalyzed PE were more stable than those produced from PE with broad MWD.

### 2.3.3 Effect of Crystallization

Kanai and White (1985) incorporated the effect of crystallization on viscosity by multiplying the viscosity by an exponential function of the crystallinity, as shown in the equation below:

$$\eta = \eta_0 e^{\frac{E}{RT}} e^{GX} \quad (17)$$

where  $\eta_0$  is the zero-shear viscosity of the melt at the reference temperature,  $E$  is the activation energy of melt flow,  $R$  is the universal gas constant,  $T$  is the melt temperature,  $X$  is the fraction of crystallinity, and  $G$  is a constant obtained from Figure 11.

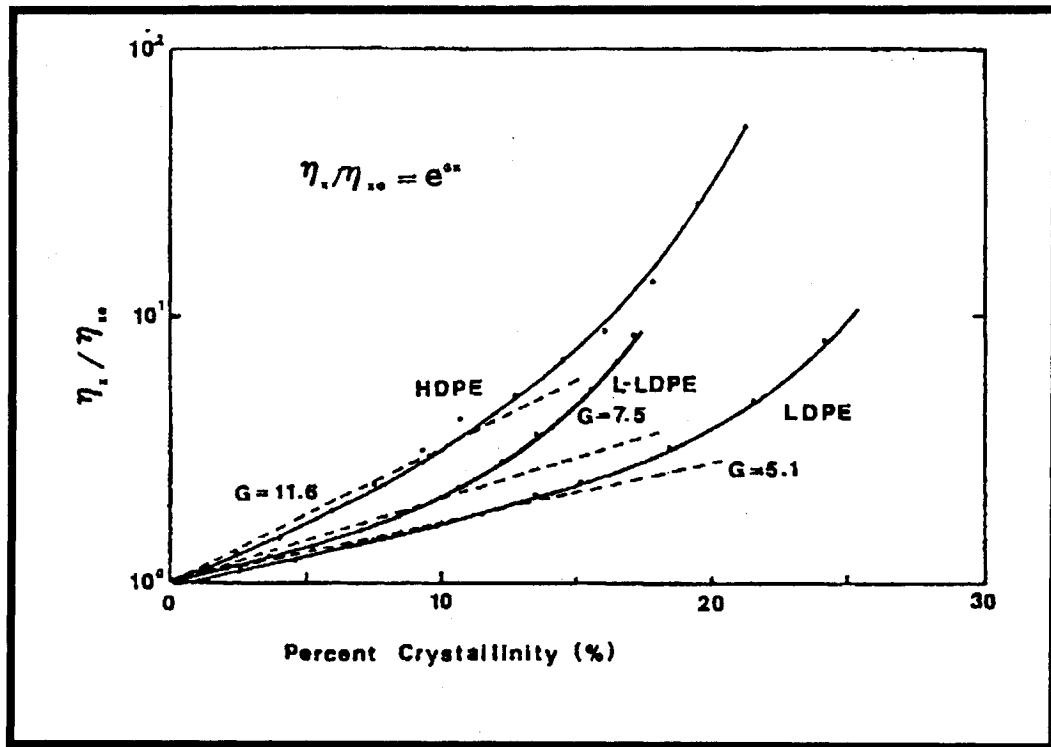


Figure 11: Apparent viscosity as a function of percent crystallinity. Source: Kanai and White (1985).

Crystallization was thought to be the reason for the plateau in the temperature profile observed in the vicinity of the freeze line. However, it is likely that the heat transfer coefficient employed by Kanai and White might have influenced the plateau. They followed the approach of Menges and Predohl (1972) in estimating the heat transfer coefficient by dividing the machine direction into three zones. In each zone, they used a different value for the empirical constant in the heat transfer correlation. Kanai and White (1984) obtained a significant drop in the heat transfer coefficient in the area of the reported plateau in the temperature profile. However, they reported that the plateau in the temperature profile was due to the crystallization process.

Bullwinkle et al. (2001) employed simultaneous on-line Infrared temperature measurements and small angle light scattering to follow LLDPE during the film blowing

process. They observed that, if the stress level was not very high during the process, the resulting spherulites were undeformed. The reported stress and deformation rate profiles were not smooth. In fact, there was a jump or inflection point in these profiles in the vicinity of the freeze line due to the crystallization.

Ghaneh-Fard et al. (1996) determined the stress tensor in the film for two LLDPE films by measuring flow birefringence. They showed that when the tensile stress is less than  $1 \times 10^6 \text{ Pa}$ ., the stress optical law is described by the following equation:

$$n_i = c \tau_i \quad (18)$$

They assumed that the refractive index ( $n_i$ ) in any direction is proportional to stress component ( $\tau_i$ ) in the same direction and that the magnitude of the stress-optical coefficient ( $c = 2.6 \times 10^{-9} \text{ m}^2/\text{N}$ ) [Janeschitz-Kriegl (1983)] does not depend on the strain rate or temperature. Polarized light from a *He-Ne* gas laser beam ( $\lambda = 632.8 \text{ nm}$ ) was used. The bubble is located between the source of the polarized light and a detector. The polarized light passed through the two sides of the bubble. The bubble was assumed to be stable and perfectly symmetrical. After passing through the bubble, the beam was detected by the detector. The following procedure was employed to carry out their experiments:

1. Measure the blowing angle and use it as the light incident angle ( $\theta_i$ ).
2. Calculate the refraction angle ( $\theta_r$ ) from the measured light incident angle using the following equation:

$$\sin \theta_r = \sin \theta_i / 1.49$$

3. Calculate the birefringence ( $\Delta n(\theta_r)$ ) using the following equation:

$$\delta = \frac{2\pi \Delta n(\theta_r) d}{\lambda \cos \theta_r}$$

where  $\lambda$  is the wave length,  $\delta$  is the measured retardation, and  $d$  is the film thickness

4. Perform the above steps at two different incident angles and employ the following equation to calculate the birefringence.

$$\Delta n(\theta_r) = (n_1 - n_3) \cos^2 \theta_r + (n_2 - n_3) \sin^2 \theta_r$$

Ghaneh-Fard et al. (1996) found that crystallization was the main factor that affected orientation development. Birefringence data were used to calculate the extensional viscosity below the onset of crystallization. Ghaneh Fard et al. (1997) employed the above birefringence method to evaluate the effect of the take-up ratio (TUR or DR), the blow-up ratio (BUR), and the freeze line height (FLH) on the birefringence and bubble behavior for LLDPE. Some of their results are shown in Figure 12.



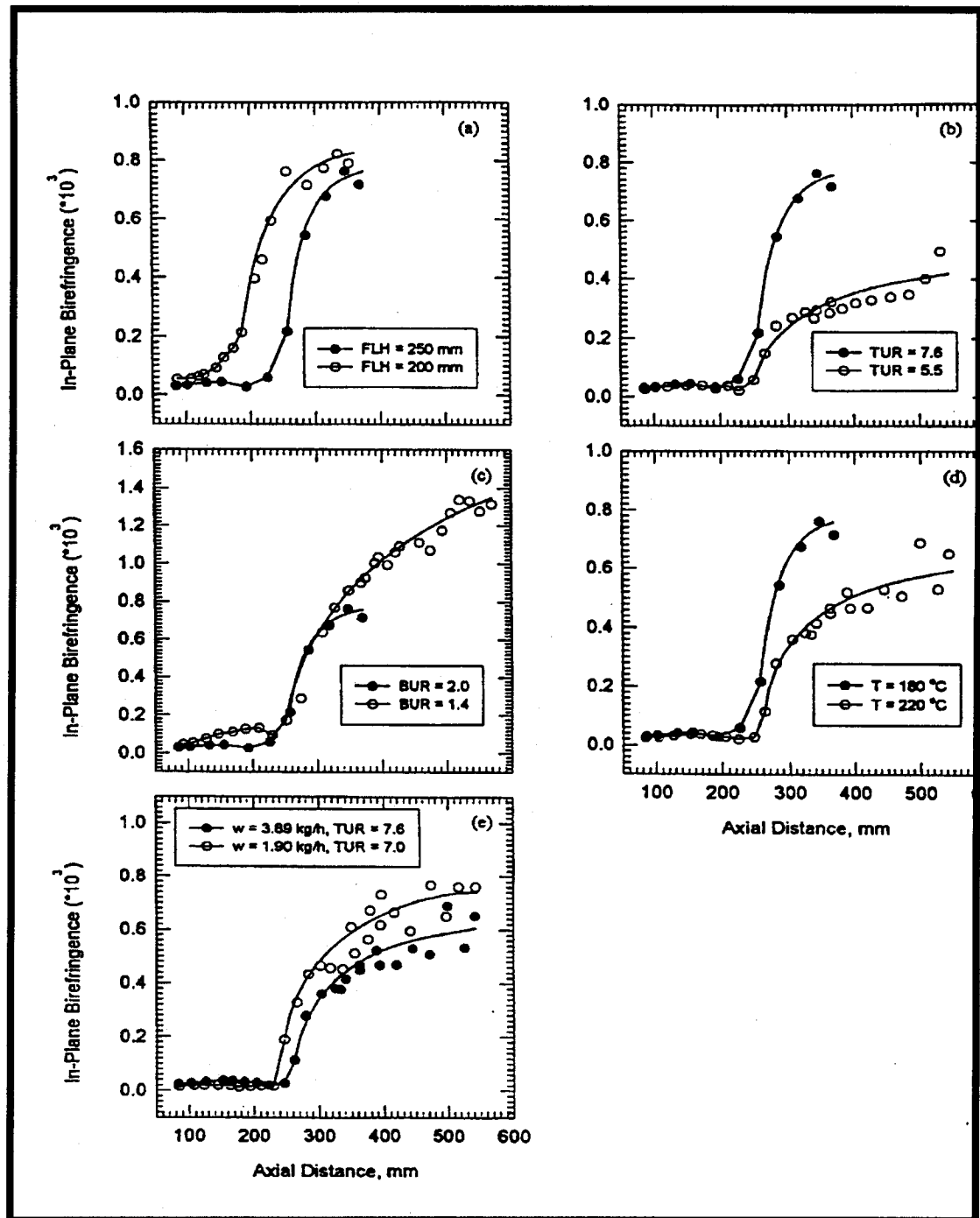


Figure 12: The effect of the freeze line height (FLH), the take-up ratio (TUR), the blow-up ratio (BUR), and the extrusion temperature on the in-plane birefringence. Source: Ghaneh-Fard et al. (1997).

## 2.4 Rheological Considerations

Pearson and Petrie (1975) employed a Newtonian model, Equation (1) in developing the theoretical framework of the film blowing process. Petrie (1973) extended the treatment by using the Maxwell model, in view of the viscoelastic nature of the melt. Han and Park (1975) employed the power law model to evaluate the effect of viscosity change on process stability. Lou and Tanner (1985) compared the Maxwell and Leonov models, in order to incorporate the effect of strain hardening. They showed that the Maxwell model gave better predictive results. Cain and Denn (1988) employed the Newtonian, Maxwell and Marrucci models in a study to explore the effect of viscoelasticity on process stability. Kanai and White (1985) incorporated crystallization to study the behavior of semi-crystalline polymers. Cao (1990) used a two-phase multi-zone model to predict the viscoelastic and the visco-elastic-plastic behavior of the film in the process. Doufas and McHugh (2001) proposed a two-dimensional microstructural model to explore the effect of crystallization. Sidiropoulos (2000) employed the PTT model to describe the extensional properties of the melt.

Viscoelastic melts maintain stresses for some time after the cessation of deformation. This period of time is known as the relaxation time. Such behavior should be incorporated in rheological constitutive equations. The principle of frame invariance has to be preserved in any constitutive equation to predict the nonlinear behavior of the melt at large deformation rates [Larson (1988)]. If the frame of the reference is deformed with the material elements, then the frame invariance can be achieved by incorporating the upper convected time derivative in the constitutive equation and the use of the Finger tensor. The Newtonian and Maxwell models cannot describe the viscoelastic behavior of polyethylenes [Yoon and Park (1992)].

Many models assume that polymer chains undergo a large number of conformations and that the ends of any chain deform affinely, which means that the deformation of the polymer chain is equal to the deformation of the entire polymer melt. However, chains in most real melts move non-affinely, as a result of the slippage of the chains relative to each other and the extension of some folded chains. Slippage reduces

the impact of the deformation rate on the stress. The polymer melt is considered to form transient networks, in which the polymer chains are strands that are not chemically cross-linked. These strands join to form junctions and then break free at equal rates, as long as the conditions keep changing, according to the temporary network theory formulated by Green and Tobolsky (1946). The breakage probability increases upon increasing the chain extension, which causes the effect of the stresses to be nonlinear, depending on the magnitude of applied stresses. Thus, the predicted viscosity in extensional flow might reach a maximum value, then it may drop or it can reach a plateau at that value.

The above behavior was modeled by Phan-Thien and Tanner (1977, 1978) to obtain a new constitutive equation, that ultimately involves multiplying the stress in the upper convective Maxwell model (UCM) by an extensional function,  $Y(\tau)$ . The extensional function can take two forms: an exponential form for melts that exhibit a maximum in the viscosity profile, and a linear form for melts that show a plateau at the maximum viscosity [Tanner (2000)]. The slippage of the polymer chains is incorporated using an empirical constant multiplied by the deformation rate tensor in the UCM. The slippage and extensional parameters ( $\xi$  and  $\epsilon$ ) can be treated as model-adjusted parameters [Khan and Larson (1987)], and their values can be obtained from the literature *e.g.* Tas (1994) or by conducting shear and transient experiments. The relevant equations in the Phan-Thien and Tanner (PTT) model are given below.

$$\tau_i Y(\tau) + \lambda \left[ \tau_i + 2\xi(\tau_i \dot{D}_i) \right] = 2\eta \dot{D}_i \quad (19)$$

$$Y(\tau) = \exp\left(\frac{\epsilon\lambda}{\eta} \text{tr} \tau_i\right) \quad (20)$$

$$Y(\tau) = \frac{\epsilon\lambda}{\eta} \text{tr} \tau_i \quad (21)$$

where  $\eta$  and  $\lambda$  are the viscosity and relaxation time of the melt,  $\tau_i$  is the stress in  $i$ -direction, and  $\dot{D}_i$  is the deformation rate in the  $i$ -direction. The subscript  $i$  refers to the principal direction: machine, hoop and transverse directions.

Khan and Larson (1987), and Maia (1998) compared several constitutive equations (Johnson-Segalman, White-Metzner, Marrucci, Giesekus, Larson, and PTT equations) and concluded that the PTT model gives a more accurate description of extensional flows. Maia defined the slippage constant as a function of the deformation rate. Tas (1994) concluded that the PTT model was superior to other constitutive equations (Wagner, Giesekus, and Leonov), when employed to predict biaxial extension. He also found that the value of the extensional parameter was two orders of magnitude lower than the value of the slippage parameter, which was in agreement with the observation of Phan-Thien (1978). On the other hand, Cao and Campbell (1990) compared several constitutive equations (Newtonian, Maxwell, Giesekus, PTT, White-Metzner, and Larson) and did not find the same advantages for the PTT model. This was probably because they used a simplified version of the PTT equations that employed a linear extensional function instead of the exponential form. They also set the slippage parameter to zero. This effectively reduced the PTT equation to the Giesekus model.

# Chapter 3

## 3 SCOPE AND OBJECTIVES

The primary goal of the present work is to develop a microstructure and product-oriented two-dimensional model of the film blowing process that incorporates crystallinity, viscoelasticity, and cooling effects. The model covers the whole process from the die exit to the nip rolls. It employs the Phan-Thien and Tanner (PTT) constitutive model for the melt region and the Neo-Hookean constitutive model for the semi-solid region. It will be applied for a wide range of processing conditions and different types of polyethylene. The proposed model takes into consideration the effects of stress-induced orientation on crystallization and the interactions between crystallinity and rheology. The predictions of the model are validated by comparison with analytical and computational solutions reported in the literature and experimental data reported by various researchers.

The specific objectives of the thesis are outlined below:

1. Develop a two-dimensional model of the film blowing process that describes the variation of temperature in the thickness and in the machine directions, and predicts the variations of dimensions, deformation, and stresses from the die exit to the nip rolls.
2. Incorporate crystallization and viscoelastic effects to predict crystallinity, orientation, and birefringence in the blown films.
3. Employ a realistic heat transfer coefficient.
4. Establish the accuracy and robustness of the model by comparing the model predictions to available analytical and computational results for a variety of film blowing systems.
5. Validate the proposed model by comparing model predictions to experimental film blowing reported data.

6. Validate the proposed model by comparing model predictions regarding film crystallinity and orientation to experimental data obtained on blown films.

The development of the two-dimensional model of the film blowing process and the treatment of the heat transfer coefficient are given in Chapter 4. In additions, Chapter 4 presents the numerical scheme that is employed in the computer simulation, and the input parameters required to run the simulation. It also provides the results of tests of the accuracy, stability, and robustness of the model.

Chapter 5 provides validation of the proposed model by comparison of model predictions to experimental data reported in literature. Moreover, experimental data obtained on blown films in our laboratories are compared to the crystallinity and orientation values predicted by the proposed simulation.

The conclusions, the main contributions to knowledge, and suggestions for future studies are highlighted in chapter 6, which is followed by a list of references.

# Chapter 4

## 4 MATHEMATICAL MODEL

This chapter describes the proposed mathematical treatment of the dynamics, kinematics, energetics, and rheology of the film blowing process. The equations of motions follow the framework of Pearson and Petrie (1970). A system of seven main equations is employed to model the process: one continuity equation, two force balance equations, one energy equation, and three constitutive equations. The proper boundary conditions are identified to solve the system of equations. A new correlation is proposed to estimate the variable heat transfer coefficient. Furthermore, a set of auxiliary equations is suggested to calculate orientation, viscosity and relaxation time for the melt, and relaxation modulus for the solid-like film.

### 4.1 Description of the Film Blowing Process

The film blowing process is modeled with a two-dimensional simulation in the domain  $0 \leq z \leq L$  and  $h_0 \geq h \geq h_f$ .  $L$  is the total vertical distance between the die exit and the nip rolls, and  $z$  is the axial distance moving away from the die exit, while  $h$  is the film thickness marching outward in the direction normal to the film.  $h_f$  and  $h_0$  are the final film thickness and the gap thickness of the die, respectively. In the following, a superscript asterisk signifies a dimensionless variable. Otherwise, the variables are dimensional. The dimensionless variables are defined in the nomenclature section, along with the corresponding dimensional variables. A schematic of the film blowing process is shown in Figure 13.

The film is regarded as a thin membrane under the influence of the forces resulting from the longitudinal boundary traction and the difference in pressure between the inside and the outside of the produced bubble. As soon as the molten tube leaves the die exit, it is subjected to fast cooling and tensile stresses. These conditions cause

significant crystallization, which has important effects on the film structure. Thus, the model presented in this study incorporates the changes in the rheological behavior and the morphological characteristics of the blown film, in order to obtain a realistic prediction of the properties of the final film.

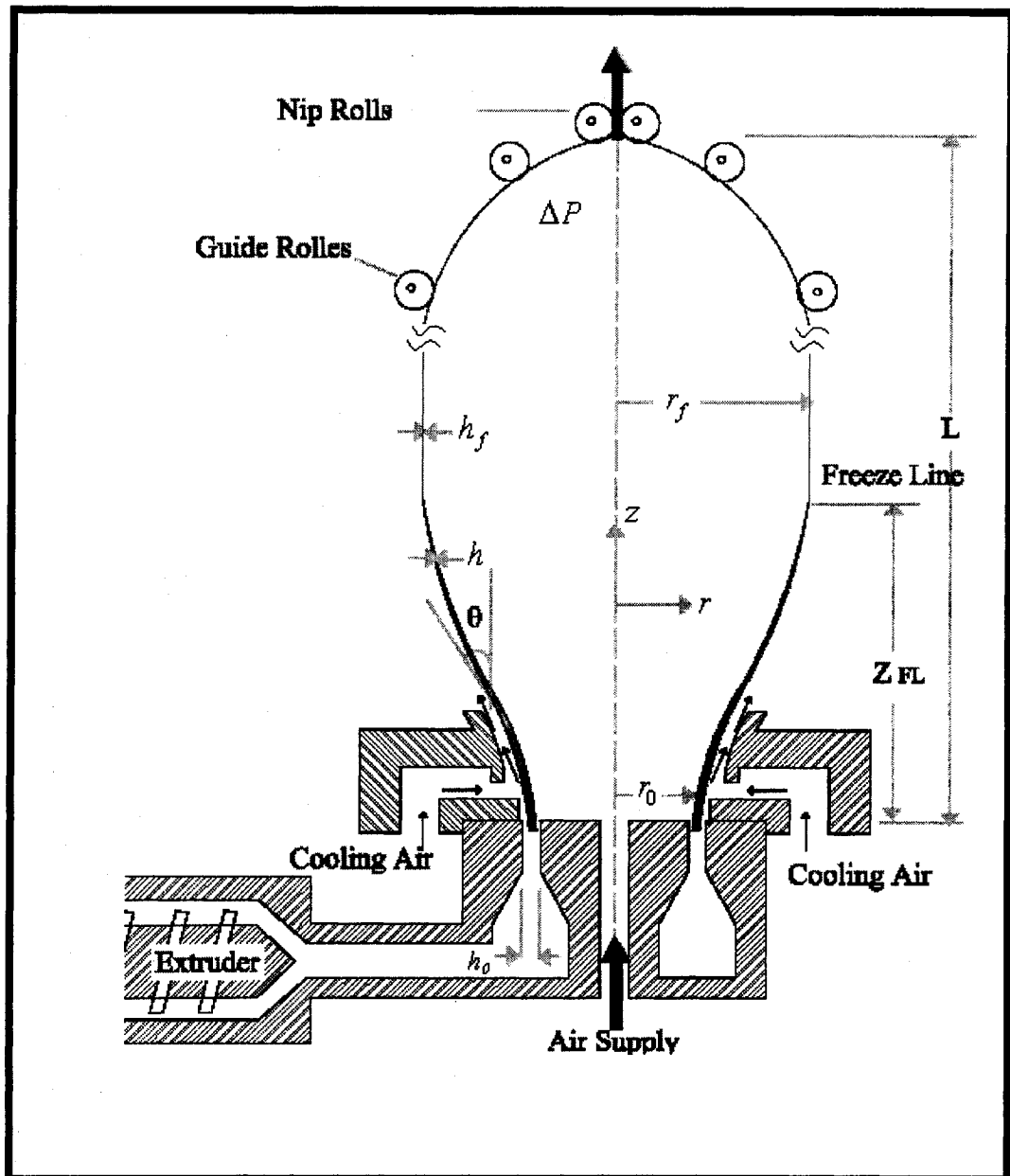


Figure 13: Schematic of the film blowing process.



The process is assumed to be at steady state, and the bubble is assumed to be axisymmetric with respect to the vertical  $z$ -axis. Since, the thickness of the film is very small, relative to the radius of the bubble, it is treated as a thin membrane that has two radii of curvature in the machine and hoop directions,  $R_1$  and  $R_3$  [Pearson and Petrie (1970)]. The radii of curvature are related to the radius of the tube by using the geometrical relations of the thin shell theory. Figure 14 shows a schematic of the differential element of the film, along with the directions of the stress components in the machine and hoop directions. The thin shell approximation [Gibson (1965), Leissa (1973)] is also used in formulating the force balance. The following relationships are used for  $R_1$  and  $R_3$  [Pearson and Petrie (1970)]:

$$R_1 = \frac{-\sec^3 \theta}{\frac{d^2 r}{dz^2}} = - \frac{\left(1 + \left(\frac{dr}{dz}\right)^2\right)^{3/2}}{\frac{d^2 r}{dz^2}} \quad (22)$$

$$R_3 = \frac{r}{\cos \theta} = r \sqrt{1 + (dr/dz)^2} \quad (23)$$

$$\tan \theta = \frac{dr}{dz} \quad (24)$$

The subscripts 1, 2, and 3 refer to the meridian (machine), the thickness (normal), and the hoop (transverse) directions, respectively.

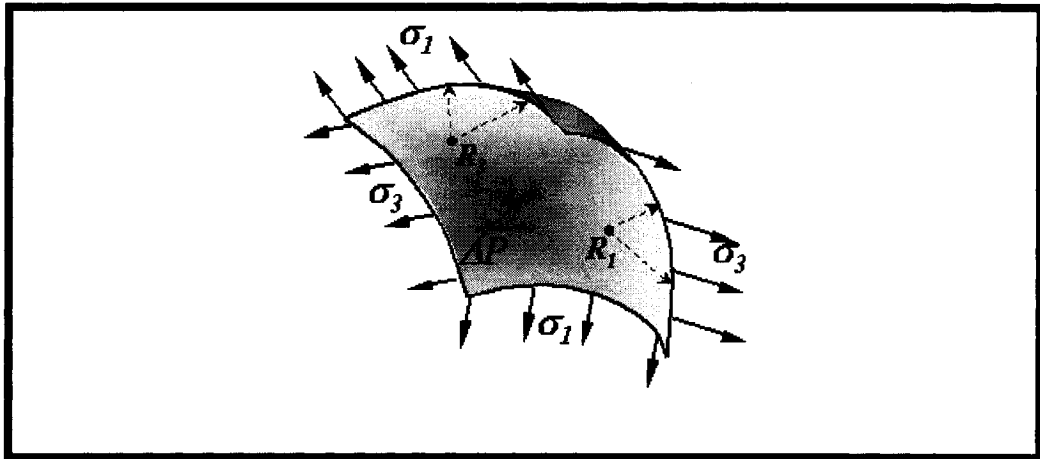


Figure 14: The film is assumed to be a thin membrane that has two radii of curvature.

## 4.2 Mass Balance

The mass flow rate of the polymer is conserved throughout the process and is calculated by the following equation:

$$\dot{m} = \rho Q = \rho \cdot 2\pi r h v \quad (25)$$

While the density is assumed to be constant, allowance is made for variation of the crystallinity, which influences both the flow characteristics (e.g. the viscosity and viscoelastic parameters) and energetics in the energy equation. Furthermore, the effect of density variation in the energy equation is reduced by the use of thermal diffusivity, which tends to undergo little change, compared to thermal conductivity, under the prevailing experimental conditions [Kamal et al. (1983)]. The equation of continuity, in its final dimensionless form, is:

$$\dot{r} \dot{h} \dot{v} = 1 \quad (26)$$

## 4.3 Force Balance

In formulating the momentum balance, air friction, inertia, gravity force, and surface tension are neglected. The pre-process stresses in the die are also ignored. Thus, it is assumed that the processing conditions are such that melt instability is not encountered at the exit of the die. Extrusion swell has been ignored

Two equations are needed to describe the relationships among the normal stresses, inflation pressure, and take-up force in two directions [Pearson and Petrie (1970)]. The approach of Agassant (1991) is adopted in formulating the two force balance equations that are constructed by employing the representation shown in Figure 15 of the differential element of the film that was shown in Figure 14. The first equation is for forces in the machine direction, while the second equation is for forces in the thickness direction.

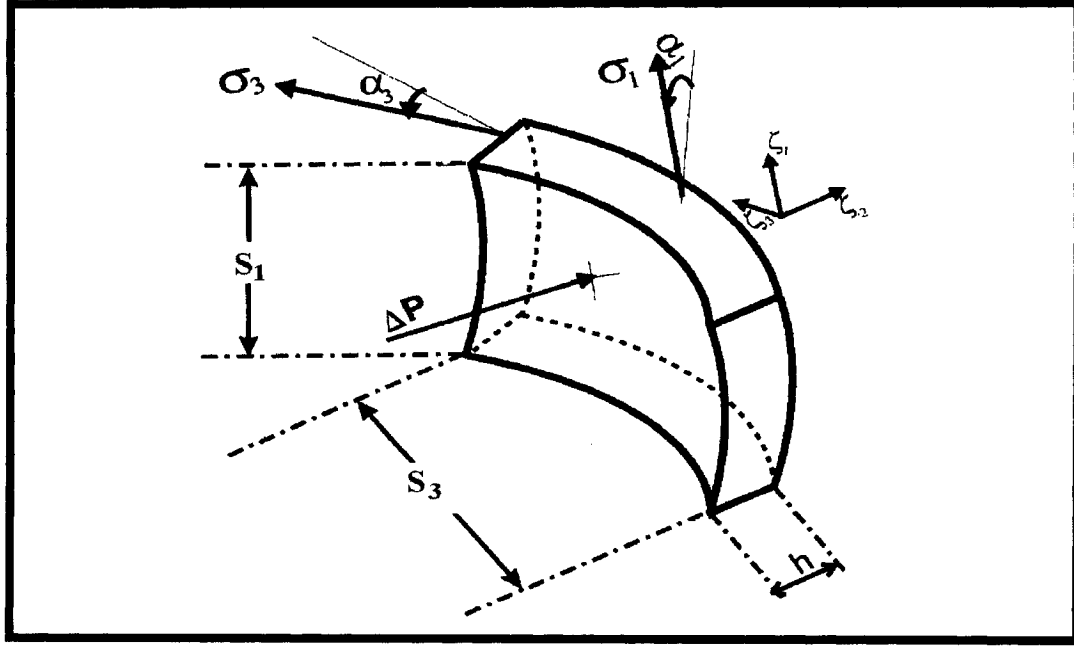


Figure 15: Dimensional representation of the differential element of the film.

It should be noted that  $\zeta_1$ ,  $\zeta_2$  and  $\zeta_3$  are local coordinates of the differential element in Figure 15.  $\alpha_1$  and  $\alpha_3$  are the angles of curvature in the machine and hoop directions.

#### 4.3.1 Force Balance in the Normal Direction

$$\text{Force due the internal pressure} = \Delta P \cdot S_1 \cdot S_3 \quad (27)$$

$$\text{Force due to the meridian stresses} = 2S_3 \cdot h \cdot \sigma_1 \cdot \sin \alpha_1 \quad (28)$$

$$\text{Force due to the hoop stresses} = 2S_1 \cdot h \cdot \sigma_3 \cdot \sin \alpha_3 \quad (29)$$

$$\text{Force due to the element weight} = \rho \cdot S_1 \cdot S_3 \cdot h \cdot g \cdot \sin \theta \quad (30)$$

$$\begin{aligned} \sin \alpha_1 &\cong \alpha_1 \cong \frac{S_1}{2R_1} \\ \sin \alpha_3 &\cong \alpha_3 \cong \frac{S_3}{2R_3} \end{aligned} \quad \begin{array}{l} \text{(the angle of curvature is very small)} \\ \end{array} \quad (31)$$

$$\Delta P(S_1 S_3) = 2S_3 \cdot h \cdot \sigma_1 \left( \frac{S_1}{2R_1} \right) + 2S_1 \cdot h \cdot \sigma_3 \left( \frac{S_3}{2R_3} \right) - \rho \cdot S_1 \cdot S_3 \cdot h \cdot g \cdot \sin \theta \quad (32)$$

$$\Rightarrow \frac{\Delta P}{h} = \frac{\sigma_1}{R_1} + \frac{\sigma_3}{R_3} - \rho g \sin \theta \quad (33)$$

Substituting for  $R_1$  and  $R_2$  and ignoring the effect of gravity give the following equation:

$$\frac{\Delta P}{h} = \frac{\sigma_1}{- \sec \theta} \frac{d\theta}{dz} + \frac{\sigma_3}{r \sec \theta} \quad (34)$$

Rearranging the above equation gives:

$$\frac{d\theta}{dz} = \frac{1}{\sigma_1} \left( \frac{\sigma_3}{r} - \frac{\Delta p}{h \cos \theta} \right) \quad (35)$$

which describes the change in the blowing angle along the machine direction

### 4.3.2 Force Balance in the Machine Direction

The forces acting on a film element at position  $(r, z)$  consist of the components of the draw force, the pressure force, and the weight of the film, as follows:

$$F(z) = F_0 + \Delta p \cdot \pi(r^2 - r_0^2) + \int 2\pi r h \rho g \frac{dz}{\cos \theta} \quad (36)$$

$$\text{But } F(z) = 2\pi r h \sigma_1 \cos \theta \quad (37)$$

$$\Rightarrow F_0 = 2\pi r h \sigma_1 \cos \theta - \Delta p \cdot \pi(r^2 - r_0^2) - \int 2\pi r h \rho g \frac{dz}{\cos \theta} \quad (38)$$

Equation (38) is differentiated with respect to  $z$  after ignoring the gravity effect:

$$2\pi(r'h\sigma_1 \cos \theta + rh'\sigma_1 \cos \theta + rh\sigma_1' \cos \theta - rh\sigma_1 \theta' \sin \theta) = 2\pi \Delta p r r'$$

Dividing by  $2\pi \cos \theta$  and substituting for  $\theta'$  from Equation (35) yields:

$$r'h\sigma_1 + rh'\sigma_1 + rh\sigma_1' - rhr' \left( \left( \frac{\sigma_3}{r} - \frac{\Delta p}{h \cos \theta} \right) \right) = \frac{\Delta p r r'}{\cos \theta} \quad (39)$$

$$r'h\sigma_1 + rh'\sigma_1 + rh\sigma_1' - rhr' \left( \frac{\sigma_3}{r} \right) + rr' \left( \frac{\Delta p}{\cos \theta} \right) = \frac{\Delta p r r'}{\cos \theta} \quad (40)$$

Canceling similar terms, dividing by  $rh\sigma_1$ , and rearranging produce:

$$\sigma_1' = \frac{r'}{r} (\sigma_3 - \sigma_1) - \frac{h'}{h} \sigma_1 \quad (41)$$

Equation (41) is rewritten in the following form to calculate the thickness reduction:

$$\frac{h'}{h} = \frac{r'}{r} \left( \frac{\sigma_3 - \sigma_1}{\sigma_1} \right) - \frac{\sigma_1'}{\sigma_1} \quad (42)$$

### 4.3.3 Final Equations of Motion

The final equations of motion that are employed in the current work are written in dimensionless form as follows:

$$\frac{\dot{h}'}{\dot{h}} = \frac{\dot{r}'}{\dot{r}} \left( \frac{\dot{\sigma}_3 - \dot{\sigma}_1}{\dot{\sigma}_1} \right) - \frac{\dot{\sigma}_1'}{\dot{\sigma}_1} \quad (43)$$

$$\theta' = \frac{1}{\dot{\sigma}_1} \left( \frac{\dot{\sigma}_3}{\dot{r}} - \frac{2B}{\dot{h} \cos \theta} \right) \quad (44)$$

In the above and hereafter, the prime refers to the derivative of the corresponding dimensionless variable with respect to  $z^*$ . Moreover, the radii of curvature are eliminated from the equations by using their geometrical relationships with the bubble radius and the blowing angle, in order to avoid instabilities that might be encountered due to the large axial curvature in the vicinity of the freeze line. This approach was followed by André et al. (1998).

Equation (38) is combined with Equation (33), after ignoring the gravity effect and substituting from Equations (22) and (23). The terms of the resulting equations are rendered dimensionless as follows.

The force balance in the machine direction becomes:

$$\sigma_1 - v(F^* + r^2 B) \left[ 1 + \left( \frac{dr}{dz} \right)^2 \right]^{1/2} = 0 \quad (45)$$

and the force balance in the thickness direction becomes:

$$(F^* + r^2 B) \frac{d^2 r}{dz^2} + 2rB \left[ 1 + \left( \frac{dr}{dz} \right)^2 \right] - \frac{\sigma_3}{vr} \left[ 1 + \left( \frac{dr}{dz} \right)^2 \right]^{1/2} = 0 \quad (46)$$

where

$$B = \frac{\pi \Delta p r_0^3}{\eta Q} \text{ and } F^* = \frac{F r_0}{\eta Q} - B \left( \frac{r}{r_0} \right)^2 = F_z - r^{*2} B \quad (47)$$

where the following Newtonian definition of the stresses is employed in the above equations

$$\sigma_1 = 2\eta v_1 \cos \theta \frac{dv}{dz} \quad (48)$$

$$\sigma_3 = 2\eta v_1 \cos \theta \frac{dr}{r.dz} \quad (49)$$

to give the following non-dimensional Newtonian model.

$$2r^{*2} (F^* + Br^{*2}) r^{*''} = 6\eta^* r^{*'} + (1 + r^{*'}{}^2) (F^* - 3Br^{*2}) r^* \quad (50)$$

$$\frac{h^{*'}}{h^*} = -\frac{1}{2} \frac{r^{*'}}{r^*} - \frac{1}{4\eta^*} (1 + r^{*'}{}^2) (F^* + Br^{*2}) \quad (51)$$

The above two Newtonian constitutive Equations (50) and (51) were only used to check the validity of the current work when a comparison was made with limiting classical Newtonian cases reported in the literature, e. g. by Kanai and White (1985) and Cain and Denn (1988). Two interesting observations may be noted from Equations (50) and (51). Firstly, the equations are uncoupled. Secondly, a blow-up ratio of unity can be achieved only when  $F^* = 3B$ . In the isothermal case, because  $\eta^* = 1$  and  $r^{*'} = r^{*''} = 0$ , Equation (50) yields  $F^* = 3B$ . Moreover, when the blow-up ratio is equal to one, the thickness reduction can be calculated from the following equation:

$$h = h_0 \exp(-Fz/3) \quad (52)$$

Using Equation (47) and considering  $\eta^* = 1$  and  $r^{*'} = r^{*''} = 0$  reduce Equation (51) to

$$\frac{h^{*'}}{h^*} = -F/3, \text{ which can be integrated with respect to } z \text{ to yield Equation (52).}$$

## 4.4 Energy Balance

### 4.4.1 Main Energy Equation

The film undergoes strong and fast cooling during the process. The general form of the energy equation is employed to model heat transfer throughout the process:

$$\rho C_v \frac{DT}{Dt} = -\nabla \cdot q - T \left( \frac{\partial p}{\partial T} \right)_v (\nabla \cdot v) - (\tau : \nabla v) + \rho \Delta H_f \frac{DX}{Dt} \quad (53)$$

The following assumptions are employed to solve the above equation:

- i) The flow is incompressible, viscous dissipation is negligible, which means that the second and third terms of the right hand side (R.H.S) of Equation (53) are neglected.
- ii) The last term in the R.H.S of the equation is due to the heat released during crystallization.
- iii) The system is considered to be at steady state

Therefore, the above equation may be rewritten as follows:

$$\rho C_p \left( v_z \frac{\partial T}{\partial z_l} + v_r \frac{\partial T}{\partial r_l} + \frac{v_\phi}{r} \frac{\partial T}{\partial \phi_l} \right) = -k \left( \frac{1}{r} \frac{\partial}{\partial r_l} \left( r \frac{\partial T}{\partial r_l} \right) + \frac{1}{r^2} \frac{\partial^2 T}{\partial \phi_l^2} + \frac{\partial^2 T}{\partial z_l^2} \right) + \rho \Delta H_f v_l \frac{\partial X}{\partial z_l} \quad (54)$$

Furthermore, the following assumptions are made:

- i) The heat capacity,  $C_p$ , the thermal conductivity,  $k$ , the density,  $\rho$ , and the latent heat of crystallization,  $\Delta H_f$ , are all assumed to be constant.
- ii) There is no temperature gradient in the hoop direction ( $\phi$ )
- iii) There is no convection (bulk motion) in the thickness direction.
- iv) Heat conduction is significant only in the thickness direction, because  $Pe \gg 1$  in the machine direction and  $\ll 1$  in the thickness direction, where  $Pe$  is Peclet number.

Thus, Equation (54) becomes:

$$\rho C_p \left( v_z \frac{\partial T}{\partial z_l} \right) = -k \left( \frac{1}{r} \frac{\partial}{\partial r_l} \left( r \frac{\partial T}{\partial r_l} \right) \right) + \rho \Delta H_f v_l \frac{\partial X}{\partial z_l} \quad (55)$$

where the local coordinates of the differential element and time are related to the global cylindrical coordinates of the bubble as follow:

$$\partial z_l = \cos \theta \cdot \partial z \quad (56)$$

$$\partial r_l = \cos \theta \cdot \partial r \quad (57)$$

$$v = v_z \quad (58)$$

$$dz = v \cdot dt \quad (59)$$

With the above coordinate transformation, the energy equation becomes:

$$\frac{\rho C_p v}{k} \frac{\partial T}{\partial z} = - \left( \frac{\partial^2 T}{\partial r^2} + \frac{\cos \theta}{r} \frac{\partial T}{\partial r} \right) + \rho v \Delta H_f \frac{\partial X}{\partial z} \quad (60)$$

Equation (60) is multiplied by  $(r_0/v_0 T_0)$  to render it dimensionless. After employing the dimensionless terms and rearranging, the energy equation is reduced to the following form:

$$v \frac{\partial T^*}{\partial z} = \frac{\alpha}{r_0 v_0} \left[ \frac{\partial^2 T^*}{\partial r^2} + \frac{\cos \theta}{r} \frac{\partial T^*}{\partial r} \right] + \frac{\Delta H_f}{C_p T_0} \cdot v \cdot \frac{\partial X}{\partial z} \quad (61)$$

$X$  is the absolute crystallinity of the material.

#### 4.4.2 Boundary Conditions

It is assumed that the volume of the air trapped inside the bubble is so small that its temperature is the same as that of the inner surface of the film, which implies an adiabatic condition at the inner surface. The combined effect of radiation and convection heat transfer from the film to the cooling air and the surroundings is introduced as a boundary condition at the outer surface of the film. An adaptation of the heat transfer



coefficient obtained by Sidiropoulos (2000) is employed for this purpose. The melt temperature at the die exit is assumed to be known and so high that no crystallization occurs in the melt prior to leaving the die. The following dimensionless boundary conditions are employed:

$$\text{at the outer film surface:} \quad d\dot{T}/d\dot{r} = -\frac{HTC_{combined}}{r_0 k} \left( \dot{T}_{surface} - \dot{T}_{air} \right) \quad (62)$$

$$\text{at the inner film surface:} \quad d\dot{T}/d\dot{r} = 0 \quad (63)$$

$$\text{at the die exit:} \quad \dot{T} = 1, \quad X = 0 \quad (64)$$

$HTC_{combined}$  is the effective heat transfer coefficient, combining both convection and radiation;  $T_{air}$  is the temperature of the cooling air; and  $T_{surface}$  is the temperature of the film surface. Equation (61) is discretized by employing the Crank-Nicholson scheme as follows:

$$\frac{v^{i+1}}{\Delta z} (T_j^{i+1} - T_j^i) = \frac{\alpha}{r_0 v_0} \left( \frac{1}{(\Delta r)^2} (T_{j-1}^{i+1} - 2T_j^{i+1} + T_{j+1}^{i+1}) + \frac{1}{r\Delta r} (T_{j+1}^{i+1} - T_j^{i+1}) \right) + \frac{\Delta H_f}{C_p T_0} v^{i+1} \frac{\Delta \chi}{\Delta z} \quad (65)$$

And the boundary condition is written as follows:

$$\frac{1}{\Delta r} (T_j^i - T_{j-1}^i) = -\frac{HTC_{combined} r_0}{k} (T_{j-1}^i - T_{air}) \quad (66)$$

### 4.4.3 Heat Transfer Coefficient

#### 4.4.3.1 Previous Work

The problem involves convective heat transfer from a moving surface to a strong cooling fluid. The surface is changing in shape, thickness, and velocity. Furthermore, the viscosity of the moving film is changing rapidly. Many researchers investigated the heat transfer for stretching and moving surfaces with constant and variable thickness [Helge *et al.* (2000), Devi *et al.* (1986), Lee and Tsai (1989)]. Others considered the boundary-layer behavior for continuous moving surfaces [Sakiadis (1961)]. Menges (1975) suggested the following relationship between the Nusselt number ( $Nu$ ) and the Grashof

( $Gr$ ), Prandtl ( $Pr$ ), and Reynolds ( $Re$ ) numbers. The relationship is then reduced as follows:

$$Nu = b.Gr^l.Pr^m.Re^n = b.Re^n \quad (67)$$

where  $b$ ,  $l$ ,  $m$ , and  $n$  are empirical constants. The above dimensionless numbers are defined as follows:

$$Nu = \frac{hr}{k} \quad (68)$$

$$Gr = \frac{\bar{\rho}^2 \beta g L^3 \Delta T}{\mu^2} \quad (69)$$

$$Pr = \frac{C_p \mu}{k} \quad (70)$$

$$Re = \frac{v \rho (z - Z_{FL})}{\mu} \quad (71)$$

where  $h$  is the heat transfer coefficient,  $r$  is the die radius,  $k$  is the thermal conductivity,  $\rho$  is the fluid density,  $\beta$  is the thermal coefficient of volumetric expansion,  $g$  is the gravitational acceleration,  $L$  is a characteristic length,  $\mu$  is the viscosity  $C_p$  is the heat capacity, and  $Z_{FL}$  is the freeze line height. The effect of buoyancy was ignored and only the effect of the velocity of the cooling air was considered. Thus, Equation (67) becomes a simple empirical function of the cooling air velocity. Kanai and White (1984) employed the formulation of Menges and divided the vertical length of the bubble to three arbitrary regions. They employed different empirical constants in each region. The resulting discontinuity in the heat transfer coefficient produces numerical singularities that limit the ability to deal with various bubble shapes and processing conditions. Kakac (1987) proposed correlations of the heat transfer coefficient for the mixed convection regime in laminar boundary layer flow. Some correlations are shown in Table 1.

Table 1: Nusselt number formulation for some cases at Laminar flow.

For vertical cylinders in a longitudinal flow field	For moving sheets vertical and inclined
$k_1 = \frac{4x}{\sqrt{Re}}$ $k_2 = 4 \left( \frac{Gr}{Re^2} \right)^{-0.25} k_1$ $A = 0.311 + 0.127k_1 - 0.004646k_1^2$ $B = 0.353 + 0.155k_2 - .0105k_2^2$	$A = 1.886 Pr^{13/32} - 1.445 Pr^{1/3}$ $B = 0.75\sqrt{Pr} \cdot (2.5(1+2\sqrt{Pr}+2Pr))^{-0.25}$

$$Nu_F = A \cdot Re^{0.5}$$

$$Nu_N = B \cdot Gr^{0.25} \quad (72)$$

$$Nu = (Nu_F^n - Nu_N^n)^{1/n}$$

$Nu_N$  refers to Nusselt number for natural convection, while  $Nu_F$  refers to forced convection. However, the laminar flow assumption is not valid in the case of the film blowing process, because of the strong airflow coming from the air ring. The stretching of the film produces an unsteady profile of the air velocity near the surface [Devi *et al.* (1986)], which renders the above correlations even less suitable for the film blowing process.

The air velocity varies significantly along the film because of the bubble shape and the blowing angle. In their analysis to the problem of cooling a continuous moving sheet by stagnant air, Lee and Tsai (1989) noted that the temperature decreased rapidly near the die exit because of a small boundary layer thickness. They also noted that the heat transfer coefficient showed strong power law dependence along the axial direction. Sakiadis (1961) defined a new class of boundary-layer problems for continuous moving flat surfaces, and then extended his work to continuous cylindrical surfaces. He concluded that the air velocity near the surface is proportional to the film velocity.

#### 4.4.3.2 Proposed Method to Estimate the Heat Transfer Coefficient (HTC)

In the film blowing process, heat transfer from the film surface to the cooling air takes place by convection and radiation only. In the following, a generalized function for the heat transfer coefficient in the film blowing process is proposed, taking into consideration the findings of other researchers. The correlation accounts for the cooling air velocity, the bubble curvature, the film temperature, and the cooling air temperature. The cooling air was assumed to flow in parallel to the bubble surface with a variable velocity. The effect of the buoyancy on the heat transfer was taken into consideration, because it was possible that there could be regions where there are stagnation points due to bubble shape and film characteristics. Buoyancy introduces the effect of the temperature difference between the surface and the cooling air on the heat transfer. The increase in the cooling air temperature was assumed to be negligible, because of the low variation in the heat capacity of the cooling air within the considered temperature ranges involved in the process

The results of Sidiropoulos (2000) indicate that there is a strong relationship between the heat transfer coefficient, on one hand, and the surface temperature and bubble radius, on the other hand. They also show that the heat transfer coefficient (HTC) decays exponentially from a maximum near the die exit to its value at the freeze line (see Figure 16). Hence, in this work, an exponential function was employed. The function takes into consideration the bubble shape, the film and cooling air temperatures, and the air velocity, maintaining a small number of fitting parameters. An analysis of the results of Sidiropoulos was employed to obtain the necessary parameters.

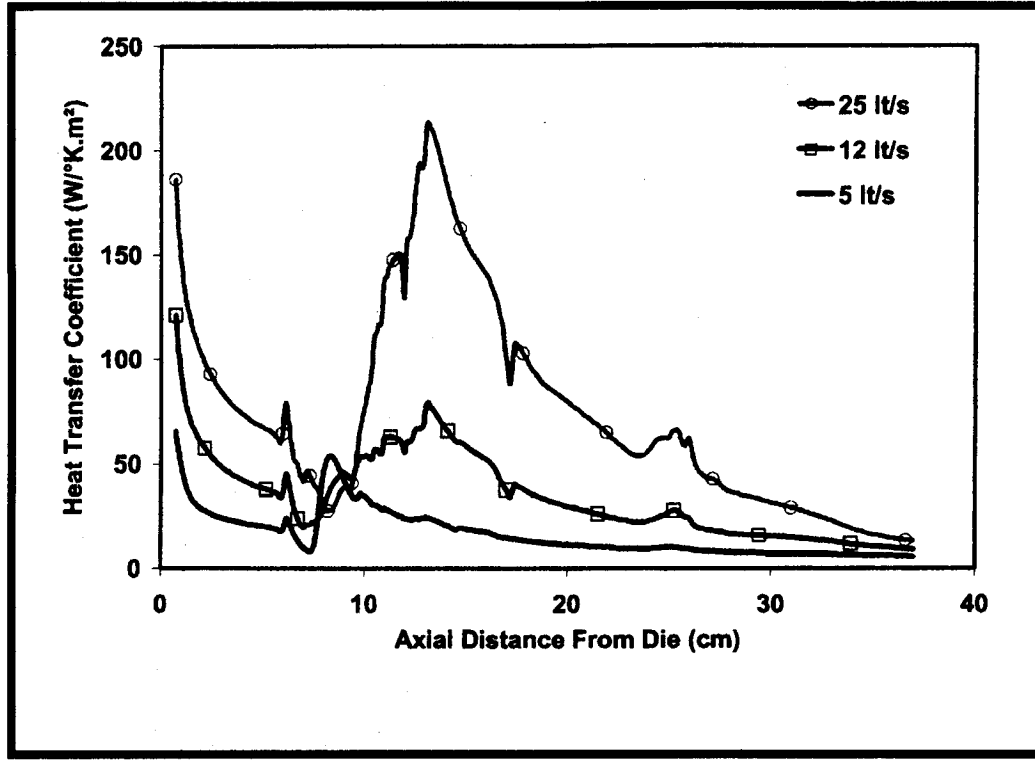


Figure 16: The HTC profiles on LLDPE film surface as shown by Sidiropoulos (2000) for different flow rates of the cooling air

The following general function is proposed:

$$HTC = F_1 \left( \left( T^* - T_{air}^* \right) r^* \right) F_2(z^*) + \Omega \quad (73)$$

$F_1$ , incorporates the effect of dimensionless temperature difference between the film surface and the cooling air and the effect of the dimensionless bubble radius;  $F_2$  incorporates the effect of the air velocity, by comparing the profiles of the heat transfer coefficient at different rates of the cooling air.  $\Omega$  was included to account for the end effects near the die exit and after the freeze line. It is suggested that  $F_1$  and  $F_2$  have the following forms:

$$F_1 = c_1 + c_2 \exp \left( c_3 \left( T^* - T_{air}^* \right) + c_4 r^* \right) \quad (74)$$

$$F_2 = \frac{C}{1 + \exp\left(0.5 z_{FL}^* - z^*\right)} \quad (75)$$

Equations (74) and (75) are substituted into Equation (73) to give the following:

$$HTC = C \left[ \frac{560 - 780 \cdot \exp\left(-1.27(T_{surface} - T_{air}) - 0.035 \cdot r\right)}{1 + \exp(0.5 z_{FL} - z)} \right] + \Omega \quad (76)$$

The values of the constants were obtained by fitting a two-dimensional function to the profiles of the heat transfer coefficient reported by Sidiropoulos (2000).  $F_1$  was obtained first, then a correction was made by employing  $F_2$  to account for variation of the volumetric flow rate of the cooling air. The portion of the data near the die exit was ignored initially in order to obtain the values of the constants  $c_1$ ,  $c_2$ ,  $c_3$ , and  $c_4$ . Figures 17 and 18 were used for this purpose. Subsequently, the function  $F_2$  was introduced, in order to account for the cooling air behavior, as the temperature drops steadily and the bubble expands continuously until the freeze line. Figure 19 shows good agreement between the results obtained using Equation (76) and the data obtained by Sidiropoulos (2000).

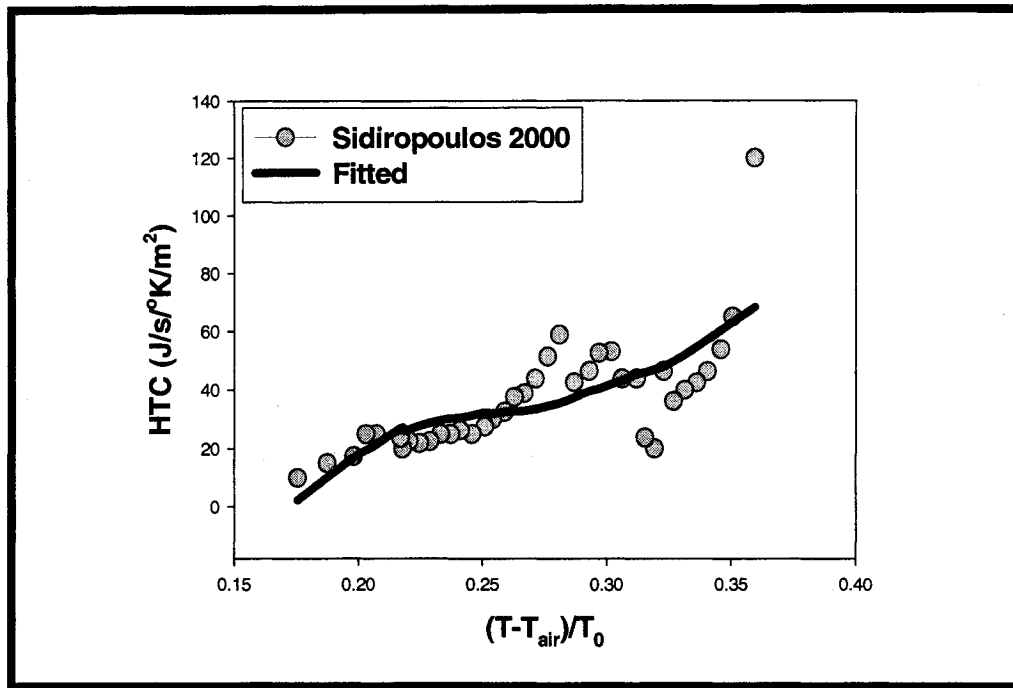


Figure 17: The heat transfer coefficient as a function of temperature

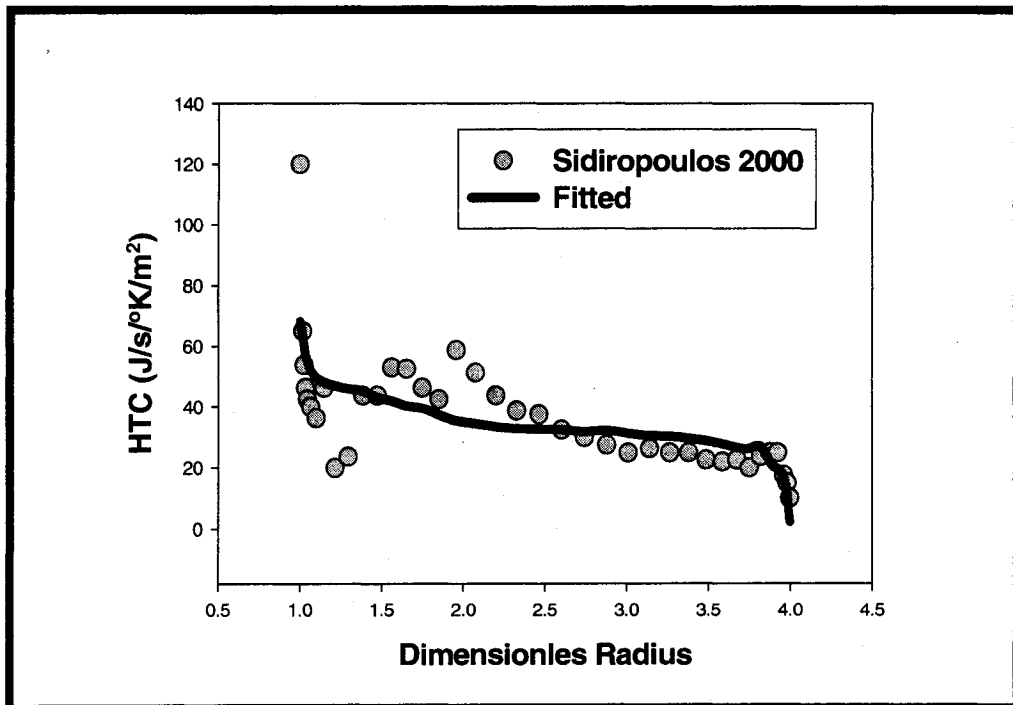


Figure 18: The heat transfer coefficient as a function of the bubble radius.

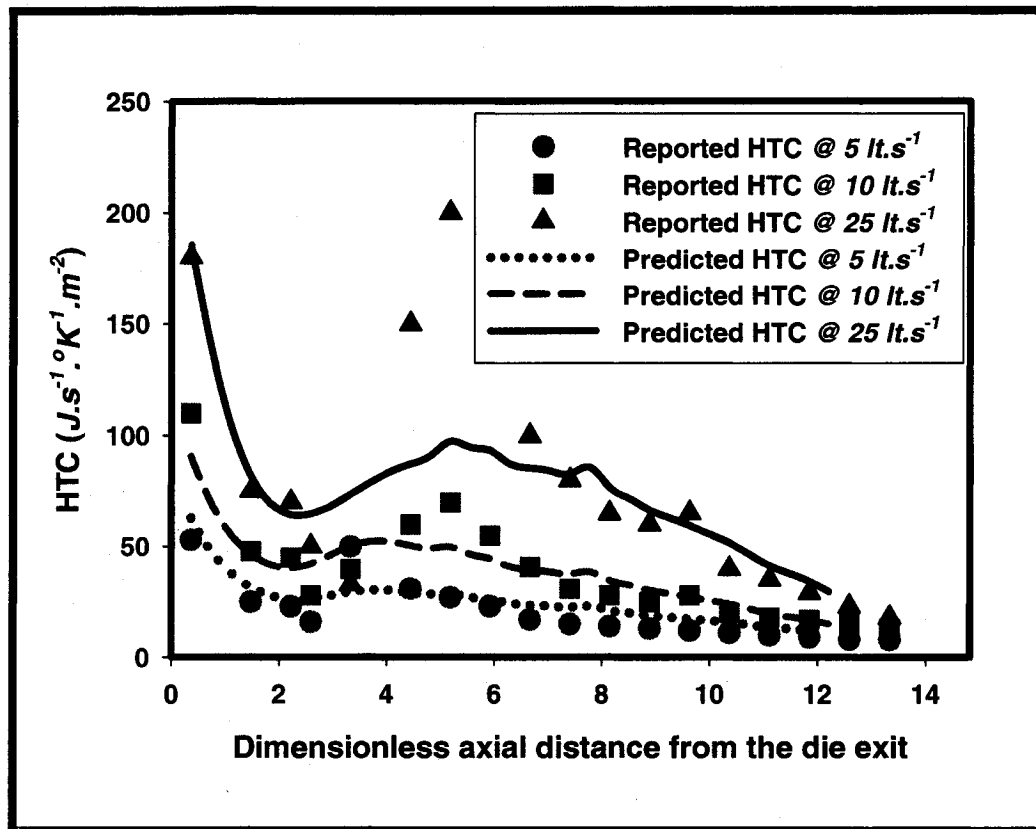


Figure 19: A comparison between the predicted heat transfer coefficient (lines) and the heat transfer coefficient reported (symbols) by Sidiropoulos, (2000) for three different volumetric flow rates.



Sidiropoulos (2000) calculated the heat transfer coefficient as a function of the axial distance for three different volumetric flow rates. In all cases, there were dips followed by peaks, nearly halfway to the freeze line.  $F_2$  was employed to simulate that behavior.  $\Omega$  was added to the function to account for the initial cooling effect on the film both at the lip of the die exit and after the freeze line. It was defined as follows:

$$\Omega = A \exp(-z^2) + B \quad (77)$$

The exponential term collapses to zero after a very short distance from the die exit, as its role is only to introduce the initial effect of the cooling air at the die exit due to the sudden jet issuing from the air ring. 'B' describes the behavior of the cooling system after the freeze line. 'A' and 'B' were found to show linear dependence on the volumetric flow rate of the cooling air, as shown in Table 2. Linear regression was employed to find 'A', 'B', and 'C' as functions of the cooling air flow rate. Figure 20 shows the profiles of the heat transfer coefficient without the exponential term in  $\Omega$ . Figure 21 shows the profiles of the heat transfer coefficient without  $F_2$ . They decrease monotonically until they reach a plateau without exhibiting any peak.

Table 2: Values of A, B, and C used.

$V_{air} (lt.s^{-1})$	A	B	C
25	180	40	2
10	90	25	1
5	60	11	0.6

$$A = 6V_{air} + 30$$

$$B = 1.4V_{air} + 7.4$$

$$C = 0.084V_{air}$$

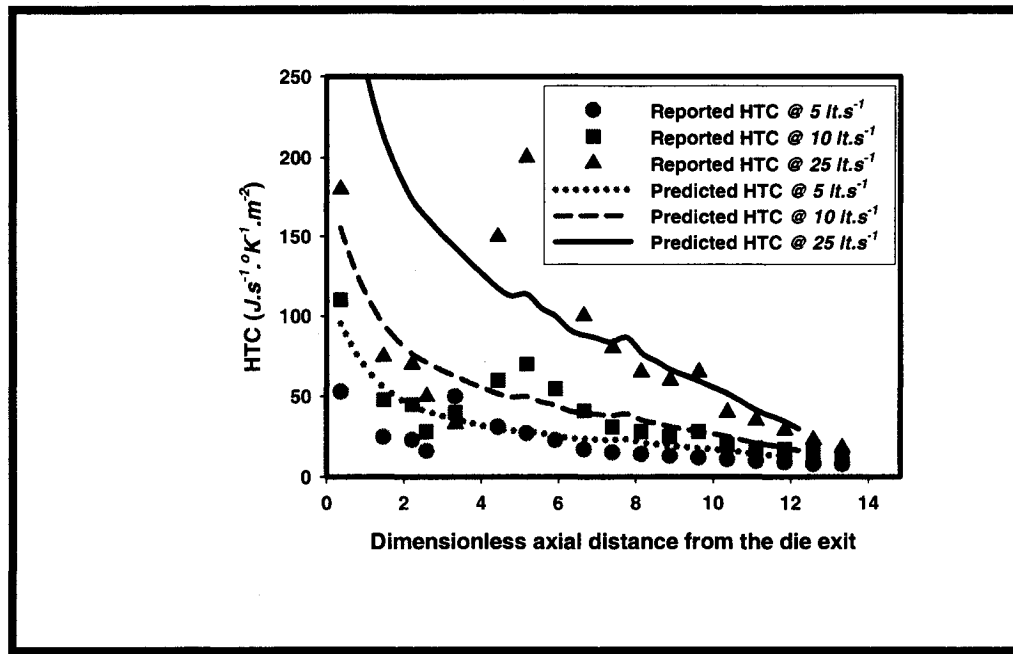


Figure 20: The behavior of the heat transfer coefficient when it is defined as a function of temperature and radius only.

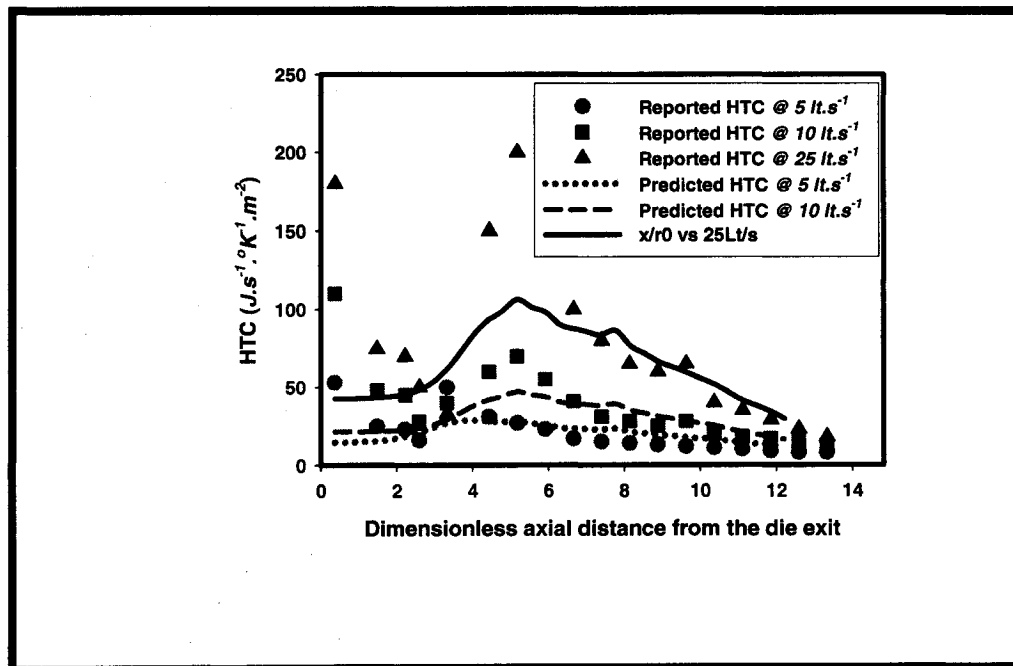


Figure 21: The effect of eliminating the initial turbulence near the die exit on the heat transfer coefficient.

## 4.5 Rheological Description of the Process

The shear stresses in the annular die are neglected, since melt is assumed to be at a temperature that is high enough to relax all pre-process stresses. The flow outside the die is regarded as homogeneous, under biaxial extension. Employing the above assumptions, along with postulation that the polymer has a constant density, the deformation rate tensor is written in the diagonal form Equation (78):

$$\dot{D}_i = \dot{v} \cos \theta \begin{pmatrix} \frac{1}{v} \frac{d \dot{v}}{d z} & 0 & 0 \\ 0 & \frac{1}{h} \frac{d \dot{h}}{d z} & 0 \\ 0 & 0 & \frac{1}{r} \frac{d \dot{r}}{d z} \end{pmatrix} \quad (78)$$

The key variables are the stresses ( $\sigma_i$ ), the deformation rate ( $\dot{D}$ ), the deformation ( $D$ ), the viscosity ( $\eta$ ), the relaxation time ( $\lambda$ ), and the relaxation modulus ( $G$ ).

### 4.5.1 Constitutive Equations in Molten Phase

The stresses in the melt are modeled using the Phan-Thien and Tanner (PTT) constitutive equation, because it is the most suitable model for extensional flows [Larson (1988), Tas (1994), Tanner (2000)]. The PTT constitutive model describes the extensional behavior of the film with the parameter  $\varepsilon$  and the slippage property of the polymer chains with the parameter  $\xi$  [Larson (1988)].

$$\tau_i Y(\tau) + \lambda \left[ \tau_i + 2\xi (\tau_i \dot{D}_i) \right] = 2\eta \dot{D}_i \quad (79)$$

Several studies showed the superiority of the PTT model for describing extensional flow, such as those of Khan and Larson (1987), Tas (1994), and Maia (1999). Each compared several constitutive equations (such as Johnson-Segalman, White-Metzner, Marrucci,

Giesekus, Larson, and PTT equations). The upper convective time derivatives, Equation (80), recover frame invariance and provide the Finger measure of the deformation rate to express the deformation rate history.

$$\overset{\nabla}{\tau}_i = \frac{d\tau}{dt} - [\nabla_v][\tau_i] - [\tau_i][\nabla_v] \quad (80)$$

$$Y(\tau) = \exp\left(\frac{\varepsilon\lambda}{\eta} \text{tr}\tau_i\right) \quad (81)$$

The extensional function, Equation (81), expresses the extensional properties of the flow. The exponential form is more favorable for describing the rheological behavior of melts in extensional processes than the linear form [Tanner (2000)], because the former describes the extensional behavior in a more real way than the latter [Phan-Thien (1978)]. It was found that employing the linear form predicts a plateau in the extensional viscosity at high extensional rates without showing shear thinning, which is not realistic. The extensional viscosity was predicted to decrease after reaching a maximum, only when the exponential form was employed [Phan-Thien (1978)]. Alves et al. (2003) reported that they were able to simulate planar contraction at high elasticity only by employing the exponential form of the PTT extensional function.

In the current work, the method of Lin et al. (2002) was followed to calculate the value of  $\xi$  by fitting Equation (82) to dynamic data for various LLDPE and LDPE melts, assuming  $\eta(\dot{\gamma}) = \eta^*(\omega)$ .

$$\eta(\omega) = \sum \frac{\lambda_i g_i}{1 + \xi(2 - \xi)(\lambda_i \omega)^m} \quad (82)$$

The values of  $\xi$  were found in the range of 0.147- 0.153. Therefore,  $\xi = 0.15$  was employed in the current work, which was the same value reported by Tas (1994). The value employed for the parameter  $\varepsilon$ , which was 0.06, was also taken from Tas (1994) for the sake of consistency. It will be shown later that varying these two parameters within the range reported in the literature influences the predictions of the model only slightly.

In the present work, the total stress in any direction is composed of the deviatoric element and the pressure acting on the fluid, as follows:

$$[\sigma] = -p[I] + [\tau] \quad (83)$$

The stress is calculated using the following viscoelastic expression:

$$[\tau] + \lambda \frac{\delta[\tau]}{\delta t} = 2\eta[\dot{D}] \quad (84)$$

The second term is the upper convective time derivative, in which the Finger tensor is used to track the deformation history:

$$\frac{\delta[\tau]}{\delta t} = \frac{d[\tau]}{dt} - [\nabla \bar{v}][\tau] - [\tau][\nabla \bar{v}]^T \quad (85)$$

$$[\nabla \bar{v}]^T [\tau] = \begin{bmatrix} \frac{\partial v_1}{\partial \xi_1} & 0 & 0 \\ 0 & \frac{\partial v_2}{\partial \xi_2} & 0 \\ 0 & 0 & \frac{\partial v_3}{\partial \xi_3} \end{bmatrix} \begin{bmatrix} \tau_1 & 0 & 0 \\ 0 & \tau_2 & 0 \\ 0 & 0 & \tau_3 \end{bmatrix} = \begin{bmatrix} \tau_1 \frac{\partial v_1}{\partial \xi_1} & 0 & 0 \\ 0 & \tau_2 \frac{\partial v_2}{\partial \xi_2} & 0 \\ 0 & 0 & \tau_3 \frac{\partial v_3}{\partial \xi_3} \end{bmatrix} \quad (86)$$

$$[\tau][\nabla \bar{v}]^T = \begin{bmatrix} \tau_1 & 0 & 0 \\ 0 & \tau_2 & 0 \\ 0 & 0 & \tau_3 \end{bmatrix} \begin{bmatrix} \frac{\partial v_1}{\partial \xi_1} & 0 & 0 \\ 0 & \frac{\partial v_2}{\partial \xi_2} & 0 \\ 0 & 0 & \frac{\partial v_3}{\partial \xi_3} \end{bmatrix} = \begin{bmatrix} \tau_1 \frac{\partial v_1}{\partial \xi_1} & 0 & 0 \\ 0 & \tau_2 \frac{\partial v_2}{\partial \xi_2} & 0 \\ 0 & 0 & \tau_3 \frac{\partial v_3}{\partial \xi_3} \end{bmatrix} \quad (87)$$

$$\frac{d[\tau]}{dt} = \begin{bmatrix} \frac{d\tau_1}{dt} & 0 & 0 \\ 0 & \frac{d\tau_2}{dt} & 0 \\ 0 & 0 & \frac{d\tau_3}{dt} \end{bmatrix} = v \cos \theta \begin{bmatrix} \frac{d\tau_1}{dz} & 0 & 0 \\ 0 & \frac{dp}{dz} & 0 \\ 0 & 0 & \frac{d\tau_3}{dz} \end{bmatrix} \quad (88)$$

$$[\nabla \bar{v}][\tau] + [\tau][\nabla \bar{v}] = 2 \begin{bmatrix} \tau_1 \frac{\partial v_1}{\partial \xi_1} & 0 & 0 \\ 0 & \tau_2 \frac{\partial v_2}{\partial \xi_2} & 0 \\ 0 & 0 & \tau_3 \frac{\partial v_3}{\partial \xi_3} \end{bmatrix} = 2 \cos \theta \begin{bmatrix} \tau_1 \frac{\partial v}{\partial z} & 0 & 0 \\ 0 & \tau_2 \frac{\partial h}{\partial z} & 0 \\ 0 & 0 & \tau_3 \frac{\partial r}{\partial z} \end{bmatrix} \quad (89)$$

Substituting Equations (88) and (89) into Equation (85) and putting the result into Equation (84) yields:

$$\tau_1 + \lambda v \cos \theta \frac{d\tau_1}{dz} - 2\lambda \tau_1 \cos \theta \frac{dv}{dz} = 2\eta \cos \theta \frac{dv}{dz} \quad (90)$$

$$p + \lambda v \cos \theta \frac{dp}{dz} - 2\lambda p \frac{v}{h} \cos \theta \frac{dh}{dz} = 2\eta \frac{v}{h} \cos \theta \frac{dh}{dz} \quad (91)$$

$$\tau_3 + \lambda v \cos \theta \frac{d\tau_3}{dz} - 2\lambda \tau_3 \frac{v}{a} \cos \theta \frac{dr}{dz} = 2\eta \frac{v}{r} \cos \theta \frac{dr}{dz} \quad (92)$$

The extensional function and the slippage parameter are introduced into the Maxwell equations (44 – 46) to obtain the PTT constitutive equations:

$$\lambda v \cos \theta \frac{d\tau_1}{dz} = 2\eta \cos \theta \frac{dv}{dz} - Y\tau_1 + 2(1 - \xi)\lambda \tau_1 \cos \theta \frac{dv}{dz} \quad (93)$$

$$\lambda v \cos \theta \frac{dp}{dz} = 2\eta \frac{v}{h} \cos \theta \frac{dh}{dz} - Yp + 2(1 - \xi)\lambda p \frac{v}{h} \cos \theta \frac{dh}{dz} \quad (94)$$

$$\lambda v \cos \theta \frac{d\tau_3}{dz} = 2\eta \frac{v}{r} \cos \theta \frac{dr}{dz} - Y\tau_3 + 2(1 - \xi)\lambda \tau_3 \frac{v}{a} \cos \theta \frac{dr}{dz} \quad (95)$$

$$\text{Now: } \sigma_1 = \tau_1 - \tau_2 \quad (96)$$

$$\sigma_2 = 0 = -p + \tau_2 \quad (97)$$

$$\sigma_3 = \tau_3 - \tau_2 \quad (98)$$

$$\dot{\sigma} = \dot{\tau} - \dot{P} \quad (99)$$

where  $P$  is the pressure right at the moving surface of the fluid. Because the only non-zero components of the stress, the deformation, and the deformation rate tensors are the extensional components, which are the diagonal components, tensor indication is replaced by the subscript “ $i$ ” (1, 2, or 3), which indicates the direction of the stress component (machine, thickness, or hoop, respectively). The velocity is eliminated using the continuity equation. The above equations can be made dimensionless by multiplying

by  $\frac{r_0}{\eta v_0}$ , and then by rearranging the terms so the equations take the final form of the PTT model, which is used to simulate the melt behavior in the viscoelastic region. The relevant equations are listed in dimensionless form as follows:

$$\begin{aligned} \dot{\sigma}'_1 = & \frac{2\eta^*}{De}(\dot{D}_1 - \dot{D}_2) - \frac{r^* h^* \sigma_1^*}{De \cos \theta} \exp\left(\frac{\varepsilon De^*}{\eta^*}(\sigma_1^* + \sigma_3^* + 3P^*)\right) \\ & + 2(1 - \xi)\left(\sigma_1^* \dot{D}_1 + P^*(\dot{D}_1 - \dot{D}_2)\right) \end{aligned} \quad (100)$$

$$\begin{aligned} \dot{P}' = & \frac{2\eta^*}{De}(\dot{D}_2) - \frac{r^* h^* P^*}{De \cos \theta} \exp\left(\frac{\varepsilon De^*}{\eta^*}(\sigma_1^* + \sigma_3^* + 3P^*)\right) \\ & + 2(1 - \xi)\left(P^* \dot{D}_2\right) \end{aligned} \quad (101)$$

$$\begin{aligned} \dot{\sigma}'_3 = & \frac{2\eta^*}{De}(\dot{D}_3 - \dot{D}_2) - \frac{r^* h^* \sigma_3^*}{De \cos \theta} \exp\left(\frac{\varepsilon De^*}{\eta^*}(\sigma_1^* + \sigma_3^* + 3P^*)\right) \\ & + 2(1 - \xi)\left(\sigma_3^* \dot{D}_3 + P^*(\dot{D}_3 - \dot{D}_2)\right) \end{aligned} \quad (102)$$

#### 4.5.2 Crystallinity and Orientation

Kanai and White (1985) proposed Equation (103) to describe the effect of crystallinity on the melt viscosity.

$$\eta^*(X) = \exp(\Psi X) \quad (103)$$

$\Psi$  is an empirical consistency parameter that is adjusted according to the polymer type. They obtained  $\Psi$  by fitting viscosity data for samples of known crystallinity levels. The parameter,  $\Psi$ , could vary depending on the material and conditions employed. However, the above expression was shown to be reasonably accurate. It was used by various researchers, including Kanai (1999) and Ziabicki (1974, 1999). It should be noted that the crystallinity,  $X$ , refers to the absolute fractional crystallinity in the material and not the

fraction of crystallizable portion as suggested by some other researchers [Doufas and McHugh (2001)]. This is because the viscosity and other properties of the film depend on the absolute crystallinity (the weight fraction of the crystalline phase in the film and not on the so-called relative crystallinity, i. e., fraction of crystallizable portion.

In the present work, the function of Kanai and White (1985) is employed in the overall viscosity function to incorporate the effect of crystallinity on the viscosity. The following expression describes the dimensionless viscosity of the melt, which incorporates the measured dynamic shear constants ( $\lambda_i$  and  $g_i$ ) of the melt:

$$\eta^*(T, X, II_2) = \eta_0^{-1} \exp \left( \frac{E}{R_g} \left( \frac{1}{T} - \frac{1}{T_0} \right) + \Psi X \right) \sum_{i=1}^n \frac{\lambda_i g_i}{1 + \xi (2 - \xi) (\lambda_i II_2)^m} \quad (104)$$

$II_2$  is the second invariant of the deformation rate tensor and  $n$  is the number of Maxwell modes. The activation energy of the polymer ( $E$ ) and universal gas constant ( $R_g$ ) are obtained from dynamic rheological measurements. The temperature dependence of the viscosity and the relaxation time is consistent with the work done by Andre *et al.* (1998) and Sidiropoulos (2000).

Nagamatsu (1961) described the effect of crystallinity on the relaxation modulus. He measured the relaxation modulus for polyethylene samples of known degrees of crystallinity. From the plotted curves of the relaxation modulus vs. degree of crystallinity, he deduced Equation (105). In the present work, Equation (105) and  $\lambda \equiv \frac{\eta}{G}$  are employed to obtain the effect of crystallinity on the relaxation time. The resulting equation was approximated by  $\lambda(X) \equiv \frac{\eta}{G} = \exp(\phi X)$  to avoid numerical problems that might occur at very low values of crystallinity.

$$G(X) = \left( \frac{X}{1 - X} \right) \left( \frac{1 - X_\infty}{X_\infty} \right) \quad (105)$$



where  $X$  is the absolute crystallinity, and  $X_\infty$  is the ultimate achievable crystallinity in the material. The resulting dimensionless relaxation time (Deborah number) is defined as a function of temperature and crystallinity:

$$De(T, X) = \frac{\lambda_0 v_0}{r_0} \exp \left( \frac{E}{R_g} \left( \frac{1}{T} - \frac{1}{T_0} \right) + \phi X \right) \quad (106)$$

The zero-shear viscosity ( $\eta_0$ ) and zero-shear relaxation time ( $\lambda_0$ ) were estimated from the following relationships:

$$\eta_0 = \sum_{i=1}^n \lambda_i g_i \quad (107)$$

$$\lambda_0 = \sum_{i=1}^n \lambda_i^2 g_i / \sum_{i=1}^n \lambda_i g_i \quad (108)$$

In the above equations, the dimensionless viscosity and the dimensionless relaxation time (Deborah number) were defined as functions of temperature using the Arrhenius relationship (since the melt temperature is more than 100 °C higher than the glass transition temperature [Ferry (1980)]). The effect of the deformation rate on the viscosity was employed by using the formulation of Tanner (2000), Equation (82), since the extensional viscosity in melts was shown to be proportional to the shear viscosity [Lin et al (2002)].

#### 4.5.3 Constitutive Equation for the Solid-Like Phase

As the film temperature decreases, the material starts to exhibit solid-like behavior. From that point (commonly known as the freeze line) onward, the film is assumed to behave as a Neo-Hookean material. Thus, the Neo-Hookean equations are used to calculate the stresses. In the solid-like region, the film is characterized by a growing relaxation modulus. Soskey and Winter (1985) reported that the extensional relaxation modulus and the shear modulus have similar time dependence in the linear viscoelastic range. Catstiff et al. (1956) reported that the relaxation modulus grows faster

and spreads over a narrower range of temperature for polymers with higher crystallinity. The value of relaxation modulus of the solid films is several orders of magnitude higher than that of the polymer melt, which means that the stresses approach the equilibrium state much faster when the film solidifies.

The transition boundary between liquid-like melt and solid-like film is assumed to take place when the variation in blowing angle becomes null, as calculated by Equation (44). André et al. (1998) showed that convergence might be reached with a single-phase viscoelastic melt model if the initial blowing angle is guessed accurately; therefore, his approach was implemented in the current work to reach convergence at the freeze line. At this point, known as the freeze line (FL), deformation does not cease in all directions and the magnitudes of the deformation vary according to the extensional force. In other words, the stresses at the freeze line become high enough to resist further deformation in at least one direction. The increase in the stresses is due to the increase in the viscosity, as a result of the drop in the temperature, which may or may not be accompanied by a significant increase in the crystallinity. No boundary conditions are imposed on the thickness or the deformation rate at the freeze line. Otherwise the problem becomes over-determined mathematically, which causes decoupling of the continuity equation from the rest of the equations. The freeze line was defined according to the above criteria to correspond as closely as possible to the real situation. A definition based on an arbitrarily specified crystallinity or temperature level would not be realistic. In such cases, it is likely that the freeze line may be forced to occur either prematurely or too late. The deformation components are evaluated in that region using the following equations:

$$D_i^{FL} = \frac{\dot{\sigma}_i^{FL} + \dot{P}^{FL}}{2G^{FL}} \quad (109)$$

$$D_1 = D_1^{FL} + \ln \left( \frac{\dot{v}}{\dot{v}^{FL}} \right) \quad (110)$$

$$D_2 = D_2^{FL} + \ln \left( \frac{\dot{h}}{\dot{h}^{FL}} \right) \quad (111)$$

$$D_3 = D_3^{FL} + \ln \left( \frac{\dot{r}}{\dot{r}^{FL}} \right) \quad (112)$$

where the superscript “FL” indicates the value at the freeze line. The above expressions of deformation are incorporated in the following Neo-Hookean type equations (in dimensionless macroscopic form) to evaluate stress in the solid-like region,

$$\sigma_i^* = 2 G^* (D_i - D_2) \quad (113)$$

$$P^* = 2 G^* D_2 \quad (114)$$

where  $P^*$  is the dimensionless pressure right at the moving surface of the fluid. However, in order to use the above equations, the relaxation modulus function for the solid-like film is needed. Nagamatsu (1961) showed that the crystallinity and orientation impact the effects of time and temperature on the relaxation modulus and induce vertical translation along the log modulus axis. Following a similar approach, the following equations are employed to calculate the relaxation modulus:

$$G(t, T, X) = \exp \left( \frac{c_1 \cdot (T - T_r)}{c_2 + T - T_r} + c_3 (T - T_r) \right) \sum g_i \cdot \exp(-t/\lambda_i) \quad (115)$$

In Equation (115), the rheological constants  $g_i$  and  $\lambda_i$  are obtained from the reported experimental data at the reference temperature ( $T_r$ ), which was 20 °C [Nagamatsu (1961)]. Nagamatsu measured the stress relaxation curves of three types of polyethylene at temperatures between 20 and 80 °C to establish master curves for the stress relaxation modulus. From these curves, he determined the horizontal shift factor due to temperature and the vertical shift factor due to the crystallinity. In the current work, the Williams-Landel-Ferry (WLF) equation was fitted to the curve of the temperature shift factor obtained by Nagamatsu to determine the values of parameters  $c_1$ , and  $c_2$ . Also, an exponential function was fitted to the vertical shift factor obtained by Nagamatsu to determine the value of  $c_3$ . These solid rheological properties were assumed to be the same for all the polyethylene cases considered in the current work. It is worth

noting that the above equations show the possibility of stress growth after the freeze line because the stresses in this region (solid-like) are dictated by the amount of deformation (not the deformation rate) and relaxation modulus.

## 4.6 Crystallization Kinetics

In the film blowing process, polyethylene crystallizes and forms a semi-crystalline phase. Crystallization is due to the under-cooling and extensional stress. Crystallization kinetics is described by Nakamura's nonisothermal model [Nakamura *et al.* (1972)], which evolved from the Avrami isothermal model. Ziabicki (1999) showed that the crystallization rate constant depends on the polymer temperature and the orientation of polymer chains that results from the induced-stresses:

$$\frac{dX}{dt} = N \cdot X_{\infty}(T) \cdot K(T) \cdot (1 - X) \cdot (-\ln(1 - X))^{\frac{N-1}{N}} \quad (116)$$

$$K(T) = K_{max} \cdot \exp \left[ \frac{-4.0 * \ln 2.0 * (T - T_{max})^2}{\beta^2} + A \cdot \sum f_i \right] \quad (117)$$

Coupling of the crystallization kinetics and the orientation is not universal. The parameter "A" is the dimensionless Ziabicki constant of stress- induced orientation [Ziabicki (1976)]. The value of this parameter may vary from one polymer to another, and it could be dependent on the stress applied and amount of supercooling. Ziabicki assumed that nucleation and growth rates are unaffected by the level of orientation, so the effect of orientation on the melting temperature can be studied at different extension ratios. In the absence of reliable data, the value of Ziabicki's constant (A) was fixed at 1000 for all experiments to avoid exaggerating the effect of orientation on crystallinity.  $N$  is the Avrami constant under quiescent conditions, and  $\beta$  is a material characteristic, which is the half-width of the empirically observed curve for  $K(T)$ .  $X_{\infty}$  is the ultimate crystallinity, which is defined as a function of temperature. It was obtained by fitting isothermal crystallization data reported by Lungu (2000). The probabilistic parameter,  $f_i$ , represents the average orientation, which is proportional to the applied stress field

[Macosko (1994)]. The orientation is calculated from the birefringence, which is calculated from the stress optical relationship.

$$f = \frac{\Delta n_i}{\Delta n_0} \quad (118)$$

$$\Delta n_i = c \sigma_i \quad (119)$$

where  $\Delta n_i$  is the calculated birefringence,  $\Delta n_0$  is the intrinsic birefringence, and  $c$  is the stress-optical constant. Internal stresses and interfacial effects may contribute to the magnitude of the birefringence, but orientation-induced birefringence due to the crystalline and amorphous components is the dominant factor [Ward (1997)].

## 4.7 Boundary Conditions

At the die exit, swelling is neglected and the initial radius and thickness of the polymeric tube are assumed to be equal to the radius and gap thickness of the die exit. The initial blowing angle,  $\theta_0$ , depends on the polymer type and traction forces, and it is guessed using a numerical shooting technique. The initial film velocity,  $v_0$ , is determined from the mass flow rate of the polymer at the die exit. The initial temperature is the melt temperature at the die exit, at which the zero-shear viscosity and relaxation time are estimated. Normal stresses in the machine and hoop directions at the die exit are calculated using the following momentum equations.

$$\dot{\sigma}_1 \left( 0, h \right) = \frac{F + B}{\cos \theta} \quad (120)$$

$$\dot{\sigma}_3 \left( 0, h \right) = \frac{2B}{\cos \theta} \quad (121)$$

The normal stress in the thickness direction,  $\sigma_2$ , is zero because  $\tau_2 = p$ . The above equations are deduced from the force balance in the machine direction (Equation (38)) and the force balance in the thickness direction (Equation (33)). The thickness and

the radius are equal to unity at the die exit, because they are rendered dimensionless, which means that  $r = r_0$  and  $h = h_0$ , respectively.

## 4.8 Numerical Methods

### 4.8.1 Algorithm

The film is divided into a large number of imaginary parallel thin annular layers, as shown in Figure 22. The total thickness is the sum of the thicknesses of these sub-layers. There is no velocity gradient in the thickness direction because the flow is assumed to be extensional. The variation in the material properties of the layers is only due to the temperature drop in the thickness and machine directions. The number of steps in the axial direction is determined by dividing the distance between the die exit and the nip rolls by the integration step size chosen. The distance is chosen to be 35 times the outside radius of the die exit, and the integration step size is chosen to be 0.002 (the method of selecting the step size will be shown below).

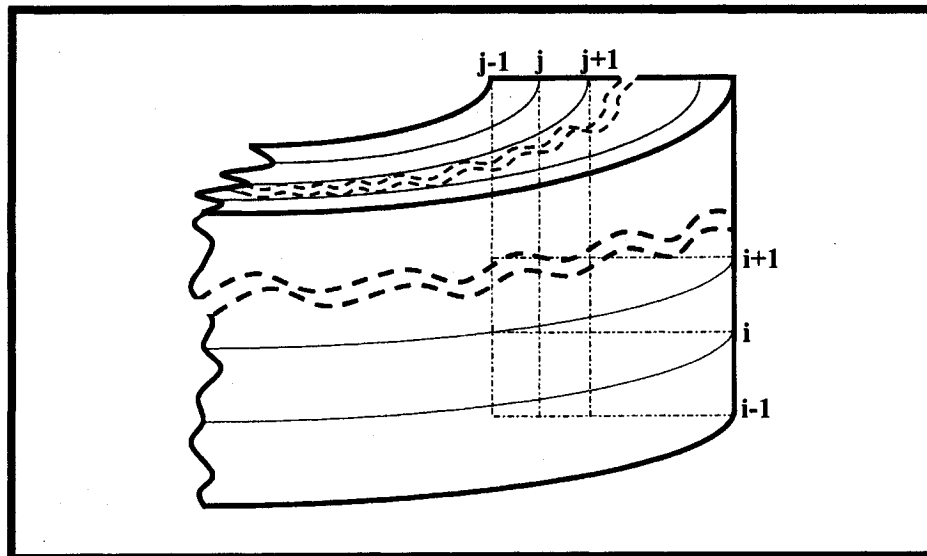


Figure 22: A mesh map of a portion of the film.

All equations are solved simultaneously using two numerical techniques: the finite difference and Runge-Kutta methods. The finite difference method employed to solve the energy equation is the Crank-Nicolson scheme, since it is unconditionally stable. The fourth-order Runge-Kutta method is used to solve the other equations, because of its simplicity and accuracy.

The computational algorithm is outlined in Figure 23. The initial conditions of the temperature, stresses, film velocity, film thickness, and the bubble radius at the die exit are known. The simulation is conducted in the axial distance, moving away from the die exit row by row. At each row, the solution is performed outward from the inner surface. The rheological properties and crystallinity of the film are calculated first. Then, the stresses are calculated at that temperature. Simultaneously, the calculated values of the stresses are used to calculate the evolution of the bubble radius and reduction in the thickness. At the end of the simulation, the film is transformed to an  $(i \times j)$  nodal map. The axial number of nodes,  $i$ , is determined according to the integration step desired. The number of divisions,  $j$ , is optimized by considering both the computational time and the accuracy. It was found from running several trials, that the accuracy does not improve significantly beyond 20 divisions, which is consistent with the number reported by Sidiropoulos (2000). Based on evaluation of convergence for dimensionless step sizes between 0.0008 and 0.028, a step size of 0.002 in the machine direction, was chosen as will be shown later.

The Newton-Raphson method is employed to guess the value of the initial blowing angle at a fixed initial guess of the take-up force and inflation pressure, so that zero blowing angle is obtained at the freeze line. Once the zero-blowing angle is obtained, the simulation switches to the Neo-Hookean model and continues the calculation until the maximum axial distance is reached. If the blow-up ratio and the final film velocity at the nip rolls are equal to the desired BUR and DR, then a solution is found. Otherwise, a two-variable Newton-Raphson method is employed to search for new values (the roots) of the take-up force and inflation pressure, until the bubble radius and the film velocity yield the desired blow-up ratio and draw ratio at the nip rolls.

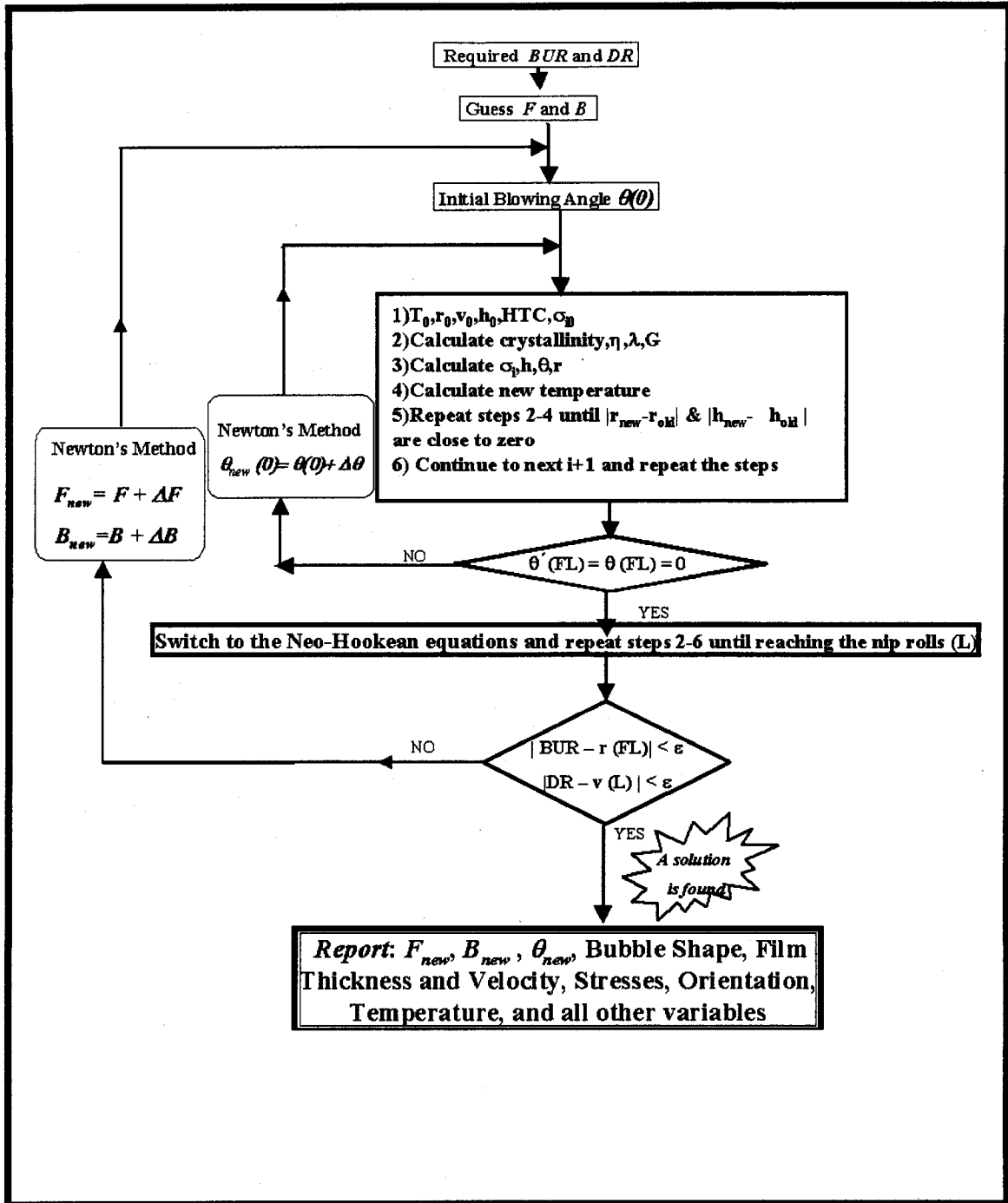


Figure 23: The algorithm of the numerical computation



## 4.8.2 Input Parameters

Three types of parameters need to be specified before running the simulation: the processing parameters, the model parameters, and the rheological parameters. The processing parameters (Table 3) are fixed experimentally, to yield the desired film thickness and final film properties. These data are based on film blowing experiments for different polyethylene resins extruded under a variety of processing conditions. The model parameters (Table 4) are determined from the literature and experiments. The rheological parameters (Table 5) are determined from dynamic and extensional rheological experiments.

Table 3: Processing conditions for the film blowing process.

	C587	C863	D582	F751	G583	H866
Take-up force, $F$ ( <i>Dimensionless</i> )	1.7	1.3	1.82	1.1	1.2	1.2
Inflation pressure, $B$ ( <i>Dimensionless</i> )	0.27	0.17	0.34	0.24	.12	0.1
Initial blowing angle, $\theta$ ( <i>Degrees</i> )	9	5	8	25	13	14
Initial radius, $r_0$ (m)	0.0385	0.0385	0.0385	0.0385	0.0385	0.0385
Initial flow rate ( $\text{kg.hr}^{-1}$ )	18.1	17.9	18.0	7.5	18.4	18
Initial thickness, $h_0$ (m)	.00254	.00089	.00089	.00127	.00089	.00089
Die exit temperature, $T_0$ ( $^{\circ}\text{C}$ )	221	221	220	177	217	222
Air temperature, $T_a$ ( $^{\circ}\text{C}$ )	25	25	25	25	25	25

Table 4: Material properties used in the computations.

Model parameter	Value	Units	Source
$\Psi$	5.1 (C587,C863, D582, G583, H866), 7.5 (F751)	<i>Dimensionless</i>	Kanai 1984
Constant of stress-induced orientation, A	1000 (all films)	<i>Dimensionless</i>	Ziabicki 1976
Avrami exponent, $N$	2 (all films)	<i>Dimensionless</i>	Lungu 2000
Half-width of $K(T)$ curve, $\beta$	30.3 (C587, C863) 32.9(D582) 28.8 (F751) 44.3 (G583) 18.2 (H866)	$^{\circ}C$	Lungu 2000
Avrami rate constant of crystallization, $K_{max}$	0.017 (C587, C863) 0.018 (D582) 0.013 (F751) 0.007 (G583) 0.01 (H866)	$s^{-1}$	Lungu 2000
Heat capacity, $C_p$	2.3 (all films)	$J.g^{-1}.^{\circ}K^{-1}$	Dole (1967)
Thermal conductivity, $k$	0.33 (all films)	$J.m^{-1}.s^{-1}.^{\circ}K^{-1}$	Dole (1967)
Thermal diffusivity $\alpha$	$1.6 \cdot 10^{-7}$ (all films)	$m.s^{-2}$	Dole (1967)
$\Delta H$ , heat of fusion	290 (all films)	$J.g^{-1}$	Dole (1967)
Density, $\rho$	923 (C587, C863) 919 (D582) 919 (F751) 920 (G583) 919 (H866)	$kg.m^{-3}$	Kamal (2001)

Table 5: Rheological properties for polymers used in this work

Property	Value	Source
$\lambda_0$ (s)	1.4 (C587, C863) 0.4 (D582), 2.1 (F751) 1.2 (G583), 2.2 (H866)	Estimated [polymer (G) rheology]
$\eta_0$ (Pa. s)	11304 (C587, C863) 7943 (D582), 11630 (F751) 10814 (G583), 16855 (H866)	Estimated [polymer (G) rheology]
$\varepsilon$	0.05	Phan-Thien 1978
$\xi$	0.15	Tas 1994
$c_1$	-10	Estimated [experiments of Nagamatsu 1961]
$c_2$	470	Estimated [experiments of Nagamatsu 1961]
$c_3$	0.0165	Estimated [experiments of Nagamatsu 1961]
Power law constant, $m$	0.24	Estimated [polymer (G) rheology]

$k$	Dynamic constants of the liquid-like melt (G583)		Dynamic constants of the solid-like film	
	$\lambda_k$ (s)	$g_k$ (Pa)	$\lambda_k$ (s)	$g_k$ (MPa)
1	0.00439	284300	1.9	85
2	0.02765	60110	9.3	65
3	0.1171	18830	24.3	12
4	0.4867	4766	101.4	46.4
5	2.096	928.2	5395.1	65.2
6	11.41	134.4	5395.1	65.1

### 4.8.3 Evaluation of the Numerical Scheme

In the simulation, Newton's method was employed to estimate the missing boundary conditions, such as the initial blowing angle. The Crank-Nicolson scheme was employed to solve the energy equation, and the fourth order Runge-Kutta method was used to solve the rest of the equations. The Crank-Nicolson method, which was employed to solve the energy equation, is known to be unconditionally stable [Reddy (1993), Hanna and Sandall (1995), Allen (1998)]. A solution is convergent, if the difference between the numerical solution and the exact (analytical) solution tends to zero [Noye (1976)]. The solution is consistent if that difference approaches zero as the grid spacing gets smaller. The solution is considered stable if the cumulative effect of all round-off errors does not increase unboundedly as the number of iterative steps increases. When the analytical solution is not known, it is usually not possible to demonstrate convergence and stability theoretically [Mickley (1957), Fletcher (1991)]. If a numerical method is proved to be stable, it is proved to be convergent as well [Mickley (1957), Allen (1998)].

The following sections deal with the results of a variety of tests that have been carried out to evaluate the accuracy, convergence, and stability of the solutions obtained by the simulation. Moreover, they include the results of various tests that were carried out to evaluate the robustness of the simulation.

#### 4.8.3.1 Convergence Evaluation

Two techniques were employed to study the effect of the step size. The first is based on the Richardson extrapolation to estimate the local error [Hanna and Sandall (1995)], and the second technique evaluates the relative error as a function of the step size. It should be noted that data of resin G583 is used here to evaluate the performance of the numerical scheme to solve the proposed model.

#### 4.8.3.1.1 Richardson Extrapolation

In the Richardson extrapolation, the solution,  $Y$ , is a function of a known approximate solution  $y(h)$  and the step size,  $h$ , that is employed to obtain the approximate solution as follows [Hanna and Sandall (1995)]:

$$Y = y(h) + a_1 h^p + a_2 h^q + O(h^r) \quad h \rightarrow 0, (p < q < r) \quad (122)$$

$a_1, a_2$ , are constants independent of the step size, and  $p, q$ , and  $r$  are constants that depend on the numerical method. If the step size is small enough to obtain a good approximation, the last two terms of Equation (122) can be neglected and a formula for the global error ratio,  $R_g$ , can be estimated by knowing the approximate solutions at  $h, h/2$ , and  $h/4$ , as follows:

$$R_g = \frac{[y(h/2) - y(h)]}{2^p [y(h/4) - y(h/2)]} \quad (123)$$

The constant,  $p$ , is estimated from Equation (123), and an appropriate range for the error ratio is  $0.8 \leq R_g \leq 1.2$ . Therefore, if the proposed simulation gives a stable and good approximation to the solution,  $R_g$  should increase exponentially by reducing the step size by a factor of 2:

$$p = \log \left\{ \frac{[y(h/2) - y(h)]}{[y(h/4) - y(h/2)]} \right\} / \log 2 \quad (124)$$

The simulation was carried out at various dimensionless step sizes as shown in Figure 24. The figure provides qualitative evidence of convergence, since the procedure suggests that it should be possible to obtain a solution from Equation (122).

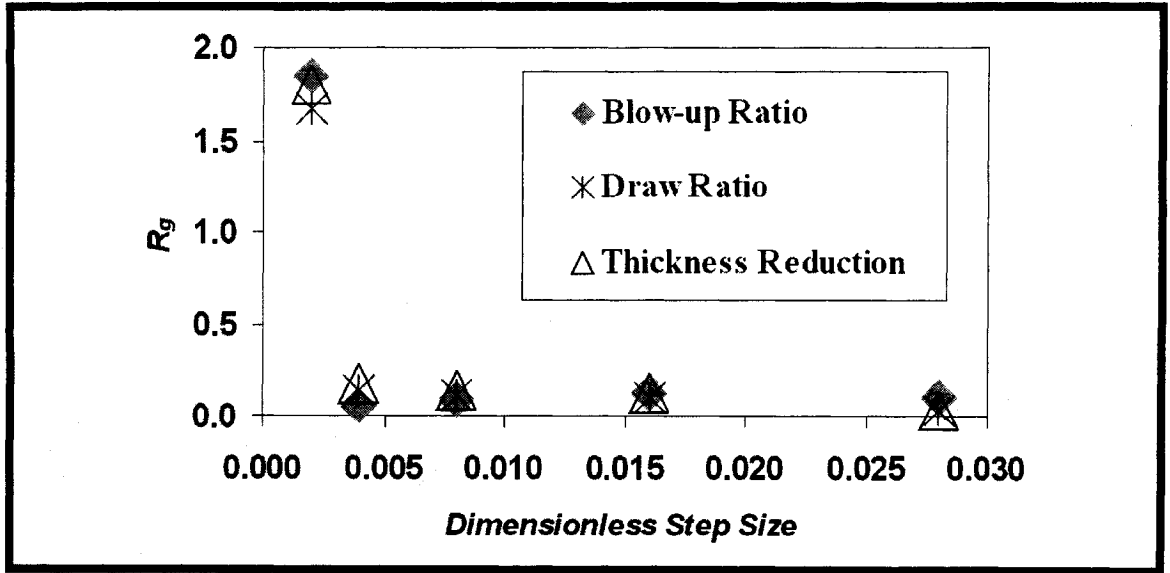


Figure 24: The estimated  $R_g$  for the approximated solution of the blow-up ratio, draw ratio, and thickness reduction as a function of the step size. *The properties of resin G583 were employed.*

#### 4.8.3.1.2 Effects of Step Size

In another test, convergence was evaluated by calculating the difference between the solution (for any of the variables, e.g. the radius or thickness) at the smallest achievable step size ( $y_a$ ) and the solution obtained at various step sizes ( $y_h$ ) and dividing the difference by  $y_a$ , as follows:

$$R = \frac{|y_a - y(h)|}{y_a} * 100\% \quad (125)$$

The solution obtained with the smallest achievable step size,  $y_a$ , is assumed to be the closest to the analytical solution, since the analytical solution is unknown [Mickley et al. (1957)]. The smallest achievable dimensionless step size was 0.0008 and the largest step size was 0.028. The above ratio was plotted as a function of the step size, as shown in Figure 25. The results show that the smaller was the step size, the more bounded was the error. This behavior of the relative error indicates that the solution is convergent. The step size that was employed in carrying out the simulation was 0.002. Figure 25 shows that, with this choice, the solution is fairly accurate within reasonable computational time

#### 4.8.3.2 Stability of the Numerical Solution

In this technique, a small error is deliberately induced at a specific random nodal position to perturb the solution. The error stays bounded without any propagation in the domain of the integration in the case of a stable numerical scheme. Therefore, an error of magnitude (0.001) was induced at the axial nodes (2, j), (20, j), (100, j), and (500, j) in separate tests, where “j” refers to the nodal position in the thickness direction. This perturbation was applied to the solution for the blow-up ratio, as shown in Figure 26. The error did not propagate and stayed bounded all the time till the end of the process, as seen in Figure 27. The above perturbation test was also applied to the solution for the thickness reduction ratio. The error (0.001) remained bounded all the time as shown in Figure 28. This is another indication of the simulation stability. The above simple test is not comprehensive. In order to make it comprehensive it should be applied at each node of the mesh. Alternatively, one may apply Fourier transform to the differential equations and solve to obtain the amplification factor to find the regions of stability. These comprehensive tests were not carried out.

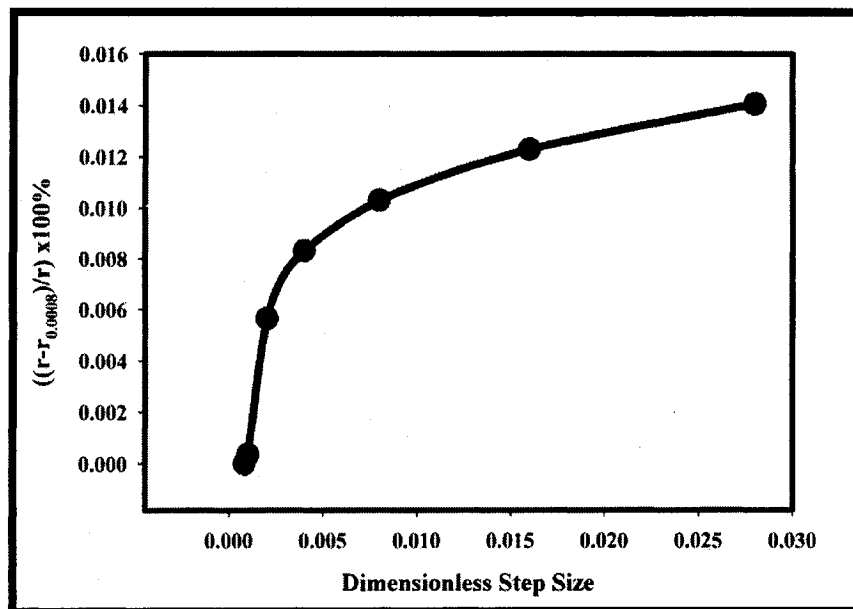


Figure 25: The estimated relative error, R, for the approximated solution of the blow-up ratio as a function of the step size. The employed polymer is film G583. All information regarding the properties and processing conditions are specified in Tables 3-5.

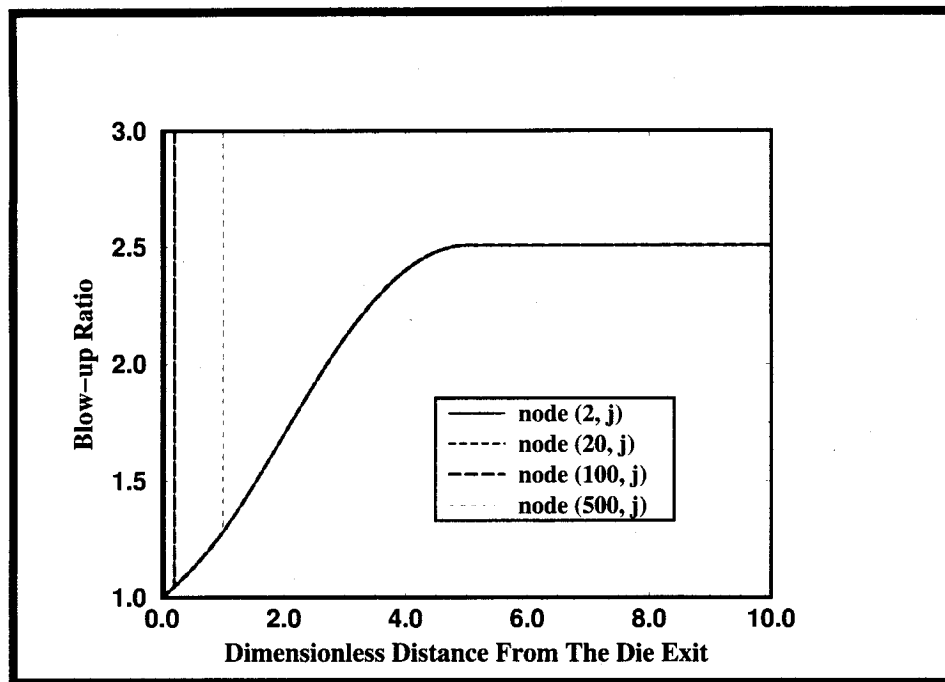


Figure 26: The location of the induced error did not affect the solution for the blow-up ratio. The employed polymer is film G583. All information regarding the properties and processing conditions are specified in Tables 3-5.

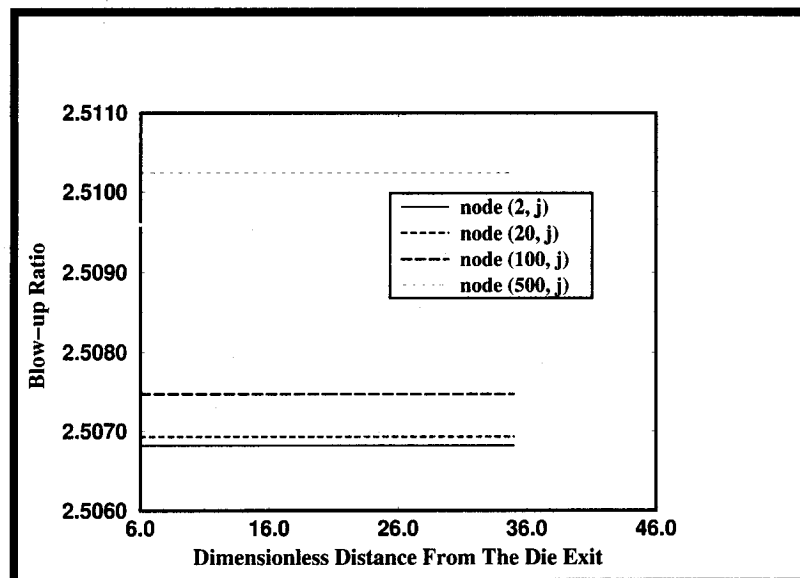


Figure 27: The induced error in the solution for the blow-up ratio did not propagate, which was an indication of the stability of the numerical scheme. The employed polymer is film G583. All information regarding the properties and processing conditions are specified in Tables 3-5.



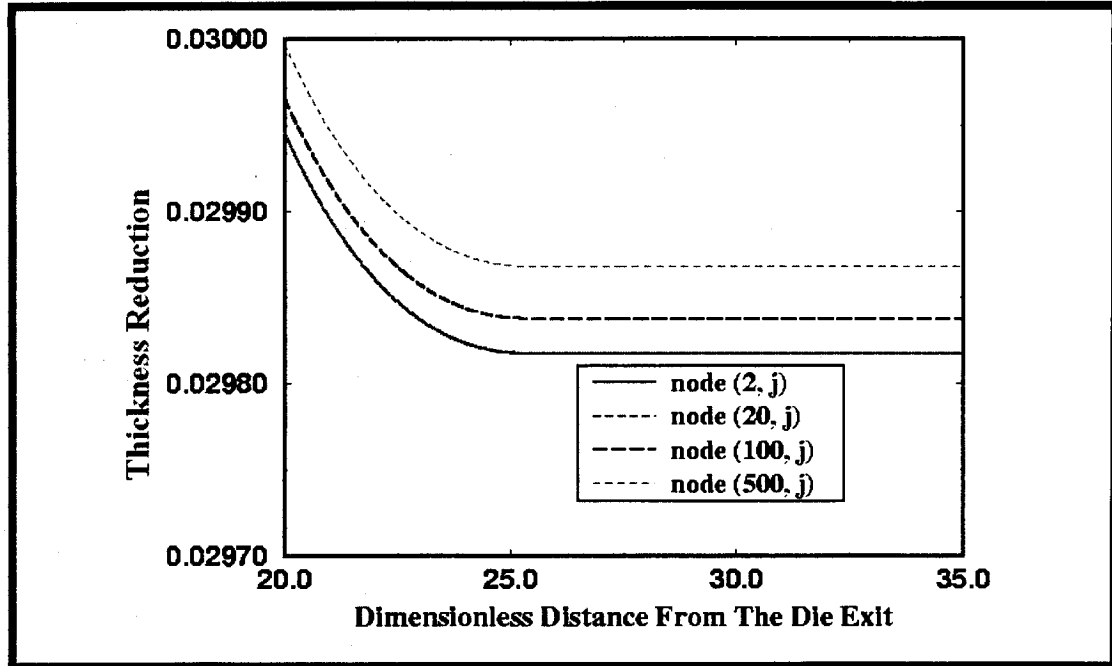


Figure 28: The induced error in the solution for the thickness ratio did not propagate, which was an indication of the stability of the numerical scheme. The employed polymer is film G583. All information regarding the properties and processing conditions are specified in Tables 3-5.

### 4.8.3.3 Robustness of the Model

#### 4.8.3.3.1 Effect of Rheological Parameters

In order to test the robustness of the simulation, the influence of variation of some of the parameters in the PTT constitutive equation ( $\xi$  and  $\varepsilon$ ) was evaluated, as shown in Figures 29 –32. In the simulation, the above parameters were varied within the ranges reported in the literature [Tas (1994), Phan-Thien (1978), Tanner (2000)]. The solution obtained by the simulation for over 100% variation within the range of these parameters, led to only small differences in the important predictions. The differences were rather small, especially when considered relative to the solutions obtained with the values selected for the parameters employed in this study (shown by bold lines in the Figures).

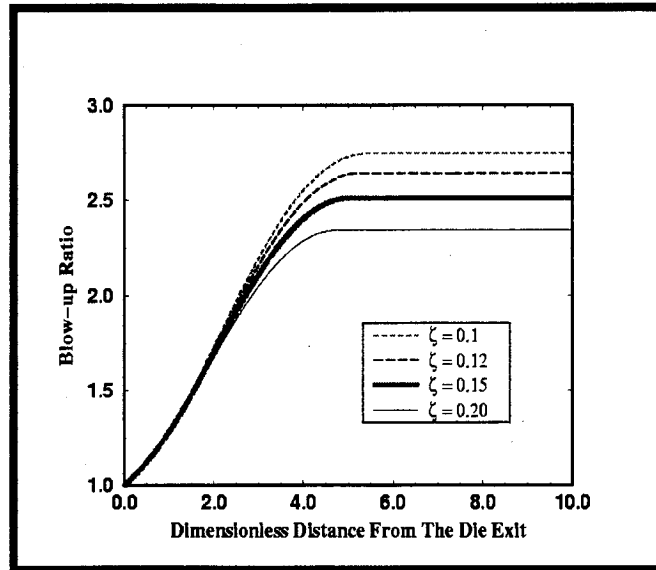


Figure 29: The effect of  $\xi$  on the bubble shape. The employed polymer is film G583. All information regarding the properties and processing conditions are specified in Tables 3-5.

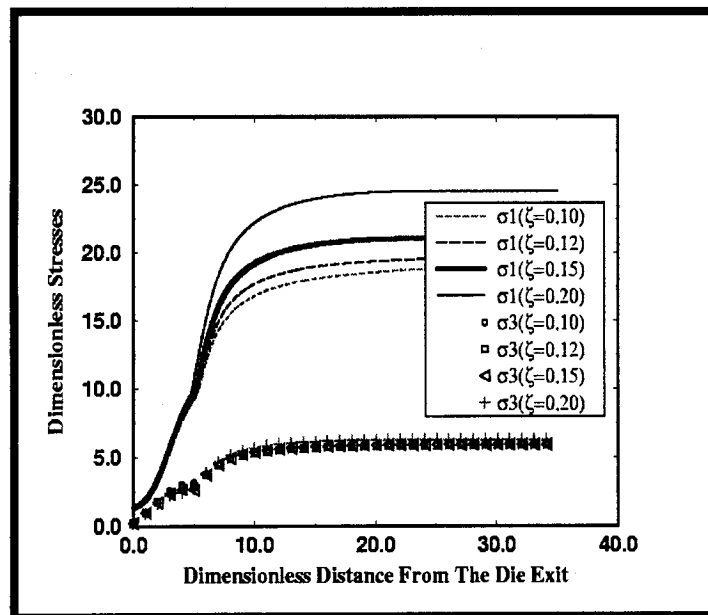


Figure 30: The effect of  $\xi$  on the evolution of the stresses. The employed polymer is film G583. All information regarding the properties and processing conditions are specified in Tables 3-5.

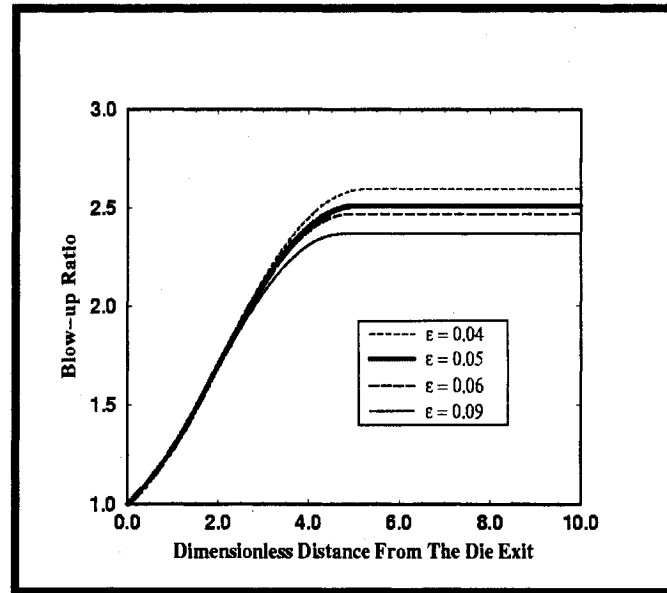


Figure 31: The effect of  $\varepsilon$  on the shape of the bubble. The employed polymer is film G583. All information regarding the properties and processing conditions are specified in Tables 3-5.

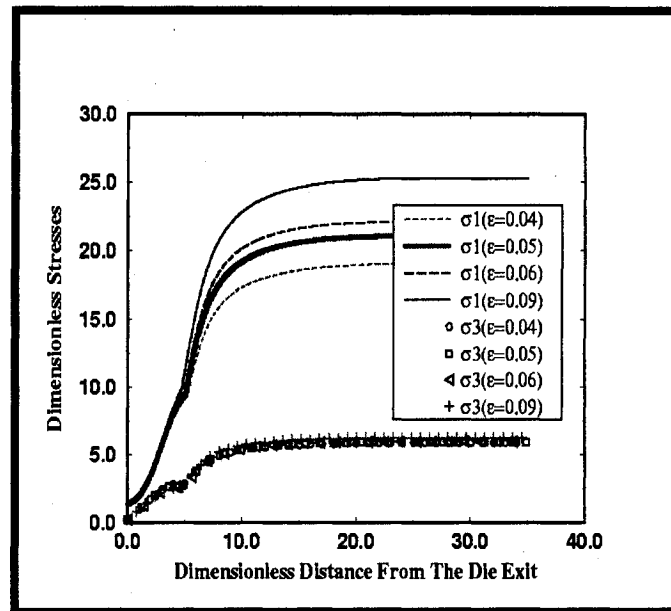


Figure 32: The effect of  $\varepsilon$  on the evolution of the stresses. The employed polymer is film G583. All information regarding the properties and processing conditions are specified in Tables 3-5.

In the test, the values of the take-up force, inflation pressure, and initial angle were guessed at the selected values of PTT parameters ( $\xi = 0.15$ ,  $\varepsilon = 0.05$ ) to give the specified BUR and DR for polymer G. Then, the resulting take-up force, inflation pressure, and initial blowing angle were used to predict the bubble shape and process behavior and the values of  $\xi$  and  $\varepsilon$  were changed. The results are shown in Figures 29-32. The figures show that the melt becomes more stretchable in the machine direction as  $\xi$  and  $\varepsilon$  increase. This is understandable, because as these parameters increase, the chains of the melt will be more able to slip and extend (the non affine motion is higher). The take-up force is much higher than the pressure force, which makes the polymer response faster in the machine direction.

It is useful at this point to discuss the behavior of the film above the freeze line. While stresses in the normal direction become too low to cause further expansion of the bubble radius, stresses in the axial and hoop directions are large enough to cause axial deformation and reduction in thickness. Thus, deformation in the machine and thickness directions continues after the freeze line despite freezing of the bubble radius. The extent of deformation depends on the traction force and film temperature. Based on our temperature predictions and data found in the literature [e.g., Luo and Tanner (1985), Ghauch-Fard et al. (1997), Tas (1994)], the temperature at the freeze line is sufficiently high to allow further planar deformation due to extensional force in the machine direction. This deformation in the machine and the thickness directions causes continuous growth in the stress in the machine direction but at a different rate, due to the change in the state of the polymer from melt-like to solid-like. Thus, the changes observed in the slope of the curves for stress after the freeze line (Figures 30 and 32) are due to the change in the rheological model that describes the behavior of the material in that region. Ideally, the transition should be smooth. However, in order to obtain a smooth transition, the two rheological models need to be matched in that zone. Unfortunately, it was not possible to obtain data on material properties in the vicinity of the freeze line. This should be an important objective in future research. In the meantime, the curves provide a reasonable idea about the behavior of the film beyond the freeze line.

The parameters of the relaxation modulus in the solid-like region seem to affect the draw ratio after the freeze line as seen in Figures 33-35. Crystallinity and orientation develop fast at the freeze line, which influences the stress and the reduction in the thickness. However, since the bubble radius does not change after the freeze line, the draw ratio behavior balances the reduction in the thickness.

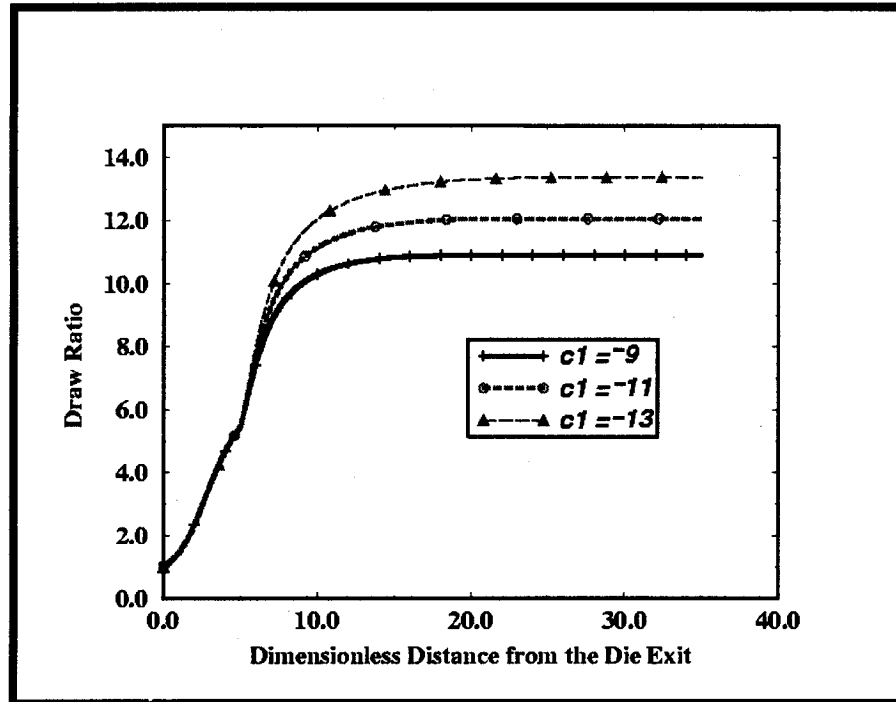


Figure 33: The effect of  $c_1$  on the film velocity. The employed polymer is film G583. All information regarding the properties and processing conditions are specified in Tables 3-5. Simulation value: -10.

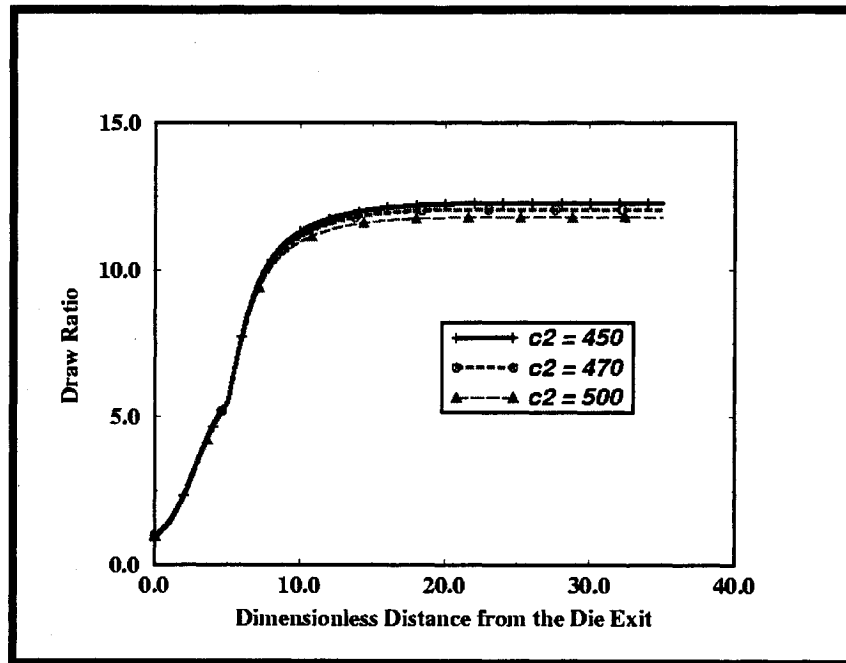


Figure 34: The effect of  $c_2$  on the film velocity. The employed polymer is film G583. All information regarding the properties and processing conditions are specified in Tables 3-5. The simulation value: 470.

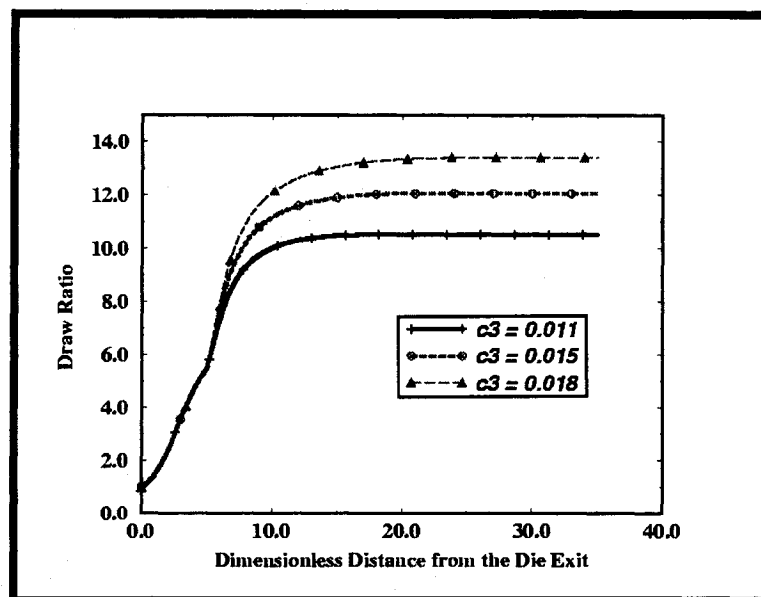


Figure 35: The effect of  $c_3$  on the film velocity. The employed polymer is film G583. All information regarding the properties and processing conditions are specified in Tables 3-5. The simulation value: 0.0165.

#### 4.8.3.3.2 The Parameters $\psi$ , $\phi$ , and $A$

The parameter  $\psi$  proposed by Kanai and White (1985) was employed to incorporate the effect of crystallization on viscosity. Kanai and White (1985) developed this relation for the film blowing process, assuming Newtonian behavior. The parameter  $\psi$  was considered to be a property of the polymer. In the current work, the crystallinity remained at a low level until the film reached the vicinity of the freeze line. This suggests that  $\psi$  and  $\phi$  may not be important in determination of the blow-up radius. This is supported by the results shown in Figures 36 and 37, where the values of  $\psi$  and  $\phi$  were varied over a wide range without causing significant changes in the prediction of the blow-up ratio (BUR). This is understandable, considering that the temperature at the freeze-line is above 105°C, where the crystallization rates are low.

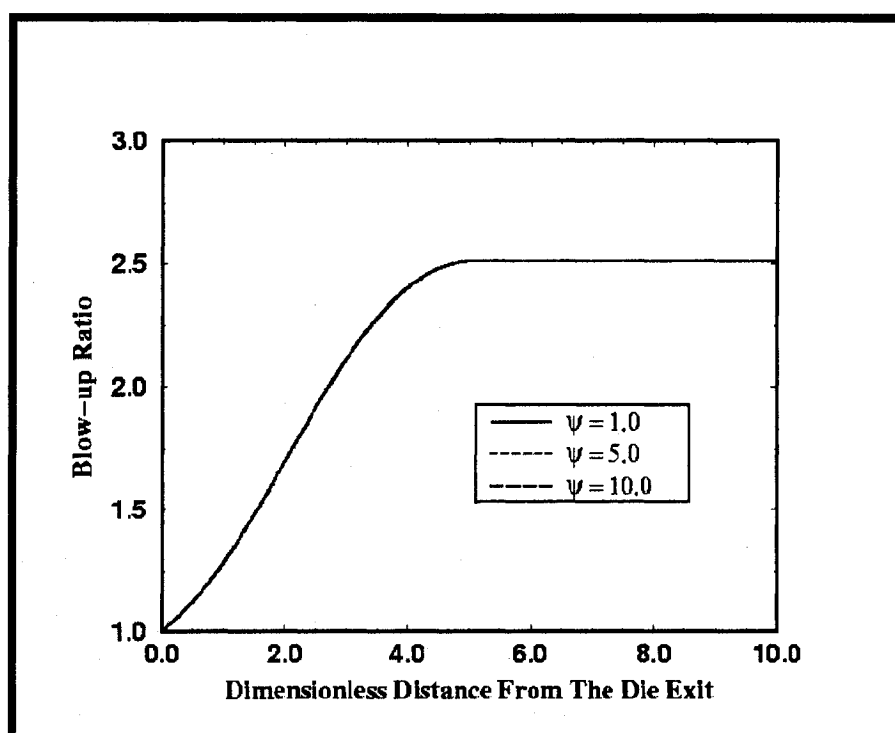


Figure 36: The effect of  $\psi$  on the bubble shape. The employed polymer is film G583. All information regarding the properties and processing conditions are specified in Tables 3-5.

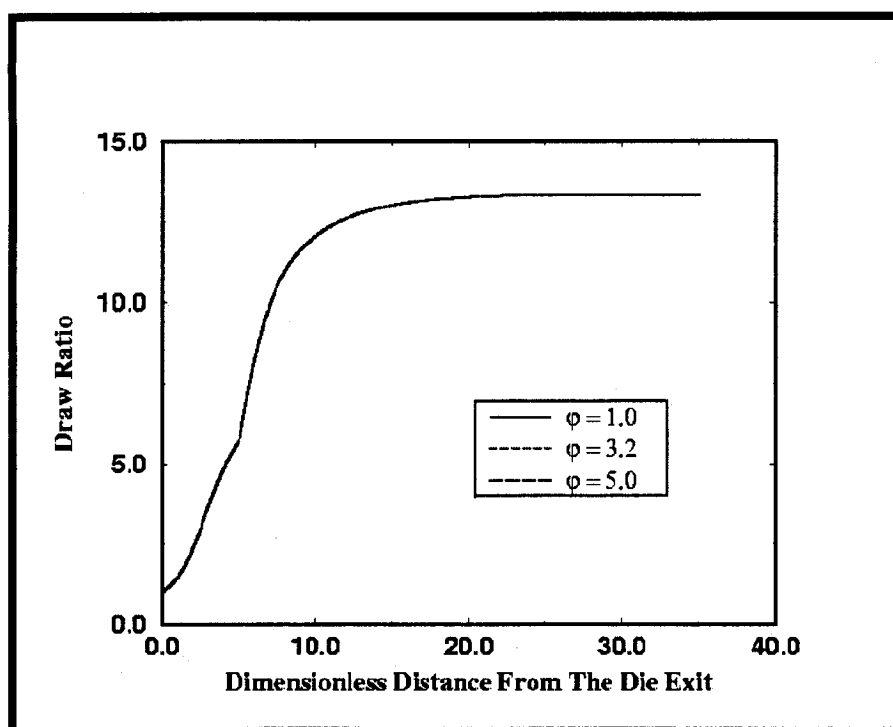


Figure 37: The effect of  $\phi$  on the evolution of the draw ratio. The employed polymer is film G583. All information regarding the properties and processing conditions are specified in Tables 3-5.

In the absence of reliable data, the value of Ziabicki's constant ( $A$ ) was fixed at 1000, for all experiments, to avoid exaggerating the effect of orientation on crystallinity. However, the results shown in Figures 38 and 39 indicate that variation of " $A$ " had a negligible effect on the predictions of bubble shape and film velocity, when the parameter was varied from 1000 to 10000, since the orientation in the blown films is relatively weak.



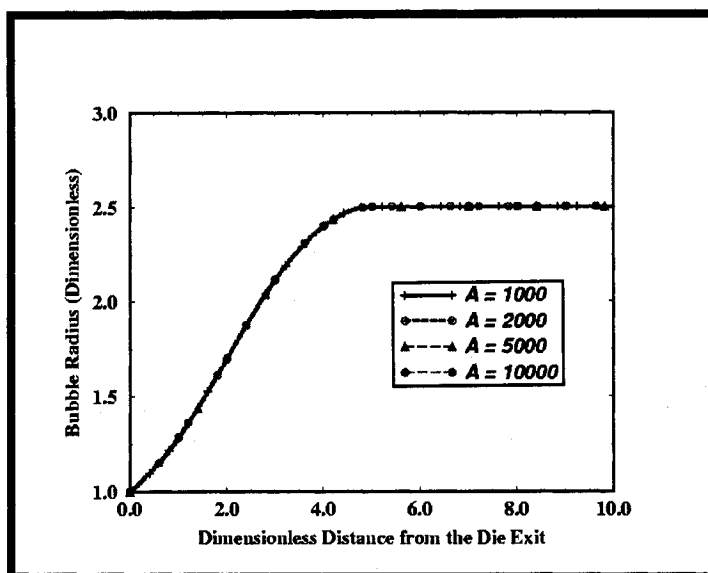


Figure 38: The effect of  $A$  on the evolution of the blow-up ratio. The employed polymer is film G583. All information regarding the properties and processing conditions are specified in Tables 3-5.

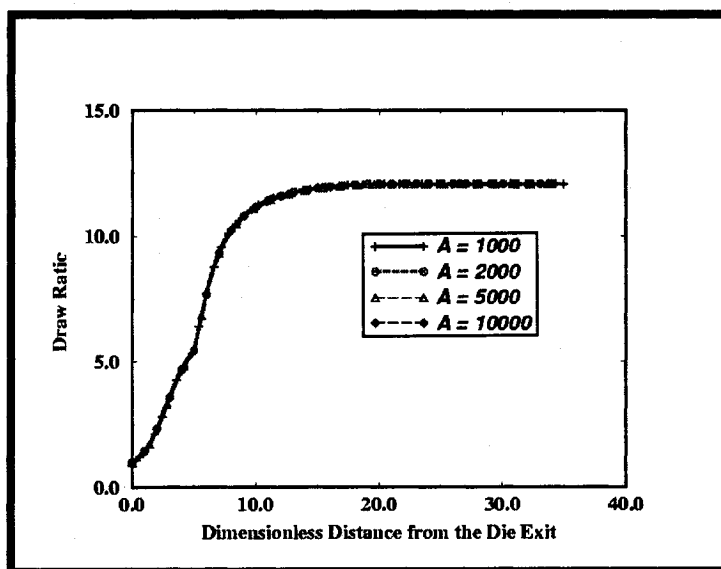


Figure 39: The effect of  $A$  on the evolution of the draw ratio. The employed polymer is film G583. All information regarding the properties and processing conditions are specified in Tables 3-5.

# Chapter 5

## 5 VALIDATION OF THE MODEL

This chapter provides validation of the proposed film blowing simulation by comparing the predictions of the simulation with results reported in the literature based on analytical and computational solutions of limiting cases and on experimental data.

### 5.1 Comparison With Analytical and Numerical Solutions

In this section we compare the predictions of the proposed film-blowing model with analytical and computational results reported by various researchers.

#### 5.1.1 Analytical Solution For Isothermal Newtonian Melt

Cain and Denn (1988) obtained an analytical solution for blowing an isothermal Newtonian melt. They showed that the model yields  $BUR=1$  when  $\bar{F} = 3\bar{B}$ . Under these conditions, thickness reduction can be predicted by the following equation:

$$h/h_0 = \exp(-\bar{F}z/3) \quad (126)$$

Their work was explained in detail in chapter 2 of the present work. Figure 40 shows that predictions of the proposed model for the thickness reduction are effectively identical with the results obtained by the analytical model.

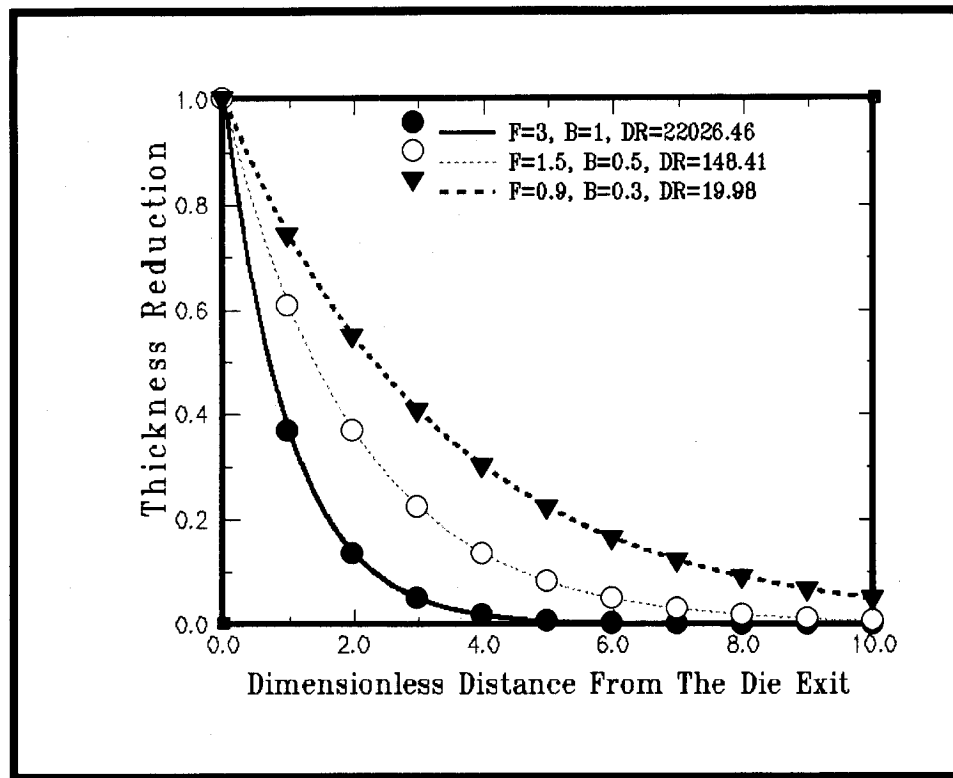


Figure 40: The numerical solutions (lines) for the Newtonian cases when  $F=3B$  are consistent with the analytical solutions (symbols) reported by Cain and Denn (1988).

### 5.1.2 Non-Isothermal Newtonian Solution

Kanai and White (1985) obtained a solution of the film blowing of a non-isothermal Newtonian melt. They assumed an exponential function for dependence of viscosity on temperature and crystallinity. The simulation was one-dimensional (no radial variations in temperature). Figures 41 and 42 show that the proposed simulation yields the same results as those obtained by Kanai and White under the same conditions.

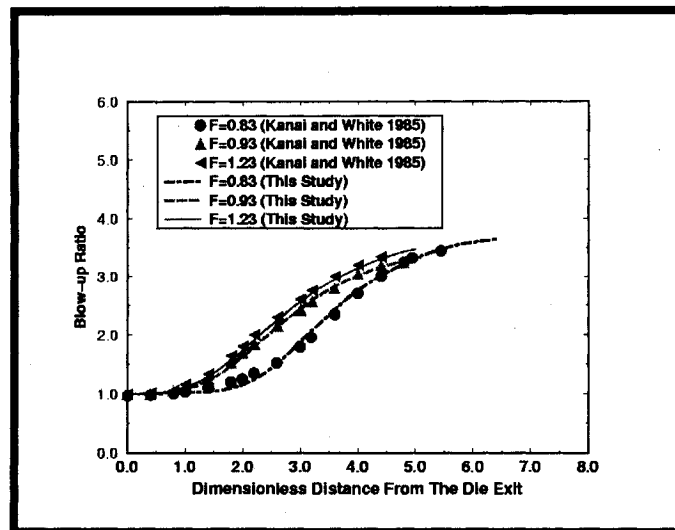


Figure 41: Comparison of predicted bubble shapes, using 1-D nonisothermal Newtonian model [lines] with the predictions of Kanai and White [symbols] (1985) at different dimensionless take-up force ( $F$ ) and constant dimensionless inflation pressure ( $B = 0.309$ ).

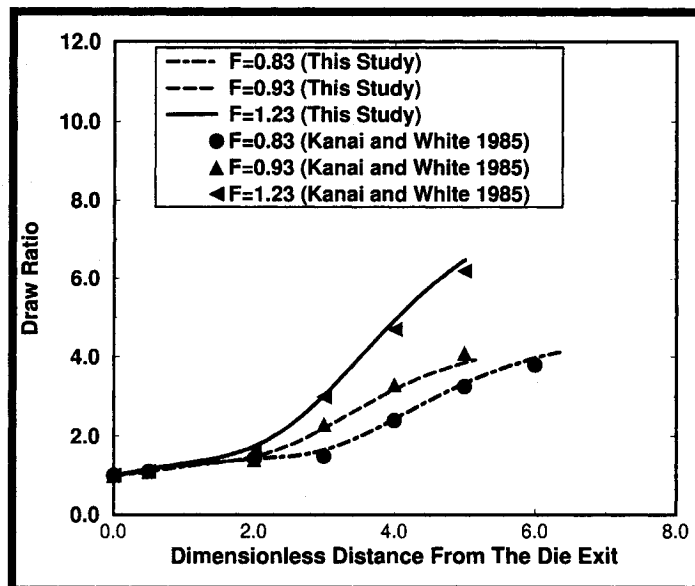


Figure 42: Comparison of predicted draw ratio, using 1-D nonisothermal Newtonian model [lines] with the predictions of Kanai and White [symbols] (1985) at different dimensionless take-up force ( $F$ ) and constant dimensionless inflation pressure ( $B = 0.309$ ).

### 5.1.3 Isothermal Viscoelastic Melt

Luo and Tanner (1985) obtained a one-dimensional solution for the film blowing of an isothermal Maxwell fluid at different Deborah numbers ( $De$ ). The results are compared to the predictions of the proposed simulation in Figure 43. It is seen that good agreement is obtained between the two solutions. The results of Luo and Tanner were also supported by the work of Cao (1990) and André et al. (1998).

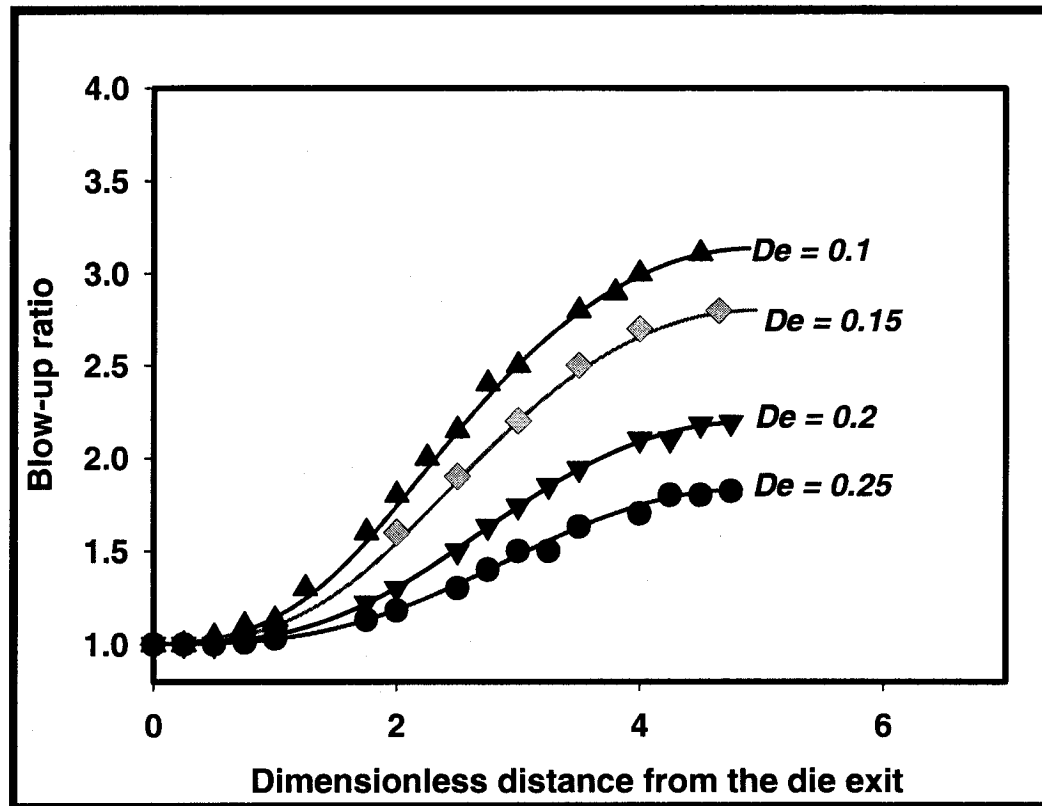


Figure 43: Comparison of bubble shapes predicted by the proposed model, using 1-D isothermal Maxwell model [lines] with the predictions of Luo and Tanner [symbols] (1985) at different Deborah numbers ( $De$ ) and constant dimensionless Take up force ( $F=0.134$ ) and inflation pressure ( $B = 0.2$ ).

## 5.2 Comparison With Experimental Results

In order to obtain further validation of the proposed simulation of the film blowing process, the predictions of the simulation were compared to experimental data reported in the literature. For this purpose, the results were compared with the experimental results reported by Butler et al. (1993), Ghaneh-Fard et al. (1997), and Tas (1994).

### 5.2.1 Sources of Experimental Data

Butler et al (1993) and Ghaneh-Fard et al. (1997) employed different types of linear low-density polyethylene (LLDPE). Also, Butler employed an internal cooling system, which required changing the thermal boundary condition at the inner surface of the film from the adiabatic condition to the following condition:

$$\frac{d\dot{T}}{dr} = \left( \frac{300}{T_0} - \dot{T}_{surface} \right) \quad (127)$$

where  $T_0$  is the extrusion temperature at the die exit, and  $\dot{T}_{surface}^*$  is the temperature of the internal surface of the film. Since Butler did not report the exact internal cooling conditions, the above equation was used by fitting experimental data. Tas (1994) used three types of LDPE under different processing conditions, varying take-up force and inflation pressure.

The above researchers employed different die dimensions, polymers, and processing conditions, as will be shown later in the section of the experimental data. The relevant data regarding the processing conditions and material properties are summarized in Tables 6-9 and Figure 44. The melt rheological properties of the polymers are listed in Table 8 and Figure 44. The data for resin G583 are employed for LLDPE resins, in the absence of data regarding rheology or crystallization, and the data for resin F751 are employed for LDPE resins in the absence of data regarding crystallization or rheology.

The rheological properties for the solid-like phase were the same in all cases, as shown in Table 8.

Butler and Ghaneh-Fard employed similar standard experimental techniques to obtain the velocity profiles. A tracer was placed on the bubble surface, and the movement of the tracer was recorded by video camera. Computer image analysis was applied to the taped images. Tas employed Laser Doppler velocimetry to measure the axial velocity profiles. A detailed description can be found elsewhere [Butler (1993), Ghaneh-Fard (1997), Tas (1994)].

### 5.2.2 Experimental Data

The data are based on film blowing experiments reported in the literature by Butler (1993), Ghaneh-Fard (1997), and Tas (1994), for different polyethylene resins extruded under a variety of processing conditions. The processing conditions for the film blowing process are listed in Table 6. The material properties and model parameters are listed in Table 7. The Rheological properties are listed in Table 8. The melt rheological properties and crystallization kinetics of the polymers in the cases of Butler and Ghaneh-Fard were assumed to be similar to those of resin 'G' for lack of information. The rheological properties of Nagamatsu (1961) were employed in all cases to model the solid-like film behavior. The general differences among the researches are listed in Table 9.

Table 6: Processing conditions for the film blowing process.

Source Reference	Butler et al (1993)	Ghaneh-Fard et al. (1997)	Tas (1994)
Material	(LLDPE)	(LLDPE)	(LDPE)
Initial radius, $r_0$ (m)	0.1	0.025	0.0384
Initial thickness, $h_0$ (m)	0.0018	0.0009	0.0008
Die exit temperature, $T_0$ ( $^{\circ}C$ )	246	220	175
Air temperature, $T_a$ ( $^{\circ}C$ )	25	25	25

Table 7: Material properties used in the computations

Model parameter	Value	Units	Source
$\Psi$	5.1 (LLDPE), 7.5 (LDPE)	<i>Dimensionless</i>	Kanai (1985)
$A$ , Constant of stress-induced orientation	1000	<i>Dimensionless</i>	Ziabicki (1976)
$N$ , Avrami exponent	2	<i>Dimensionless</i>	Lungu (2000)
$\beta$ , the half-width of $K(T)$ curve.	44.3 (LLDPE), 28.8 (LDPE)	$^{\circ}\text{C}$	Lungu (2000)
Heat capacity, $C_p$	2.3	$\text{J.g}^{-1}.\text{K}^{-1}$	Dole (1967)
Thermal conductivity, $k$	0.33	$\text{J.m}^{-1}.\text{s}^{-1}.\text{K}^{-1}$	Dole (1967)
Thermal diffusivity $\alpha$	$1.6 \times 10^{-7}$	$\text{m.s}^{-2}$	Dole (1967)
$\Delta H$ , heat of fusion	290	$\text{J.g}^{-1}$	Dole (1967)
Density, $\rho$	925 (Butler), 918 (Ghaneh-Fard), 921(Tas)	$\text{kg.m}^{-3}$	Kamal (2001)



Table 8: Rheological properties for polymers used in the study.

Property	Value	Source
$\lambda_0$ (. s)	1.2	Estimated [polymer (G) rheology]
$\eta_0$ (Pa. s)	10814	Estimated [polymer (G) rheology]
$\varepsilon$	0.05	Phan-Thien 1978
$\xi$	0.15	Tas 1994
$c_1$	-10	Estimated [experiments of Nagamatsu 1961]
$c_2$	470	Estimated [experiments of Nagamatsu 1961]
$c_3$	0.0165	Estimated [experiments of Nagamatsu 1961]
$m$ , power law constant	0.24	Estimated [polymer (G) rheology]

	Dynamic constants of the liquid-like melt						Dynamic constants of the solid-like film	
	LLDPE (Butler or Ghaneh-Fard)		LDPE (Tas. L1)		LDPE (Tas,L1o)			
$k$	$\lambda_k$ (s)	$g_k$ (kPa)	$\lambda_i$ (s)	$g_i$ (k. Pa)	$\lambda_i$ (s)	$g_i$ (k. Pa)	$\lambda_k$ (s)	$g_k$ (M Pa)
1	0.004	284.3	0.000077	272.0	0.000061	229.0	1.9	85
2	0.028	60.1	0.000705	105.0	0.000429	95.1	9.3	65
3	0.117	18.	0.00513	60.2	0.00241	56.5	24.3	12
4	0.487	4.8	0.0359	31.6	0.0135	33.3	101.4	46.4
5	2.096	0.928	0.242	13.7	0.0729	17.8	5395.1	65.2
6	11.41	134.4	1.58	4.5	0.394	8.4	5395.1	65.1
7	0	0	10.1	1.0	2.04	3.3	0	0
8	0	0	72	0.15	12.4	0.96	0	0

Table 9: General differences among Butler (1993), Ghaneh-Fard (1997), and Tas (1994).

	Bulter	Ghaneh-Fard	Tas
Used Polymer	NG-LLDPE	LLDPE	LDPE
Cooling System	External and Internal	External	External
Blow-up ratio	3	2	1.5-2.5
Draw ratio	18	9.5	4-7
Freeze-line height (cm)	55	25	21

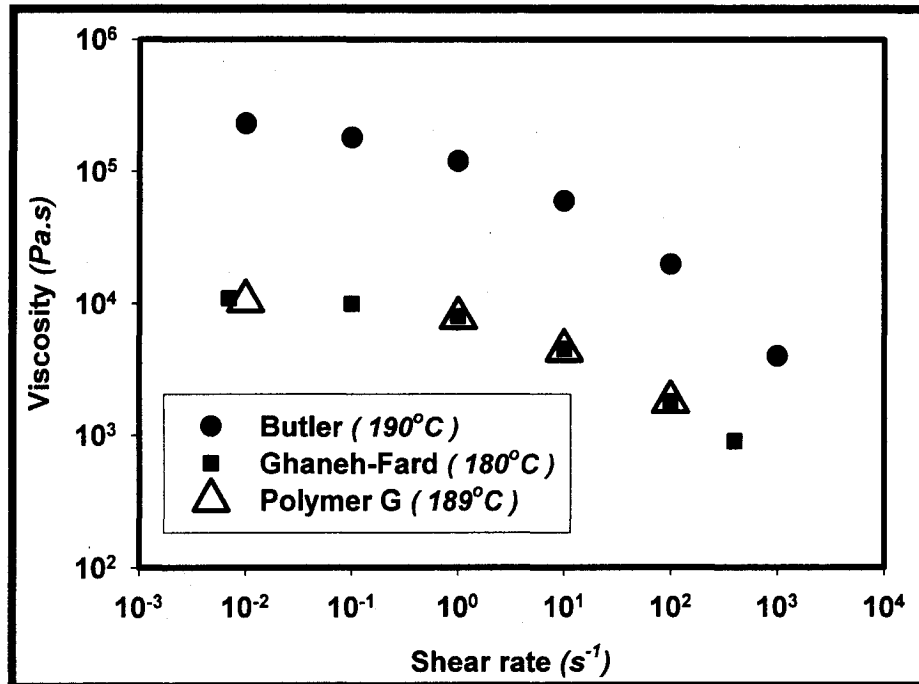


Figure 44: The melt viscosity profiles of the LLDPE used in this study.

## 5.2.3 Comparison of Experimental Results With Model Predictions

### 5.2.3.1 General Comparison

In the present work, the initial blowing angle at the die exit, the dimensionless inflation pressure, and the take-up force, are treated as part of the solution that is calculated by the simulation, as shown in Table 10. Newton's method is employed to guess the values of these key variables of the film blowing process, which are listed in Table 10.

Table 10: Predicted solution for key parameters.

	Butler (LLDPE)	Ghaneh-Fard (LLDPE)	Resin G583 (LLDPE)	Tas (LDPE)
Take-up force, $F$ ( <i>Dimensionless</i> )	1.7	2.1	1.7	5.7 - 7.7 ( $N$ )
Inflation pressure, $B$ ( <i>Dimensionless</i> )	0.21	0.05	0.17	95-135 ( $Pa$ )
Initial blowing angle, $\theta$ ( <i>Degrees</i> )	6	-2	0	-2 -1

### 5.2.3.2 Comparison With Results of Butler (1993)

Figure 45 shows that the bubble shapes and film thickness predicted by the simulation are in good agreement with the experimental measurements. It also shows that the position of the freeze line was accurately predicted. Figure 46 shows that good agreement is obtained between the temperature profile predicted by the present film blowing simulation and the measured temperature profile reported by Butler (1993). Figure 46 also shows that when the ultimate crystallinity is considered to depend on temperature, as suggested in this work, crystallization continues for a long time after the temperature plateaus near the freeze line. On the other hand, when the ultimate crystallinity is assumed to be constant (i.e., 0.3), the bulk of crystallization occurs within a short space near the freeze line. Thus, incorporating a temperature-dependent ultimate crystallinity yielded better agreement with Butler's measured temperature profile. We show only the predicted value of crystallinity because Butler did not report the profiles of the crystallinity. Figure 46 also shows a significant difference between the temperatures of the internal and external surfaces of the film due to the poor conductivity of polymers. The difference diminishes near the freeze line. Cao (1990) and André (1999) reported similar observations.

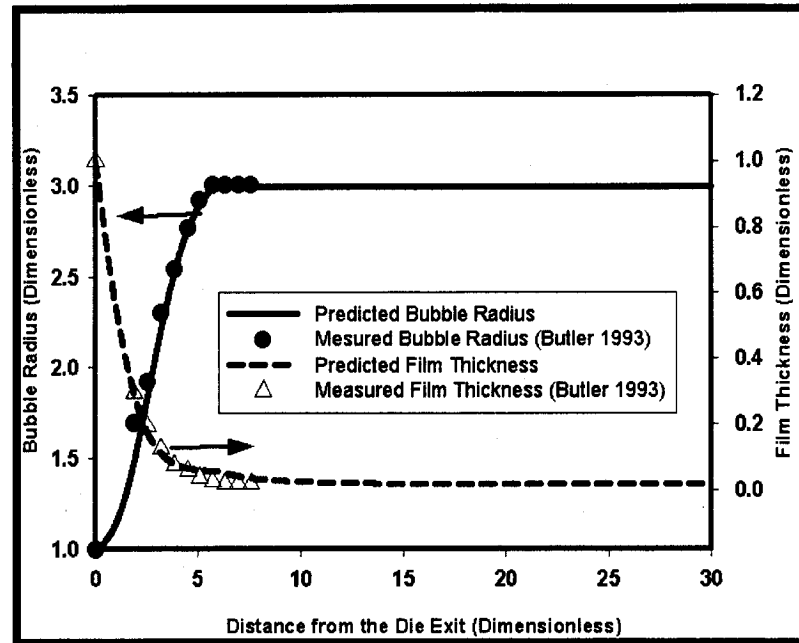


Figure 45: Comparison of predicted bubble radius and film thickness with Butler's measured results at the conditions specified in Tables 6-9.

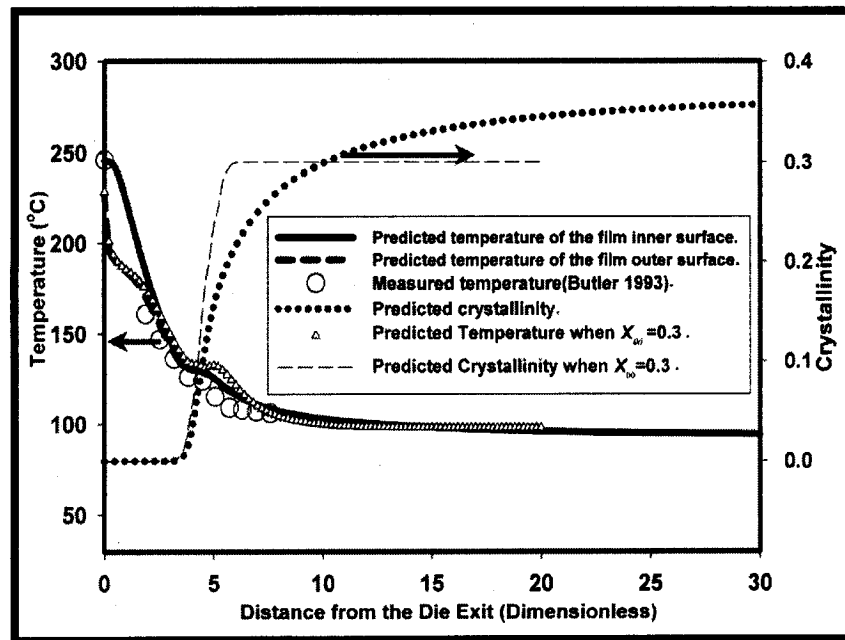


Figure 46: The effect of the ultimate crystallinity on the predicted temperature and crystallinity development, for conditions specified in the tables for experimental conditions employed by Butler (1993).

### 5.2.3.3 Comparison With Results of Ghaneh-Fard (1997)

Figure 47 shows that the bubble shapes and film velocities predicted by the simulation are in good agreement with the experimental measurements. However, the bubble neck, in the case of Ghaneh-Fard (1997), was somewhat longer. This might be due to the uncertainty about the location of the air ring. Nonetheless, the position of the freeze line, the blow-up ratio, and the draw ratio were accurately predicted.

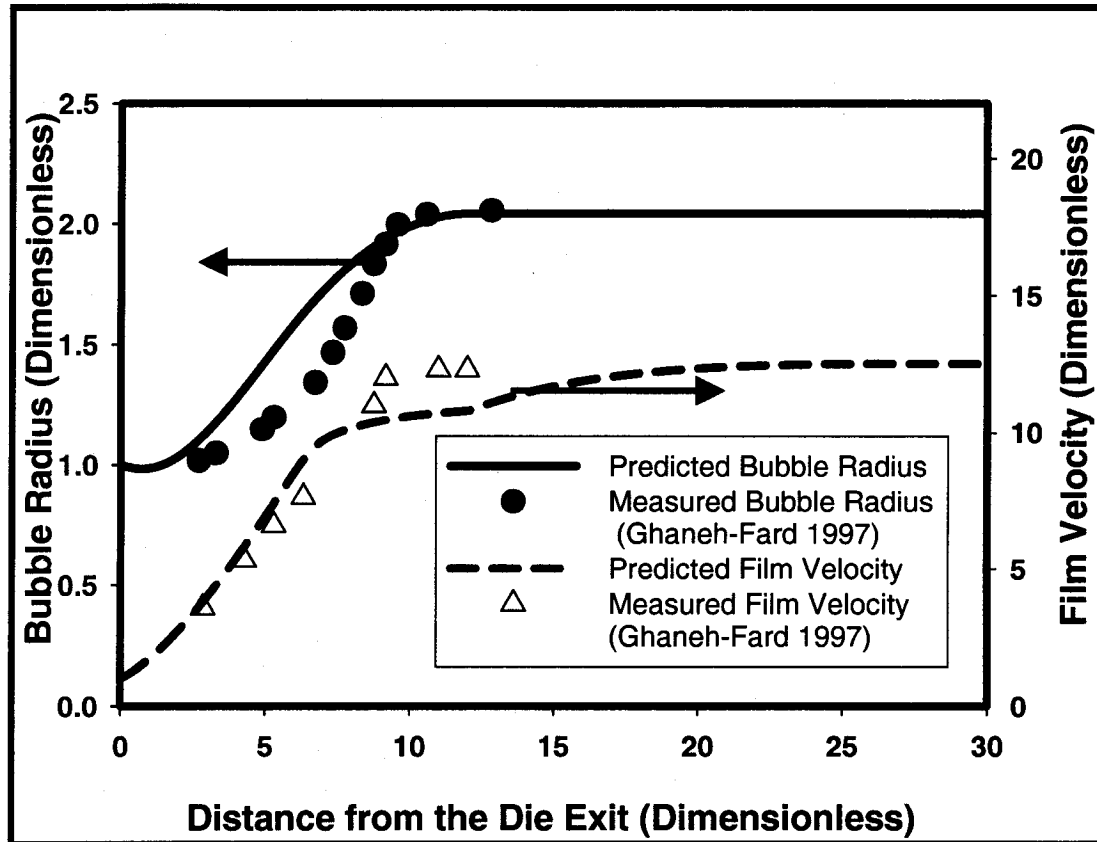


Figure 47: Comparison of predicted bubble radius and film velocity with measured results of Ghaneh-Fard (1997), at the conditions specified in Tables 6-9.

### 5.2.3.4 Comparison With Results of Tas (1994)

Figures 48 and 49 show the sensitivity of bubble radius and velocity to the inflation pressure and take-up force, according to the experiments of Tas (1994). Since Tas did not report the volumetric flow rate of the cooling air, one of the experiments (L1Exp12) was employed to guess the volumetric flow rate of the cooling air. This was done using the take-up force and inflation pressure as fixed inputs without allowing them to be guessed. Then, computations were carried out, at various values of the air flow rate, to match the predicted blow-up ratio, draw ratio, and the temperature profile to the values measured by Tas. The estimated volumetric flow rate of the cooling air was then employed in the subsequent simulations to predict (reproduce) the measured take-up force and inflation pressure that were reported by Tas (1994). These values were experimentally employed by Tas to obtain the blow-up and draw ratios reported in his thesis and shown in Figures 48 and 49. The figures show that the velocity increased slightly after the freeze line in some cases. It is clear that the simulation captured the freeze line and the transition in the velocity profile.

Considering the thickness comparison, it should be noted that Tas reported the final thickness values of all films, which was 60 microns, and did not report the whole thickness profiles. Figure 50 shows the dimensionless thickness profiles of all films predicted by the proposed film-blowing model. It also shows that the proposed simulation successfully predicted the final thickness values of all films. Other properties such as the film temperature profiles were predicted, as shown in Figures 51 and 52. It can be seen that the temperature continued to decrease after the freeze line. Tas did not show data after the freeze line. The present work predictions of the temperature decrease after the freeze line are consistent with results obtained by many researchers, such as Ghaneh-Fard (1997). Figure 53 shows that the present model predicts a temperature variation across the film thickness in addition to the temperature drop along the machine direction. The temperature variation across the thickness is due to the low thermal conductivity of polymer melts. Other researchers such as André (1999) made similar observations.

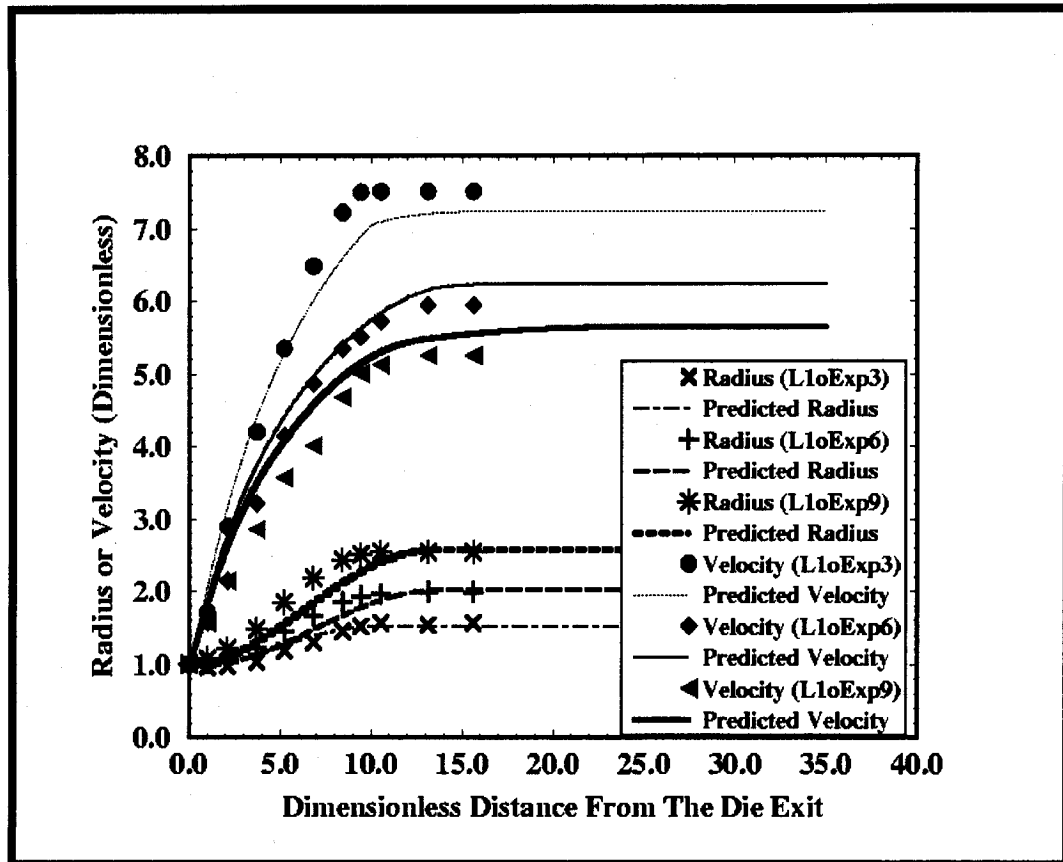


Figure 48: Comparison of predicted bubble radius and film velocity (lines) with measured results (symbols) of Tas (1994), at the conditions specified in Tables 6-10. Exp 3 (inflation pressure = 135 Pa, Take-up Force = 6.6 N), Exp 6 (120 Pa, 6.7 N), Exp 9 (105 Pa, 5.7 N).



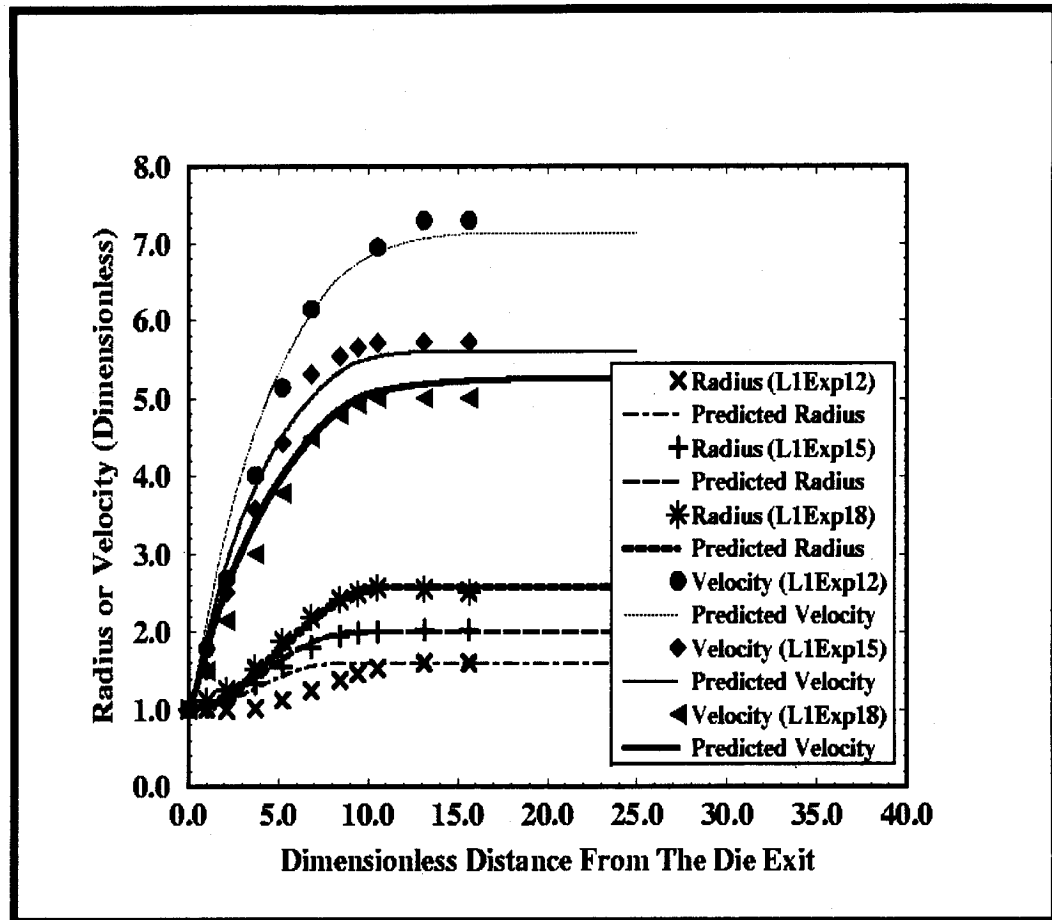


Figure 49: Comparison of predicted bubble radius and film velocity (lines) with measured results (symbols) of Tas (1994), at the conditions specified in Tables 6-10. Exp.12 (inflation pressure=118 Pa, Take-up Force=7.6 N), Exp.15 (108 Pa, 7.7 N), Exp.18 (95 Pa, 6.9 N).

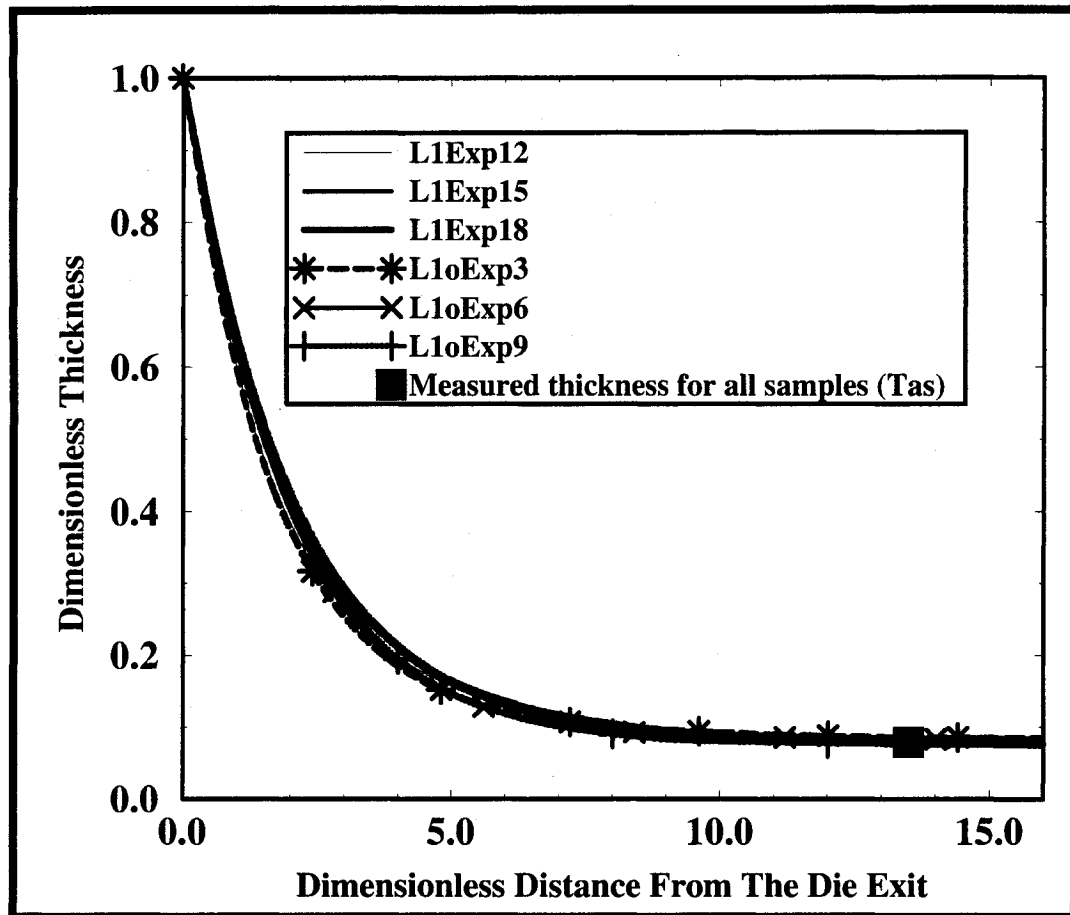


Figure 50: Comparison between the predicted film thickness (lines) and the measured results (symbols) of Tas (1994). The processing conditions are specified in Tables 6-10.

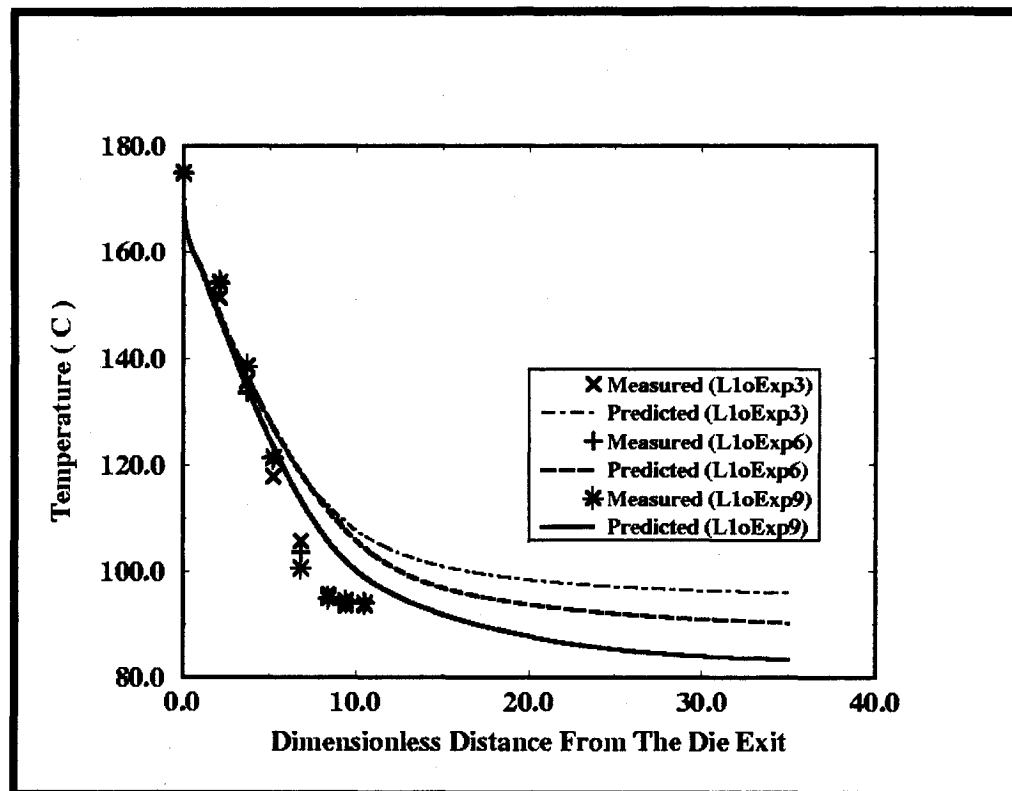


Figure 51: Comparison of predicted temperature profiles (lines) with measured results (symbols) of Tas (1994), at the conditions specified in Tables 6-10. Exp 3 (inflation pressure = 135 Pa, Take-up Force = 6.6 N), Exp 6 (120 Pa, 6.7 N), Exp 9 (105 Pa, 5.7 N).

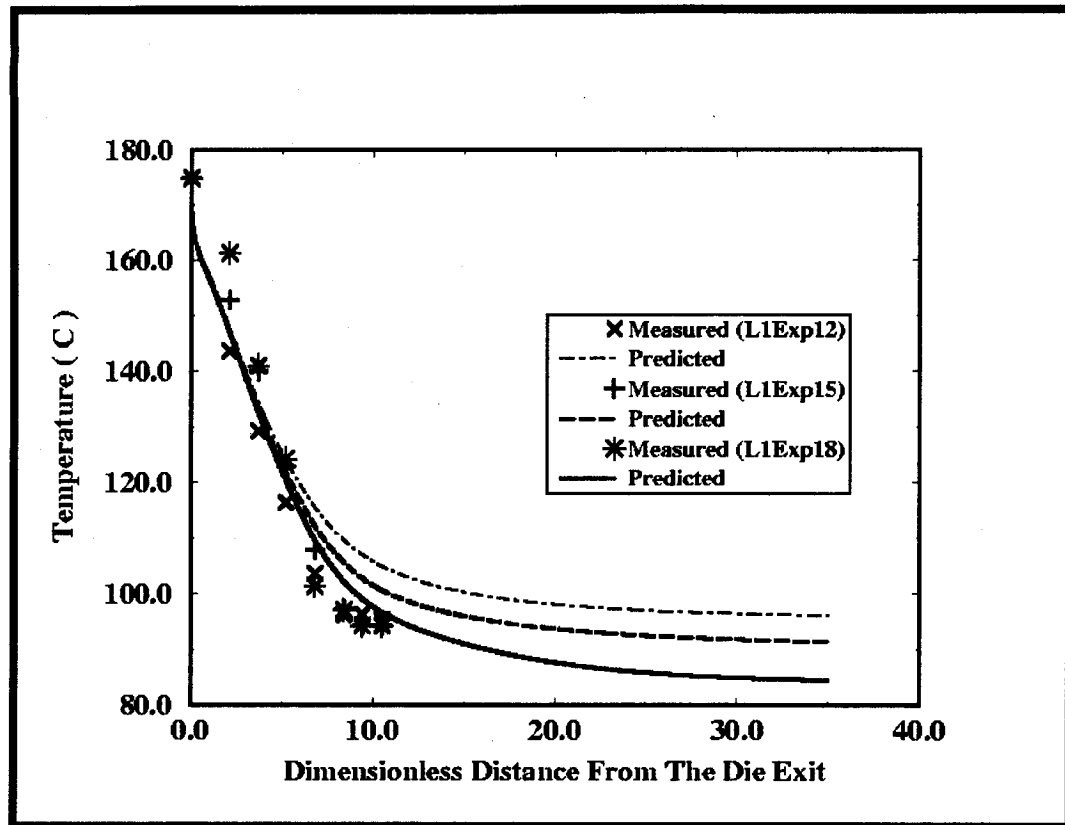


Figure 52: Comparison of predicted temperature profiles (lines) with measured results (symbols) of Tas (1994), at the conditions specified in Tables 6-10. Exp.12 (inflation pressure=118 Pa, Take-up Force=7.6 N), Exp.15 (108 Pa, 7.7 N), Exp.18 (95 Pa, 6.9 N).

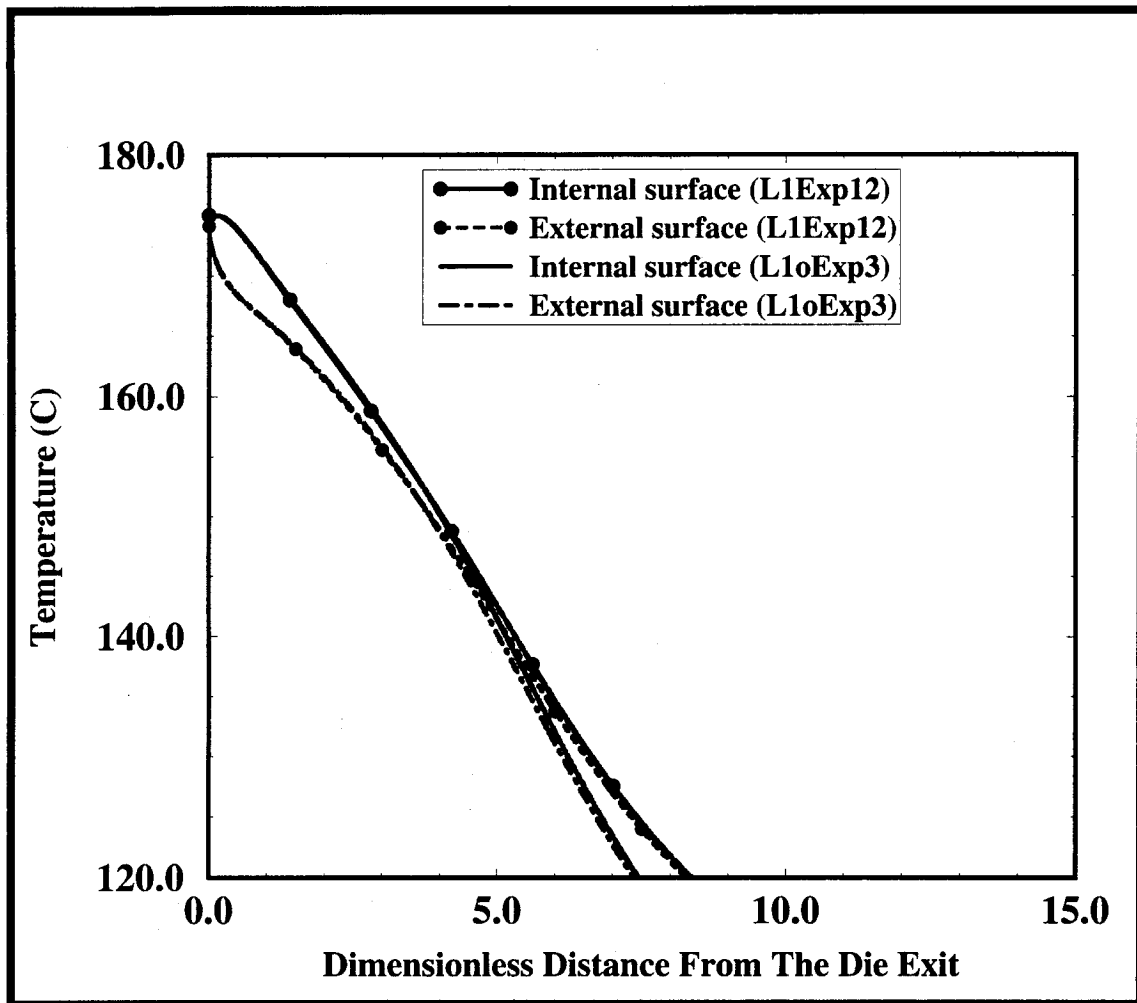


Figure 53: The predicted temperature difference between the external and internal surfaces of the films. The processing conditions are specified in Tables 6-10.

## 5.3 Prediction of Microstructural Properties

This section reports the results of predictions by the proposed film blowing simulation for crystallinity, birefringence, and orientation of blown films. Differential scanning calorimetry (DSC) is employed to measure the absolute crystallinity for selected films. Birefringence and orientation were measured using polarized light microscopy and Fourier transform infrared (FTIR) analysis. This section also provides validation of the proposed film blowing simulation by comparing the predictions of the simulation with the measured microstructural properties.

### 5.3.1 Background

#### 5.3.1.1 Interaction Between Crystallization and Orientation

Polyethylene is a semi-crystalline polymer. When polyethylene crystallizes from the melt, the chains form structures of chain folded lamellae. The crystalline characteristics of blown films are significantly different from those obtained by crystallization of quiescent melts, due to the effect of stress-induced orientation and cooling rate. Ziabicki and Jarecki (1985) proposed that the chain orientation affects the enthalpy ( $\Delta h$ ) and entropy ( $\Delta s$ ) of both the semi-crystalline and amorphous phases. Therefore, the equilibrium crystallization temperature ( $T_m$ ) and the bulk free energy per kinetic segment ( $\Delta g$ ) are affected by the orientation as follows:

$$T_m = \frac{\Delta h_o + \delta h}{\Delta s_o + \delta s} = T_m^o \frac{1 + \delta h / \Delta h_o}{1 + \delta s / \Delta s_o} \quad (128)$$

$$\Delta g = (\Delta h - T\Delta s) + \delta h - T\delta s = \Delta g_o + \delta g \quad (129)$$

where  $\delta h$ ,  $\delta s$ , and  $\delta g$  are the difference in value due to stress-induced orientation. The subscript 'o' refers to the equilibrium value without the orientation effect. Now, the critical cluster size ( $z$ ), to form the crystal is defined by the following equation:

$$z = -\left(\frac{2a}{3\Delta g}\right)^3 \quad (130)$$

where  $a$  is the interface free energy per kinetic segment. The derivations of Turnbull and Fisher (1949) and Frank and Tossi (1961) show that the Gibb's free energy ( $\Delta G$ ), which determines the degree of nucleation, can be defined by the following equation.

$$\Delta G = \frac{4a^3}{27(\Delta g)^2} - a - \Delta g \quad (131)$$

Substituting for  $\Delta g$  and rearranging give the following:

$$\Delta G = \frac{\Delta G_0}{\left(1 + \frac{\delta g}{\delta g_0}\right)^2} \quad (132)$$

Ziabicki and Jarecki (1985) proposed estimating the nucleation rate from the Gibb's free energy using the following equation:

$$\dot{N} \approx c \exp\left(\frac{-\Delta G}{kT}\right) \quad (133)$$

where  $c$  is an unknown constant and  $k$  is the Boltzmann constant. Equation (133) indicates that stress-induced orientation enhances nucleation, and therefore crystallization.

### 5.3.1.2 Orientation in Polyethylene Films

A large number of studies have considered the effect of film blowing or casting processing conditions on crystallization and orientation. Bunn (1939) compared X-ray diffraction patterns of branched polyethylene and proposed the first model to describe the molecular orientation. He concluded that the unit cell is orthorhombic and that the chain axis lies along the crystallographic c-axis. Keller (1955) and Keller and Sandeman (1955)

investigated the orientation in polyethylene for hot-drawn polyethylene tubes and suggested two models, based on observations from X-ray diffraction patterns and infrared spectroscopy. The first model (row structure model) is a structure where the crystallographic  $b$ -axis is oriented perpendicular to the draw direction (or in our case machine direction), and the  $a$ - and  $c$ - axes were twisting around the  $b$ -axis. The second model is a structure where the crystallographic  $c$ -axis is mainly oriented parallel to the draw direction. This model was called  $c$ -model. They used the area under the peaks shown in the FTIR spectra to measure the orientation. The  $730\text{ cm}^{-1}$  band indicates the level of crystallographic  $a$ -axis orientation, the  $720\text{ cm}^{-1}$  band indicates the level of the crystallographic  $b$ -axis orientation, and the  $724\text{ cm}^{-1}$  band indicates the level of the amorphous orientation. Keller and Machine (1976) showed that at high stress, the  $a$ - and  $b$ -axes are oriented perpendicular to the machine direction, while the  $c$ -axis is oriented parallel to the machine direction (the machine direction is the direction of the high stresses). They also showed that at low stresses, the  $a$ - and  $c$ - axes were twisting around the  $b$ -axis, and the  $b$ -axis was perpendicular to stress direction. The  $b$ -axis is the growth direction of the stacked lamellae forming due to the crystallization [Desper (1969)]. The  $a$ -axis is usually longer than the  $b$ -axis [Small et al. (2003)]. In the row structure model, the amorphous fractions were oriented perpendicular to the machine direction.

Desper (1969) employed, birefringence, FTIR and X-ray pole figures to investigate the structure and properties of blown polyethylene films. At low cooling rates, he showed that the  $a$ - and  $c$ - axes have equal degrees of orientation parallel to the machine direction. The orientation of the  $a$ -axis in the machine direction increased with increasing cooling rate. He assumed that the growth of crystallites starts from the film surface and proceeds inward, mainly in thickness direction, forming a planar front. Because of the orientations of the  $a$ - and  $b$ -axes, the orientation of the chain axes in the crystalline region is mainly perpendicular to the machine direction [Aggarwal et al. (1959)].

In a study on orientation in polyethylene films made by film blowing and flat casting, Aggarwal et al. (1959) proposed two limiting cases of orientation, shown in Figure 54. Firstly, the  $a$ -axis is mainly oriented in the machine direction and the  $b$ - and  $c$ -



axes are oriented perpendicular to the machine direction. Secondly, the *c*-axis is oriented in the machine direction. Then they employed FTIR and X-ray pole figures techniques to determine which of the two models is the correct one. They found that the *c*-axis was not oriented in the machine direction, supporting the first model. Consequently, the amorphous preferred orientation was in the direction perpendicular to the machine direction.

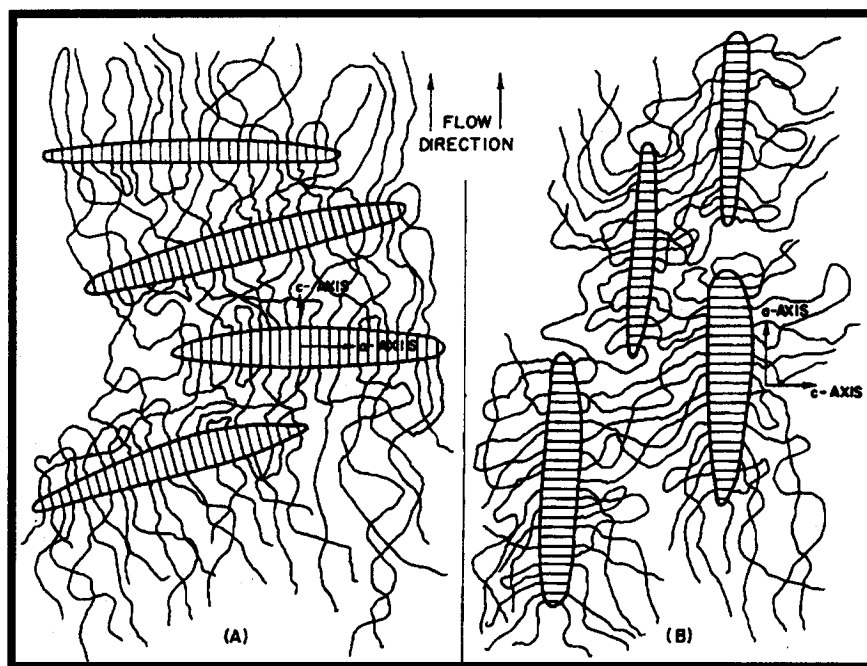


Figure 54: (A) is the *c-model* postulation of the orientation structure. (B) is the *a-model* postulation of the orientation structure. Source: Aggarwal et al. (1959).

Zhang et al. (2004) studied different types of PE (HDPE, LDPE, LLDPE) blown films. They employed FTIR and scanning electron microscopy to show the structural differences between the three types of PE. They reported that HDPE showed *c*-axes orientation in the thickness direction and *a*-axis orientation in the machine direction. The LDPE showed *b*-axis orientation (lamellae growth direction) perpendicular to MD and relatively balanced orientation in the thickness and hoop directions. LLDPE showed spherulite-like superstructure that was not isotropic. LLDPE exhibited small *b*-axis

orientation perpendicular to the machine direction (or the stress direction) and  $a$ -axis orientation in the machine direction. In addition, increasing the take up ratio showed an increase in the  $a$ -axis orientation in most LLDPE samples. Zhang et-al. concluded that the type of orientation exhibited by the films indicated transcrystalline morphology. HDPE had row-nucleated structure with non-twisted lamellae and LDPE had row-nucleated structure with twisted lamellae.

The relationship between the crystallinity and chain orientation in blown films was investigated by various researchers [White and Spruiell (1981), Cole and Ajji (2001), and Krishnaswamy (2000)]. Fourier Transform Infrared (FTIR) analysis is the most common method for measuring chain orientation [Cole and Ajji (2001)]. Orientation is strongly affected by the degree of crystallinity and the magnitude of tensile stress [Keller (1955, 1967)]. White and Spruiell (1981) defined the orientation factors for both the chain axis and the three crystallographic axes (Figure 55). The orientation factors represent the second moments of the biaxial orientation, which were defined as the angles between the crystallographic axes and the film directions (machine, hoop, and thickness). Kissin (1992) employed FTIR and used the Spruiell and White orientation factors (1981) to calculate the orientation in blown films. He compared the results with those obtained using wide-angle X-ray scattering (WAXS) measurements. He assumed that there is no preferential orientation of  $a$ -axis and  $b$ -axis with respect to the machine and transverse directions. He also assumed that the total orientation of the  $c$ -axis in the thickness (normal) direction is small. While Kissin's approach worked well when applied to HDPE, it did not predict the orientation in other types of PE, such as LLDPE. Krishnaswamy (2000) modified Kissin's approach by assuming that the  $a$ -axis and  $c$ -axis have no preferred orientation with respect to the MD and TD and that the orientation of  $c$ -axis is highly perpendicular to MD. Then, he was able to determine the orientation for various HDPE and LLDPE blown films. The difference in the assumptions was based on whether the preferred orientation of the crystallites in the semicrystalline phase of the film was in the direction where the tensile stress was higher. Keller and Machin (1967) reported that in polyethylene films, random or weak orientation of the amorphous chains was encountered when low or intermediate stresses were applied. Most researchers showed

that the crystalline a-axis is more oriented in the machine direction, [Keller and Sandeman (1955), Keller (1967), Desper (1969), Zhang (2001)]. To avoid predetermining the direction of any of the crystallographic axes, Cole and Ajji (2001) assumed that the transition moments have no preferred orientation around the chain axis. Such assumption allowed determination of the biaxial orientation with better accuracy for several types of polymers under various processing conditions.

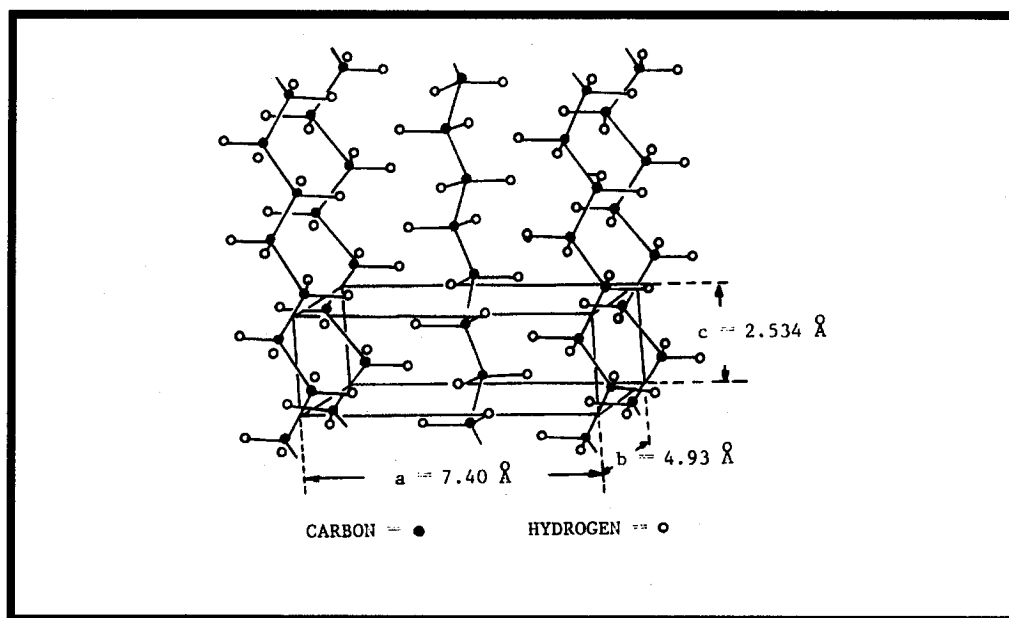


Figure 55: Crystallite structure of polyethylene [Samuels (1973)].

## 5.3.2 Experimental

### 5.3.2.1 Materials

The study involved blown films based on five different polyethylene resins. The properties of the resins are shown in Table 11. The data related to the relevant material and processing parameters have been reported in Tables 3-5. Some additional information regarding the processing conditions is shown in Table 12. Films C587 and C863 were produced from the same resin. The main difference was in the die gap employed. Nova Chemicals (Alberta, Canada) supplied all films. The rheological properties of the resins were obtained from shear dynamic data provided by Nova Chemicals. IRIS software was

used to deduce the values of  $g$ 's,  $\lambda$ 's and the optimum number of Maxwell modes to fit the viscosity profiles for these resins. The deduced data are listed in Table 13.

Table 11: The resin properties for the blown films used in this study, *Kamal (2001)*.

Sample	Comonomer	Reaction Medium / Catalyst	Branching per 1000 carbon atoms	Density (kg.m <sup>-3</sup> )	Mw (g.mol <sup>-1</sup> )	Mw/Mn
<b>C587</b>	Hexene	Gas/Ziegler-Natta	18.87	923	111300.0	3.1
<b>C863</b>	Hexene	Gas/Ziegler-Natta	18.87	923	111300.0	3.1
<b>D582</b>	Hexene	Gas/Metallocene	15.41	919	98000.0	2.2
<b>F751</b>	LDPE	Gas	n/a	919	88000.0	7.3
<b>G583</b>	Octene	Solution/Ziegler-Natta	15.80	920	106000.0	6.2
<b>H866</b>	Butene	Solution/Ziegler-Natta	18.90	919	120000.0	4.8

Table 12: The tested films and related film blowing parameters and processing conditions.

	Sample	BUR	DR	FL	$h_0$ (mm)	$h$ ( $\mu$ m)	$T_0$ ( $^{\circ}$ C)
<b>set 1</b>	<b>C587</b>	2.5	37.0	4.3	2.5	27.0	221
	<b>C863</b>	2.5	12.3	5.9	0.9	29.0	221
	<b>D582</b>	2.5	14.8	4.3	0.89	24.0	220
	<b>F751</b>	2.5	9.0	2.6	1.3	58.0	177
	<b>G583</b>	2.5	13.7	4.3	0.9	26.0	217
	<b>H866</b>	2.5	13.2	5.3	0.9	27.0	222
<b>set 2</b>	<b>C24</b>	2.4	16.1	n/a	0.9	23.0	221
	<b>C26</b>	2.6	14.9	n/a	0.9	23.0	221
	<b>C28</b>	2.8	13.8	n/a	0.9	23.0	221
	<b>C30</b>	3.0	13.5	n/a	0.9	22.0	221
	<b>C32</b>	3.2	12.6	n/a	0.9	22.0	221
	<b>C34</b>	3.4	13.1	n/a	0.9	20.0	221

Table 13: The rheological properties for resins of the blown films tested in this study.

$k$	<b>C587 and C863</b>		<b>D582</b>		<b>F751</b>		<b>G583</b>		<b>H866</b>	
	$\lambda_k$ (s)	$g_k$ (Pa)	$\lambda_k$ (s)	$g_k$ (Pa)	$\lambda_k$ (s)	$g_k$ (Pa)	$\lambda_k$ (s)	$g_k$ (Pa)	$\lambda_k$ (s)	$g_k$ (Pa)
<b>1</b>	<b>0.00297</b>	<b>367500</b>	<b>0.00449</b>	<b>420400</b>	<b>0.00285</b>	<b>67820</b>	<b>0.0044</b>	<b>284300</b>	<b>0.00426</b>	<b>314100</b>
<b>2</b>	<b>0.01985</b>	<b>96020</b>	<b>0.02474</b>	<b>79150</b>	<b>0.02163</b>	<b>15930</b>	<b>0.0277</b>	<b>60110</b>	<b>0.03192</b>	<b>74880</b>
<b>3</b>	<b>0.08145</b>	<b>31630</b>	<b>0.09753</b>	<b>17240</b>	<b>0.09539</b>	<b>7944</b>	<b>0.1171</b>	<b>18830</b>	<b>0.1698</b>	<b>20920</b>
<b>4</b>	<b>0.3313</b>	<b>7597</b>	<b>0.6456</b>	<b>979.3</b>	<b>0.404</b>	<b>3788</b>	<b>0.4867</b>	<b>4766</b>	<b>0.9136</b>	<b>4266</b>
<b>5</b>	<b>1.485</b>	<b>1287</b>	<b>9.057</b>	<b>21.69</b>	<b>1.718</b>	<b>1539</b>	<b>2.096</b>	<b>928.2</b>	<b>5.06</b>	<b>642.1</b>
<b>6</b>	<b>9.16</b>	<b>142.2</b>			<b>7.566</b>	<b>445.3</b>	<b>11.41</b>	<b>134.4</b>	<b>41.66</b>	<b>58.31</b>
<b>7</b>					<b>75.54</b>	<b>36.96</b>				

### 5.3.2.2 Differential Scanning Calorimetry (DSC)

DSC is widely used to measure the absolute crystallinity. The heating experiment yields melting curves that measure heat flow as a function of time. The amount of absolute crystallinity ( $X$ ) is estimated by dividing the trace area ( $A$ ) under the melting curve by the specific heat of melting ( $\Delta H_f$ ).

#### 5.3.2.2.1 Apparatus

A Pyris-1 differential scanning calorimeter (Perkin-Elmer, Wellesley, MA, USA), equipped with a data acquisition computer system and software, was employed to carry out the DSC experiments. Ice was used as the cooling medium. The computerized output shows melting and cooling curves and associated data regarding onset and peak melting temperatures, in addition to the area under any specified part of the melting curve.

#### 5.3.2.2.2 Procedure

The procedure to determine the crystallinity of the films was as follows.

1. Three samples were taken from each film to run three experiments on each film. Each sample consisted of several strips from the same film.
2. Two pans having approximately the same weight were selected.
3. Several strips were cut from the film using a sharp knife.
4. The strips were stacked on top of each other in one of the pans, until a minimum weight of 4mg of that sample were obtained. The pan then was sealed. Care was taken to minimize voids between strips.
5. Both pans were loaded in the D.S.C. in the sample holder. The holder was closed and nitrogen flow was started.
6. The programmed sequence of the experiment was set as follows:
  - a. The sample was held at 50°C before heating.
  - b. The sample was heated from 50°C to 180°C at a heating rate of 10 (°C.min<sup>-1</sup>).
  - c. The sample was then held at 180°C for 5 minutes.

- d. The sample was cooled from 180°C to 50°C at a cooling rate of 10 (°C.min<sup>-1</sup>).
  - e. At 50°C, the sample was held for one minute.
  - f. The sample was heated again from 50°C to 180°C at a heating rate of 10 (°C.min<sup>-1</sup>).
  - g. The sample was held at 180°C for 5 minutes then cooled to 50°C.
7. The thermograms were recorded during the entire experiment by the Pyris-1 software.
  8. The traces were separated into two melting trace and one crystallization trace.
  9. Each of the separated traces was analyzed individually, employing the same software to obtain the areas and other relevant data.
  10. In each experiment, the software subtracted the contribution of the empty aluminum pan to the DSC curves.
  11. The base line of each trace was assumed to have a sigmoidal form and was used to separate the heat capacity from the latent heat.
  12. After subtracting the base line from the DSC traces, the absolute crystallinity was calculated according to Equation (134).

$$X = \frac{A(J.g^{-1})}{\Delta H_f(J.g^{-1})} \quad (134)$$

where the value of the latent heat of fusion ( $\Delta H_f$ ) used for polyethylene in this study is 292.6 J.g<sup>-1</sup> [Dole (1967)]. The area ( $A$ ) of the first melting was used to evaluate the effect of the processing conditions on the blown film.

### 5.3.2.3 Birefringence

When polarized light passes through a transparent anisotropic material, the ray follows a path that is directionally dependent. There are two important directions of interest in which the refractive indices are detected: the machine (M) and the transverse (T) directions of the sample. In birefringence experiments, the phase retardation is measured. The phase retardation,  $\delta$ , is proportional to the value of the birefringence,

$\Delta n_{MT}$ . Orientation increases the birefringence [Osswald (1996)], because higher orientation causes stronger polarizability of the chains. When an extensional process is applied to a polymeric melt, the polymer becomes more birefringent [Janeschitz-Kriegl (1983)].

If the material is completely isotropic or the orientation of the polymer chains of that material is completely random, the birefringence will be zero. However, if the tested material is perfectly oriented (fully anisotropic material), the birefringence will have its maximum value,  $\Delta n^o$ , and that value is known as the intrinsic birefringence. The intrinsic birefringence of the crystalline phase,  $\Delta n_c^o$ , is not the same as that of the amorphous phase,  $\Delta n_{am}^o$ . The measured birefringence of a semi-crystalline polymer is an average or global value, which is defined by the following equation [Ward (1997), Janeschitz-Kriegl (1983)].

$$(\Delta n)_{Total} = X\Delta n_c + (1 - X)\Delta n_{am} + \Delta n_f \quad (135)$$

$$f_c = \Delta n_c / \Delta n_c^o \quad (136)$$

$$n_i - n_2 = C(\sigma_i - \sigma_2) \quad (137)$$

$X$  is the crystallinity. The form birefringence,  $\Delta n_f$ , is the noise coming from the phase boundaries, voids in the sample, the deformation of the electric field, and internal stress. This term is usually negligible [Ward (1997), Macosko (1999)]. The ratio between the measured birefringence and intrinsic birefringence defines the average orientation of the polymer chain.  $C$  is the stress optical coefficient.  $(\Delta n)_{Total}$  is determined by considering that the intensity of the light emerging from the analyzer is proportional to the square of the amplitude of the light wave [Lee (1950), Dally and Riley (1991)], as follows:

$$I = k \cdot \sin(2\alpha) \cdot \sin^2(\Delta n \cdot \pi h / \lambda) \quad (138)$$

where “ $I$ ” is the light intensity, “ $k$ ” is a proportionality constant, “ $h$ ” is the sample thickness,  $\lambda$  is the light wavelength, and “ $\alpha$ ” is the angle between the principal direction

(MD) and the axis of polarization. When extinction is reached, a dark fringe is seen indicating that the intensity of the light is zero, which means that:

$$\frac{h\Delta n}{\lambda} = 0, 1, 2, 3, \dots$$

### 5.3.2.3.1 Apparatus

#### The Polarized Light Microscope

The polarized light microscope employed in this study was Olympus System Microscope, Model BX50 supplied by Olympus America Inc., Melville, New York, U.S.A. The microscope was equipped with a polarizing rotatable stage, rotatable analyzer, compensator adapter, and Iris diaphragm. A 45mm green filter (IF550) was placed on the light source at the base of the microscope to obtain the best light resolution. The light source supplied *e-line* light with a wavelength ( $\lambda$ ) of 546.1 nm.

#### Rotatable Analyzer

The analyzer was U-AN360P, supplied by the same manufacturer as above. It was installed in the analyzer slot of the microscope. It had a rotating dial, which was used to estimate the phase retardation.

#### Compensators

Three different compensators were used for measuring the retardation in the samples of the blown films. The three compensators, which are listed in Table 14, were supplied by the manufacturer of the microscope.

Table 14: The measuring range of the compensators,  $\lambda = 546.1$  nm (*e-line*).

Compensator	Range
Thick Berk (U-CTB)	0-20 $\lambda$
Berk (U-CBE)	0-3 $\lambda$
Senarmont (U-CSE)	0-1 $\lambda$



### 5.3.2.3.2 Procedure

- 1) Five samples were taken from each blown film. Each sample was cut from different position using a sharp knife. The machine direction was indicated on each sample. The samples were cut from positions away from the edges of the film to avoid the end effects.
- 2) Before placing the sample on the stage, the polarizer and the analyzer were set at right angle to each other.
- 3) The compensator was engaged in the light path.
- 4) The sample was placed on the rotating stage of the microscope.
- 5) The stage was rotated until extinction was obtained. Extinction was obtained when the sample was seen as a completely dark object.
- 6) From the extinction position, the stage was rotated 45°.
- 7) In the case of the U-CSE compensator, the analyzer was rotated until total extinction was reached. The angle at this position, by which the analyzer was rotated, was noted, to be used to calculate the retardation from the following equation:

$$retardation = \frac{546 \times |\theta - \theta_0|}{180} \times 10^{-9} (m)$$

where  $\theta_0$  is the extinction angle without the sample, and  $\theta$  is the extinction angle after placing the sample on the stage.

- 8) In the case of employing (U-CTB) and (U-CBE) compensators, the compensator was rotated until black fringes were seen in the view. The angle of rotation at which the black fringes were seen was noted, to be employed in calculating the retardation using the following equation:

$$retardation = \frac{2\pi \left[ \sqrt{1 - \sin^2 \theta / \omega^2} - \sqrt{1 - \sin^2 \theta / \varepsilon^2} \right]}{\frac{1}{\varepsilon^2} - \frac{1}{\omega^2}}$$

where  $\pi$  is the compensator invariable, and  $\omega$  and  $\varepsilon$  and are the refractions of the ordinary and extraordinary rays, respectively. These values are listed in Table 15, and were provided by the same manufacturer.

Table 15: Constants of the compensators.

		<i>e-line (<math>\lambda = 546.1 \text{ nm}</math>)</i>
U-CBE	$\varepsilon =$	1.37859
	$\omega =$	1.39043
	$\pi =$	7414.34
U-CTB	$\varepsilon =$	1.66158
	$\omega =$	1.48762
	$\pi =$	5677.96

9) The birefringence was then calculated as follows:

$$\Delta n_{13} = \frac{\text{retardation}}{\text{thickness}}$$

10) Each sample was measured twice with each one of the compensators.

### 5.3.2.4 FTIR Experiments

Fourier Transform Infrared analysis, commonly known as (FTIR), is the simultaneous measuring of all infrared frequencies when an infrared ray passes through a material by using an optical device called an interferometer. The analyzed material is scanned in the interferometer. The interferometer produces encoded signals, which are decoded via the Fourier transformation mathematical technique. This transformation is presented as the final spectral data, which are used for characterization analysis. When a polarizer is engaged to control the direction of polarization of the infrared ray, then a polarized infrared is produced and a different spectrum is obtained at each polarization angle when an anisotropic sample is tested. Using these spectra in some mathematical

formulations gives information about the level of anisotropy or, in other words, the degree of orientation of particular structural units that exist in the tested sample.

In this work, the tested materials are samples of blown polyethylene films, and the structural units are the conventional crystallographic  $a$ ,  $b$ , and  $c$  axes of the crystallites in the crystalline phase, and the chain axis in the amorphous phase in the sample. The orientation of the axes is defined with respect to the macroscopic directions of the sample: the machine direction (1 or M), the transverse direction (3 or T), and the thickness direction (2 or N). The polarization direction of the IR beam is defined with respect to the machine direction. Therefore, the polarization is parallel when the polarized ray is set to be parallel to the machine direction of the sample, and the polarization is called perpendicular when the polarized ray is set to be parallel to the transverse direction of the sample.

For an anisotropic material, the spectra depend on the polarization direction because the material absorbs different amounts of the ray in each direction. Each spectrum represents the absorbance of the ray for all frequencies. When the IR ray radiates toward the sample at some intensity ( $I_o$ ), a fraction of that ray is absorbed and the rest transmits at a lesser intensity ( $I$ ). The absorbance is related to these intensities by the following equation [Ward, (1997)]:

$$A = \log((\mu E)^2 \frac{I}{I_o}) \quad (139)$$

where  $E$  is the electromagnetic vector of the polarized ray, and  $\mu$  is the transition moment vector. The absorption takes place when the IR radiation causes infrared-active vibrational motion to particular molecules of the polymer chain [Ward, (1997)]. These vibrations take place in a particular direction, which is called the transition moment axis, only when the IR-ray and the transition moment have the same frequency and direction [Ward (1997)]. Figure 56 shows the assumed configurations of the polymer chain axis and its transition moment with respect to the directions of the sample.

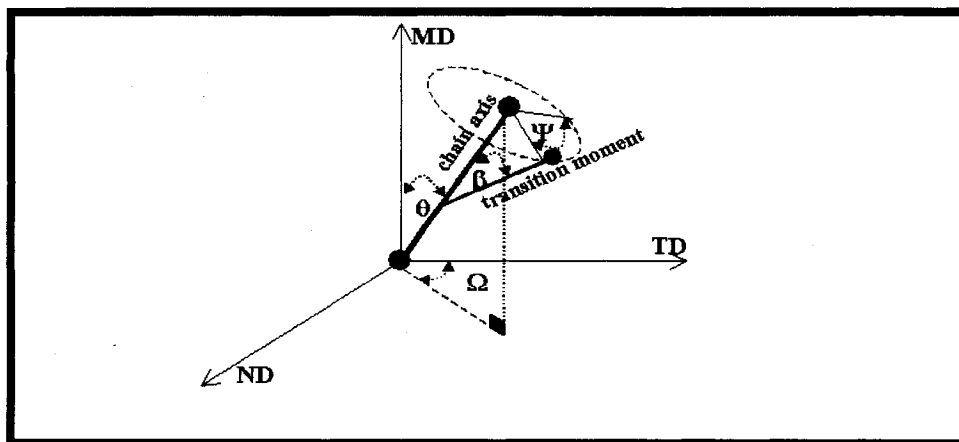


Figure 56: A schematic of the orientation of the chain axis and its transition moment with respect to the sample directions.

For any material, the absorption peaks can be measured at well-known wave frequencies (bands) at different polarization directions. The location of these peaks is associated with particular transition moments. The intensity of these peaks varies when the polarization direction is changed. The most used set-up is the parallel and perpendicular polarized IR with respect to the machine direction of the sample. Once these two spectra are known, the dichroic ratio ( $D_c$ ) can be calculated by dividing the parallel absorbance ( $A_{||}$ ) by the perpendicular absorbance ( $A_{\perp}$ ) at the same frequency. Once the dichroic ratio is known, the Herman orientation functions of the chain axis with respect to the machine direction can be calculated [Ward (1997)].

The value of the Herman's orientation function,  $f$ , can be obtained from more general relationships that account for biaxial or poly-axial stretching of the film. These relationships are based on statistical functions that describe the distribution of the orientations of the structural units, which may be written in terms of the three Euler angles [Jarvis, (1980)]. Karacan (1993) showed how one could employ Jarvis' relationships to obtain information about the orientation of polymer chains in polypropylene films. The same method is implemented in this work to obtain the orientation of the crystallographic axes in the crystallized phase and orientation of the chains in the amorphous phase for several samples of blown polyethylene films. Jarvis' method is widely used and it is summarized in the following discussion.

After the absorbances  $A_M$ ,  $A_T$ , and  $A_{MN}$  are experimentally measured, the values of the imaginary parts of the refractive indices  $k_i$  are calculated by the following equations:

$$k_i = \frac{A_i}{4\pi h \lambda \log_{10} e} \quad (140)$$

$i = M, T, \text{ or } N$

where  $h$  is the thickness of the sample, and  $\lambda$  is the wavelength at which the relevant peak is observed. Once the values of  $k_i$  are calculated, they are used to calculate the values of  $\phi_m$ ,  $\phi_t$ , and  $\phi_n$ , using the following equation:

$$\phi_i = \frac{6n_i k_i}{(n_i^2 + 2)^2} \quad (141)$$

where  $n_i$  are the refractive indices in the  $i$  direction. The orientation averages are calculated using the following equations:

$$\frac{2\phi_M - \phi_T - \phi_N}{\phi_M + \phi_T + \phi_N} = 2P_{200}(\beta)P_{200} + 4P_{200}(\beta)P_{222} - 4P_{202} \quad (142)$$

$$\frac{\phi_T - \phi_N}{\phi_M + \phi_T + \phi_N} = 4P_{200}(\beta)P_{220} + \frac{4}{3}P_{200}(\beta)P_{222} - \frac{4}{3}P_{222} \quad (143)$$

To solve the above two equations, the transition moment angles ( $\beta$ ) for the parallel peaks are assumed to be zero, which reduce the equation to the following:

$$\frac{2\phi_M - \phi_T - \phi_N}{\phi_M + \phi_T + \phi_N} = 2P_{200} \quad (144)$$

$$\frac{\phi_T - \phi_N}{\phi_M + \phi_T + \phi_N} = 4P_{220} \quad (145)$$

Also, for the perpendicular peaks, the transition moment angles ( $\beta$ ) are assumed to be  $90^\circ$ , which reduces the same equations to the following forms:

$$\frac{2\phi_M - \phi_T - \phi_N}{\phi_M + \phi_T + \phi_N} = -(P_{200} + 6P_{202}) \quad (146)$$

$$\frac{\phi_T - \phi_N}{\phi_M + \phi_T + \phi_N} = -2(P_{220} + P_{222}) \quad (147)$$

$P_{lmn}$  are the expansion coefficients (moments) of the probability distribution function of finding a structural unit oriented within the generalized solid angle. The expansion coefficient are equal to the average value of the spherical harmonic functions,  $p_{lmn}$ , taken over the distribution function [Karacan (1993), Ward (1997)].  $P_{200}$  is the average over the second-order Legendre polynomial.  $P_{202}$  indicates the preferred orientation of the chains around their own axes.  $P_{220}$  is a measure of the departure from uniaxial symmetry of the chain axis distribution.  $P_{222}$  is a combined measure of the level uniaxial orientation and orientation of the chains around their own axes.

In the case of polyethylene films, the peaks of interest are located at frequencies  $720 \text{ cm}^{-1}$  and  $730 \text{ cm}^{-1}$ , which are decomposed, using nonlinear regression, to three well-defined peaks:  $719 \text{ cm}^{-1}$ ,  $724 \text{ cm}^{-1}$ , and  $730 \text{ cm}^{-1}$ . The peak  $719 \text{ cm}^{-1}$  arises due to the absorbance of the transition moment that is parallel to the crystallographic b-axis in the crystalline phase. The transition moment that is parallel to the a-axis shows an absorbance peak at  $730 \text{ cm}^{-1}$ , and the transition moment that is perpendicular to the chain axis in the amorphous phase give rise to the  $724 \text{ cm}^{-1}$  peak. Since all of the above transition moments are perpendicular to the polymer chain, there is not enough information to solve all of the above equations. However, it is assumed that the transition moments have no preferred orientation around the chain axis, thus the Euler angle,  $\psi$ , is randomly distributed, which nulls  $P_{202}$  and  $P_{220}$  [Cole and Ajji (Ward 1997)].

The refractive indices do not change significantly with the polarization direction. Therefore, Cole and Ajji [Ward (1997)] assumed  $\Phi_i = A_i$ . They also assumed that the absorbance, when the sample is tilted at angle 45 degree, can be obtained by the following equation:

$$A_N = \frac{\cos \alpha}{\sin^2 \alpha} (A_{MN} - A_M \cos \alpha) \quad (148)$$

$$\sin \alpha = \frac{\sin 45}{n} \quad (149)$$

where  $\alpha$  is the angle, at which the ray passes through the sample because of the refraction.. The structural absorbance that corresponds to an unoriented sample is defined as follows:

$$A_o = \frac{A_M + A_T + A_N}{3} \quad (150)$$

Then, Cole and Ajji [Ward (1997)] calculated the Herman orientation functions of a given axis “*i*” with respect to sample direction “*j*” by employing the following equation:

$$f_{ij} = \frac{1}{3 \cos^2 \gamma_{ij} - 1} \left( \frac{A_j}{A_o} - 1 \right) \quad (151)$$

where  $\gamma_{ij}$  is the angle between the molecular axis of interest, *i* (which could be *a*, *b*, or *c*), and any sample direction, *j* (which could be M, T, or N). When both methods of Jarvis et al. (1980) and Cole and Ajji (1997) were employed, both produced the same results.

#### 5.3.2.4.1 Apparatus

Bomem-Michelson spectrometer, Model 100 (ABB Bomem Inc., Quebec, Canada), in conjunction with Perkin-Elmer gold wire-grid polarizer, was employed to perform the polarized infrared measurements. It has a scanning frequency range of  $6000 - 200 \text{ cm}^{-1}$ , with resolution of  $4 \text{ cm}^{-1}$ . 50 scans were conducted for each sample. The sample holder was designed to permit tilting of the sample  $45^\circ$  with respect to the horizontal and vertical planes. The spectrometer was connected to a computer for data acquisition and analysis.

The wire-grid polarizer has a polarizing element which is a gold wire-grid vapor-deposited on silver bromide substrate. The parallel-polarized spectra were obtained with

the polarization direction parallel to the machine direction, and the perpendicular polarized spectra were obtained with the polarization direction parallel to the transverse direction of the sample. Tilting the sample  $45^\circ$  with respect to the direction of the parallel-polarized IR (as shown in Figure 57) made it possible to collect the  $45^\circ$  spectra.

#### 5.3.2.4.2 Procedure

- 1) The infrared spectrometer was turned on for 4 hours before running the test.
- 2) The polarizer was inserted in the sample holder and placed in the desired direction (parallel to MD or TD).
- 3) The background was scanned.
- 4) The film sample was inserted between the polarizer and the detector on the sample holder.
- 5) The experiments were carried out using the three different configurations illustrated in Figure 57.
- 6) The spectra for each of the above configurations were collected, individually, by the Bomem data acquisition program.
- 7) These spectra were processed later by the Sigma Plot software to subtract the base line and to decompose the spectra to three well-defined peaks. These three peaks are described in the Table 16.

Table 16: Peaks of interest in polyethylene films.

Peak number	Origin of contribution	Configuration of the transition moment
$719\text{ cm}^{-1}$	$\text{CH}_2$ group, rocking	Parallel to the crystallographic b-axis in the crystalline phase
$724\text{ cm}^{-1}$	$\text{CH}_2$ group, rocking	Perpendicular to the chain axis in the amorphous phase
$730\text{ cm}^{-1}$	$\text{CH}_2$ group, rocking	Parallel to the crystallographic a-axis in the crystalline phase



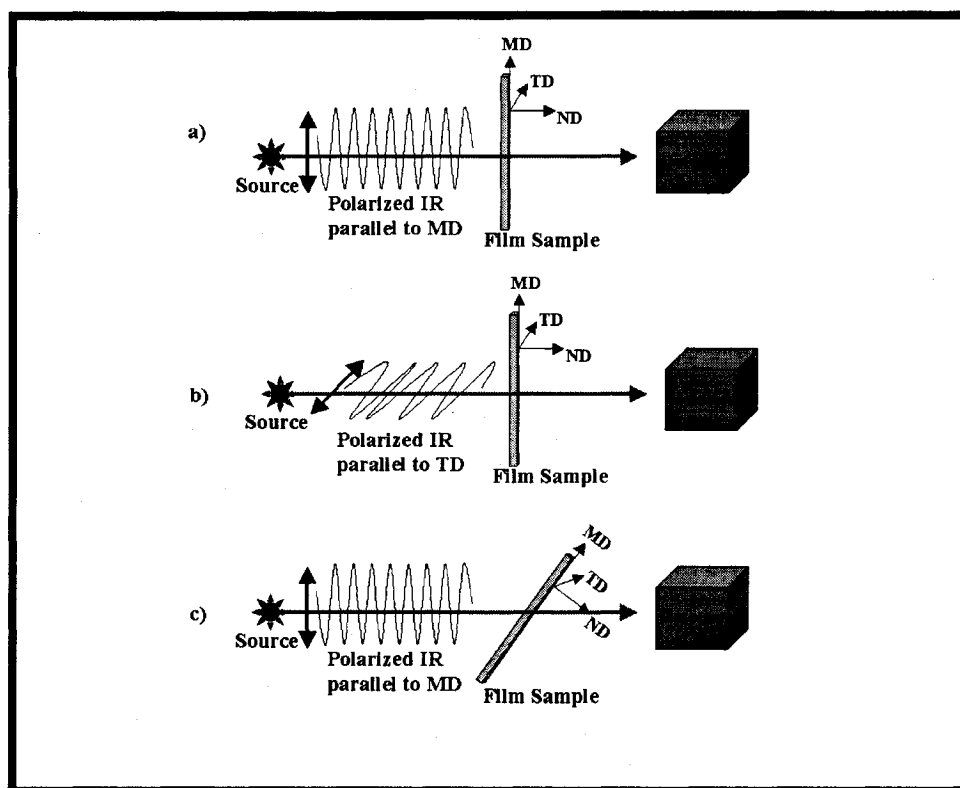


Figure 57: The polarized IR in parallel position to the MD (a), parallel to TD (b), and 45° position (c).

### 5.3.3 Results and Discussion

The results of the crystallinity experiments are compared with the predicted absolute crystallinity by the simulation. The DSC experiments are combined with the birefringence results and the amorphous orientation is predicted by the simulation to estimate the orientation of the crystallographic c-axis. The estimated orientation is then compared with the measured c-axis orientation. The orientation of all crystallographic axes and amorphous chains was determined by the FTIR method.

#### 5.3.3.1 Effects of Blow-up Ratio and Draw Ratio

The areas of the two endothermic melting traces and the exothermic crystallization traces are shown in Table 17. The value of the first heat of melting ( $\Delta H$ ) is of interest in this study, since it represents the heat released as a result of melting the crystalline phase that was formed during the film blowing process. The standard

deviation in the collected measurements for the first melting peak is larger than that for the second melting. The larger standard deviation might be due to the stacking of the strips in the pan, which could create voids filled with air in the tested samples. The second melting peak gave information about the crystallinity of the resin. All stresses were relaxed during the first melting.

The crystallinity values based on the first melting are shown in Table 17. The effects of processing conditions and resin properties on the bubble shapes are shown in Figure 59. The evolution of crystallinity for these systems is shown in Figure 60. The differences between the crystallinity that were calculated from the first melting peak and those calculated from the second melting peak were not significant for samples C587, C863, D582, F751, G583, and H866. The situation is somewhat different for the films obtained from resin C at different blow-up ratios. Here, there are significant differences in the crystallinity obtained in the first and second melting. While the role of orientation-induced crystallization may not be ruled out, it can be seen from Figure 58 that the process residence time due to the change in velocity may play an important role. It should be noted that films C24-C34 are made from a modified C resin, which is different from that employed in resin C863.

In preparing films C24-C34, the blow-up ratio was increased continuously and the draw ratio was decreased, which most likely caused the cooling rate to be decreased, as shown in Figure 58. In Figure 58, the lower x-axis indicates the process time, which was calculated as follows:

$$time = \frac{r_0}{v_0} \int \frac{dz^*}{v^*} \quad (152)$$

$r_0$  and  $v_0$  are the initial tube radius and velocity at the die exit.  $v^*$  is the dimensionless velocity of the film and  $z^*$  is the dimensionless distance from the die exit.

Table 17: The measured crystallinity from DSC spectra. The processing conditions at which the films were manufactured are listed in Table 12.

Film	weight mg	The Trace of the First Melt			The Second Melt			The Crystallization Trace			Density g.cm <sup>-3</sup>	Predicted Absolute Crystallinity
		$\Delta H$ J.g <sup>-1</sup>	Absolute Crystallinity	Standard Deviation	$\Delta H$ J.g <sup>-1</sup>	Absolute Crystallinity	Standard Deviation	$\Delta H_c$ J.g <sup>-1</sup>	Absolute Crystallinity	Standard Deviation		
C587	4.010	83.64	0.29	0.0086	85.33	0.30	0.0023	75.33	0.26	0.0015	0.923	0.30
C863	4.644	89.41	0.31	0.0143	84.00	0.29	0.0013	76.52	0.27	0.0003	0.923	0.32
D582	4.844	99.00	0.34	0.0173	105.00	0.36	0.0017	70.04	0.24	0.0005	0.919	0.33
F751	6.572	60.57	0.21	0.0042	63.82	0.22	0.0010	63.83	0.22	0.0010	0.919	0.22
G583	5.482	74.99	0.26	0.0143	75.02	0.26	0.0016	88.11	0.31	0.0003	0.920	0.24
H866	5.697	103.83	0.36	0.0115	104.22	0.36	0.0008	83.70	0.29	0.0005	0.919	0.35
C2.4	6.001	77.87	0.26	0.0188	100.79	0.35	0.0008	80.20	0.28	0.0015	0.923	0.27
C2.6	4.640	89.41	0.31	0.0035	99.51	0.35	0.0003	85.61	0.30	0.0034	0.923	0.31
C2.8	5.079	98.06	0.34	0.0151	99.98	0.35	0.0015	84.38	0.29	0.0020	0.923	0.34
C3.0	4.700	103.83	0.35	0.0154	101.95	0.35	0.0016	83.33	0.29	0.0052	0.923	0.36
C3.2	4.827	112.48	0.39	0.0257	98.29	0.34	0.0037	80.08	0.28	0.0015	0.923	0.38
C3.4	4.053	115.37	0.40	0.0174	99.58	0.35	0.0011	81.69	0.28	0.0028	0.923	0.40

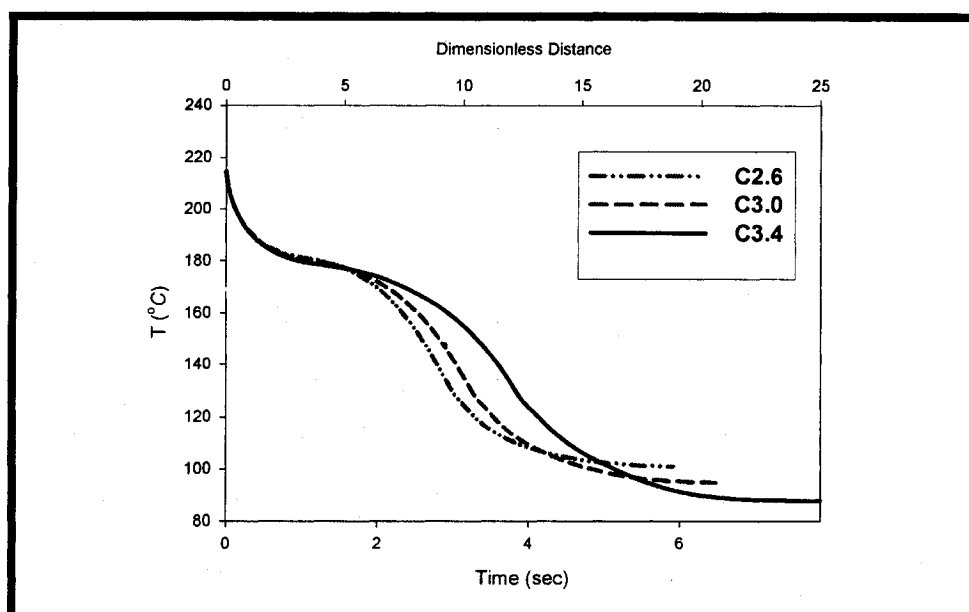


Figure 58: Larger blow-up ratios and smaller draw ratios decrease the cooling rate.

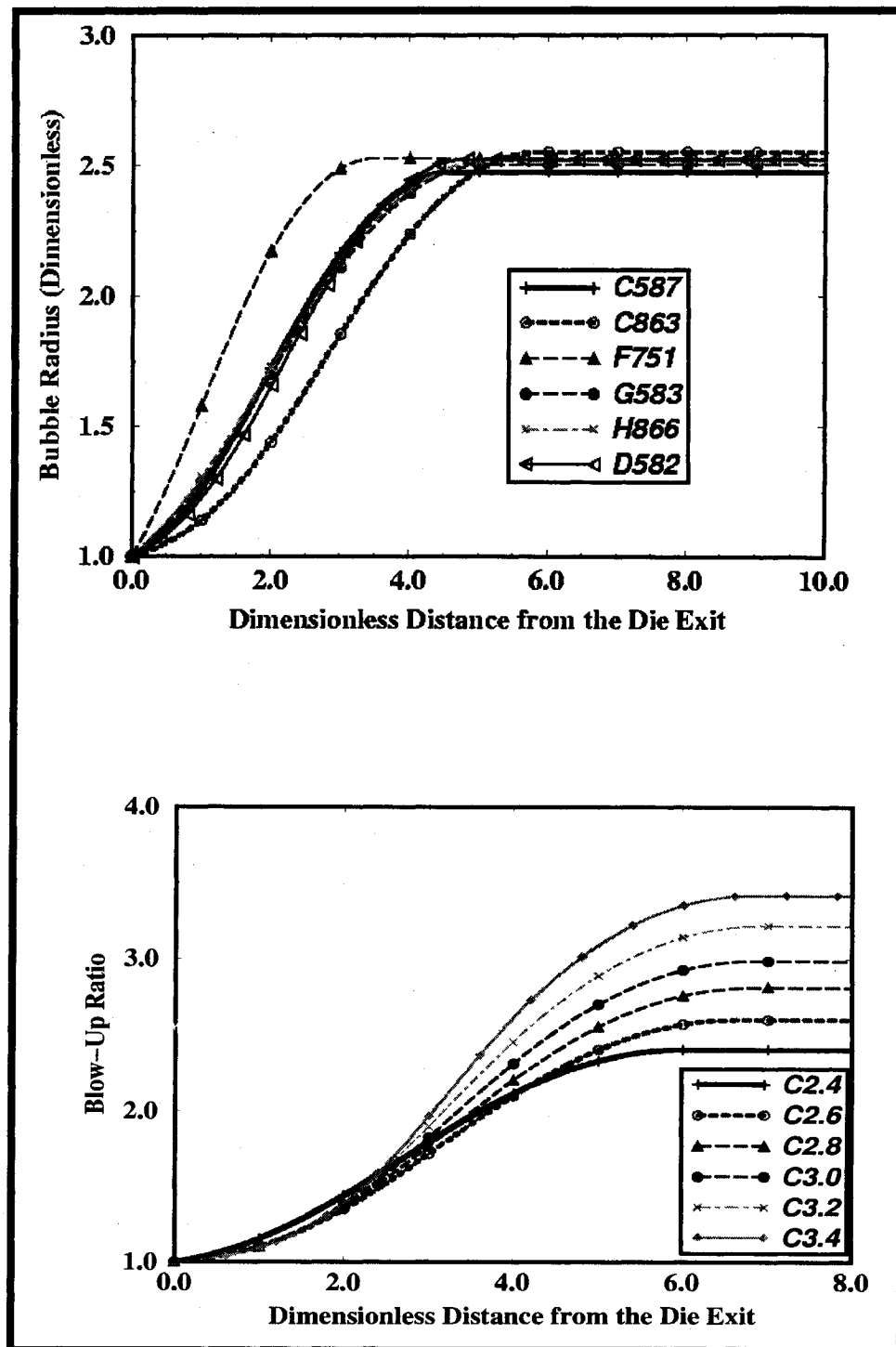


Figure 59: The predicted bubble shapes for the various blown films.

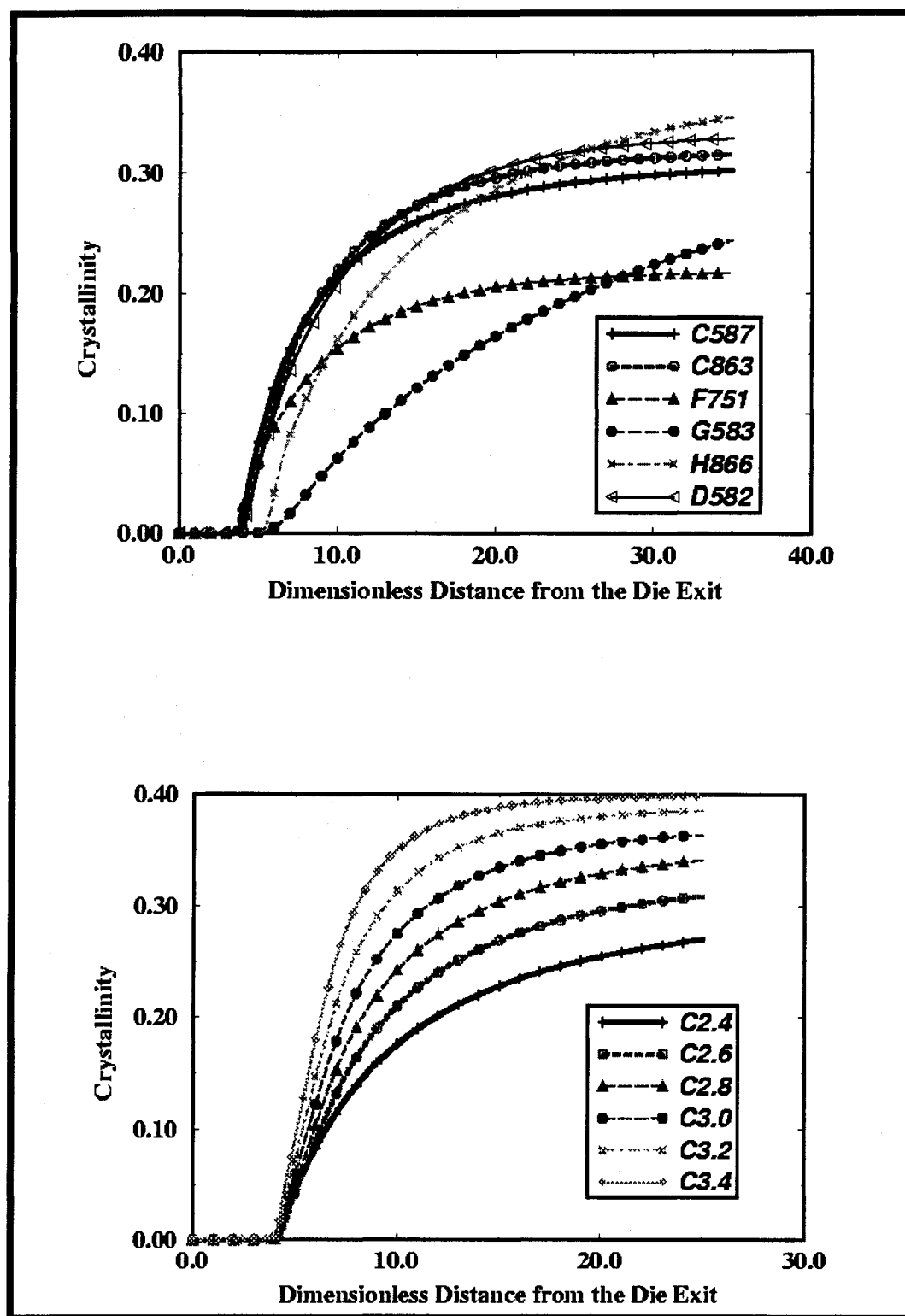


Figure 60: The predicted evolution of absolute crystallinity for the various blown films.

The differences in the properties and bubble shapes of the films produced from different resins cause significant differences in temperature profiles as shown in Figure 61. These differences result in differences in the velocity profiles as shown in Figure 62, and the stress profiles as shown in Figure 63. The differences in the stress and velocity profiles result in significant differences in the thickness reduction profiles, as shown in Figure 64. All these changes cause the measured and predicted chain orientation to vary substantially as will be discussed later. The orientation of the amorphous phase shown in Figure 65 was calculated using the rheoptical law  $n_i = c\tau_i$  and Equation (118). After calculating the refractive index ( $n_i$ ) from the stress ( $\tau_i$ ), the amorphous orientation is calculated using Equation (118).

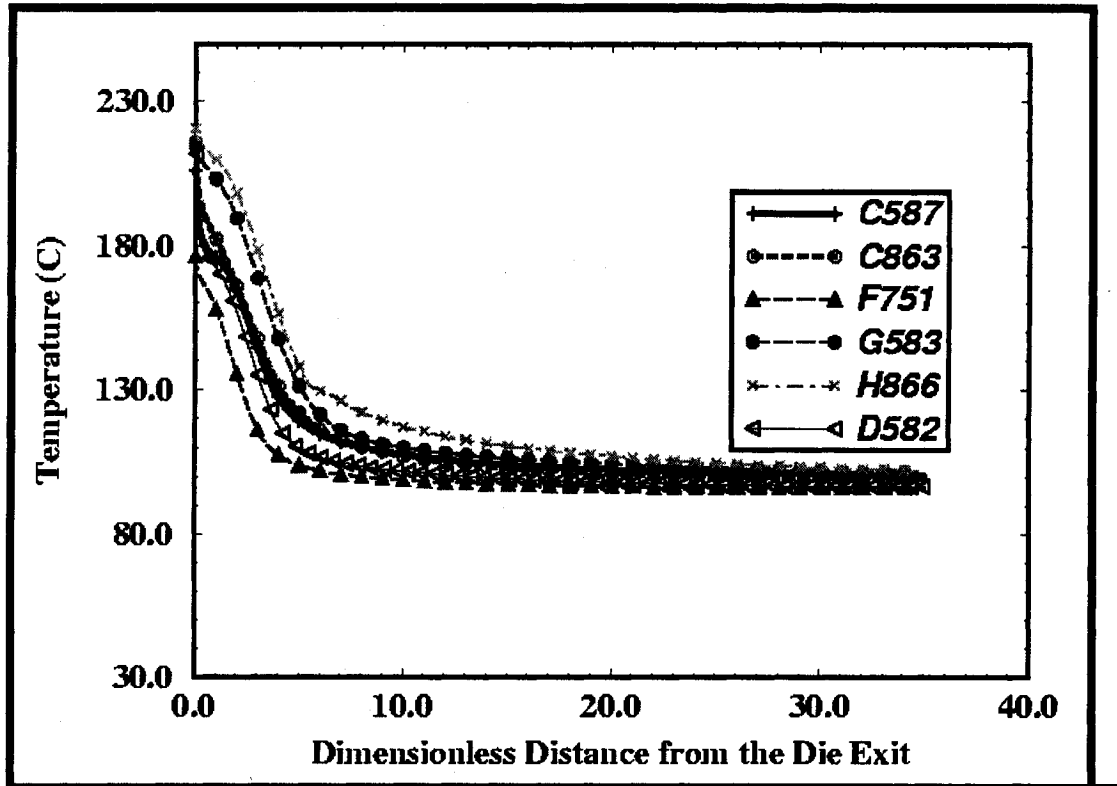


Figure 61: The temperature profile along the machine direction for the various blown films. The processing conditions are shown in Table 12.

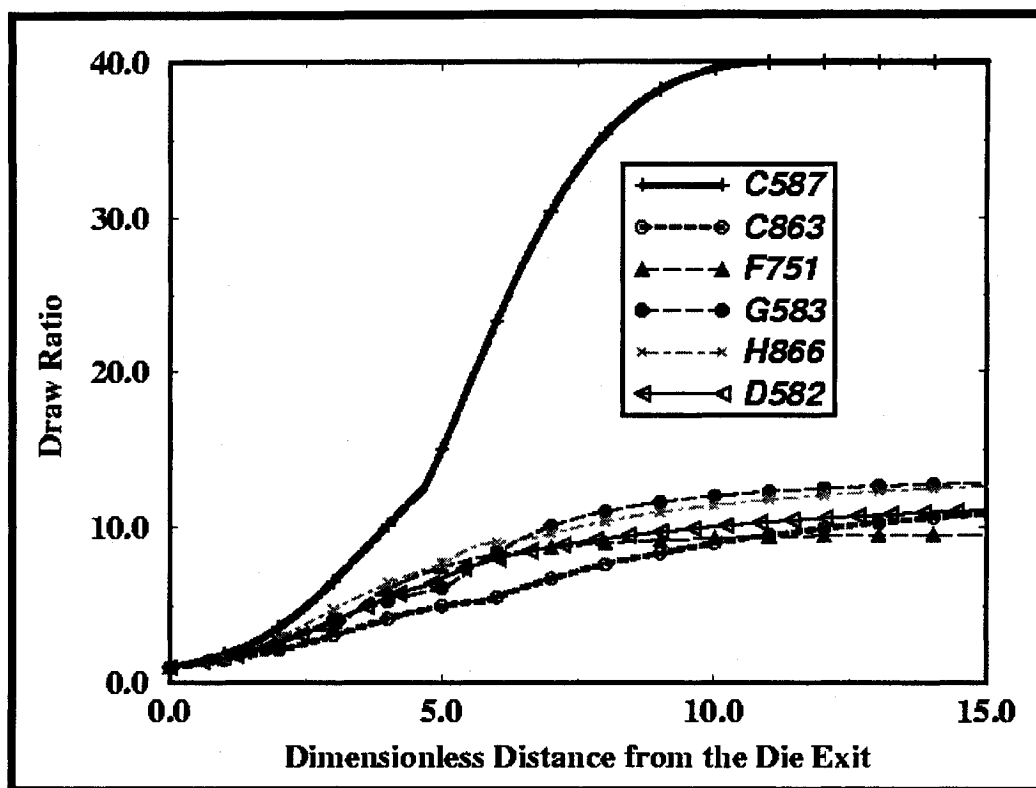


Figure 62: The draw ratio for various films. The processing conditions are shown in Table 12.

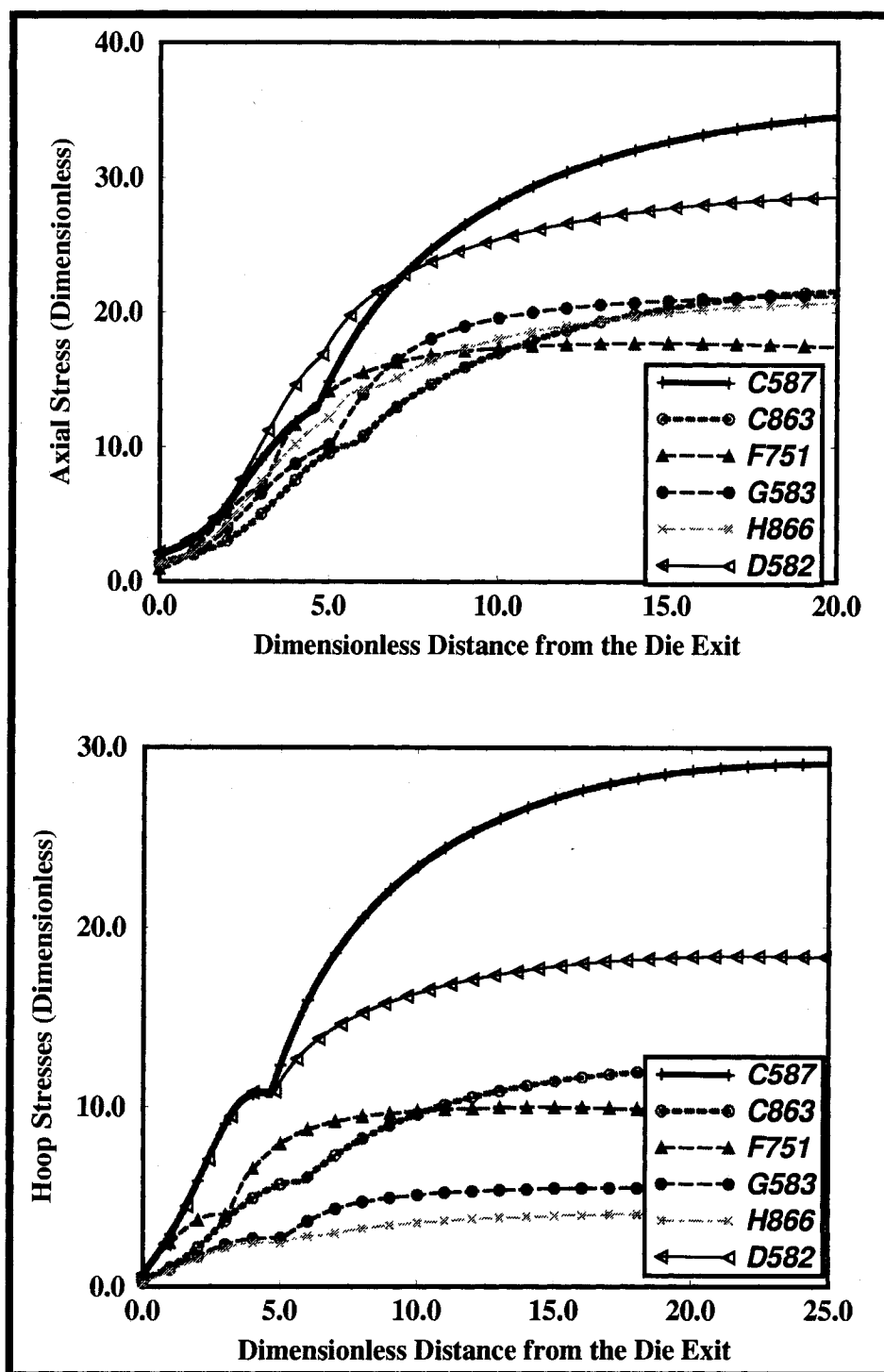


Figure 63: The stress profiles for various films. The processing conditions are shown in Table 12.



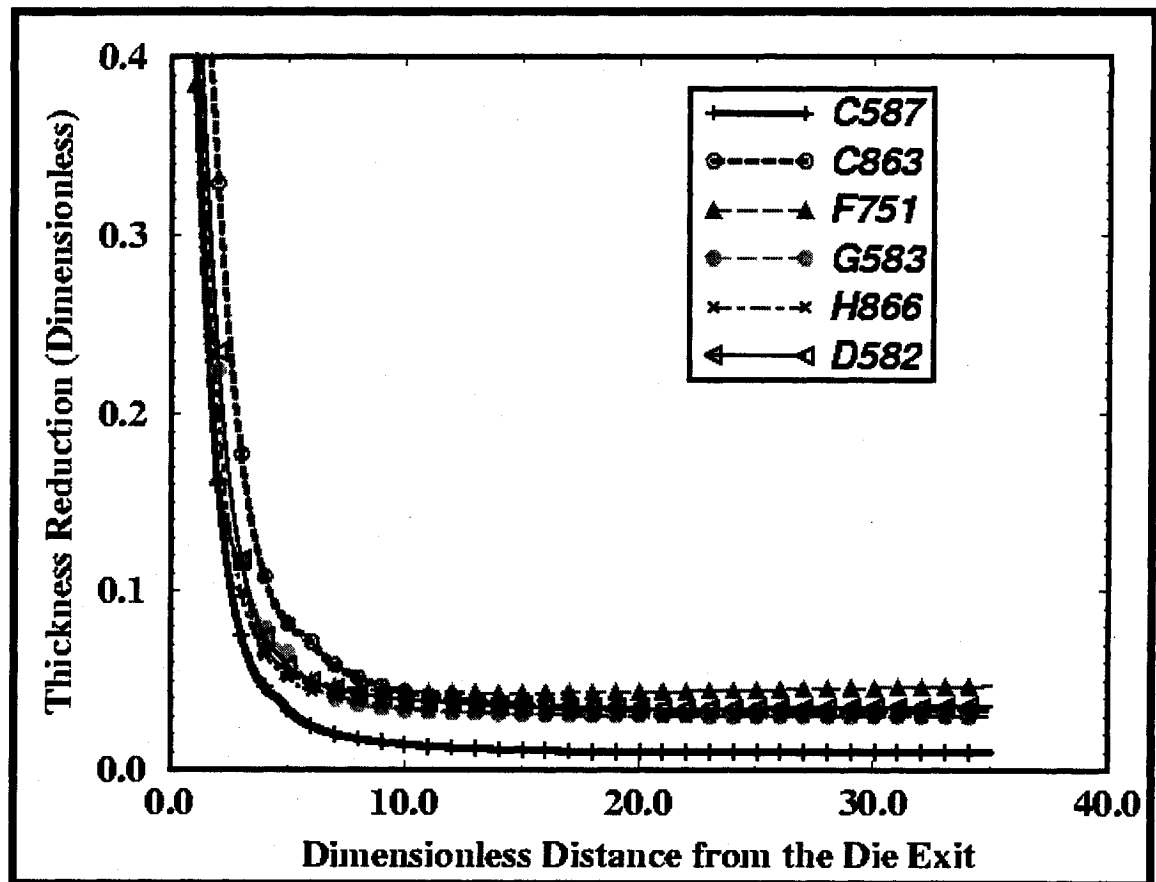


Figure 64: The predicted thickness profiles for various films. The processing conditions are shown in Table 12.

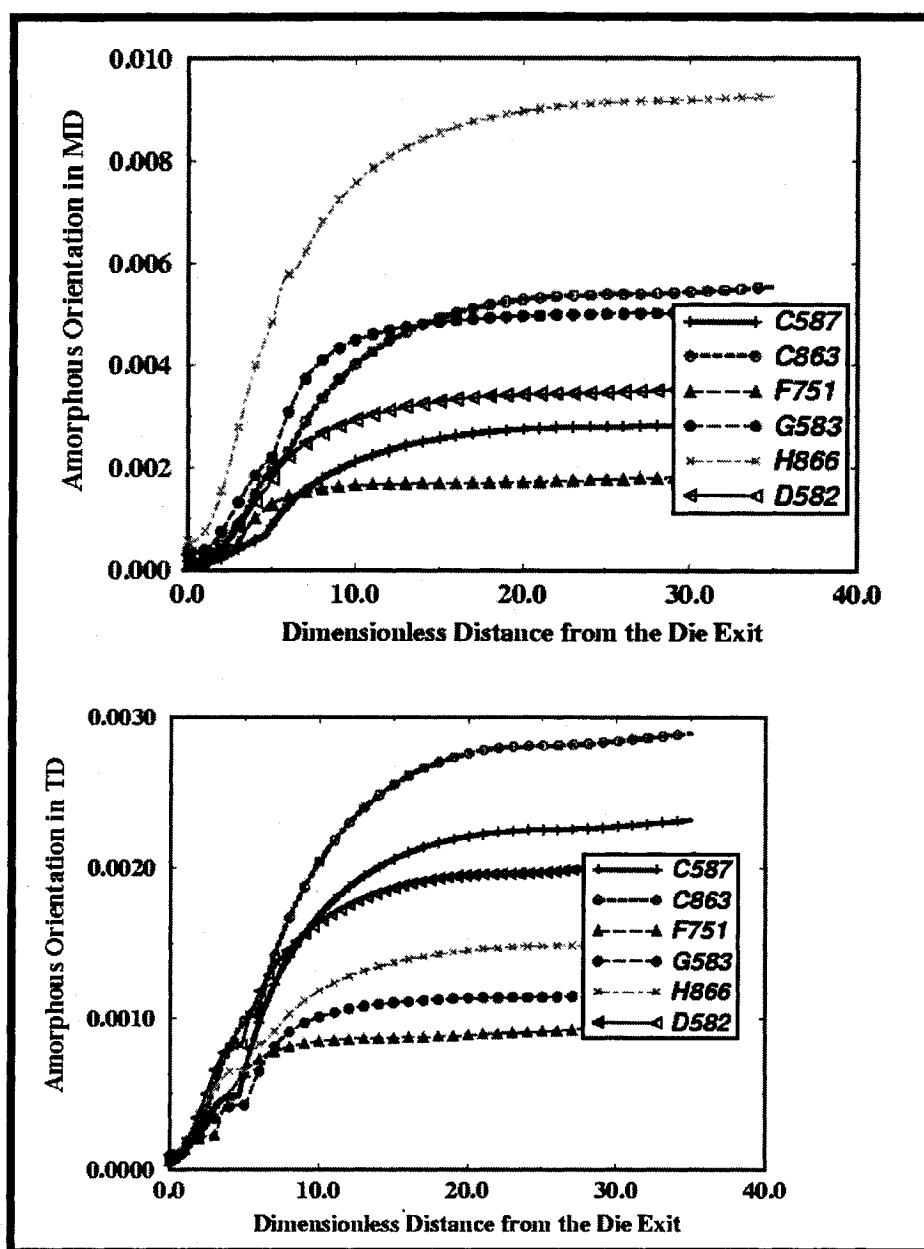


Figure 65: The predicted amorphous orientation for various films. The processing conditions are shown in Table 12.

### 5.3.3.2 Comparison Between the Measured and Predicted Crystallinity

Figure 66 shows good agreement between the predicted and measured crystallinity for all the blown films considered in this study. The proposed film blowing process simulation successfully captured the effects of resin properties and processing conditions on the crystallinity. These films were produced by the film blowing process under the conditions specified in Tables 3-5 and 12. The resin properties are shown in Table 11.

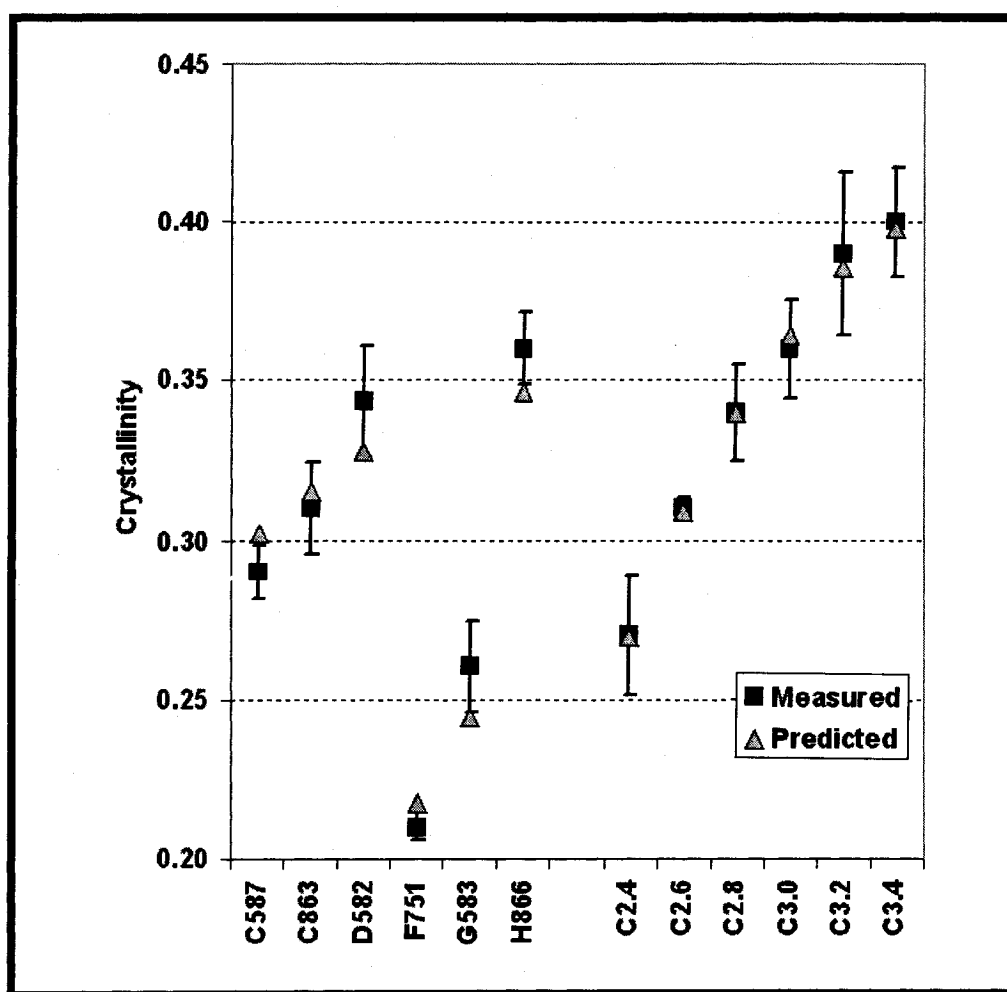


Figure 66: Comparison between the measured (squares with error bars) and predicted (triangles) crystallinity.

### 5.3.3.3 Orientation in the Blown Films

The magnitude of the birefringence is a measure of the biaxial orientation. The implemented experimental set-up allows measuring the in-plane birefringence, which is  $|n_1 - n_3|$ , the difference in the refractive indices between the machine and transverse directions of the sample.

Three compensators were employed to acquire the value of the birefringence and to verify the accuracy of these methods. Figures 67 and 68 show the results obtained for all films that were investigated in this study. There was a strong consistency between the results obtained by employing compensators (CBE) and (CSE). However, compensator (CTB) did not yield the same degree of consistency. The measuring scale of compensator (CTB) was much wider than that of the other two compensators (see Table 14), which means that the other two compensators could provide more precise measurement of the weak birefringence in the films. The level of anisotropy of polyethylene was low, because the orientation was relatively weak, and the crystallinity was not very high. Hence, the birefringence was not very strong. It was easier to see the birefringence in all samples, when the other two compensators (U-CBE) and (U-CSE) were employed.

Figure 67 shows that sample F751 had lower birefringence than most of the samples. Sample F751 was the only LDPE sample, and generally, the magnitude of orientation in LDPE is lower than that in the LLDPE because the degree of long chain branching in LDPE is higher than that in LLDPE. Also, the draw ratio and crystallinity were lower for F751 than those of the rest of the samples. The orientation in sample C587 was higher than the orientation in sample C863, which might be due to the higher draw ratio in the former sample. It could be also because of the effect of the cooling rate. In the former sample, the freeze line was higher, and therefore the cooling rate was lower, thus the crystallites would be larger. Samples G583 and H866 showed higher birefringence than the rest of the samples. Figures 63 and 65 show that the ratios of axial stresses to hoop stresses and the ratios of the machine to transverse orientation are higher for these

films than for the other films. It is interesting to note that both of these resins have higher  $M_w/M_n$  than the rest of the samples.

Figure 67 shows the birefringence variation with respect to the blow-up ratio and draw ratio, in samples C24 to C34. It is clear that the magnitude of the birefringence decreased as the blow-up ratio increased and the draw-ratio decreased. This observation is consistent with the birefringence calculated from FTIR measurements, as shown in the same figure. In general, the measured birefringence was weak for all samples. This might be due to the weak orientation of the amorphous phase, as will be shown later. In any case, there is good agreement between the results of the FTIR and the birefringence methods. Keller and Machin (1967) reported that in polyethylene films, random or weak orientation of the amorphous chains was encountered when low or intermediate stresses are involved. In fact, they attributed the negative birefringence observed in some of their samples to amorphous chain orientation in the transverse direction. This is consistent with our observation that the amorphous chain was randomly distributed between the machine and the transverse directions with slight preference toward the latter. Thus, the birefringence was weak.

We considered that orientation of the crystalline phase is determined by the orientation of the crystalline c-axis with regard to the direction of interest [Keller and Sandeman (1955), Aggarwal et al. (1959)].

1. The FTIR method is used to measure the orientation functions for crystallographic a and b axes in the crystalline phase and the chain axis in the amorphous phase in the machine and transverse directions. The orientation function of the crystallographic c-axis is calculated in each direction as follows:

*In the machine direction*

$$f_{cry,l} = f_{c,l} = -f_{a,l} - f_{b,l} \quad (153)$$

*In the transverse direction*

$$f_{cry,3} = f_{c,3} = -f_{a,3} - f_{b,3} \quad (154)$$

where subscripts a, b, and c indicate the crystallographic axes and subscripts 1 and 3 indicate the machine and transverse directions.

2. The overall orientation function is calculated by assuming that the orientation functions arising from different phases can be added as follows:

*In the machine direction*

$$(f_1)_{overall} = Xf_{cry,1} + (1 - X)f_{am,1} \quad (155)$$

*In the transverse direction*

$$(f_3)_{overall} = Xf_{cry,3} + (1 - X)f_{am,3} \quad (156)$$

The crystallinity value ( $X$ ) was experimentally measured using the DSC.

3. The overall orientation is then used to calculate the birefringence as follows:

$$(n_1 - n_3)_{overall} = \Delta n_0 (f_1 - f_3)_{overall, FTIR} \quad (157)$$

The calculated values of overall birefringence using Equation(157) (estimated from the FTIR) are compared with the overall birefringence measured by the polarized light microscope (PLM) and shown in Figure 67. In the PLM experiments, three different compensators are employed.

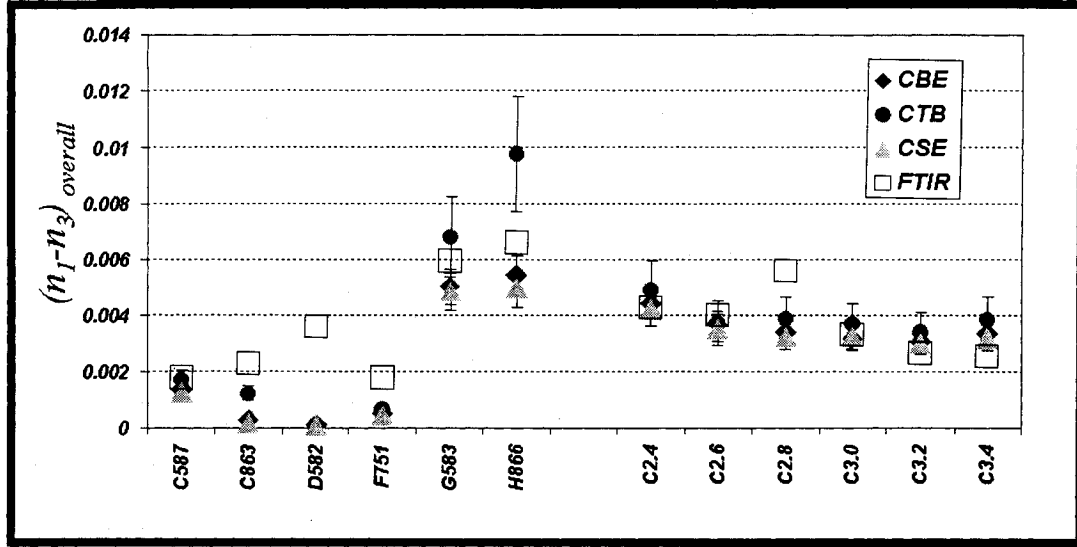


Figure 67: A comparison between the overall birefringence estimated by the FTIR and the birefringence measured by the polarized light microscope (PLM).

4. The FTIR was also employed to estimate the birefringence contribution from the crystalline phase as follow:

$$(n_1 - n_3)_{cry, FTIR-measured} = \Delta n_0 (f_{c,1} - f_{c,3}) \quad (158)$$

where  $f_{c,1}$  is the orientation function of the c-axis in the machine direction and  $f_{c,3}$  is the orientation function of the c-axis in the transverse direction. The orientation functions of the c-axis were calculated using Equations (155) and (156).

5. In the simulation, the calculated stress values in the machine and transverse directions ( $\sigma_1$  and  $\sigma_3$ ) in the final film are employed in the stress-optical relationship to estimate the birefringence as follows:

$$(n_1 - n_3)_{am,model} = 2.6 \times 10^{-9} (\sigma_1 - \sigma_3) \quad (159)$$

6. The birefringence that is calculated using Equation (159) is assumed to be the same as the amorphous contribution ( $\Delta n_{am}$ ).

$$(n_1 - n_3)_{overall, measured PLM} = X(n_1 - n_3)_{cry, estimated} + (1 - X)(n_1 - n_3)_{am, model} \quad (160)$$

$$(n_1 - n_3)_{\text{cry, estimated}} = \frac{(n_1 - n_3)_{\text{overall, measured PLM}} - (1 - X)(n_1 - n_3)_{\text{am, model}}}{X} \quad (161)$$

where  $X$  is the crystallinity measured by the DSC. Equation (161) was employed to estimate the birefringence contribution of the crystalline phase from data collected with each compensator. Figure 68 compares  $\Delta n_{\text{cry, estimated}}$  with the values measured for with  $(f_{c,1} - f_{c,3})$  FTIR.

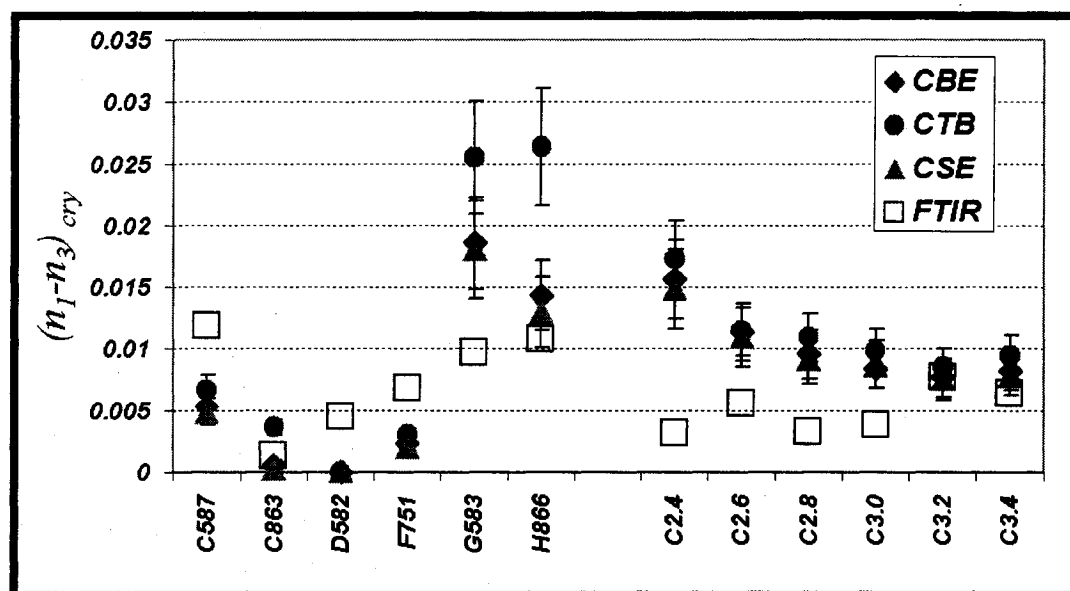


Figure 68: A comparison between the crystalline contribution to birefringence obtained by FTIR and the crystalline contribution to birefringence estimated using the model and the PLM results.

Estimating the amorphous orientation is a challenging task, due to its weak influence when compared with the influence of the crystalline phase. Keller and Machin (1967) reported that, in polyethylene films, random or weak orientation of the amorphous chains was encountered when low or intermediate stresses were applied. In fact, this explained the negative birefringence they observed in some of their samples due to amorphous chain orientation in the transverse direction. As indicated earlier, this is consistent with our observation that the amorphous chains were randomly distributed between the machine and the transverse directions with slight preference towards the latter, thus the birefringence was weak.



### 5.3.3.4 FTIR Analysis

The orientation measurements were carried out using the FTIR. In this work the orientation factors  $f_a, f_b, f_c$  and  $f_{am}$  were calculated by employing four different methods: Jarvis (1980), Kissin (1992), Krishnaswamy (2000), and Cole and Ajji [Ward (1997)]. The results obtained by employing the methods of Jarvis and Cole and Ajji were identical, and the curves coincided with each other. While the method of Kissin was based on the assumption that the crystallographic c-axis was unlikely to be oriented in the normal direction, Krishnaswamy assumed that the a-axis was more likely to be oriented in the machine direction. There were no assumptions of a preferred orientation in any of the axes in the Cole and Ajji approach, which makes it the selected approach in the present study. The method of Cole and Ajji does not predetermine the orientation of any of the crystallographic axes.

The orientations in several LLDPE and LDPE blown films were studied and compared. The differences in the processing conditions and parameters of the blown films are shown in Table 12. The films are produced from various resins, as shown in Table 11. The orientations of the crystallographic b-axis, the amorphous chain axis, and the crystallographic a-axis, were investigated by extracting information from the absorption at frequencies  $719\text{cm}^{-1}$ ,  $724\text{cm}^{-1}$  and  $730\text{cm}^{-1}$ , respectively. The results were combined with the crystallinity information obtained using the differential scanning calorimeter (DSC), and then compared to the results obtained by the birefringence method. Subsequently, the experimental results were compared with the orientation predicted by the proposed simulation of the film blowing process. Figure 69 shows the standard fitting using the method suggested by Cole and Ajji [Ward (1997)], which was employed in this study to decompose the FTIR spectra into three peaks that correspond to the crystallographic a-axis and b-axis, and the amorphous orientation.

In all film samples, the parallel spectra indicate that the  $730\text{cm}^{-1}$  bands are stronger than the  $719\text{cm}^{-1}$  bands, suggesting that the crystallographic a-axis is more oriented in the machine direction. This is consistent with the observation of most researchers, such as Keller (1955, 1967), Desper (1969) and Zhang (2001). The film

samples are divided into two sets, as shown in Table 12. Set 1 is the first six samples and Set 2 is the last six samples. The last six samples (Set 2) were prepared from different batches and at different times. Therefore they cannot be compared with C587 and C863. They were blown to different blow-up ratios. The details of the resin comparison are shown in Table 11. Moreover, the details of the processing conditions are shown in Table 12.

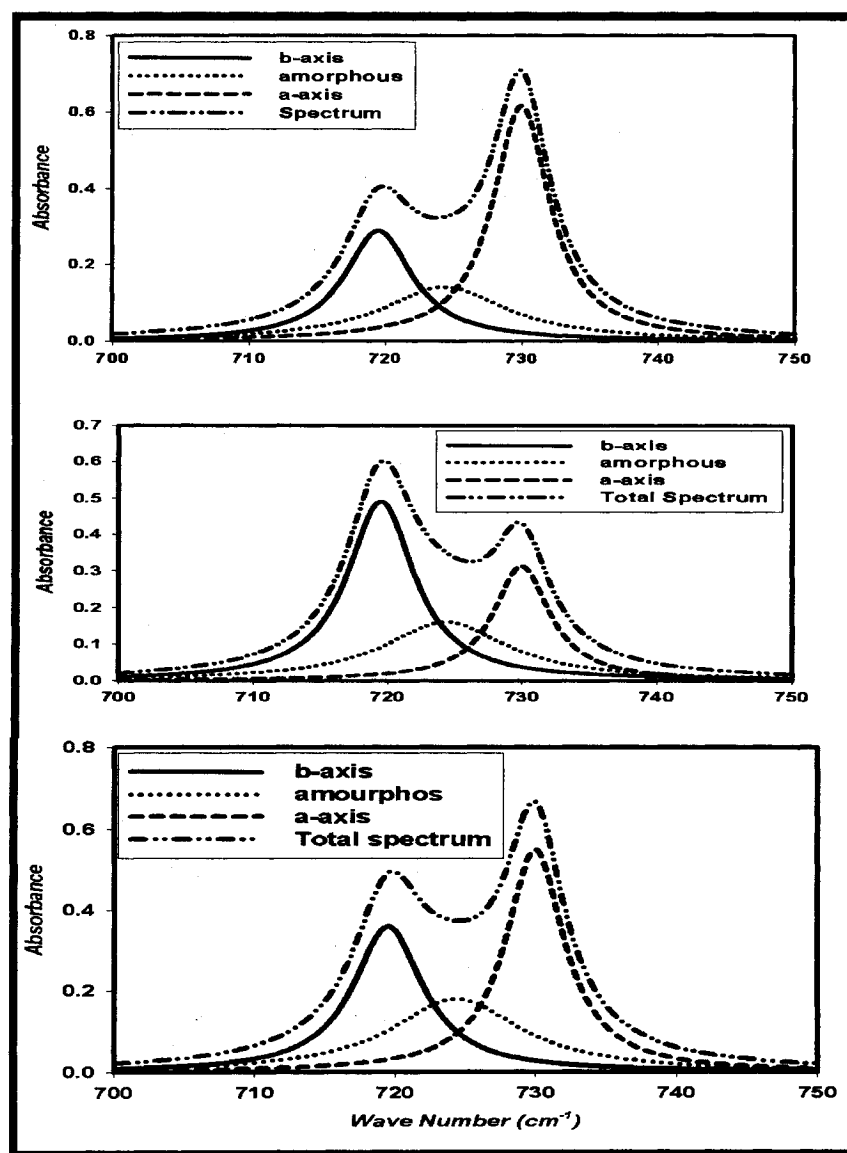


Figure 69: The FTIR parallel (top), perpendicular (middle), and 45° tilted angle (bottom) spectra of film C583 and the fitted peaks of interest.

### 5.3.3.4.1 Orientation of the Crystallographic Axes and the Amorphous Chains in the Films

Triangle plots are used to represent  $\langle \cos^2 \theta_{ij} \rangle$ , which indicate the Herman's orientation functions as shown in Figure 70. The apices of the triangle represent the three macroscopic directions of the samples, and  $\theta_{ij}$  is the angle between the crystalline axis (or chain axis in the amorphous phase),  $i$ , and the sample direction,  $j$ , (M, N, or T). The quantity,  $\langle \cos^2 \theta_{ij} \rangle$ , was calculated from the average orientation as follows.

$$\langle \cos^2 \theta_{ij} \rangle = \frac{2f + 1}{3} \quad (162)$$

If the sample is isotropic (no preferred orientation), the above quantities will appear at the center of the triangle. However, if one of the micro-structural axes is fully oriented toward the machine direction, the corresponding  $\langle \cos^2 \theta \rangle$  will coincide with the MD apex of the triangle, etc. Hence, the more a specific axis is oriented towards one direction, the closer will be the corresponding point on the triangle to the apex that corresponds to that particular direction. For instance, Figure 70 shows that the a-axis is more oriented in the machine direction and the c-axis is more oriented in the normal direction. The chains in the amorphous phase are oriented perpendicular to the thickness direction, which is consistent with results obtained by Kamal et al. (1992). Orientation of the amorphous phase is perpendicular to the crystalline c-axes. The amorphous phase is oriented in the MD-TD plane.

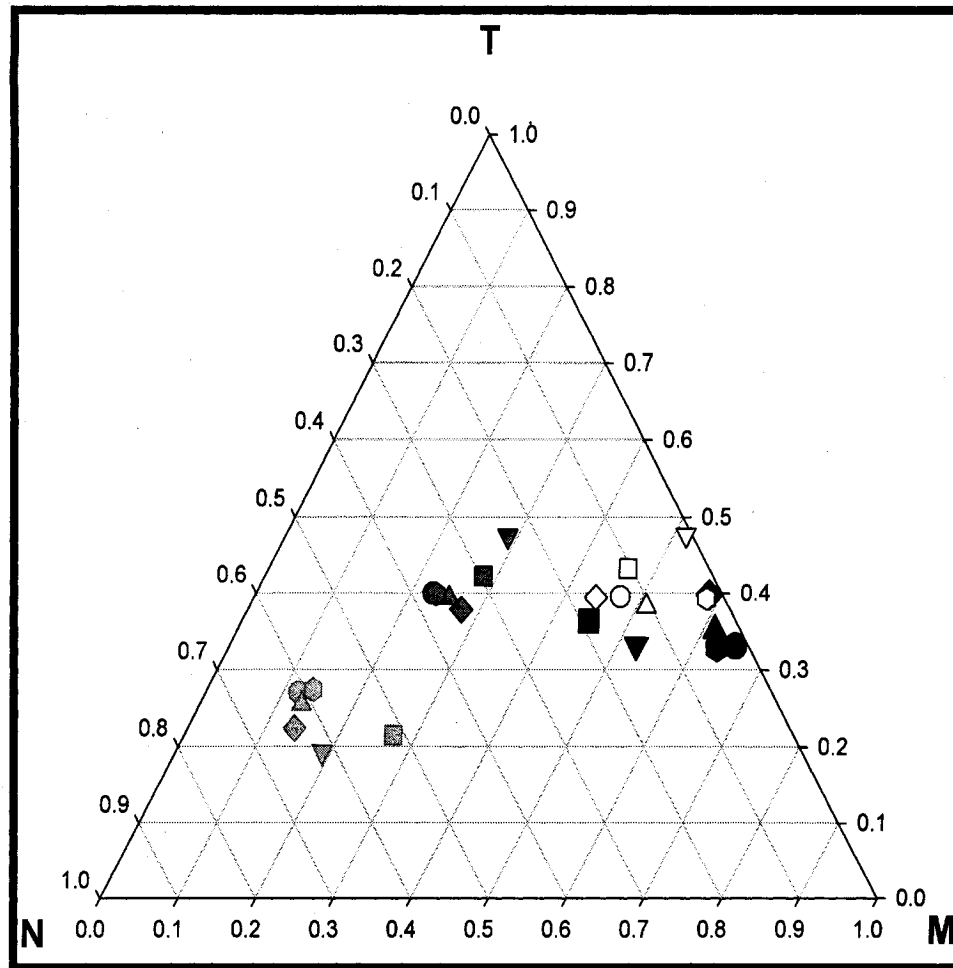


Figure 70: The average orientation of the all axes: a-axis (black), b-axis (dark gray), c-axis (light gray), and amorphous chain (white) in the machine (M), transverse (T), and thickness directions of the samples: C587 (circle), C863 (down-triangle), D582 (square), F571 (diamond), G583 (up-triangle), and H866 (hexagon).

Figure 70 shows the average orientation in the samples of Set1 (C587, C863, D582, F571, G683 and H866) estimated by employing the general approach suggested by Cole and Ajji [Ward (1997)]. The preferred orientation of the crystallographic a-axis is in the machine direction for all samples. This observation is consistent with experimental results reported by Zhang *et al.* (2001). When C587 and C863 are compared, the a-axis in sample (C587) appears to be more oriented in the machine direction. The die gap was

larger and the draw ratio was higher in the case of C587. It is also noted that the b-axis is oriented towards the thickness direction in film C587. The growth axis of the lamellae is parallel to the crystalline b-axis [Keller and Machin (1967), Ajji and Cole (2000)]. Because film C587 was thicker and thus experienced higher temperatures, the crystal growth was for a longer duration. According to the Neumann-Stefan theory, the crystallization front forms a solidified layer that moves towards the direction of higher temperature in the film [Janeschitz-Kriegl *et al.* (1995)]. The observation regarding b-axis orientation is consistent with the measured orientation by Zhang *et al.* (2003), Ajji *et al.* (2003), Haber and Kamal (1992), and Krishnaswamy and Sukhadia (2000).

The amorphous orientation appears to be distributed somewhat between the machine and the transverse directions. The amorphous region shows slightly more orientation towards the normal direction when the thinner die was used (C863). This may be attributed to the lower draw ratio in the case of (C863). Keller and Machin (1967) showed that the amorphous orientation in polyethylene films was either perpendicular to the machine direction or is random. Zhang *et al.* (2003) reported that the amorphous chain has no preferred orientation.

#### **5.3.3.4.2 The Effects of Blow-up and Draw Ratios**

Samples C24, C26, C28, C30, C32, and C34, were produced from modified resin C587. The blow-up ratio (BUR) was increased by steps of 0.2 from sample C24, for C24, C26, C28, C30, C32, and C34 in that order. In the same order, the estimated draw ratios decreased slightly. No information was provided regarding the freeze line or the cooling conditions.

It appears that the greatest influence of the blow-up ratio is on the orientation of the amorphous chains. The effect on the orientation of the crystallographic axes is relatively small. Figure 71 shows that the crystalline c-axis became less oriented in the machine direction as the blow-up ratio was increased, and the a-axis became more oriented in the machine direction. The crystallographic b-axis seems to move closer to the normal direction of the sample at higher blow-up ratios, which is in agreement with

Zhang et al (2001, 2003). They observed that, the b-axis became more oriented in the normal direction as they decreased the draw ratio. The estimated draw-ratios in the second set of the samples (Table 12) were high. Thus, the b-axis was more oriented in the normal direction, because the growth of the crystals favors the direction with minimum stresses. The above observations are most apparent upon comparing the results in Figures 70 and 71.

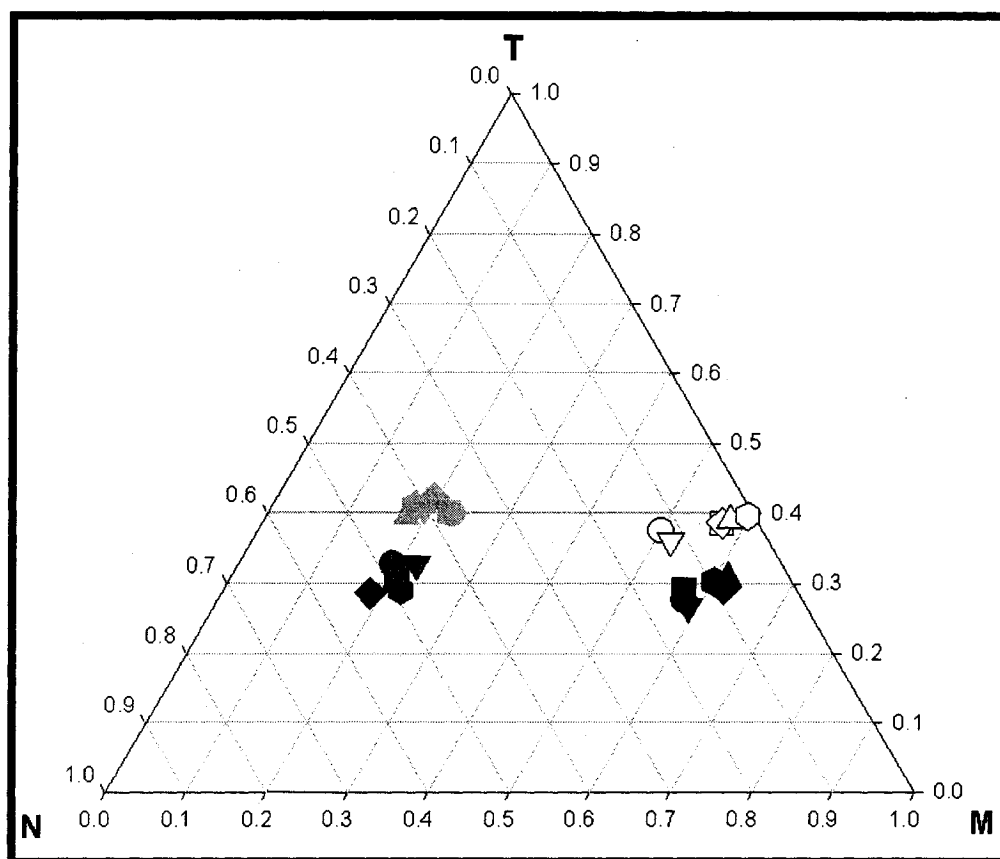


Figure 71: The average orientation of the all axes: a-axis (black), b-axis (dark gray), c-axis (light gray), and amorphous chain (white) in the machine (M), transverse (T), and thickness directions of the samples: C24 (circle), C26 (down-triangle), C28 (square), C30 (diamond), C32 (up-triangle), and C34 (hexagon).

Figure 71 shows that the amorphous chains become more oriented in the normal direction, as the blow-up ratio is lowered. The changes in the draw ratio are small, in comparison with the changes in the blow-up ratio. However, the effect of the draw-ratio was stronger, because it is much higher than the blow-up ratio.

### 5.3.3.5 Comparative Film Blowing Behavior of HDPE, LDPE, and LLDPE

A comparison is made between three types of polyethylene: HDPE (rheological properties are the same as that used by Kanai and White (1984)), LDPE (resin F751), and LLDPE (resin G863). The HDPE simulation was based on the assumption that the same die was used as for the LLDPE and LDPE (shown in Table 3). The predicted dimensionless take-up force and inflation pressure were 1.1 and 0.047. The extrusion temperature was 180°C for HDPE, 177°C LDPE, and 217°C for LLDPE. The predicted initial blowing angle was 1°. The final thickness of the HDPE film was 110 microns, which was much thicker than that produced by Kanai and White (1984), because the die gap thickness (1 mm) employed in the present simulation was larger than that used by them (0.55 mm). Their die radius (1.6 cm) was also much smaller than the radius (3.9 cm) employed in this work. HDPE showed the longest bubble neck, while LDPE showed the shortest neck, as shown in Figure 72. This characteristic behavior is due to the evolution of the stresses that dictate the blowing angle and thickness reduction. Figure 73 shows that the stresses grow much faster in the case of blowing LDPE, although the extrusion temperatures were not very different.

Because the crystallinity evolves to higher levels in HDPE, the temperature profile tends to be higher for HDPE than for LLDPE and LDPE, as shown in Figure 74. In the present simulation, the heat transfer coefficient depends strongly on the bubble radius, which changes at a slower rate in HDPE. Thus, the heat exchange between the film and cooling air is slower and, therefore, the temperature of the film is higher. In addition, more heat is released due to the crystallization of HDPE. The heat released due to crystallization shifts the temperature profile up and contributes to the appearance of the plateau in the temperature profile.

If the stress levels are close, crystallinity differences are reflected in the average orientation. Thus, the orientation in HDPE films is higher than in the other types of PE films, as shown in Figure 75. However, when crystallinity values are small or when the differences in the crystallinity are not large, stress differences are reflected in the average orientation as seen in Figure 75 when LDPE is compared with LLDPE.

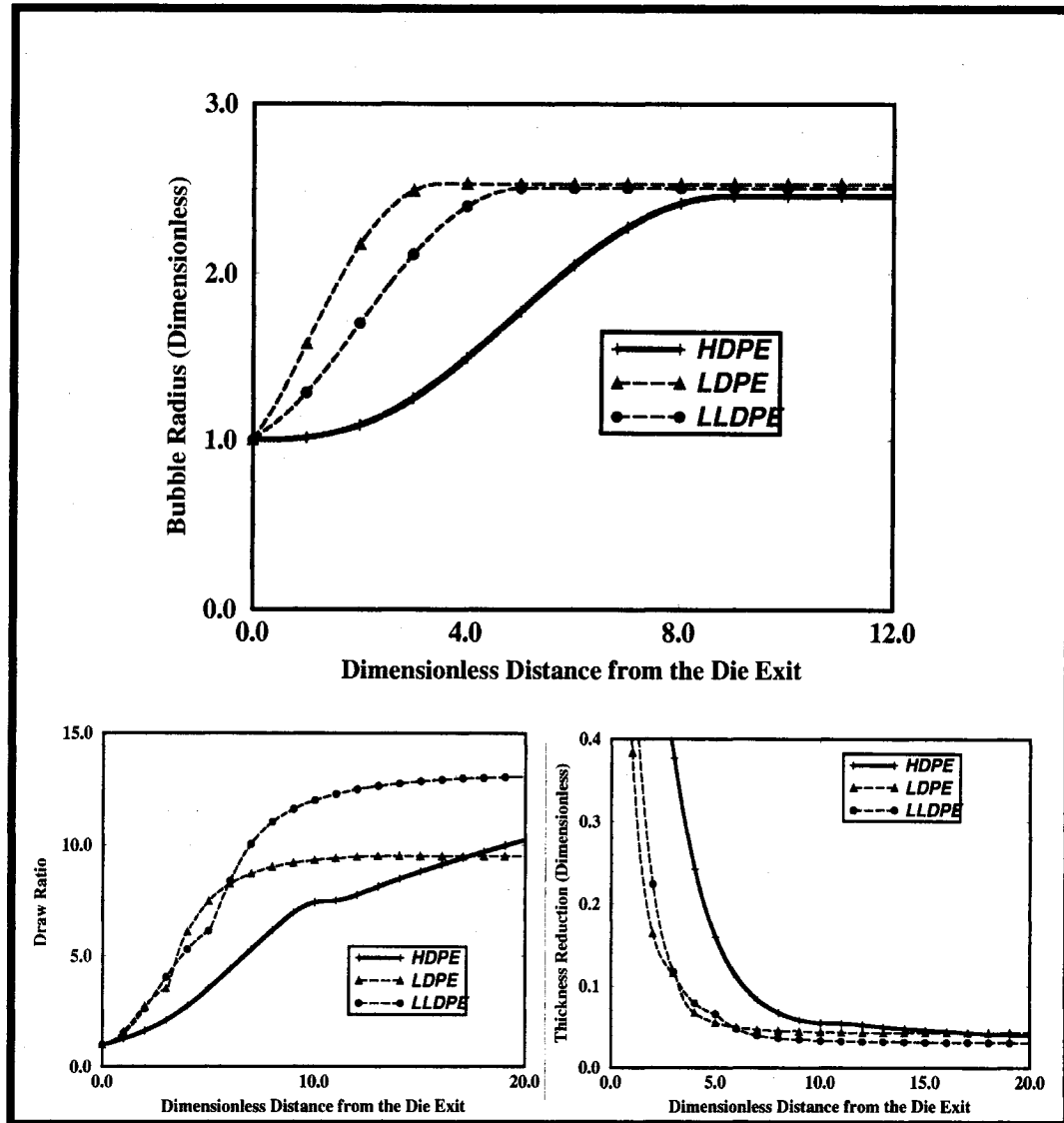


Figure 72: A comparison between the bubble shapes, draw ratios, and reduction in the thickness in HDPE, LDPE, and LLDPE.



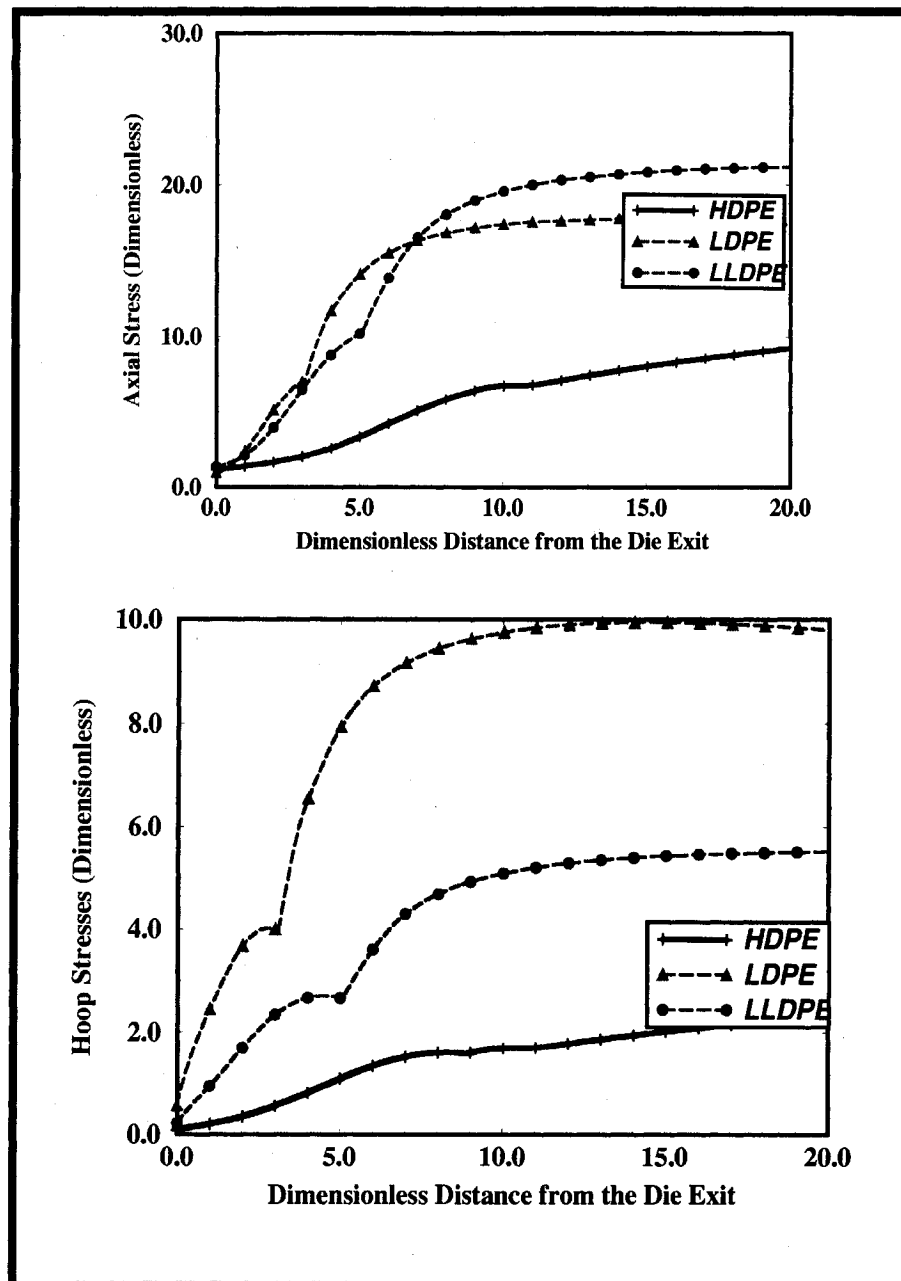


Figure 73: The stress profiles in HDPE, LDPE, and LLDPE.

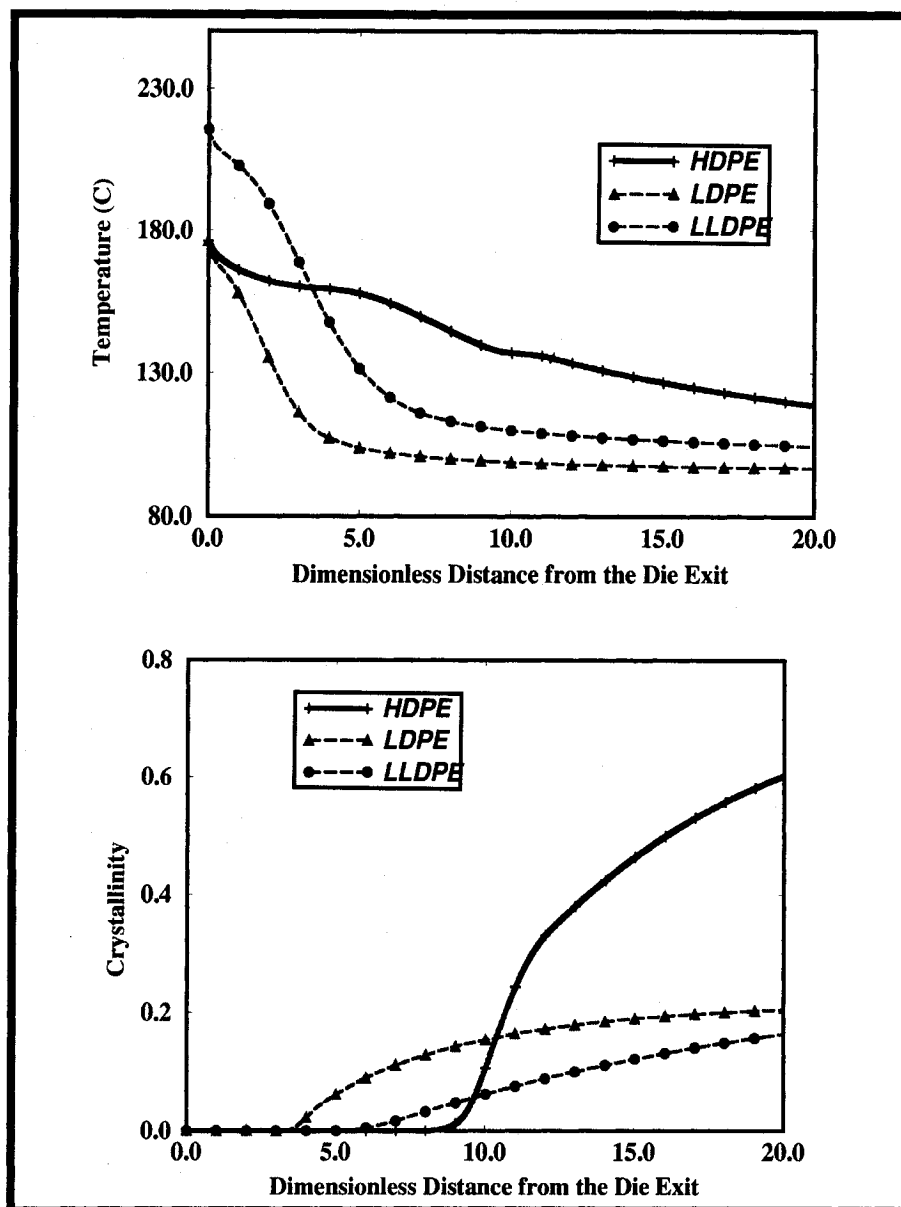


Figure 74: HDPE, LDPE, and LLDPE films have significant differences in the temperature and crystallinity profiles.

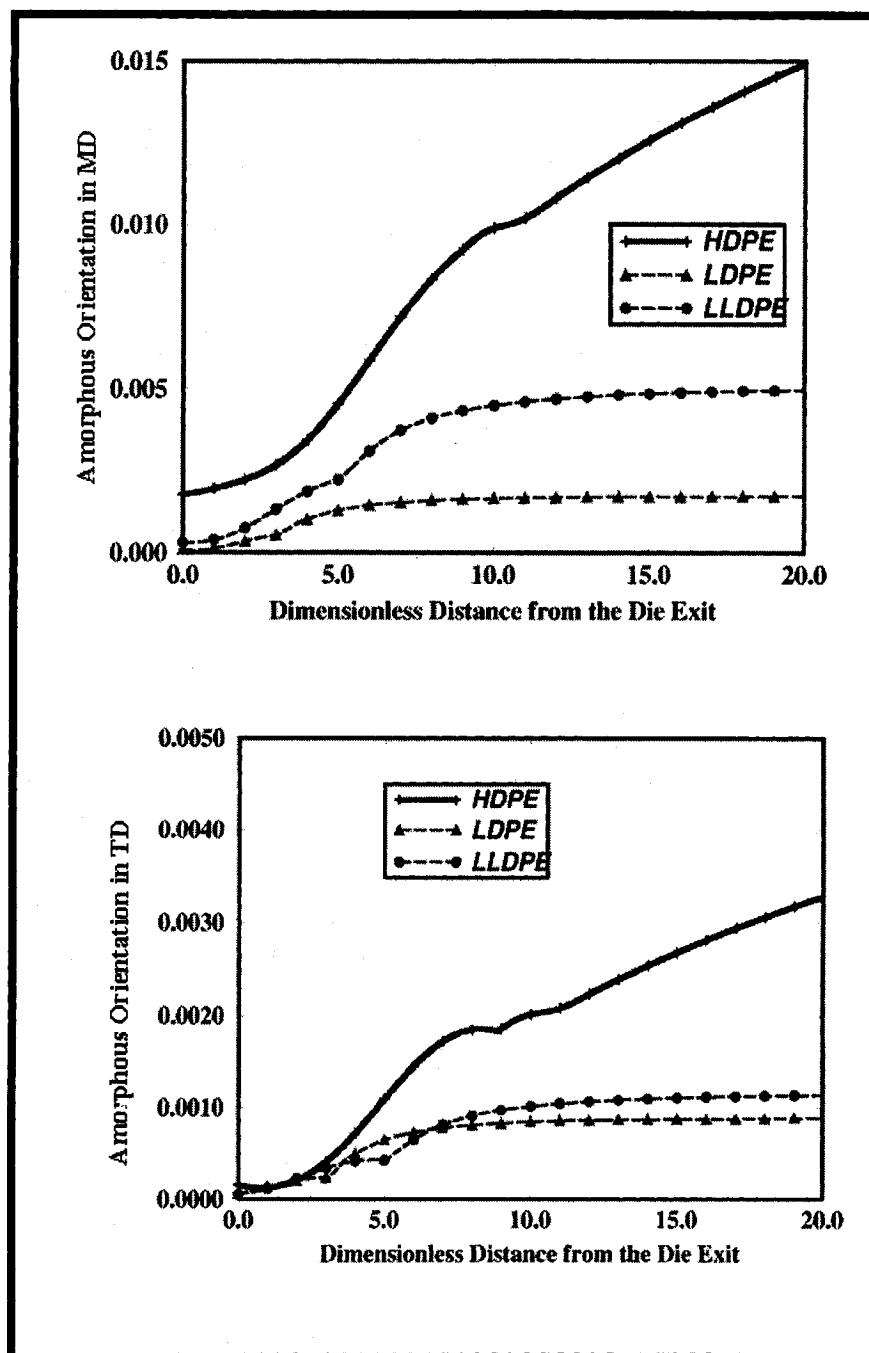


Figure 75: HDPE, LDPE, and LLDPE have significant levels of amorphous orientations due to the differences in stress and crystallinity profiles.

# Chapter 6

## 6 CONCLUSIONS, ORIGINAL CONTRIBUTIONS, AND FUTURE WORK

### 6.1 Summary

In the present work, a two-dimensional, microstructure-and-product oriented model of the film blowing process was developed to predict the evolution of bubble shape dimensions, temperature, deformation, stresses, crystallinity, and orientation during the process.

The entire process from the die exit to the nip rolls was covered. The rheological behavior of the film was described by employing the Phan-Thien Tanner (PTT) constitutive equation from the die exit to the freeze line (liquid-like region). Then, from the freeze line to the nip rolls, a Neo-Hookean constitutive equation was employed to describe the rheological behavior of the film (solid-like region). In the first region, before the freeze line, the viscosity and relaxation time were dependent on the crystallinity and the temperature of the film, along with the second invariant of the deformation rate tensor. In the solid-like region, the relaxation modulus was taken as a function of crystallinity, temperature, and the dynamic shear constants.

Since film blowing is a highly nonisothermal process, a two-dimensional energy equation was employed. The combined radiation and convection heat transfer coefficient was defined as a function of the temperature difference between the film surface and cooling air, the bubble radius, and the cooling air velocity. The heat transfer coefficient function was obtained by analysis of data found in the literature. Temperature change in the thickness direction was predicted. This change is due to the strong cooling at the exterior surface of the film and the weak conductivity of polymers in general.

The calculated stresses were employed to predict the refractive indices in three directions, using the stress-optical relationship. The difference in the refractive indices defines the birefringence. From the birefringence, the stress-induced orientation was predicted. The predicted orientation was incorporated in the crystallization, according to Ziabicki's equation.

The robustness of the simulation was evaluated, by comparing the predictions of proposed simulation with relevant calculated results in the literature, and experimental results for four different groups of researchers.

## **6.2 Conclusions**

- 1) The predictions of the simulation were compared to analytical solution of limiting cases reported in the literature. There was excellent agreement between the results.
- 2) The predictions of the simulation were compared to computational solutions for limiting cases reported in the literature. There was excellent agreement between the results.
- 3) The predictions of the simulation were compared to experimental data reported in the literature by three independent groups, using different materials and processing conditions. Predictions regarding bubble shape and the distributions of film thickness and temperature were in very good agreement with experimental results.
- 4) The robustness of the simulation was tested by evaluating the influence of various rheological, crystallization, and orientation parameters on the predictions. The results indicated that the model is valid over a wide range of these parameters. It also indicates that the selected parameters were appropriate.
- 5) The predictions of the simulation were compared to experimental measurements on films produced from different resins under known experimental conditions. Experimental data regarding the final crystallinity,

orientation, and refractive indices of the film were in reasonable agreement with the predictions of the simulation.

- 6) The simulation was employed to compare bubble shape and behavior for HDPE, LDPE, and LLDPE. The predictions were in harmony with observations relating to the general comprehensive film blowing behavior of these resins.
- 7) In the view of the above, it may be concluded that the proposed simulation provides a realistic and accurate description of the film blowing process.
- 8) The temperature drop in the thickness direction was significant in the liquid like region. However, it kept decreasing continuously along the machine direction until it became negligible in the vicinity of the freeze line.
- 9) Most of the crystallinity evolved in the vicinity of the freeze line and thereafter. The use of variable ultimate crystallinity was important for obtaining accurate predictions of the average crystallinity and temperature profiles.
- 10) While the bubble diameter tends to remain constant after the freeze line, both the simulation and experimental evidence indicate that the thickness of the film and stresses continue to change above the freeze line.

### **6.3 Original Contributions**

- 1) A computer simulation has been developed to describe the film blowing process. It is the most detailed and comprehensive model of the process. It is the only simulation that predicts the bubble shape, film dimensions, the distributions of temperature, orientation, stress, and absolute crystallinity along the machine direction and across the film thickness. A new correlation is proposed to predict the heat transfer coefficient incorporating film temperature, bubble shape, and the cooling dynamics (the velocity and temperature of the cooling air).
- 2) This is the first simulation to predict the absolute crystallinity and orientation in the film blowing process and to show their effects on the

distributions of temperature, stresses, bubble shape, and film velocity. It is also the first to incorporate experimental data regarding the effect of crystallinity on relaxation modulus of the solid-like film.

- 3) This is the first simulation to predict the commonly observed differences in the bubble shapes and process kinematics between HDPE, LDPE, and LLDPE.

## **6.4 Suggested Future Study**

- 1) The validation and upgrading of computer simulation of the film blowing process requires detailed and accurate data regarding the dynamics of the process under various conditions and for a variety of resins. Such data require detailed and dependable on-line measurements of the distribution of process variables (e.g. crystallinity, orientation, etc.).
- 2) This work presents a comprehensive study of the film blowing process under steady state conditions. Expanding this study to the unsteady conditions and under the influence of some perturbation, can contribute to understanding the effect of the start-up dynamics on the predictions. It would also help in understanding factors influencing bubble instabilities and in development of process control strategies.
- 3) The proposed model treats the melt after it exits from the die and assumes that the melt dimensions are the same as those of the die. It would be more realistic to start the simulation at the entrance to the die, in order to account for stress and thermal effects during flow in the die and to take into consideration phenomena, such as melt swell.
- 4) Since the rheological behavior of the solid-like film is an important element that has to be integrated in modeling the film blowing process, extensional experiments can be conducted to obtain more accurate profiles of the relaxation modulus for different polymers under various temperatures. Moreover, the rheological behavior of the film in the transition zone between the liquid-like and the solid-like regions should be studied

carefully to overcome the discontinuity that takes place when the transition occurs from liquid-like melt to solid-like film.

- 5) The prediction of orientation is an essential feature of any useful simulation of the film blowing process. Orientation prediction is achieved through the stress-optical relationship. An important variable in the stress-optical functions is the stress optical coefficient (SOC). More work should be done to incorporate the effect of temperature, stress, and deformation, on the SOC. Furthermore, a study should be conducted to obtain the value of the stress-optical coefficient for the crystalline portion of the polymer.



## REFERENCES

Adamson, A., "Physical Chemistry of Surfaces", New York, Interscience Publishers, 1967.

Agassant, J.F., Avenas, P., Sergent, P., Carreau, P.J., "Polymer Processing: Principles and Modeling", New York, Hanser Publishers, (1991).

Aggarwal, S.L., Tilley, G.P., Sweeting, O.J., "Orientation in extruded polyethylene films", J. App. Polym. Sci., 1, 91-100 (1959).

Ajji, A., Cole, K. C., "Characterization of biaxial orientation in polyolefin films", ANTEC, 2, 1610-1614 (2000).

Ajji, A., Zhang, X., Elkoun, S., "Biaxial orientation in polyethylene films: comparison of infrared spectroscopy and X-ray techniques", ANTEC 1459-1463 (2003).

Alaie, S.M., Papanastasiou, T.C., "Modeling of Non-isothermal Film Blowing with Integral Constitutive Equations", Intern. Polym. Process VIII 51-65 (1993).

Allen III, M.B., Isaacson, E.L., "Numerical analysis for applied science", New York, Wiley-Interscience publication, (1998).

Alves, M.A., Oliveira, P.J., Pinho, F.T., "Benchmark solution for the flow of Oldroyd B- and PTT fluids in planar contractions", J. Non-Newtonian Fluid. Mech., **110**, 45-75 (2003).

Anderton J., "The world of film", Canadian Plastics, 29-31, February 2000.

André, J. M., "Modélisation thermomécanique et structurale du soufflage de gaine de polyethylene", Ph.D. Thesis, Ecole des mines de Paris, (1999).

André, J. M., Agassant, J. F., Demay, Y., Haudin, J. M., Monasse, B., "Numerical Modeling of the Polymer Film Blowing Process", Int. J. Forming Proc., **1**, 187-210 (1998).

Babel, A. K., Campbell G. A., "Two-phase simulation of tubular film blowing of crystalline polymers", Int. Polym. Process. **VII**, 240-247 (1992).

Babel, A.K., Cao, B., Campbell G.A., "On the application of a viscoplastic elastic model to uniaxial elongational flow", J. of Plastic Film and Sheeting, **9**, 224-245, (1993).

- Baird D., Collias D., "Polymer Processing, Principles and Design", New York, John Wiley and Sons, 1998.
- Bird R., Stewart W., Lightfoot E., "Transport phenomena", Wiley International edition, (1960).
- Burden, R.L., Faires, J.D., "Numerical Analysis", Pacific Grove, California, Brooks/Cole Publishing company, (1997).
- Butler T., "Blown Film Frost Line Freeze Line Interactions", Polymers, Laminations and Coating conference, 1993.
- Butler, T. I., Patel R., Lai S. Y., Spuria J., "Blown Film Frost Line Freeze Line Interactions", Proc. TAPPI, 13-25 (1993).
- Cain J., Denn M., "Multiplicities and Instability in Film Blowing", Polym. Eng. Sci., **28**,1527-1541 (1988).
- Cain, J., "A simulation of the film blowing process", Ph.D. Dissertation, University of California at Berkeley, (1988).
- Campbell, G., Cao, B., "Blown film simulation a sever test for rheological models", edited by A.A. Collyer A., Utracki L., Elsevier New York, Science Pub. Co., (1990).
- Campbell, G., Cao, B., "The interaction of crystallinity, elastoplasticity, and a two-phase model on blown film bubble shape", J. Plastic Film and sheeting, **3**, 158-170, (1987).
- Campbell, G.A., Babel, A.K., "Physical properties and processing conditions of the LDPE/LLCPE tubular blown films", Macromol. Symp., **101**, 199-206, (1996).
- Cao, B., Campbell, G., "Viscoplastic-Elastic Modeling of Tubular blown Film Processing", AIChE J., **36**, 420-430 (1990)
- Cao, B., Sweeney, P., Campbell, G., "Simultaneous surface and bulk temperature measurement of polyethylene during film blowing", ANTEC 35-38 (1989).
- Catsiff, E., Offenbach, J., Tobolsky, A. V., "Viscoelastic Properties of Crystalline Polymers: Polyethylene", J. Colloid Sci., **11**, 48-50 (1956).
- Chapra, S.C., Canale, R., "Numerical methods for engineers", New York, McGraw Hill, (1998).

- Chen, H.Y., Chau, C.C., Butler, T., Landes, B., Bishop, M., Bellmore, D., Chum, C.D., 'Orientation and property correlation on LLDPE blown films', ANTEC, 1401-1405 (2003).
- Dally J.W., Riley, W.F., "Experimental stress analysis", New York, McGraw-Hill, Inc., (1991).
- Desper, C. R., "Structure and properties of extruded polyethylene film", J. App. Polym. Sci., 13, 169-191, (1969)
- Devi, C.D.S., Takhar, H. S., Nath, G., "Unsteady, three-dimensional, boundary layer flow due to a stretching surface", Int. J. Heat Mass Transfer, 29(12), pp 1996-1999, (1986).
- Dole, M., "Crystallinity from thermal measurements", J., Polym. Sci., **18**, 57- 68 (1967).
- Doufas, A. K., McHugh A. J., "Simulation of film blowing including flow-induced crystallization", J. Rheol, **45**, 1085-1104 (2001).
- Eder, G., Janeschitz-Kriegl, H., Liedauer, S., "Crystallization processes in quiescent and moving polymer melts under heat transfer conditions", Prog. Polym. Sci. 15, 629-714 (1999).
- Feron, B., Wolf, D., Wortberg, J., "Optimized Cooling and Gauge Tolerances in Blown Film Extrusion", J., Polym. Eng. Sci., **37**, 876-881 (1997).
- Ferry, J., "Viscoelastic properties of polymers", John Wiley and sons Inc., New York, (1980).
- Ghaneh-Fard, A., Carreau, P. J., Lafleur, P. G., "Study of Kinematics and Dynamics of Film Blowing of Different Polyethylenes", Polym. Eng. Sci., **37**, 1148-1163 (1997).
- Gibson, J.E., "Linear elastic theory of thin shells", Pergamon press, New York, (1965).
- Haber, A., Kamal, M.R., "Experimental analysis of the thermoplastic film embossing process", Advances in Polym. Tech., **11**, 159-180, (1992).
- Hanna, O.T., Sandall, O.C., "Computational methods in chemical engineering", Eaglewood Cliffs, NJ, Prentice Hall, (1995).
- Harrison, P., Janssen, L.J.P., Navez, V.P., Peters, G.W.M., Baaijens, F.P.T., "Birefringence measurements on polymer melts in an axisymmetric flow cell", Rheol. Acta, **41**, 114-133 (2002).

- Hauck, J., Michaeli, W., "Investigation into the Cooling characteristics of blown film extrusion lines", SPE Antec Tech. Paper, (1998).
- Janeschitz-Kriegl, H., "Polymer melt rheology and flow birefringence", Springer, Berlin (1983).
- Janeschitz-Kriegl, H., Krobath, G., Roth W., Schausberger, A., "On the kinetics of polymer crystallization under shear", Eur. Polym. J., 19, 893-898 (1983).
- Janeschitz-Kriegl, H., Ratajski, E., Eder, G., "The Neumann-Stefan problem and its recent widening as an advanced topic of transport phenomena", Ind. Eng. Chem. Res., **34**, 3481-3487 (1995).
- Jarvis, D.A., Hutchinson, I.J., Bower D.I., Ward, I.M., "Characterization of biaxial orientation in poly(ethylene terephthalate) by means of refractive index measurements and Raman and infra-red spectroscopies", Polymer, 21, 41-54 (1980).
- Kakac S., Shan R., Aung W., "Handbook of Single-Phase Convective Heat Transfer", John Wiley and Sons, (1987).
- Kamal, M. R., Haber, A., Song, L., "The effect of processing conditions on the microstructure of embossed polyethylene films", Polym. Eng. Sc., **28**, 166-169, (1988).
- Kamal, M.R., Chu, E., "Isothermal and nonisothermal crystallization of polyethylene", Polym. Eng. Sc., **23**, 27-31, (1983).
- Kamal, M.R., Tan, V., Kashani, F., "The thermal conductivity and diffusivity of polyethylene Solids and melts", Advances in Polym. Tech., **3**, 89-98 (1983).
- Kamal, M.R., Tang, Z., Huang, T., "Morphological Characterization of PE Blown films by atomic force microscopy", Intern. Polym. Processing XVI, **4**, 376-387, (2001).
- Kanai T., White J., "Kinematics, Dynamics, and Stability of Tubular Film Extrusion of Various Polyethylenes", Pol. Eng. Sc., **24**, 1185-1201, 1984.
- Kanai, T., "Film Processing", Cincinnati, Ohio: Hanser/Gardner Publications, (1999).
- Kanai, T., White, J., "Dynamics, heat transfer, and structure development in tubular film extrusion of polymer melts: a mathematical model and predictions", J. Polym. Eng., **5**, 135-157 (1985).

- Kannan, R.M., Kornfield, J.A., "Stress-optical manifestations of molecular and microstructural dynamics in complex polymer melts", *J. Rheol.*, **38**, 1127-1150 (1994).
- Karacan, I., Taraiya, A.K., Bower, D.I., Ward, I.M., "Characterization of orientation of one-way and two-way drawn isotactic polypropylene films", *Polymer*, **34**, 13, 2691-2701, (1993).
- Kavesh, S., Schultz, J.M., "Lamellar and interlamellar structure in melt-crystallized polyethylene. II. Lamellar spacing, interlamellar thickness, interlamellar density, and stacking disorder", *J. Polym. Sci.: Part A-2*, **9**, 85-114 (1971).
- Keller, A., Machin, M.J., "Oriented crystallization in polymers", *J. Macromol. Sci. (Phys.)* B1(1), 41-91 (1967).
- Keller, A., Sandeman, I., "Investigation of unusual orientation in polyethylene by Infrared spectroscopy," *J. Polym. Sci.*, **15**, 133-150 (1955).
- Khan, S.A., Larson, R.G., "Comparison of simple constitutive equations for polymer melts in shear and biaxial and uniaxial extension", *J. Rheology*, **31**, 207-234, (1987).
- Kim, S., Lafleur P.G., Sammut, P., Huneault, A., "Effects of molecular structure of polyethylenes on their bubble instabilities in film blowing extrusion", *ANTEC*, **1**, 361-365, (2003).
- Kissin, Y. V., "Infrared method for measuring orientation in polyethylene films", *J. Polym. Sci. Part B: Polym. Physics*, **30**, 11650-1172 (1992).
- Krishnaswamy, R.K., Sukhadia, "Orientation characteristics of LLDPE blown films and their implications of Elmendorf tear performance", *Polymer*, **41**, 9205-9217, (2000).
- Krishnaswamy, R.K., "A method to characterize the biaxial orientation of the crystalline phase in polyethylene blown films", *J. Polym. Sci. Part B: Polym. Physics*, **38**, 182-193 (2000).
- Kurtz, S.J., "Relationship of stresses in blown-film Processes", *Int. Polym. Process*, **10**, 148-154 (1995).
- Laffargue, J., Parent, L., Lafleur, P.G., "Investigation of bubble instabilities in film blowing process", *Int. Polym. Process*, **17**, 347-353 (2002)
- Larson, R., "Constitutive equations for polymer melts and solutions", Boston, Butterworths, (1988).

- Lee, G. H., "An introduction to experimental stress analysis", New York, John Wiley and Sons, Inc., (1950).
- Lee, S.L., Tsai, J.S., "Cooling of continuous moving sheet of finite thickness in the presence of natural convection", *Int. J. Heat Mass Transfer*, **33**, pp 457-464, (1990).
- Leissa, A., "Vibration of shells", NASA, Washington D.C., (1973).
- Lin G-G., Shin, H-H., Chai, P-C., "Influences of side-chain structures on the viscoelasticity and elongational viscosity of polyethylene melts", *Polym. Eng. Sci.*, **42**, 2213-2221, (2002).
- Liu, C.-C., Bogue D. C., Spruiell, J. E., "Tubular Film Blowing, Part1, On-line experimental studies", *Int. Polym. Process.*, **10**, 226-229 (1995a).
- Liu, C.-C., Bogue D. C., Spruiell, J. E., "Tubular Film Blowing, Part2, Theoretical Modeling", *Int. Polym. Process.*, **10**, 230-236 (1995b).
- Lungu, C., M. Eng. Thesis, McGill University, Montreal, Quebec, Canada, (2000).
- Luo, X-L., Tanner R. I., "A computer study of film blowing", *Polym. Eng. Sci.*, **25**, 620-629 (1985).
- Macosko C., "Rheology principles, measurements, and applications", New York, VCH Publishers, (1994).
- Maia, J.M., "Theoretical modeling of fluid S1: a comparative study of constitutive models in simple and complex flows", *J. Non-Newtonian Fluid Mech.*, **85**, 107-125, (1999).
- Maltosz, M., Newman, J., "Solving 1-D boundary-value problems with BandAid: a functional programming style and a complementary software tool", *Comput. Chem. Eng.*, **11**, 45-61, (1987).
- Menges G. and Predohl W., "Certain aspects of film blowing of low-density polyethylene", *Polym. Eng. Sci.*, **15**, 394-399 (1975).
- Micic P., Bhattacharya S.N., Field, G., "Transient elongational viscosity of LLDPE/LDPE blends and its relevance to bubble stability in the film blowing process", *Polym. Eng. Sci.* **38**, 1685-1693 (1998).

- Mickley, H.S., Shewood, T.S., Reed, C.E., "Applied mathematics in chemical engineering", New York, McGraw Hill, (1957).
- Nagamatsu, K., "On the viscoelastic properties of crystalline high polymers", *Kolloid-Zeitschrift*, **172**, 141-162 (1961).
- Nakamura K., Watanabe T., Katayama K., "Some aspects of nonisothermal crystallization of polymers. I. Relationship between crystallization temperature, crystallinity, and cooling conditions", *J. App. Polym. Sci.*, **16**, 1077-1091 (1972).
- Noye, J., Numerical simulation of fluid motion: proceedings of an International Conference on the Numerical Simulation of Fluid Dynamic Systems held at Monash University', Melbourne, (1976).
- Pearson, J. R. A., Petrie C. J. S., "The flow of a tubular film. Part 1. Formal mathematical representation", *J. Fluid Mech.*, **40**, 1-19 (1970a).
- Pearson, J. R. A., Petrie C. J. S., "The Flow of a tubular film. Part 2. Interpretation of the model and discussion of the solution", *J. Fluid Mech.*, **42**, 609-625 (1970b).
- Petrie C.J.S., Petrie A., "The influence of bubble mechanics on some properties of blown film", in *Polymer Processing Society*, 15, the Netherlands June (1999).
- Petrie C.J.S., "Film blowing, blow molding, and thermoforming; computational analysis of polymer processing", edited by Pearson J.R.A., and Richardson S.M., (1988).
- Petrie C.J.S., "Mathematical modeling and the systems approach in plastics processing: the blown film process", *J., Polym. Eng. Sci.*, **15**, 708-724, (1975)
- Phan-Thien, N., "A nonlinear network viscoelastic model", *J. of Rheol*, **22**, 259-283 (1978).
- Phan-Thien, N., Tanner, R.I., "A new constitutive equation derived from network theory", *J. non-Newtonian fluid mech.*, **2**, 353-365 (1977).
- Pirkle, J.C., Braatz, R.D., "Dynamic modeling of blown film extrusion", *Polym. Eng. Sci.*, **43**, 398-418,(2003).
- Prasad, A., Shroff, R., Rane, S., Beaucage, G., "Morphological study of HDPE blown films by SAXS, SEM and TEM: a relationship between melt elasticity parameter and lamellae orientation", *Polymer*, **42**, 3130-3113 (2001).

- Ratner, A.M., "Tensile stability of cylindrical membranes", *Int. J. Non-Linear Mechanics*, **18**, 133-147, (1983).
- Reddy, J.N., "An introduction to the finite element method", New York, McGraw-Hill, (1993).
- Ries, M.E., Brereton, M.G., Ward, I.M., Cail, J.I., Stepto, R.F.T., "Rescaling approach to molecular orientation for NMR and optical properties of polymer network", *Macromol.*, **32**, 5665-5669 (2002).
- Rodriguez, F., "Principles of polymer systems", New York, McGraw Hill, (1982).
- Rohsenow, W. M., Hartnett, J.P., Cho, Y.I., "Handbook of heat transfer", 3<sup>rd</sup> edition, McGraw Hill, 1996.
- Sakiadis, B.C., "Boundary-layer behavior on continuous solid surfaces II. The boundary layer on a continuous flat surface", *A.I.Ch.E. Journal*, **7**, 221-226, 1961.
- Samuels, J.R., "Structured polymer properties", John Wiley and Sons, New York (1973).
- Sidiropoulos, V., Tian, J.J., Vlachopoulos, J., "Computer simulation of film blowing", *J. Plastic Film and Sheeting*, **12**, 107-129, (1996).
- Sidiropoulos, V., Vlachopoulos, J., "An investigation of Venturi and Coanda effects in blown film cooling", *Intern. Polym. Processing* **15**, 40-45 (2000).
- Sidiropoulos, V., Vlachopoulos, J., "Numerical simulation of blown film cooling", *J. Reinforced Plastics and Composites*, **21**, 629-637, (2001).
- Sidiropoulos, V., Wahab, Z., Vlachopoulos, J., "Numerical calculation of stresses in film blowing", *ANTEC*, (2001).
- Sidiropoulos, V., Wood, P.E., Vlachopoulos, J., "The aerodynamics of cooling of blown film bubbles", *J. Reinforced Plastics and Composites*, **18**, 529-538, (1999).
- Sidiropoulos, V., "The effects of air cooling on the film blowing process", Ph.D. Thesis, McMaster University, Hamilton, Ontario, Canada, (2000).
- Sinnott, R.K., "Coulson and Richardson's chemical engineering: chemical engineering design", vol. 6, Pergamon Press, New York, (1993).



- Soskey, P. R., Winter, H., "Equibiaxial extension of two polymer melts: Polystyrene and Low Density Polyethylene", *J. of Rheol*, **29**, 493-517 (1985).
- Sridhar, T., Nguyen, D.A., Fuller, G.G., "Birefringence and stress growth in uniaxial extension of polymer solutions", *J. non-Newtonian fluid mech.*, **90**, 299-315 (2000).
- Tanner R., "Engineering rheology", New York: Oxford University Press, (2000).
- Tas, P., Ph.D. Thesis, Eindhoven University of Technology, Eindhoven, Netherlands 1994.
- Taylor, D.J.R., Stepto, R.F.T., Jones, R.A., Ward, I.M., "Computer simulation studies of molecular orientation and the stress-optical properties of polyethylene networks", *Macromol.*, **32**, 1978-1989 (1999).
- Theocaris, P.S., "Dependence of stress-optical coefficients on the mechanical and optical properties of polymers", *J. Strain Analysis*, **8**, 267-376 (1973).
- Ward, I. M., "Structure and properties of oriented polymers", New York, Chapman and Hall, (1997).
- Ward, I.M., Coates, P.D., Dumoulin, M.M., "Solid phase processing of polymers", Cincinnati, Ohio, Hanser/Gardner Publications, Inc., (2000).
- White, F., "Fluid Mechanics", Highstown, New Jersey, McGraw Hill Inc., 1994.
- White, J.L., Cakmak, M., "Orientation, crystallization, and haze development in tubular film extrusion", *Advances in Polym. Tech.*, **8**, 27-61 (1988).
- White, J.L., Spruiell J. E., "Specification of biaxial orientation in amorphous and crystalline polymers", *Polym. Eng. Sci.*, **21**, 859-868 (1981).
- Wolf, D., Feron, B., Wortberg, J., "Numerical analysis of cooling air system in film blowing", *Int. Polym. Process*, **12**, 38-44(1997).
- Wunderlich, B., "Macromolecular physics", vol.2, Academic Press, New York, (1976).
- Yeow, Y.L., "Stability of tubular film flow: a model of the film-blowing process", *J. Fluid Mech.*, **75**, 577-591 (1976).
- Yoon, K-S., Park, C-W., "Stability of a blown film extrusion process", *Int. Polym. Process*, **14**, 342-349 (2000).

- Yoon, K-S., Park, C-W., “Stability of a two-layer blown film coextrusion”, *J. Non-Newt. Fluid Mech.*, **89**, 97-116 (2000).
- Zeppenfeld V. I. R., Kierspe, “Möglichkeiten zur Leistungssteigerung bei Luftgekuhlten blasfolienanlagen”, *KunstStoffe*, 1971.
- Zhang, X. M., Elkoun, S., Ajji, A., Huneault M.A., “Effect of crystalline structure on tear resistance of LDPE and LLDPE blown films”, *ANTEC*, 1376-1380 (2003).
- Zhang, X., Ajji, A., Jean-Marie, V., “Processing-structure-properties relationships of multiplayer films, 1. Structure characterization”, *Polymer*, 42, 8179-8195, (2001).
- Zhang, X., M., Ajji, A., Huneault, M.A., “Control of blown film tear strength anisotropy through blending of LDPE and LLDPE”, *ANTEC*, 1391-1395 (2003).
- Ziabicki A., “Fundamentals of fiber formations”, New York, John Wiley and Sons, Inc., (1976).
- Ziabicki A., “Theoretical analysis of oriented and non isothermal crystallization I. Phenomenological considerations, isothermal crystallization accompanied by simultaneous orientation or disorientation”, *Colloid and Poly. Sci*, **252**, 207-221 (1974).
- Ziabicki, A., “Crystallization of polymers in variable external conditions IV. Isothermal crystallization in the presence of variable tensile stress or hydrostatic pressure”, *Colloid and Poly. Sci*, **277**, 752-261 (1999).

## APPENDIX A

### Schematics of the Film Blowing Process

[source: (Rodriguez (1982), Kanai (1999))]

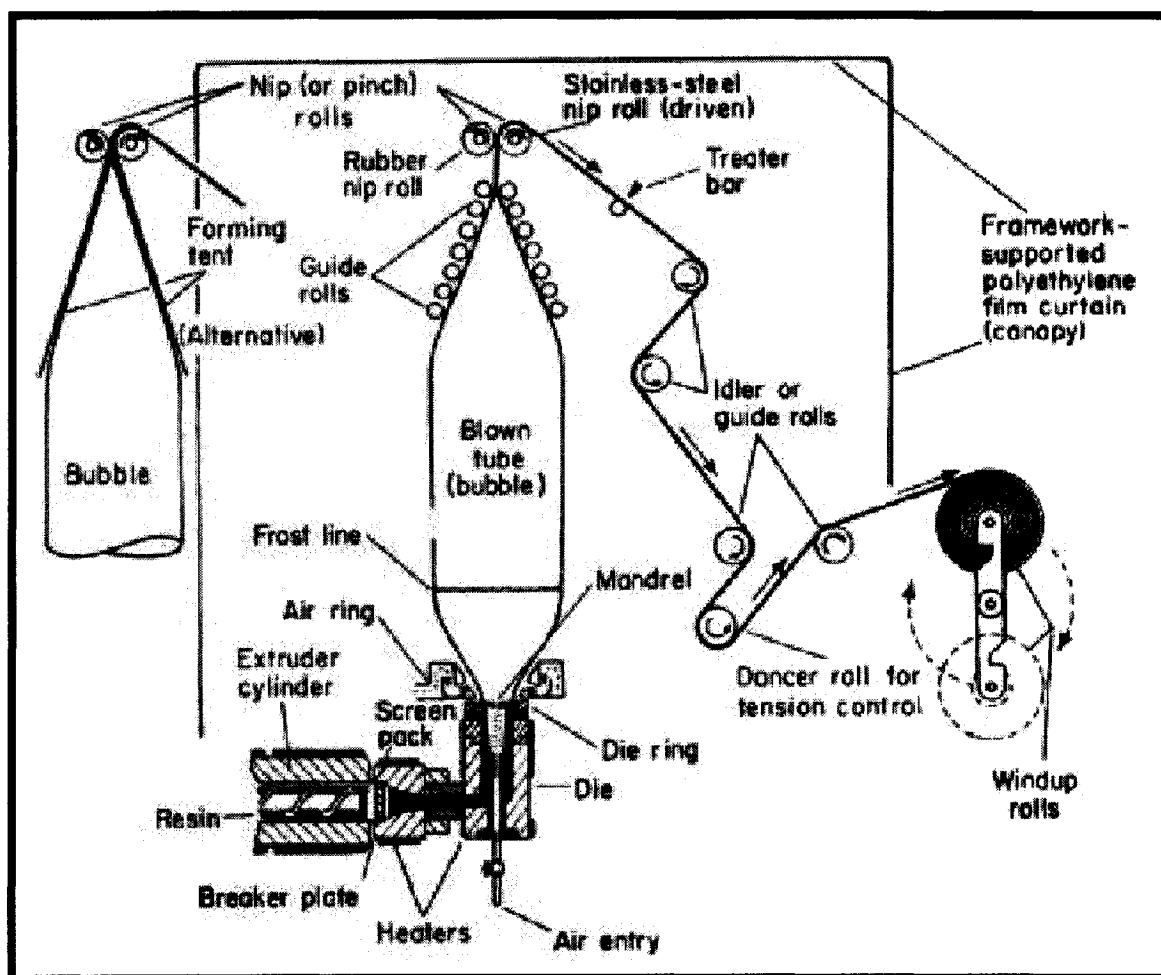


Figure A1: The stages of the entire process from the extruder to the windup rolls.

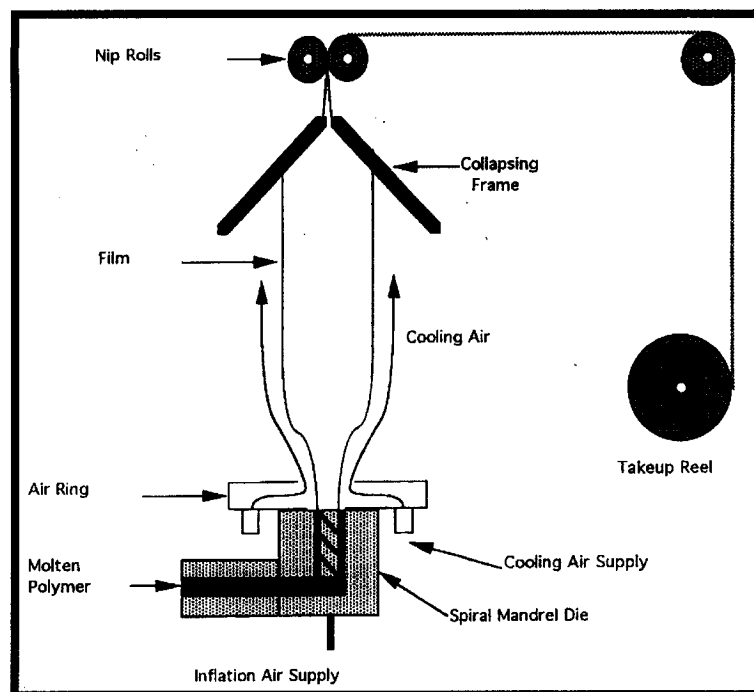


Figure A2: Schematic of the film blowing process.

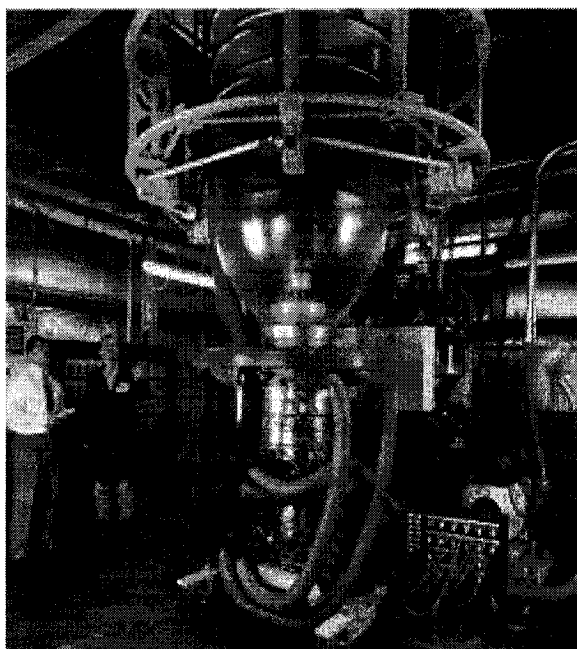


Figure A3: The film is shaped into a large tube of thin membrane.

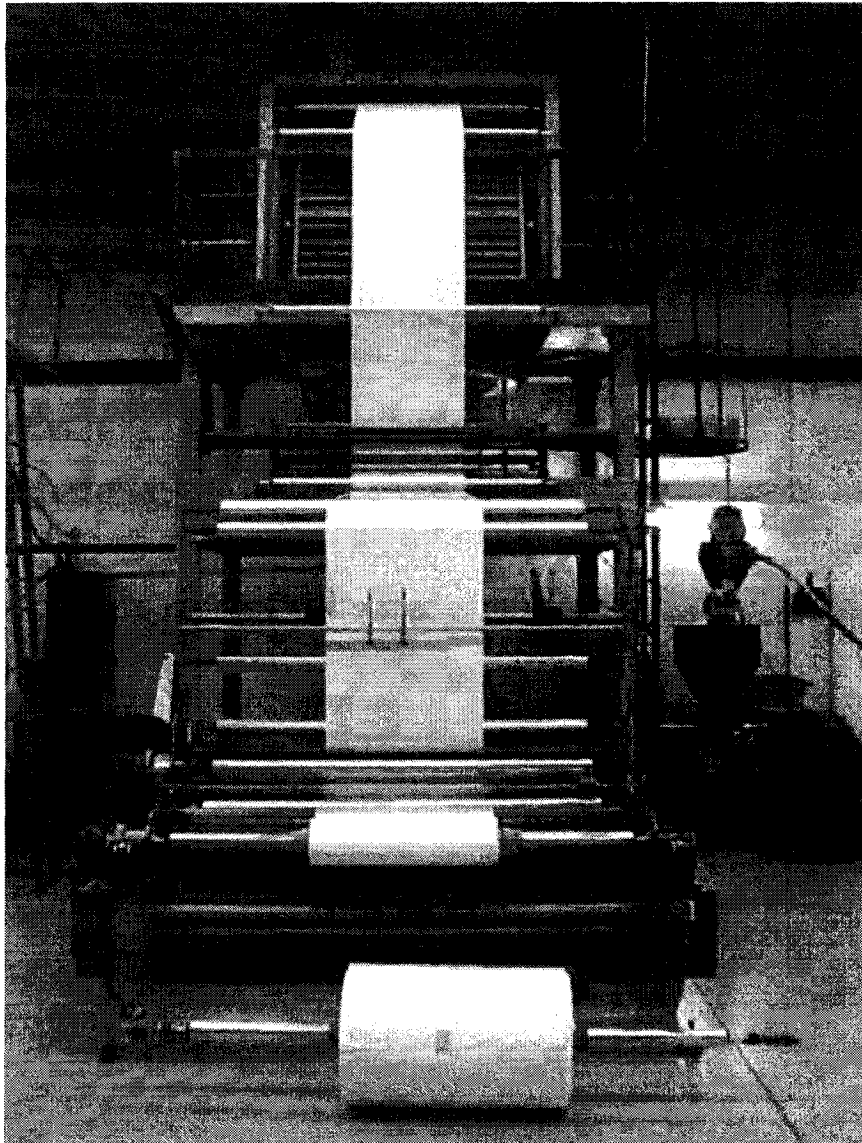


Figure A4: the tube becomes flat sheet at the windup roll

## APPENDIX B

### Polymer Ultimate Crystallinity ( $X_{\infty}$ )

One of the important aspects of this work is that it employs a realistic function for the crystallization kinetics based on experimental data. It incorporates the ultimate crystallinity, which is also based on experimental data. The ultimate crystallinity is defined as a sigmoidal function of temperature (Equation A1). Lungu conducted a series of isothermal experiments on various PE resins. He employed differential scanning calorimetry (DSC) and a method proposed by Kamal and Chu (1983) to eliminate errors that may occur because of the transient response. The resin was kept at the selected temperatures for a long time to determine the crystallization kinetics and the ultimate crystallinity at different temperatures. The results exhibited good reproducibility and accuracy. Equation A1 was obtained by fitting Lungu's data.

$$\chi_{\infty} = \frac{a_1}{1 + \exp\left(\frac{T - a_2}{a_3}\right)} \quad (\text{A1})$$

The constants in the above equation are shown in Table A1.

Table B1: The characteristic constants employed in the ultimate crystallinity function.

Resin	$a_1$	$a_2(^{\circ}\text{C})$	$a_3(^{\circ}\text{C})$
C587, C863, and C24-C34	0.43	107.6	7.8
D582	0.42	101.9	4.02
F751	0.41	96.81	4.0
G583	0.44	104.0	4.5
H866	0.50	106.6	10.6

## Isothermal Experiments

Lungu (2000) followed the following procedure in conducting the isothermal experiments and followed a method proposed by Kamal and Chu (1983) to eliminate any errors may occur because of the transient response.

1. A temperature range of 16-20°C, which was employed in the isothermal experiment was decided from the nonisothermal data.
2. The isothermal experiments were conducted above and below the reference temperature, which is the temperature where the highest crystallization rate was observed.
3. A different sample was used at each temperature in the isothermal experiments.
4. The heat of fusion absorbed by one gram of crystallizing melt during the experiment was measured.
5. In each experiment, an initial isothermal holding at 50°C was maintained for 5 minutes to bring the sample to apparatus temperature. Then, the sample is heated from 50°C to 180°C at a rate of 10°C/min.
6. At 180°C, the sample was held for 5 minutes to erase the previous thermal history.
7. After the 5 minutes holding time, the sample was quenched at a high cooling rate of 100°C/min until it reached the selected isothermal crystallization temperature.
8. The sample was held at that isothermal temperature for 15-120 minutes until the crystallization was complete, which was indicated by the termination of the heat flow increase on the instrument panel. The heat flow remains constant when ultimate crystallization is reached.
9. Once the crystallization was complete, the sample was heated again to 230°C at a rate of 10°C/min and held for 5 minutes.
10. Then, a cooling was carried out at a cooling rate of 100°C/min to bring the sample to a final temperature of  $T_f = T_{iso} + 50$ . This final temperature is usually higher than the experimental melting temperature, which ensured no crystallization took place.

11. Superimposing the two plots gives the area corresponding to the true crystallinity, and minimizes the errors due to the baseline (Figure A1).
12. The above procedure along with the following steps suggested by Kamal and Chu (1983) eliminate the transient and heat transfer effects.
13. Because the heat cannot be released from the sample (even for very small sample) fast enough to reach the match the programmed temperature, the system exhibits a transient response (Figure A2) as it approaches the true isothermal state. Therefore, steps 10 and 11 ensured elucidating the period of time before a detectable signal could be read from the instrument. This time is referred to as the induction time ( $\tau^*$ ).
14. The crystallinity is measure from the aforementioned time ( $\tau^*$ ) onwards. Figures A3 and A4 show that there is no crystallization is taking place before the induction time.

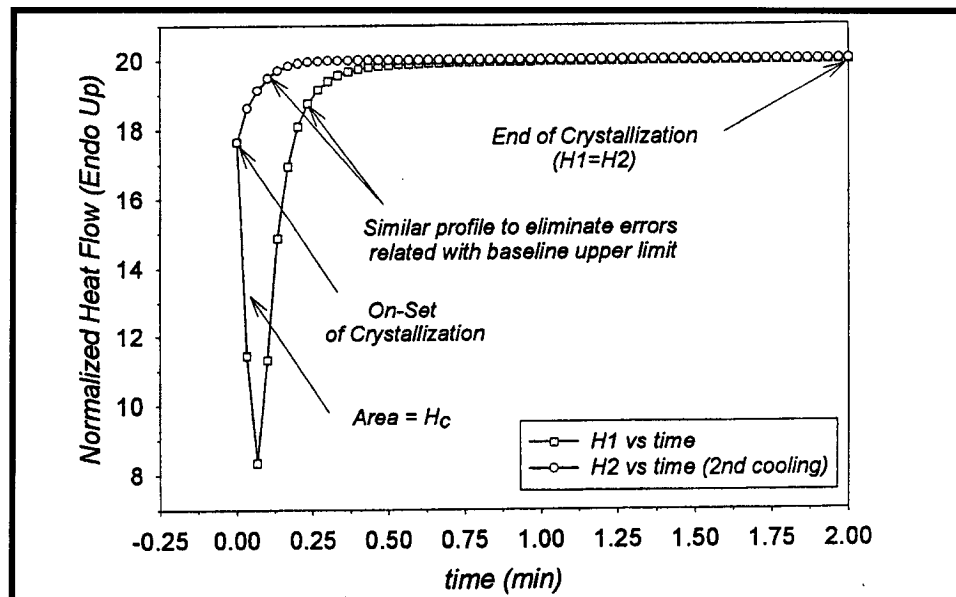


Figure B1: Typical crystallization peaks (H1-first heating, H2-second heating, after crystallization).



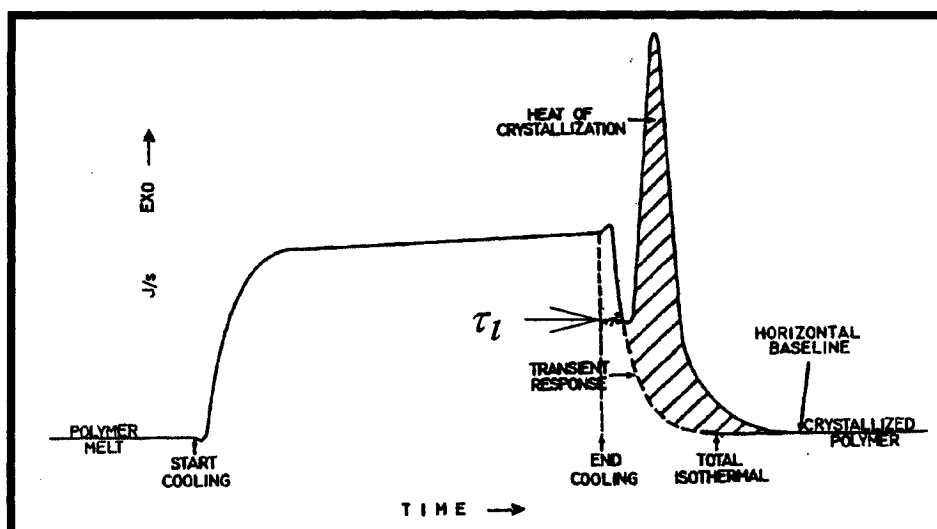


Figure B2: Transient response effect in an isothermal experiment.

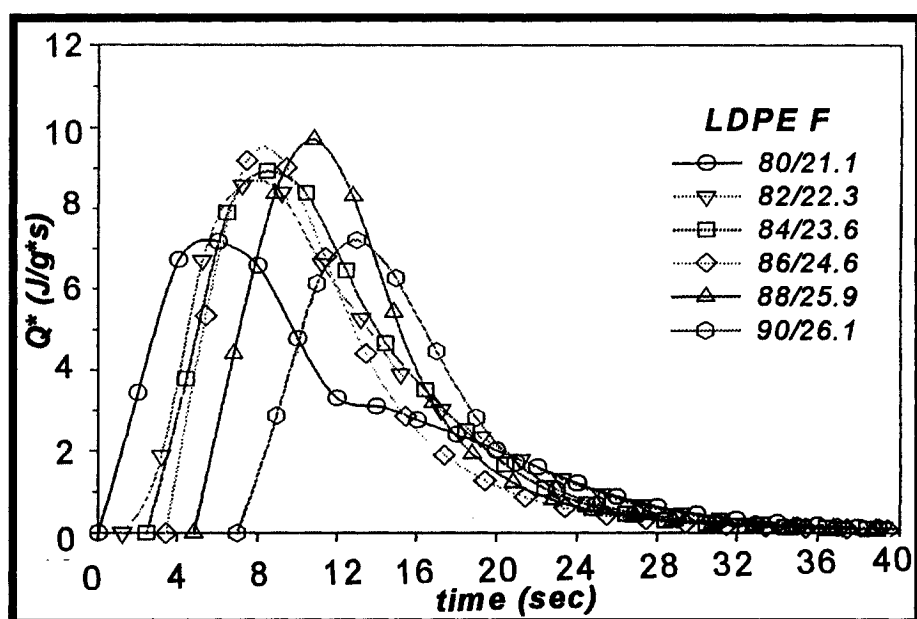


Figure B3: Isothermal exotherms for resin F751 at various isothermal temperatures.

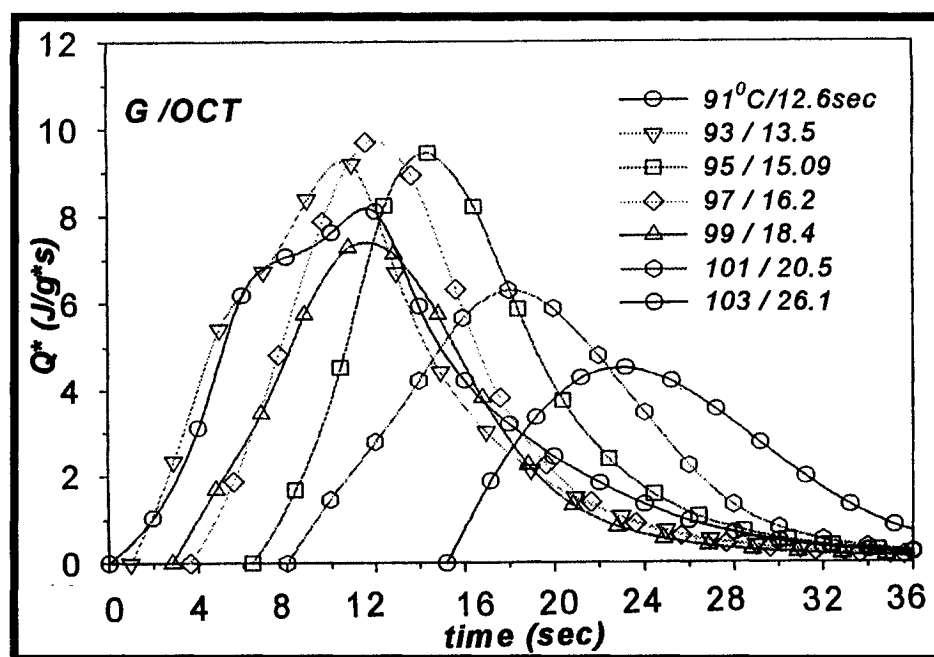


Figure B4: Isothermal exotherms for resin G583 at various isothermal temperatures.